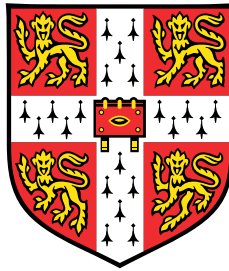


On the topological properties of the vibrations of solids



Bo Peng

彭博

Department of Physics
University of Cambridge

This dissertation is submitted for the degree of
Doctor of Philosophy

St John's College

July 2023

I would like to dedicate this thesis to my loving family.
献给我的家人。

Declaration

This thesis is the result of my own work and includes nothing which is the outcome of work done in collaboration except as declared in the Preface and specified in the text. I further state that no substantial part of my thesis has already been submitted, or, is being concurrently submitted for any such degree, diploma or other qualification at the University of Cambridge or any other University or similar institution except as declared in the Preface and specified in the text. It does not exceed the prescribed word limit for the relevant Degree Committee.

Bo Peng
彭博
July 2023

Acknowledgements

This thesis marks the end of my journey of being a student for 23 years. Through this journey, I have received tremendous help from my supervisors and my fellow colleagues, and I would like to thank my last and best supervisor, Prof. Bartomeu Monserrat. Tomeu and I got acquainted by email correspondence on electron-phonon coupling in the spring of 2018. He always replied in a few minutes, so I decided to visit Cambridge to work with him for six months. Despite being a visiting student, I was welcomed warmly by Tomeu and his group, as well as the TCM community. I immediately started thinking of Cambridge as home and decided to pursue a PhD here. It is always a privilege to work with Tomeu, as he always takes care of both my science and my career. In my very first project, he taught me hand by hand to demonstrate the way he does science, and then trained me to be as independent as possible in subsequent projects. At the end of my PhD, I am confident enough to start my independent research, thanks to Tomeu's leading by example.

The Monserrat group has always been infinitely supportive throughout my PhD and beyond. I am extremely grateful to my friend Ivona Bravić for bringing so many chemical insights into my various research projects, from topological materials to optical properties of halide perovskites. A special gratitude goes to Gunnar Felix Lange for being both a good friend and an excellent collaborator: We went to plenty of fun events such as fake horse racing and cycling along Hadrian's Wall, and Gunnar always calmed me down whenever my zealotness in life or science went too far. I am also very grateful to Yuchen Hu, a fellow Nanjinger in a foreign land, for getting me involved in all the marvelous parties and for helping me compile all the packages in my first term. I also want to thank Alya Bin Thabet Alqaydi for the massive support in coding and for organising so many interesting group events, Siyu Chen for all the interesting chats on both physics and life, Arjun Ashoka for all the sharp questions and feedback in our group meeting, Dr Sun-Woo Kim for the insights in physics and for always being nice and friendly, as well as Dr Yun Liu, Can Koçer, Antonios Alvertis, Alan Bowman, Bingcan Li, Sunil Taper and the rest of the group for all the help.

I would not have been able to finish this thesis without all my collaborators. I would like to thank Dr Tiantian Zhang for walking me through the group theory analysis and topological diagnosis, and Prof. Shuichi Murakami for the intuition in physics. A particular gratitude

goes to Dr Adrien Bouhon and Dr Robert-Jan Slager, who provided me such wonderful opportunities in working on incredibly hard but exciting projects of multi-gap topology and non-Abelian braiding with them. I am also grateful to Danny Bennett for being a super helpful collaborator and friend in a variety of projects in physics and beyond including photostriction in perovskites, as well as growing chillies, tomatoes and mushrooms. Some of my side projects continued from my Master's research, and I would like to thank all my previous supervisors and collaborators, especially Prof. Hao Zhang, Prof. Heyuan Zhu, Prof. Hongming Weng, Prof. Hezhu Shao and Prof. Desheng Fu for all the support and guidance. I am also grateful to my experimental collaborator Yujun Xie, Boyao Liu, Dr Ziqi Li and Dr Kai-Qiang Lin for making me participate in so many enjoyable joint projects. I also want to thank all my collaborators in ongoing projects, in particular, Pascal Salzbrenner, Dr Chuck Witt and Prof. Chris Pickard for helping me set up all the structural searches, and Dr Michele Simoncelli for inviting me to the exciting project on electron-phonon hydrodynamics, as well as Jenny Coulter for always being responsive to my emails within a few minutes. A special thanks goes to all my summer and Part III students, especially Juan D. F. Pottecher, Cameron Robey and Cory Jones, who helped me so much by their hard work.

Working in the TCM group always makes me super happy. I would like to thank Prof. Mike Payne for all the generous offers especially in drinks, Dr Michael Rutter for his magic in IT technology, Prof. David Khmel'nitskii for all the lectures and fairy tales, and Prof. Brian Josephson for being extremely patient when I hosted his seminar at both Lindau and TCM. A special thanks goes to Ivona Bravić, Tobias Schaich, Ariel Barr, Zuzhang Lin, Siyu Chen, Dr Jan Behrends and Dr Kadin Thompson for being such fantastic office mates. I also want to thank Gunnar Felix Lange, Danny Bennett, Beñat Mencia, Bora Karasulu, James Darby, P-L Chau, Wojciech Jankowski and Alaric Sanders for always being around the coffee area. In particular, I would like to express my gratitude to Angela F. Harper, who helped me go through my PhD application so I could secure my funding to work in the TCM group. Speaking of my funding, I would like to thank the Winton community, especially Dr Lata Sahonta and Dr Nalin Patel, for admitting me into the Winton Programme for the Physics of Sustainability, where I met plenty of friends in experimental physics such as Rakesh Arul and Filip Bošković.

In my third year, I spent three months in Rome to visit the Institute of Structure of Matter of the National Research Council (ISM-CNR). I am always passionate about Roman history ever since I was a kid, and walking from the Milvian Bridge to the Portico of Octavia and to the Theatre of Pompey was just like travelling back in history in a time-ordered way, not to mention cycling along the Appian Way. I am extremely grateful to Prof. Andrea Marini for hosting me in an institute surrounded by the Sabine Mountains and Etruscan tombs, for

showing me how to do physics by pencil and paper, and for introducing me into the beautiful mathematical formulations of non-equilibrium Green's function. A special thanks goes to Dr Fulvio Paleari for answering my questions on a daily basis, for helping me set up in a non-English speaking neighbourhood, and for providing guided tours around the eternal city of Rome. I would also like to thank Francesco Filippone, Giuseppe Mattioli and Gloria Zanotti for always taking me to lunch, for buying me Espresso every day, and for trying very hard not to speak Italian in front of a foreigner.

Despite being trapped in Cambridge without going home for four years because of the COVID-19 pandemic, I spent a happy time with my friends in St John's College, including Alexander Joseph Kusztyk, Leo Steele and the rest of the casual football players; Billy Wright, Damon Kutzin and the rest of the St John's Yales basketball club; Tom White and the rest of the gardening society; every one in the St John's beekeepers society; Dr Morgan Ng, Jovian Hch, Kilian Bachmair, as well as Xi Fang & Giovanni A. Oakes, Dommy Goddard & Leopold Kloyer. I also want to thank the entire team of the play *Copenhagen*, who gave me a chance to play the role of the German physicist Werner Heisenberg so I could both be a physicist and play a physicist at the same time. A special thanks goes to the director Jing Wang, my friend Zhengkang Qu and Prof. David Weiguo Jiang. I also want to thank the Chinese squad in Cambridge: Kehan Zhang & Zhe Xue, Canhui Liu, Zhenbin Zuo, Zhengkang Qu, Zucheng Gao, Heqing Huang, Chang Zhang & Lianglun Lai, Li Peng, Yucheng Wang, Jingze Yuan, Xiao Chen & Zihan Yan, Yunjiang Zhang & Guandong Bai, Ziyue Zeng & Zhimian Hao.

I feel an enormous gratitude to Magdalene College, especially Sir Chris Greenwood, Prof. Brendan Burchell, Prof. Paul Dupree, Prof. Stuart Martin, Sir David Clary, Prof. Jonathan Yates, and the rest of my interview panel, who offered me a Nevile Research Fellowship to start my independent research. I would like to thank Dr Nicholas Carroll, Dr Tijmen Euser, Prof. Tom Licence, Prof. Agnieszka & Colm Whelan, Prof. Franklin Aigbirhio, Prof. Neil Jones, Silke Mentchen, Alistair Mills and Dr Vitali Vitaliev for all the wonderful discussion over lunches/dinners. I am also grateful to Prof. Eamon Duffy, Prof. James Raven, Corinne Lloyd, Dr John Patterson, Dr Annja Neumann, James Potter, Mrs Aude Fitzsimons and Reverend Sarah Atkins for welcoming me to the Magdalene community. In particular, I want to thank Dr Peter Asimov, Dr Daniel Dunkelmann, Dr Hannah Marshall, Dr Cecily Whiteley, Millicent-Rose Newis, Dr Adrian Baez-Ortega and the rest of the Junior Fellows who are absolutely fantastic in serving drinks with me in the Senior Combination Room. A particular thanks goes to Ishbel Bruce for helping me set up my life in Magdalene. I also want to thank Prof. Simon Stoddart for bringing two extremely heavy 19th century bronze sculptures to

my room, and Mr Jonathan Hellyer Jones for always being charming and for playing all the beautiful 17th century music.

Last but not least, I cannot express how thankful I am to my family, especially my parents and grand parents, for their endless love and support. I shall always be infinitely grateful to my love, Jin Qin: We fell in love on the same day I secured my offer from Cambridge when we were enjoying the beautiful night view of Kotor from an abandoned Byzantine fortress built by Justinian I. We have shared so many wonderful memories afterwards, including beekeeping, gardening, newt hunting, keeping hamsters/fish/stick insects and going to the Battle of Waterloo reenactment. On my PhD journey and beyond, she is always the star shining upon me.

Abstract

This thesis presents the study of the topological properties in the atomic vibrations in solids. The state-of-the-art quantum mechanical simulation techniques are presented first to accurately describe the band structures of electrons and vibrational spectra of nuclei for topological analysis. Two concepts are introduced to investigate the non-trivial band crossing in the vibrational spectra. Depending the number of phonon bands and the intrinsic crystalline symmetry, the topological invariant carried by the band crossing can either be an integer number for a two-band subspace or a non-Abelian frame charge when at least three bands are involved. The phonon band crossing formed in a two-band subspace is simply a replica of topological semimetals in electronic systems, although the intrinsic properties of phonons, including the preservation of time-reversal symmetry and the accessibility of the bosonic excitation spectra, indicate that such single-gap topological properties are ubiquitous in phonons. Taking a step further, when three or more bands are included, these intrinsic properties provide unique advantages for phonons to fulfill the requirements for multi-gap topology, rendering phonons as the primary platform to study non-Abelian braiding. The possible experimental signatures are also described and predicted.

Table of contents

List of figures	xvii
List of tables	xix
1 Introduction	1
1.1 A historical note	1
1.2 Thesis outline	3
2 Theoretical formalism	5
2.1 Density functional theory	5
2.1.1 Many-electron wave function	6
2.1.2 Hohenberg-Kohn theorem	7
2.1.3 Kohn-Sham equations	7
2.1.4 Wannier functions	9
2.2 Lattice dynamics	10
2.2.1 Adiabatic approximation	10
2.2.2 Harmonic approximation	11
2.2.3 Phonon eigenvalues and eigenvectors	13
2.3 Topological analysis	13
3 Single-gap topology in semimetals	17
3.1 Classification of topological semimetals	17
3.1.1 Nodal-line semimetal	18
3.1.2 Weyl semimetal	19
3.1.3 Dirac semimetal	20
3.2 Topological phase transitions in β -PbO ₂	21
3.2.1 Computational details	21
3.2.2 Ground state properties of β -PbO ₂	21
3.2.3 Strain-induced topological phase transitions	23

3.2.4	Temperature-promoted gap closing	26
3.3	Conclusions and outlook	29
4	Single-gap topology in phonons	31
4.1	Recent developments of topological phonons	32
4.2	Topological phonons in oxide perovskites	32
4.2.1	Computational details	33
4.2.2	Structural phases of BaTiO ₃	34
4.2.3	Topological phonons in BaTiO ₃	36
4.2.4	Controlling topological phonons by light	37
4.2.5	Topological phonons in PbTiO ₃ and SrTiO ₃	38
4.2.6	Discussion	40
4.3	Conclusion	41
5	Surface topology of phonons	43
5.1	Degeneracies in the bulk and surface bands	43
5.2	Surface nodal line in quasi-1D double-helix crystal SnIP	44
5.2.1	Computational details	45
5.2.2	Crystal structure and phonon dispersion	46
5.2.3	Nodal ring phonons in SnIP	48
5.2.4	Topological surface states of SnIP	50
5.3	Conclusions and outlook	53
6	Multi-gap topology in phonons	55
6.1	Multi-gap topology	56
6.2	Theoretical background	57
6.2.1	Non-Abelian frame charges	57
6.2.2	Patch Euler class	60
6.2.3	Dirac strings	62
6.2.4	Global topological configuration	63
6.3	Case study: phonon braiding in monolayer Al ₂ O ₃	65
6.3.1	Computational details	65
6.3.2	Crystal structure and phonon dispersion	67
6.3.3	Band inversion upon electrostatic doping	67
6.3.4	Frame charges of undoped Al ₂ O ₃	69
6.3.5	Frame charges of -0.08 <i>e/f.u.</i> -doped Al ₂ O ₃	71
6.3.6	Frame charges of -0.10 <i>e/f.u.</i> -doped Al ₂ O ₃	72

6.3.7	Frame charges of -0.20 <i>e/f.u.</i> -doped Al ₂ O ₃	74
6.3.8	Complete picture of braiding upon doping	75
6.3.9	Topological edge states	76
6.4	Conclusions and outlook	78
7	Non-Abelian braiding of phonons: From three bands to four bands	81
7.1	Introduction	82
7.2	Non-Abelian braiding of phonons in monolayer silicates	82
7.2.1	Computational details	82
7.2.2	Silicates	83
7.2.3	Phonon band structure	84
7.2.4	Electric field induced band inversions and braiding	84
7.2.5	Three-band braiding in group 1	86
7.2.6	Four-band braiding in groups 2 and 3	92
7.2.7	Edge states	94
7.2.8	Experimental signature: Raman spectra	95
7.3	Conclusion	96
8	Side projects	97
8.1	Tunable emission of Nd-doped CsPbBr ₃	98
8.1.1	Accurate description of the band gap of CsPbBr ₃	98
8.1.2	Dopant-induced band-gap blueshift	99
8.1.3	Enhanced photoluminescence quantum yield	101
8.1.4	Summary	102
8.2	Tunable photostriction of halide perovskites	102
8.2.1	Photostriction in halide perovskites	103
8.2.2	Microscopic mechanism	103
8.2.3	Overall effects	106
8.2.4	Summary	108
8.3	Photo-induced phase transition in monolayer MoTe ₂	109
8.4	Phonon-assisted electronic states modulation of PdSe ₂	110
8.5	Monolayer fullerene networks	112
8.5.1	Monolayer fullerene networks as photocatalysts for water splitting	112
8.5.2	Stability and strength of monolayer polymeric C ₆₀	113
9	Conclusions and outlook	117
9.1	Non-Abelian braiding of nodal lines	118

9.2	Light-switchable topological phases	118
	References	121

List of figures

2.1	Topological analysis.	14
3.1	Classification of topological semimetals.	19
3.2	Ground state properties of β -PbO ₂	22
3.3	Strain effects.	24
3.4	Topological properties.	24
3.5	Temperature effects.	27
3.6	Strain-temperature phase diagram.	28
4.1	Topological phonons in tetragonal BaTiO ₃	35
4.2	Light-controlled topological properties.	36
4.3	Weyl phonons in BaTiO ₃	38
4.4	Topological phonons in tetragonal PbTiO ₃	39
4.5	Topological phonons in tetragonal SrTiO ₃	40
5.1	Types of topological surface states.	45
5.2	Structural and vibrational properties of SnIP.	47
5.3	Topological properties of SnIP.	48
5.4	Topological surface states of SnIP.	50
5.5	Zak phase analysis.	52
6.1	Multi-gap topology and non-Abelian braiding.	59
6.2	Patch Euler class for two nodes.	61
6.3	Sign of the frame charge.	63
6.4	Dirac strings.	63
6.5	Monolayer Kagome Al ₂ O ₃	68
6.6	Evolution of phonon bands upon doping.	68
6.7	Multi-gap topology of undoped Al ₂ O ₃	70
6.8	Multi-gap topology of -0.08 <i>e</i> /f.u.-doped Al ₂ O ₃	72

6.9	Multi-gap topology of -0.10 <i>e/f.u.</i> -doped Al_2O_3	73
6.10	Multi-gap topology of -0.20 <i>e/f.u.</i> -doped Al_2O_3	74
6.11	Topological configurations upon doping.	75
6.12	Topological edge states.	77
7.1	Phonons in monolayer Kagome silicate Si_2O_3	84
7.2	Braiding of phonons in group 1.	88
7.3	Euler class calculations.	91
7.4	Braiding of phonons in groups 2 and 3.	93
7.5	Raman signature.	96
8.1	Optical properties of $\text{CsPbBr}_3:x\text{Nd}^{3+}$ nanocrystals.	100
8.2	Band structures of CsPbBr_3	101
8.3	Lattice constants of CsPbBr_3 under selective excitations.	105
8.4	Photostriction of CsPbBr_3	107
8.5	Excited state potential-energy surface of monolayer MoTe_2	110
8.6	Lattice dynamics and electron-phonon coupling in PdSe_2	111
8.7	Photocatalysis of monolayer fullerene networks.	113
8.8	Thermodynamic stability of monolayer fullerene networks.	115

List of tables

3.1	Ground state properties of β -PbO ₂	23
8.1	Calculated band gaps of CsPbBr ₃	99

Chapter 1

Introduction

1.1 A historical note

On August 26, 1735, half a decade before the continuing political turmoil in Russia, the 28-year-old Leonhard Euler presented a paper on the Seven Bridges of Königsberg problem to the Academy of Sciences in St Petersburg. In this paper, he ascribed the Königsberg problem to the geometry of position (*geometria situs*), as “neither geometry, nor algebra, nor even the art of counting was sufficient to solve it” [1]. He reformulated the problem as a graph: by replacing the land mass with an abstract node, only the evenness and oddness of the number of bridges touching the node is relevant. This prefigured the idea of topology, which is not concerned with the distance or shape, but the integer related to global structures such as the number of the bridges [2].

The concept of topology was introduced to condensed matter systems in the 1980s [3]. Condensed matter systems represent many-particle systems such as electrons and nuclei that can be described by quantum mechanics, whose whole foundation is based on the initial discoveries in the 1920s. Werner Heisenberg first made the breakthrough in his paper in 1925, “Quantum-theoretical reinterpretation of kinematic and mechanical relations” [4], and after two months Max Born and Pascual Jordan formulated Heisenberg’s theory into matrix mechanics in their paper “On quantum mechanics” [5, 6]. In the spring of 1926, Erwin Schrödinger introduced the concept of wave function in his wave mechanics [7, 8]. To find a relativistic wave equation of the electron, Paul Adrien Maurice Dirac, a Research Fellow at St John’s College Cambridge, proposed the Dirac equation in two papers published in 1928 [9, 10], forming the basis of all of Chemistry and almost all of Physics [11]. One year later, Hermann Weyl predicted the massless fermions with a definite handedness based on a simplified version of the Dirac equation for relativistic particles [12, 13]. In 1937, the same year when Ettore Majorana introduced the concept of a particle satisfying the

Dirac equation that is its own antiparticle [14], Conyers Herring found that Weyl fermions may exist as quasiparticles in the electronic energy bands of solids with certain crystalline symmetry [15] based on the avoided crossing theorem proposed by John von Neumann and Eugene Paul Wigner in 1929 [16]. For example, when two bands touch in a nonmagnetic material without inversion symmetry, the degenerate points act as sources and sinks of the quantised Berry flux through any local isoenergy surface enclosing the node, where the flux of the Berry curvature [17] is defined as the Chern number [18] and the point-like degeneracies are referred to as the Weyl points. Recent years have witnessed a surge of publications on material candidates with such topological properties in their band structures, based on the foundation laid by Charles Kane, Eugene Mele and Shou-Cheng Zhang [19–22].

The discovery of phonons occurred in parallel with the development of quantum theory. In 1900, Lord Kelvin delivered the famous speech on the two “clouds” [23], with the second problem being the question of the equipartition theorem to the heat capacity that drives the development of quantum physics [24]. In 1907, Albert Einstein applied Max Planck’s work on energy quanta [25, 26] to the specific heat of solids, and assumed that the solids contain a large number of independent quantum harmonic oscillators in three dimensions with the same vibrational frequency [27]. In 1912, Peter Debye realised that the vibrations in solids are not independent oscillations of individual atoms, but collective modes similar to a sound wave, providing better predictions of the specific heat at low temperatures [28]. Based on Dirac’s ideas on second quantisation for quantum many-body states [29], Igor Tamm introduced the concept of “elastic quanta” of the crystal lattices in 1930 [30], while Jacov Il’ich Frenkel referred to such excitations as “heat quanta” and “sound quanta” [31, 32]. Shortly afterwards, the concept of phonons was formally introduced in Frenkel’s book *Wave Mechanics: Elementary Theory* (1932) [33]. In 1933, the same year when Schrödinger left Germany and became a Fellow of Magdalen College at Oxford, Hans Gustav Adolf Hellmann started working on understanding the interatomic forces through quantum mechanics, dealing with adiabatic nuclear dynamics that form the basis for lattice dynamics [34]: the research was interrupted when Hellmann was forced to leave Germany and went to the Soviet Union in 1934 (which eventually proved fatal). In 1954, Max Born and Kun Huang contributed fundamentally to the field of phonons by publishing the book *Dynamical Theory of Crystal Lattices* [35]. In his monumental tome *Electrons and Phonons: The Theory of Transport Phenomena in Solids* published in 1960, John Ziman provided a unified picture in understanding the transport properties of both electrons and phonons [36].

1.2 Thesis outline

The topic of this thesis is the application of quantum mechanical techniques developed for studying the intrinsic vibrational properties of solids to understand the topological properties of phonons. I introduce the concepts of single-gap and multi-gap topologies in band structures of quasiparticles including electrons and phonons. I demonstrate that, while the single-gap topology of phonons is analogous to electronic topology, phonons can be a primary platform to study multi-gap topology because of their intrinsic properties as charge neutral, spinless bosonic excitations.

In Chapter 2 I describe density functional theory that enables the description of electronic structures of solids and forms the basis for computing lattice dynamics.

In Chapter 3 I introduce the concept of single-gap topology in electronic topological semimetals and provide an example of single-gap topology in PbO_2 promoted by temperature effects including electron-phonon coupling and thermal expansion.

In Chapter 4 I extend the idea of topology from electrons to phonons and confirm the existence of topological phonons in a well-known material family called oxide perovskites. I show that the topological properties of oxide perovskites can be controlled by light, e.g. the creation and annihilation of the Weyl points, and the switch between nodal lines and nodal rings.

In Chapter 5 I discuss the advantages of phonons, compared to electrons, when studying topological properties on the surface. While degenerate lines in the surface states are hard to form in electronic systems, I present an example of the formation of degenerate lines in the phonon surface states of a quasi-one-dimensional van der Waals material SnIP .

In Chapter 6 I give a detailed description of multi-gap topology and its application in phonons. Multi-gap topology involves at least three phonon bands and can be characterised by the non-Abelian frame charges carried by the phonon band crossing points. I predict that a 2D material that was first synthesised decades ago can realise multi-gap topology in the phonon bands.

In Chapter 7 I show the first material candidate for non-Abelian braiding of phonons that involves more than three phonon bands. I predict the edge states of multi-gap topology, and propose that Raman spectroscopy can be used to observe the phonon band inversion accompanied by non-Abelian braiding.

In Chapter 8 I present a few side projects, including optical properties of rare-earth doped CsPbBr_3 , photostriction in halide perovskites, electron-phonon coupling in PdSe_2 , photo-induced phase transition in MoTe_2 , and monolayer fullerene networks.

In the end, in Chapter 9 I summarise the results presented in the thesis and outline my future research plans based on the thesis.

Chapter 2

Theoretical formalism

In this chapter I present an overview of the quantum mechanical calculations that allow us to understand the band structures of electrons and vibrational spectra of nuclei. I introduce the theoretical formalism of density functional theory that forms the starting point of all the results presented in this thesis. In the latter part of this chapter I explain the approximations to separate the electronic and nuclear motions, and discuss the computational frameworks to calculate the vibrational properties of solids.

2.1 Density functional theory

In his letter to Niels Bohr in 1929, Paul Dirac demonstrated that the simple problem of an electron scattered by a photon is no longer a two-body problem, but an infinite-body problem, because quantum mechanics plus relativity leads to an infinite sea of particles with infinite degrees of freedom [37]. This means that solving the quantum mechanical equations becomes increasingly difficult as the number of particles increases. As summarised by Paul Dirac in the famous quote [11]:

“The underlying physical laws necessary for the mathematical theory of a large part of physics and the whole of chemistry are thus completely known, and the difficulty is only that the exact application of these laws leads to equations much too complicated to be soluble. It therefore becomes desirable that approximate practical methods of applying quantum mechanics should be developed, which can lead to an explanation of the main features of complex atomic systems without too much computation.”

Density functional theory represents one of such practical methods of applying quantum mechanics to study the many-electron problem in atoms, molecules and solids and

is extensively used in condensed matter physics, materials science, chemistry and related fields [38–40]. To solve Schrödinger’s wave equation for systems with many electrons, a large number of Slater determinants is required, which is generally too complex to solve exactly and thus precludes an accurate description of the many-electron wave function even with the help of modern supercomputers. As an alternative, density functional theory replaces the many-electron wave function with the electron density $n(\mathbf{r})$ in the real, three-dimensional coordinate space. With this approach, it is possible to study large and complex systems such as real materials and biological molecules. Today, density functional theory is one of the most widely used and versatile methods for studying the electronic structure of matter, and has enabled many breakthroughs in condensed matter physics, materials science and related fields.

2.1.1 Many-electron wave function

The nonrelativistic eigenvalue equation of the Hamiltonian for the many-electron wave function Ψ is the foundation of the theory of electronic structure [40],

$$\left(-\frac{\hbar^2}{2m} \sum_j \nabla_j^2 - \sum_{j,l} \frac{Z_l e^2}{|\mathbf{r}_j - \mathbf{R}_l|} + \frac{1}{2} \sum_{j \neq j'} \frac{e^2}{|\mathbf{r}_j - \mathbf{r}_{j'}|} - E \right) \Psi = 0, \quad (2.1)$$

where \hbar , m and e are the conventional fundamental constants, \mathbf{r}_j and \mathbf{R}_l are positions of the electrons j and nuclei l respectively, Z_l are the atomic numbers of the nuclei, E is the total energy, and Ψ depends on the positions of N electrons (neglecting their spin),

$$\Psi = \Psi(\mathbf{r}_1, \mathbf{r}_2, \dots, \mathbf{r}_N). \quad (2.2)$$

Equation (2.1) is often called the (time-independent) Schrödinger equation for the many-electron wave function, and all physical properties depend parametrically on the wave function $\Psi(\mathbf{r}_1, \mathbf{r}_2, \dots, \mathbf{r}_N)$, total energy E , and \mathbf{R}_l . In particular, physically interesting quantities such as the density $n(\mathbf{r})$ can be obtained by tracing over all other variables:

$$n(\mathbf{r}) = N \int |\Psi(\mathbf{r}, \mathbf{r}_2, \dots, \mathbf{r}_N)|^2 d\mathbf{r}_2 \dots d\mathbf{r}_N. \quad (2.3)$$

Interestingly, density functional theory can be derived from the Schrödinger equation for the many-electron wave function in terms of the density $n(\mathbf{r})$ and single-particle wave function $\phi_j(\mathbf{r})$ based on the Hohenberg and Kohn theorem proposed in 1964 [38] and the self-consistent Kohn-Sham equations proposed in 1965 [39].

2.1.2 Hohenberg-Kohn theorem

The Hohenberg-Kohn formulation of density functional theory is a fundamental framework in quantum mechanics that provides a rigorous and powerful method for describing the electronic structure of many-electron systems. It was developed by Pierre Hohenberg and Walter Kohn in 1964 [38].

In the Schrödinger equation for the many-electron wave function, the electronic structure of a system is described by a wave function that contains all the information about the system's electrons. However, solving such Schrödinger equation becomes increasingly difficult as the number of electrons increases. This limitation led Hohenberg and Kohn to propose an alternative approach based on the electron density.

The central idea of the Hohenberg-Kohn formulation is that the ground-state electron density $n(\mathbf{r})$ uniquely determines the external potential energy $v(\mathbf{r})$ of a system and, consequently, all other ground-state properties, which is referred to as the first theorem of the Hohenberg-Kohn formulation. In other words, the electron density, as an observable in 3D space, is the fundamental variable in density functional theory, and can be used to describe the complex physics underlying the interactions between electrons. The first theorem implies that the ground-state energy is a functional of the density $n(\mathbf{r})$, i.e., $E[n(\mathbf{r})]$.

The second theorem of the Hohenberg-Kohn formulation is known as the Hohenberg-Kohn variational principle. This means that the ground-state energy $E[n(\mathbf{r})]$, as a functional of the exact ground state density, corresponds to the minimum of $E[n(\mathbf{r})]$ based on the minimal principle.

Using the Hohenberg-Kohn formulation, the electronic structure problem can be solved by finding the electron density $n(\mathbf{r})$ that minimises the total energy of the system. This is achieved by solving the Kohn-Sham equations, which introduce an auxiliary system of non-interacting electrons that reproduce the same density as the original interacting system.

2.1.3 Kohn-Sham equations

In 1965, Walter Kohn and Lu Jeu Sham introduced the non-interacting Schrödinger equation for non-interacting particles, i.e., the Kohn-Sham equations [39]. In the self-consistent Kohn-Sham equations, the ground-state energy and density can be obtained by calculating the eigenfunctions $\phi_j(\mathbf{r})$ and eigenvalues ε_j of non-interacting, single-particle equations [39]:

$$\left(-\frac{1}{2}\nabla_j^2 + v_{\text{eff}}(\mathbf{r}) \right) \phi_j(\mathbf{r}) = \varepsilon_j \phi_j(\mathbf{r}), \quad (2.4)$$

$$n(\mathbf{r}) = \sum_{j=1}^N |\phi_j(\mathbf{r})|^2, \quad (2.5)$$

where the effective external potential $v_{\text{eff}}(\mathbf{r})$ is split into the external potential $v(\mathbf{r})$, the Hartree potential due to the average electronic density distribution $v_{\text{H}}(\mathbf{r})$, and the exchange-correlation potential that is the functional derivative of the exchange-correlation energy $v_{xc}(\mathbf{r}) = \delta E_{xc} / \delta n(\mathbf{r})$:

$$v_{\text{eff}}(\mathbf{r}) = v(\mathbf{r}) + e^2 \int \frac{n(\mathbf{r}')}{|\mathbf{r} - \mathbf{r}'|} d\mathbf{r}' + v_{xc}(\mathbf{r}). \quad (2.6)$$

Equations (2.4)-(2.6) are known as the self-consistent Kohn-Sham equations. Starting from an approximation for $n(\mathbf{r})$, the effective potential $v_{\text{eff}}(\mathbf{r})$ can be constructed, then by solving Eq. (2.4) the eigenfunctions $\phi_j(\mathbf{r})$ can be obtained, and the density $n(\mathbf{r})$ can be recalculated from Eq. (2.5). The equations are solved iteratively until the initial and computed $n(\mathbf{r})$ are the same [41].

Despite that the exact Kohn-Sham wave functions $\phi_j(\mathbf{r})$ and energies ε_j have no “directly observable meaning” [40], $\phi_j(\mathbf{r})$ is related to the true physical density $n(\mathbf{r})$, and the highest occupied ε_j (relative to the vacuum) equals the ionisation energy.

It should be noted that how practical the Kohn-Sham equations are entirely depends on whether the exchange-correlation energy E_{xc} can describe the electron-electron interactions accurately and efficiently at the same time. A variety of approximations have been proposed. The simplest approximation for E_{xc} is called the local density approximation (LDA) [39],

$$E_{xc}^{\text{LDA}}[n(\mathbf{r})] = \int d\mathbf{r} \varepsilon_{xc}(n(\mathbf{r})) n(\mathbf{r}) d\mathbf{r}, \quad (2.7)$$

where $\varepsilon_{xc}(n)$ is the the exchange-correlation energy (per electron) of a uniform electron gas of density n . A next level of approximations are called the generalised gradient approximation (GGA) [40],

$$E_{xc}^{\text{GGA}}[n(\mathbf{r})] = \int d\mathbf{r} f^{(1)}(n(\mathbf{r}), |\nabla n(\mathbf{r})|) n(\mathbf{r}) d\mathbf{r}, \quad (2.8)$$

where $f^{(1)}(n(\mathbf{r}), |\nabla n(\mathbf{r})|)$ is a suitably chosen function of its two variables.

To simplify electronic structure calculations, the pseudopotential approximation can be used, which is based on the concept of “additional potential” introduced by Hans Hellmann in 1934 [42]. Because only the valence electrons are chemically active, the effects of the inner core electrons and the nucleus can be replaced by an effective potential, which significantly reduces the computational cost while enabling accurate description of the Coulomb potential outside the core region. One of the most commonly used pseudopotentials is generated

by the projector augmented wave method [43], which combines the advantages of both pseudopotentials and all-electron calculations.

Density functional theory has revolutionised computational materials science and quantum chemistry. It provides an efficient and accurate approach to calculate electronic properties, such as electron density distributions, energies, vibrational force constants, and potential energy surfaces, for a wide range of systems, from small molecules to complex materials. For periodic systems such as crystals, the plane-wave basis set is the natural choice. The infinite number of plane-wave basis functions requires a kinetic energy cutoff, and in combination with the pseudopotential, a much lower energy cutoff is needed to describe the wave functions accurately while still achieving computational efficiency.

2.1.4 Wannier functions

In addition to the plane-wave basis sets, localised basis sets can also be used. Based on the Kohn-Sham framework of density functional theory, the maximally localised Wannier functions can be constructed from the Bloch functions. The Wannier functions play a crucial role in the analysis of topological properties. By localising electronic wave functions onto individual lattice sites, Wannier functions facilitate the description of electronic states in periodic systems. They serve as a powerful tool to investigate the emergence of non-trivial band topology, such as characterising the topological invariant and computing the surface/edge states.

The Wannier functions can be obtained by a unitary transformation from the single-particle Bloch functions [44–49],

$$|w_{n\mathbf{R}}\rangle = V \int_{\text{BZ}} \frac{d\mathbf{k}}{(2\pi)^3} e^{-i\mathbf{k}\cdot\mathbf{R}} \sum_{m=1}^M |\phi_{m\mathbf{k}}\rangle U_{mn\mathbf{k}}, \quad (2.9)$$

where $w_{n\mathbf{R}}$ is a periodic Wannier function labelled by the Bravais lattice vector \mathbf{R} (corresponding to the conjugate variable of the crystal momentum \mathbf{k} in the Bloch representation), $\phi_{m\mathbf{k}}$ are the Kohn-Sham orbitals labelled by a band index m and a crystal momentum \mathbf{k} , M is the number of the bands in an isolated group that are separated from all the other lower and higher bands, and $U_{mn\mathbf{k}}$ are unitary matrices that mix Bloch states at \mathbf{k} .

The maximally localised Wannier functions can be used as local orbitals to construct tight-binding Hamiltonian models. This forms the basis to analyse the topological properties of materials by means of quantities such as the Wannier charge center and surface/edge states spectrum [50].

2.2 Lattice dynamics

First-principles calculations provide a powerful approach that enables a detailed understanding of the vibrational properties of solids based on density functional theory. The vibrational modes, known as phonons, provide insights into the collective behaviour of atomic displacements within a crystal lattice. The phonon frequencies and their corresponding modes of vibration can be accurately determined from the interatomic force constants by computing the potential energy surface. This comprehensive understanding of lattice dynamics is crucial for studying various phenomena in materials, including thermal expansion, heat transport, and phase transitions, thereby facilitating the design and optimisation of materials with desired thermal and mechanical properties.

Because the lattice dynamical properties primarily rely on the force constants between neighbouring atoms in the crystal lattice, studying topological phonons is relatively easier compared to topological electronic states in terms of obtaining the necessary “tight-binding” parameters and analysing the resulting eigenvectors. Unlike studying topological properties in electronic systems that requires complex calculations involving computing the electronic wave functions and constructing their Wannierised counterparts, the eigenvectors and tight-binding parameters can be directly obtained from the force constants that can be readily computed by first-principles calculations, and hence the construction of the corresponding Hamiltonian is significantly simplified, which makes the tight-binding parameters more accessible and computationally feasible for topological analysis. This straightforward procedure enables a systematic analysis of topological phonons, including the study of their topological invariant and the identification of topologically protected edge or surface states. Overall, the simplicity of calculating force constants to obtain the necessary input parameters makes the study of topological phonons more accessible, allowing for a deeper understanding of their topological properties and their potential applications in various areas of materials science and condensed matter physics.

2.2.1 Adiabatic approximation

The adiabatic approximation allows the decoupling of the lattice vibrations from the electronic degrees of freedom, as proposed by Max Born and J. Robert Oppenheimer in 1927 (also known as the Born-Oppenheimer approximation) [51]. They noticed that the proton mass is 1836 times larger the electron mass, indicating that electrons move much faster than the nuclei and can instantaneously follow the motion of the slow nuclei. This motivates the separation of the electronic and vibrational degrees of freedom.

Based on this approximation, the lattice dynamics of a system can be determined from the eigenvalues ε and the eigenfunctions χ_I :

$$\left(-\sum_I \frac{\hbar^2}{2M_I} \nabla_I^2 + \Phi(\mathbf{R}) - \varepsilon \right) \chi_I(\mathbf{R}) = 0, \quad (2.10)$$

where M_I is the nucleus mass, \mathbf{R} is the set of all the nuclear coordinates \mathbf{R}_I for the nucleus I , and $\Phi(\mathbf{R})$ is the Born-Oppenheimer energy surface corresponding to the ground-state energy of the electronic system in the field of fixed nuclei with the Hamiltonian

$$H_{\text{BO}}(\mathbf{R}) = -\frac{\hbar^2}{2m} \sum_i \nabla_i^2 - \sum_{i,I} \frac{Z_I e^2}{|\mathbf{r}_i - \mathbf{R}_I|} + \frac{1}{2} \sum_{i \neq j} \frac{e^2}{|\mathbf{r}_i - \mathbf{r}_j|} + \sum_{I \neq J} \frac{Z_I Z_J e^2}{|\mathbf{R}_I - \mathbf{R}_J|}. \quad (2.11)$$

2.2.2 Harmonic approximation

The ions in solids vibrate around their equilibrium positions \mathbf{r}_i with displacements \mathbf{u}_i , where $i \equiv (l\kappa)$ with l and κ labelling the unit cells and the atoms in each unit cell respectively. Under the harmonic approximation, the potential energy surface can be expressed as a quadratic function of the displacements of the atoms [35]

$$\Phi = \Phi_0 + \frac{1}{2} \sum_{ij} \sum_{\alpha\beta} \Phi_{i,j}^{\alpha\beta} u_i^\alpha u_j^\beta, \quad (2.12)$$

where α and β are the Cartesian indices, Φ_0 is the zeroth-order force constant evaluated at the ionic equilibrium positions, and $\Phi_{i,j}^{\alpha\beta}$ are the second-order force constants which can be evaluated as the second derivatives of Φ with respect to ionic displacements, or equivalently as the first derivatives of the atomic force on atom $j \equiv (l'\kappa')$ under an atomic displacement \mathbf{u}_i [52, 53]

$$\Phi_{i,j}^{\alpha\beta} = \frac{\partial^2 \Phi}{\partial u_i^\alpha \partial u_j^\beta} = -\frac{\partial F_j^\beta}{\partial u_i^\alpha}. \quad (2.13)$$

The calculation of second-order force constants thus amount to computing the first and second derivatives of its Born-Oppenheimer energy surface. According to the Hellmann-Feynman theorem [34, 54], when the wave function is exact, the energy gradient is equivalent to the expectation value of the derivative of the Hamiltonian. Consequently, it can be derived that the real physical force acting on an ion can be obtained from the partial derivative of the Kohn-Sham energy with respect to the position of the ion when the wave functions are very close to exact Kohn-Sham eigenstates [41]. There are two approaches to compute the

force constants based on the Hellmann-Feynman theorem, one is the finite displacement method [55–57], and the other uses density functional perturbation theory [58, 59].

In the finite different method, the force constants are approximated as a small force caused by a small displacement,

$$\Phi_{i,j}^{\alpha\beta} \simeq -\frac{\delta F_j^\beta}{\delta u_i^\alpha}. \quad (2.14)$$

In density functional perturbation theory, the first and second derivatives of Φ are derived from the Hellmann-Feynman theorem

$$\frac{\partial \Phi}{\partial u_j^\beta} = \int \frac{\partial V_u(\mathbf{r})}{\partial u_j^\beta} n_u(\mathbf{r}) d\mathbf{r}, \quad (2.15)$$

$$\frac{\partial^2 \Phi}{\partial u_i^\alpha \partial u_j^\beta} = \int \frac{\partial^2 V_u(\mathbf{r})}{\partial u_i^\alpha \partial u_j^\beta} n_u(\mathbf{r}) d\mathbf{r} + \int \frac{\partial V_u(\mathbf{r})}{\partial u_i^\alpha} \frac{\partial n_u(\mathbf{r})}{\partial u_j^\beta} n_u(\mathbf{r}) d\mathbf{r}, \quad (2.16)$$

where $V_u(\mathbf{r})$ includes both the electrostatic interactions between nuclei and the electron-nucleus interaction in Eq. (2.11), and the electron-density response $\partial n_u(\mathbf{r})/\partial u_j^\beta$ can be obtained by linearising Eq. (2.5)

$$\Delta n(\mathbf{r}) = 2\text{Re} \sum_{j=1}^N \phi_j^*(\mathbf{r}) \Delta \phi_j(\mathbf{r}) \quad (2.17)$$

where Δ is the finite-difference operator, and the variation of the Kohn-Sham orbitals $\Delta \phi_j(\mathbf{r})$ is calculated from the first-order perturbation theory

$$\left(-\frac{1}{2} \nabla_j^2 + v_{\text{eff}}(\mathbf{r}) - \varepsilon_j \right) |\Delta \phi_j(\mathbf{r})\rangle = -\left(\Delta v_{\text{eff}}(\mathbf{r}) - \Delta \varepsilon_j(\mathbf{r}) \right) |\phi_j(\mathbf{r})\rangle, \quad (2.18)$$

where $\Delta v_{\text{eff}}(\mathbf{r})$ is the first-order correction to the self-consistent potential $v_{\text{eff}}(\mathbf{r})$

$$\Delta v_{\text{eff}}(\mathbf{r}) = \Delta v(\mathbf{r}) + e^2 \int \frac{\Delta n(\mathbf{r}')}{|\mathbf{r} - \mathbf{r}'|} d\mathbf{r}' + \left. \frac{dv_{xc}(n)}{dn} \right|_{n=n(\mathbf{r})} \Delta n(\mathbf{r}), \quad (2.19)$$

and $\Delta \varepsilon_j(\mathbf{r})$ is the first-order variation of the Kohn-Sham eigenvalue $\varepsilon_j(\mathbf{r})$

$$\Delta \varepsilon_j(\mathbf{r}) = \langle \phi_j(\mathbf{r}) | \Delta v_{\text{eff}}(\mathbf{r}) | \phi_j(\mathbf{r}) \rangle. \quad (2.20)$$

2.2.3 Phonon eigenvalues and eigenvectors

Once the second-order force constants are obtained, the dynamical properties of the ionic motion are then determined by the dynamical matrix D , which plays the role of the Hamiltonian, and is obtained from the second-order force constants as [36, 60, 61]:

$$D_{\kappa\kappa'}^{\alpha\beta}(\mathbf{q}) = \sum_{l'} \frac{\Phi_{0\kappa,j}^{\alpha\beta}}{\sqrt{m_\kappa m_{\kappa'}}} e^{i\mathbf{q}\cdot[\mathbf{R}_j - \mathbf{R}_{0\kappa}]}, \quad (2.21)$$

where \mathbf{q} describes coordinate in the phonon Brillouin zone (rather than the general label \mathbf{k}), and m_κ is the mass of atom κ . The eigenvalue equation of the Hamiltonian (dynamical matrix) is then:

$$\sum_{\beta\kappa'} D_{\kappa\kappa'}^{\alpha\beta}(\mathbf{q}) e_{\mathbf{q}p}^{\beta\kappa'} = \omega_{\mathbf{q}p}^2 e_{\mathbf{q}p}^{\alpha\kappa}, \quad (2.22)$$

where p is the phonon band index, $\omega_{\mathbf{q}p}$ are the phonon frequencies and $e_{\mathbf{q}p}^{\alpha\kappa}$ are the phonon eigenvectors in matrix form.

The dynamical matrix $D(\mathbf{q})$ is a $3N \times 3N$ matrix, where 3 comes from the three Cartesian directions and N is the number of atoms in the unit cell. As a result, the eigenvectors $\mathbf{e}_{\mathbf{q}p}$ are complex column vectors with $3N$ elements

$$\mathbf{e}_{\mathbf{q}p} = \begin{pmatrix} e_{\mathbf{q}1}^x \\ e_{\mathbf{q}1}^y \\ e_{\mathbf{q}1}^z \\ \vdots \\ e_{\mathbf{q}N}^x \\ e_{\mathbf{q}N}^y \\ e_{\mathbf{q}N}^z \end{pmatrix}, \quad (2.23)$$

and can be normalised to 1:

$$\sum_{\alpha\kappa} |e_{\mathbf{q}p}^{\alpha\kappa}|^2 = 1. \quad (2.24)$$

2.3 Topological analysis

The above sections provide the theoretical frameworks to describe electronic structures and lattice dynamics, which form the basis to study the topological properties in electronic and

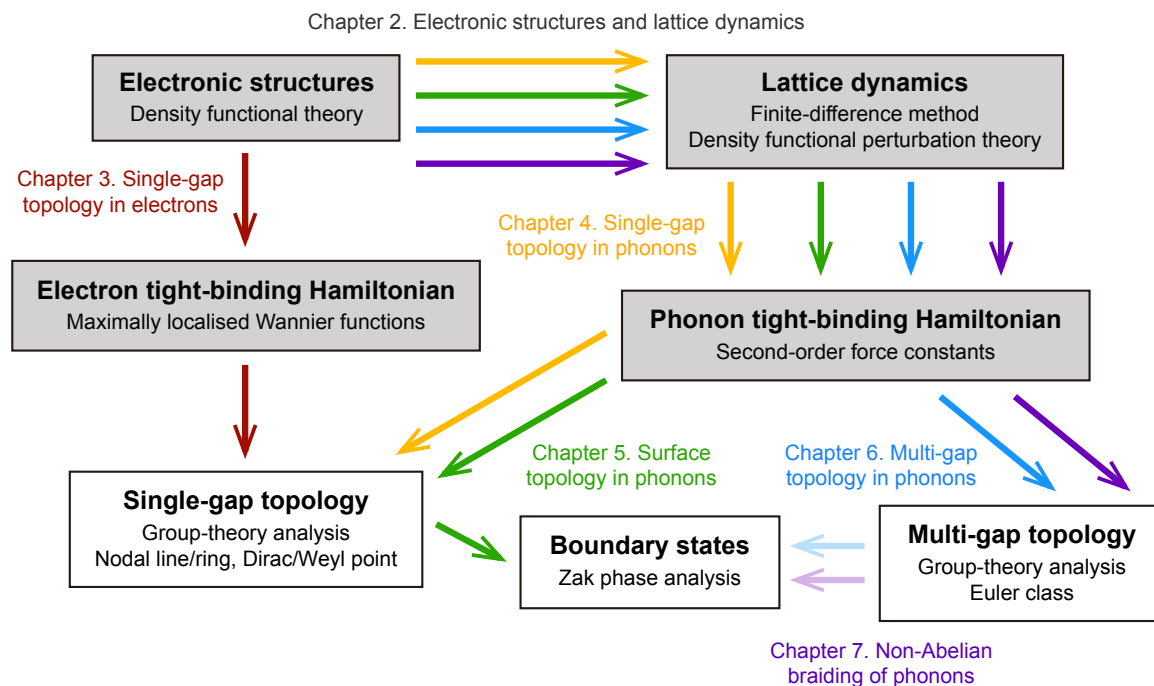


Fig. 2.1 Theoretical frameworks in Chapters 3 – 7.

phononic systems. The theoretical frameworks for topological analysis are summarised in Fig. 2.1, as will be introduced in Chapters 3 – 7.

Chapter 3 introduces the tools to study topological band crossings in electronic systems, which depend on the symmetry of specific subgroup of bands. Around the Fermi level, such crossings occur as a result of the touching of conduction and valence bands (with only one gap between the two bands). This is why such topological features in semimetallic systems are referred to as single-gap topology. Three types of topological semimetals (nodal-line/ring semimetal, Weyl semimetal and Dirac semimetal) are introduced, and their corresponding symmetry requirements are described. Group-theory analysis is applied to classify their topological properties, e.g., the nodal lines or rings can be protected by a mirror symmetry, while the Weyl points can be found in systems that break either spatial-inversion or time-reversal symmetry. With an electron tight-binding Hamiltonian, topological properties such as the surface states can be further studied (see Chapter 3).

Chapter 4 applies the same group-theory analysis to phonons as a replica of single-gap topology in electrons. These topological features are independent of the statistics of quasiparticles, i.e., topological invariants can be defined on an equal footing in fermionic and bosonic systems. For example, Chern numbers around the Weyl points can be computed using the phonon tight-binding Hamiltonian, which can be generated directly from the second-order force constants, as demonstrated in Chapter 4.

Chapter 5 extends the idea of single-gap topology from bulk states to surface states. Tools such as Zak phase analysis are introduced to characterise the topological boundary states. The Zak phase analysis is also used in helping understand the boundary states of multi-gap topology in Chapters 6 and 7. However, it is worth stressing here that although the Zak phase can trace faithfully the boundary states of single-gap topology, the bulk-boundary correspondence for multi-gap topology has not yet been fully understood.

Chapter 6 provides a detailed theoretical framework to study multi-gap topology. The concept of non-Abelian frame charges is introduced for systems with at least three bands and a real Hamiltonian. In contrast to single-gap topology that has only one gap, multiple gaps are formed between multiple bands. A new topological invariant, the Euler class, is defined to characterise the multi-gap topological features. The symmetry requirements for multi-gap topology are also discussed. By varying external stimuli, the non-Abelian frame charges can be moved around each other in reciprocal space, mimicking the non-Abelian braiding process in real space. The tools to investigate global topological configurations in the braiding processes are also incorporated into the theoretical framework introduced in Chapter 6.

Chapter 7 demonstrates the very first example of non-Abelian braiding of phonons with both three and four phonon bands. The possible experimental signatures to track the band inversion accompanied by the braiding are also simulated.

Chapter 3

Single-gap topology in semimetals

Conventionally, materials are classified into insulators and metals depending on whether the valence and conduction bands touch, i.e., whether the single gap between these two bands closes. In the transition from insulators to metals, there is an intermediate state where the single gap only closes at point(s) or along line(s) in momentum space. Recently, it has been found that such band-crossing points/lines are associated with certain topological invariants. That is why they are called topological semimetals.

In this chapter, I present the model Hamiltonian for three main classes of topological semimetals: (i) nodal-line semimetals, (ii) Weyl semimetals, and (iii) Dirac semimetals. Then I show that a topological semimetallic phase can be realised by closing the single gap between the valence and conduction bands in a trivial insulator. I find the first example of a temperature-promoted topological semimetallic phase in an otherwise trivial semiconductor at low temperatures, β -PbO₂. Both thermal expansion and electron-phonon coupling tend to close the single gap upon increasing temperature, driving PbO₂ into a topological semimetal.

This chapter is based on work published in [Bo Peng, Ivona Bravić, Judith L. MacManus-Driscoll, and Bartomeu Monserrat. *Physical Review B* 100 (16), 161101(R) (2019)]. My collaborators Ivona Bravić provided the microscopic mechanisms for strain-induced band inversion, Judith L. MacManus-Driscoll proposed possible experimental approaches to verify the prediction and Bartomeu Monserrat conceived the research idea and developed the computational framework to calculate electron-phonon coupling, while I was responsible for the rest.

3.1 Classification of topological semimetals

Single-gap topology typically involves two bands: the highest valence band below the Fermi level and the lowest conduction band above the Fermi level, with only one single

gap between the two bands. In topological semimetals, the single gap closes at point(s) or along line(s). Such gap closings are protected by symmetry: as long as the valence and conduction bands belong to different irreducible representations (irreps), the gap closing is robust and the two bands will not be gapped. Although such gap closings were studied in the early days of band theory [15], not until the last decade have their topological properties been noticed [62, 63]. These topological degeneracies exhibit unique physical properties such as topologically protected surface states [62] and exotic transport properties [64, 65], enabling various applications from spintronics [66] to topological quantum computation [67]. In addition, topological semimetals serve as a platform for obtaining various other topological states, such as topological (crystalline) insulators [68] and Chern insulators [69].

Topological semimetals have diversified classifications including nodal-line semimetal [70, 71], Weyl semimetal [72, 73], and Dirac semimetal [74–76]. For nodal-line semimetals, the two bands cross each other along one-dimensional line(s); while for Weyl and Dirac semimetals, the two bands cross at zero-dimensional points. In this section, I give a simplified overview of these classes of semimetals.

3.1.1 Nodal-line semimetal

In nodal-line semimetals, the gap closes along line(s) in momentum space. Depending on the shape of the line(s), they can be further classified into nodal rings and nodal lines. The nodal lines or rings are protected by certain crystalline symmetries such as mirror or \mathcal{PT} (where \mathcal{P} is the spatial inversion symmetry and \mathcal{T} is the time-reversal symmetry) [77, 78].

An effective two-band model Hamiltonian in the momentum space k for a spinless system can be written as,

$$H(k) = d_0(\mathbf{k})\sigma_0 + d_1(\mathbf{k})\sigma_x + d_2(\mathbf{k})\sigma_y + d_3(\mathbf{k})\sigma_z, \quad (3.1)$$

where $\sigma_{x,y,z}$ are the Pauli matrices, and σ_0 is the identity matrix. Assuming the system has mirror symmetry on the $k_x = k_y$ plane and there is a band crossing on the mirror plane, the crossing bands at \mathbf{k} satisfy $E_i(\mathbf{k}) = E_{i+1}(\mathbf{k})$ (i is the band index). Because \mathbf{k} has three variables (k_x, k_y, k_z) to satisfy two equations, i.e., $k_x = k_y$ and $E_i(\mathbf{k}) = E_{i+1}(\mathbf{k})$, the solution space must be one-dimensional, which restricts the band crossing to a 1D continuous ring/line on the mirror-invariant plane [77], as shown in the top panel of Fig. 3.1(a). Similarly, nodal-line semimetals can also be protected by other crystalline symmetry such as \mathcal{PT} . The iso-energy surface states of nodal-ring semimetals on a semi-infinite slab are a 2D drumhead-like surface within the projected bulk nodal ring on the surface plane [63, 70], as shown in the bottom panel of Fig. 3.1(a).

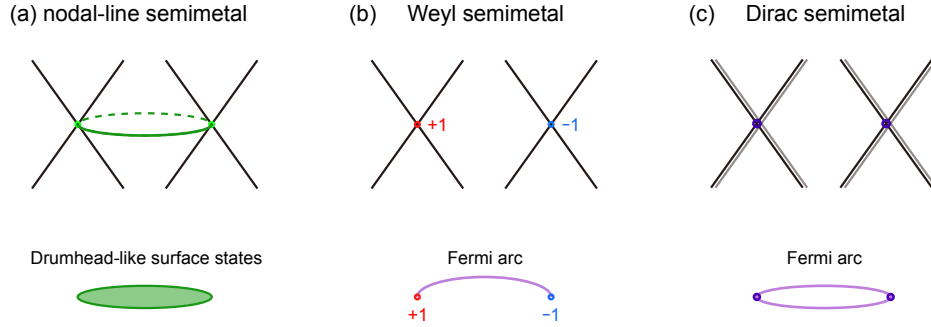


Fig. 3.1 (a) Nodal-line, (b) Weyl and (c) Dirac semimetals and their corresponding iso-energy surface states on a semi-infinite slab.

3.1.2 Weyl semimetal

Weyl fermions are massless particles with definite chirality based on the Dirac equation when the mass term is zero [12]. Their Hamiltonian can be written as

$$H = v_F \mathbf{k} \cdot \boldsymbol{\sigma}, \quad (3.2)$$

where v_F is the Fermi velocity and its sign \pm represents the chirality of Weyl fermions. In addition to the efforts in finding them in high-energy physics, their analogs, Weyl-fermion-like quasiparticles, are expected to exist as low-energy excitations of condensed matter systems [79]. Furthermore, in three-dimensional periodic lattices, Weyl fermions always appear in pairs of opposite chirality [80, 81]. The compounds hosting such Weyl fermions are called Weyl semimetals, with the Weyl nodes formed by the crossing of two non-degenerate bands close to the Fermi level [82–85], as shown in Fig. 3.1(b).

The chirality of the Weyl nodes can be associated with a topological invariant. By choosing a small spherical manifold enclosing the Weyl node, a Chern number can be defined as

$$C = \frac{1}{2\pi} \oint d^3\mathbf{k} \cdot \boldsymbol{\Omega}(\mathbf{k}), \quad (3.3)$$

where $\boldsymbol{\Omega}(\mathbf{k})$ is the Berry curvature. The Weyl nodes act as sinks and sources of Berry curvature with Chern numbers of ± 1 , indicating positive and negative monopole charges. Therefore all Weyl nodes are topologically protected. Unless two Weyl nodes with opposite chiralities meet each other in momentum space, they cannot be annihilated.

Although the Weyl points are protected by topology rather than symmetry, in the presence of extra crystalline symmetries, double- or triple Weyl points can emerge. For instance, with

C_4 symmetry, double-Weyl points can be realised with an effective model:

$$H = k_z \sigma_z + (k_x - k_y)^2 \sigma_x + k_x k_y \sigma_y, \quad (3.4)$$

where the Chern number is ± 2 .

The key features of Weyl semimetals include Fermi arcs on the surface [72, 73, 86–91] [Fig. 3.1(b)] and negative magnetoresistance [92–94]. Besides being of great interest to fundamental physics, Weyl semimetals also exhibit high carrier mobilities [94], and may find substantial applications in electronics, spintronics and thermoelectrics [91, 94, 95].

3.1.3 Dirac semimetal

Similar to Weyl semimetals, Dirac semimetals also have touching bands at discrete points in the Brillouin zone with linear dispersion. The difference is that in Dirac semimetals the band crossings are fourfold degenerate, whereas in Weyl semimetals they are twofold degenerate. The fourfold-degenerate Dirac points can be regarded as two overlapping Weyl points [96], and Dirac semimetals need extra symmetry to protect the Dirac points from being gapped. It requires both inversion and time-reversal symmetry, as the former results in $E_{\uparrow}(\mathbf{k}) = E_{\uparrow}(-\mathbf{k})$ and the latter results in $E_{\uparrow}(\mathbf{k}) = E_{\downarrow}(-\mathbf{k})$. As a consequence, the energy bands are doubly degenerate in the entire Brillouin zone. Graphene with $SU(2)$ symmetry is a typical Dirac semimetal in 2D, and its band-crossing points are near the Fermi level with the Hamiltonian:

$$H = v(k_x \sigma_x + k_y \sigma_y), \quad (3.5)$$

where both bands are doubly degenerate, as shown in Fig. 3.1(c).

Dirac points are not as stable as Weyl points, e.g., spin-orbit coupling tends to open the band gap of graphene. To enforce the fourfold degeneracy of the Dirac points, additional rotation symmetry is needed. For example, in Na_3Bi [74, 76], the Dirac nodes, induced by band inversion, are along the rotation axis with C_{6v} symmetry. Therefore the fourfold-degenerate Dirac points are protected by the axial rotational symmetry and the 3D Dirac semimetallic state is realised [74, 96]. Similarly, in Cd_3As_2 [75, 97–100], the band crossings are protected by a C_4 rotation symmetry around the k_z axis. Such protection makes the Dirac nodes quite robust within a finite range of Hamiltonian parameters. By chemical substitution in the same crystalline symmetry, new Dirac semimetals can be predicted. For example, by substituting Na and Bi atoms in Na_3Bi , I predict two new Dirac semimetals, Na_2MgPb and Na_2CdSn [101], which have been successfully synthesised [102, 103].

3.2 Topological phase transitions in β -PbO₂

In this section I describe the topological phase transitions in an otherwise trivial insulator driven by gap closing upon external stimuli such as strain and temperature. Using first-principles calculations, I present the first example of a temperature-promoted topological phase in β -PbO₂, which is a semiconductor at low temperatures. With increasing temperature, both thermal expansion and electron-phonon coupling contribute towards stabilising a topologically ordered phase, which is contrary to all known topological materials so far. The underlying microscopic mechanism is discussed, and can be employed as a guiding principle to identify other materials in which the topological order is robust at high temperatures, thus opening the door for practical room-temperature applications of topological matter.

3.2.1 Computational details

First-principles density functional theory (DFT) calculations are performed using the Vienna *ab-initio* simulation package (VASP) [104, 105]. The projector-augmented-wave potential is used with Pb $5d^{10}6s^26p^2$ and O $2s^22p^4$ valence states. Hybrid functional methods based on the HSE06 approximation are adopted [106–108] with 25% of the exact screened Hartree-Fock exchange incorporated into the semilocal exchange within the generalised gradient approximation (GGA) in the Perdew-Burke-Ernzerhof (PBE) parameterisation [109]. Based on convergence tests, I use a kinetic energy cutoff set to 500 eV and a Γ -centered $4 \times 4 \times 6$ \mathbf{k} -mesh to sample the electronic Brillouin zone. The convergence parameters for structural relaxations include an energy difference within 10^{-6} eV and a Hellman-Feynman force within 10^{-4} eV/Å. For the calculation of surface states, Wannier functions for the s orbitals of lead and the p orbitals of oxygen are generated using the WANNIER90 package [48] combined with surface Green's functions as implemented in the WANNIERTOOLS package [50, 110]. The phonon dispersion, thermal expansion within the quasiharmonic approximation, and the electron-phonon interaction are calculated using the finite displacement method within the nondiagonal supercell approach [57, 111], using coarse \mathbf{q} -point grids of size $4 \times 4 \times 4$ to sample the vibrational Brillouin zone. The temperature dependence of band structures is calculated from vibrational averages along thermal lines [112, 113].

3.2.2 Ground state properties of β -PbO₂

Lead dioxide has been one of the most widely used functional oxides since the invention of the lead-acid battery in 1860 [114]. Figure 3.2(a) illustrates the most stable tetragonal β -PbO₂ phase (space group: $P4_2/mnm$) in which each Pb atom is at the center of an O octahedral

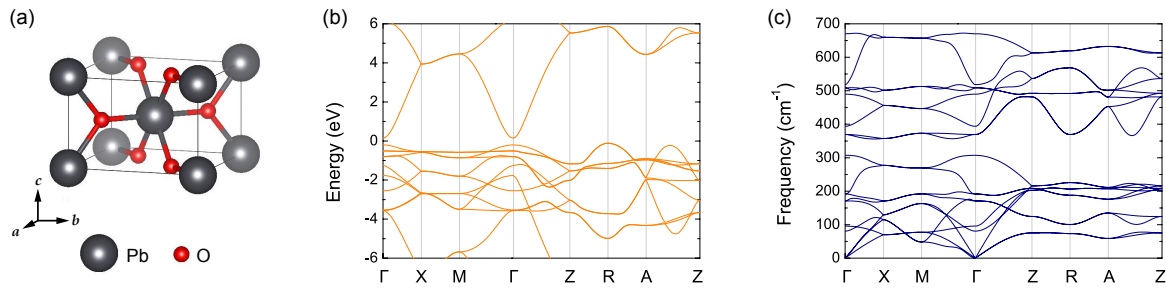


Fig. 3.2 (a) Unit cell of the crystal structure of β -PbO₂. (b) Electronic band structure of β -PbO₂ calculated using the HSE06 functional. (c) Phonon dispersion of β -PbO₂ calculated using the HSE06 functional.

age. The subsequent analysis of β -PbO₂ is based on first-principles DFT calculations using the HSE06 screened Coulomb hybrid density functional [106–108]. Compared to semilocal DFT, typically used for the study of β -PbO₂ [115, 116], the HSE06 results show significantly better agreement with experimental measurements [117, 118], providing a correct description of the structural, electronic and vibrational properties of this material.

Table 8.1 shows a comparison of the lattice parameters of PbO₂ calculated with the semilocal PBE and the hybrid HSE06 exchange-correlation functionals, and compared to experimental measurements. The HSE06 lattice parameters are within 0.5% of experimental reports [119], whereas PBE lattice parameters overestimate the experimental reports by 2.5% and 1.9% for the a and c lattice parameters, respectively. These results are in agreement with earlier reports [118].

As shown in Fig. 3.2(b), PbO₂ is a semiconductor with the valence-band maximum (VBM) at the R point and the conduction-band minimum (CBM) at the Γ point. The calculated indirect band gap of 0.24 eV and direct band gap of 0.34 eV at the Γ point agree well with previous calculations [118]. These results also agree well with hard X-ray photoelectron spectroscopy measurements, which indicate that β -PbO₂ is an intrinsic semiconductor, with the metallic behaviour exhibited by some samples arising from a partially filled conduction band due to oxygen deficiency [114, 120]. Previous DFT calculations using semilocal exchange-correlation functionals predict that β -PbO₂ is a nodal-line semimetal when spin-orbit coupling is neglected, and becomes a Dirac semimetal in the presence of spin-orbit coupling [115, 121]. In contrast, using hybrid exchange-correlation functionals leads to a semiconducting band gap of about 0.23 eV [118], which is consistent with X-ray photoemission results [120, 122], indicating the latter provides a more accurate description of the electronic structure of PbO₂.

The phonon dispersion in Fig. 3.2(c) shows no imaginary modes, thus indicating that the experimentally observed structure is stable at all temperatures. This is at odds with earlier

Table 3.1 Ground state properties of β -PbO₂ calculated using the semilocal PBE and the hybrid HSE06 functionals. The a and c lattice parameters are shown in Å. E_g , A_{1g} , and B_{1g} are the three Raman-active modes in cm⁻¹. The lowest-frequency Raman peak at 370 cm⁻¹ was probably misidentified in the experiments, which reported a value of 424 cm⁻¹ instead (see Fig. 1 in Ref. [117])

	a	c	E_g	A_{1g}	B_{1g}
PBE	5.079	3.448	350.0	480.3	579.5
HSE06	4.974	3.365	369.4	518.4	670.2
Experiment	4.961	3.385	370	515	653

DFT calculations using semilocal exchange-correlation functionals [116], but consistent with the fact that β -PbO₂ is the most stable phase under normal laboratory conditions [114]. Furthermore, the HSE06 Raman active modes are in better agreement with the experimental Raman spectrum [117] than the modes calculated using semilocal DFT, as shown in Table 3.1.

3.2.3 Strain-induced topological phase transitions

The electronic structure of β -PbO₂ can be tuned from semiconducting to metallic by small variations of the lattice constants [118, 123]. Interestingly, the normal band ordering at the Γ point is inverted under tensile lattice strain, resulting in non-trivial band topology [123]. To illustrate this, I carry out band-structure calculations under different tensile strains. Figure 3.3(a) presents the band gap at the Γ point as a function of strain in the (a,b) plane and strain along the c -axis. The strain conditions for which the system has normal band ordering correspond to trivial insulators with the magnitude of the band gap indicated by the red-yellow-white colour scale, whereas those with inverted band ordering are marked by the cyan colouring. Increasing the c lattice constant closes the band gap, leading to a nodal-line semimetal phase at strains larger than around 1.9% (as will be discussed below). On the other hand, the band gap is insensitive to the strain in the (a,b) plane. Thus the c -axis strain is a suitable tuning parameter to control the band topology of β -PbO₂.

To rationalise the behaviour of the valence and conduction bands under tensile strain, I calculate the orbital characters near the Fermi energy. As shown in Fig. 3.4(a), the unstrained lattice has a normal band ordering at the Γ point with the VBM derived from the $2p_{xy}$ orbitals of oxygen, and the CBM predominantly consists of the $6s$ orbitals of lead that hybridise with the $2p_{xy}$ orbitals of oxygen. I also depict the real-space charge densities corresponding to the respective VBM and CBM at the Γ point in Fig. 3.4(a). The VBM at the Γ point is constituted of the O $2p_{xy}$ atomic orbitals which are oriented along the (a,b) plane of the primitive cell. This feature of the valence band can be seen as the establishment of a quasi-two-dimensional

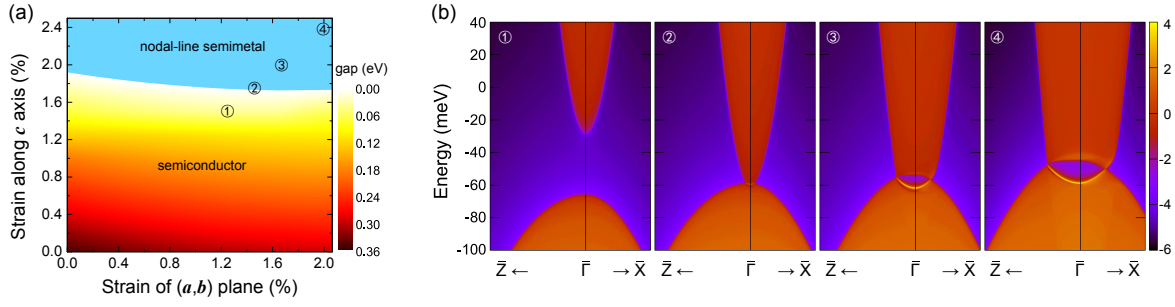


Fig. 3.3 (a) Calculated band gap at the Γ point of β - PbO_2 as a function of tensile strain. (b) Effect of tensile strain on the (010) surface states of β - PbO_2 . A warmer colour represents a higher surface contribution.

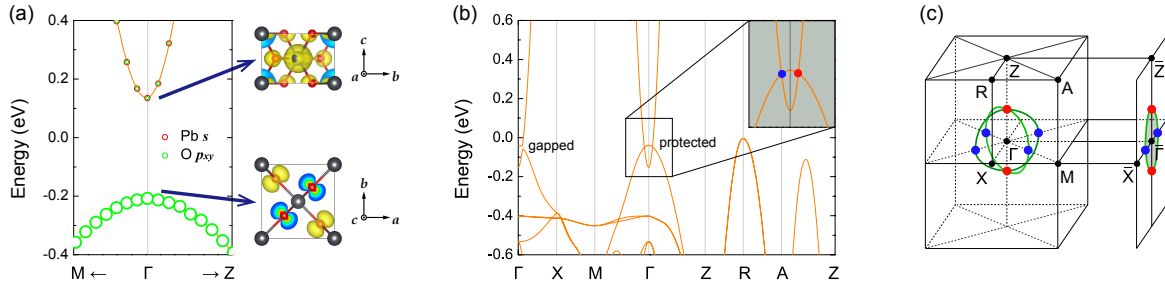


Fig. 3.4 Electronic structures for (a) unstrained and (b) strained β - PbO_2 . Charge densities of the CBM and VBM states (isosurface = 0.008) are presented in (a). (c) The bulk Brillouin zone and the surface Brillouin zone projected on the (010) surface are shown with two ring-shaped nodal lines on the $(1\bar{1}0)$ and (110) planes connecting the nodal points on the M- Γ (blue dots) and Γ -Z (red dots) high-symmetry lines. Only one pair of Dirac points along Γ -Z (red dots) remains once including the spin-orbit coupling.

subsystem in the bulk. Instead, the CBM at the Γ point resembles the diffuse Pb 6s orbital which has a three-dimensional character. This means that under uniaxial strain along the c direction the CBM experiences a reduced electron-electron repulsion arising from electrons of neighbouring atoms (in the c direction) and as a consequence its energy decreases. In contrast, the aforementioned quasi-two-dimensional character of the valence band remains invariant under out-of-plane expansion. This leads to a relative shift of the VBM and the CBM that drives the observed band inversion. This explanation is consistent with the fact that under in-plane strain, no band inversion can be observed, which underpins the relevance of the out-of-plane anisotropy of the valence band. In this case, both valence and conduction band states experience similar stabilisation effects upon expansion and therefore no crossing occurs. With larger tensile strains, β - PbO_2 will revert to the standard behaviour in which lattice expansion leads to the topologically trivial atomic limit. The other explanation is based on the ionic bonding in PbO_2 with a complete charge transfer from Pb^{+4} cations to

O⁻² anions, which separates the fully occupied O $2p_{xy}$ valence states and the unoccupied Pb $6s$ conduction states. The strain along c weakens the charge transfer, leading to partial delocalisation of the transferred charges to O ions. Consequently, the O $2p_{xy}$ valence states gain extra energy and are pushed upward, reducing the band gap and eventually leading to the band inversion.

To explain the formation of nodal lines, I examine the symmetry properties of β -PbO₂. For a fully relaxed unstrained crystal structure, β -PbO₂ is a trivial indirect-band-gap semiconductor with the minimum direct bandgap at the Γ point. Under tensile strain the band structure undergoes a band inversion at the Γ point. As shown in Fig. 3.4(b), under a modest strain of 2.07% in the (a,b) plane and 2.50% along the c -axis [corresponding to point ④ in Fig. 3.3(a)], the band gap at the Γ point is inverted with a band-inversion energy of 0.11 eV, and two band-crossing points are observed along the M- Γ and Γ -Z high-symmetry lines. The crossing points belong to two ring-shaped nodal lines on the $(1\bar{1}0)$ and (110) mirror symmetry planes, as shown in Fig. 3.4(c). In the absence of spin-orbit coupling, for each mirror plane the inverted band states have mirror eigenvalues -1 and $+1$ respectively, so the two crossing bands are disallowed by mirror symmetry to hybridise with each other and are therefore not gapped [77], forming a nodal line on the mirror plane as explained in the Section 3.1.1. The two nodal lines on the $(1\bar{1}0)$ and (110) planes are identical, which is similar to transition-metal rutile oxide PtO₂ [124]. For comparison, the band crossing on the Γ -X high-symmetry line is not protected by mirror symmetry and therefore gapped.

To illustrate the strain effect and estimate its magnitude, I calculate the surface states under tensile strain in Fig. 3.3(b) on the basis of maximally localised Wannier functions [48] and surface Green's functions [50, 110]. With an in-plane strain of 1.24% and an out-of-plane strain of 1.50%, the gap in the surface region decreases to 40 meV, and the conduction band moves below the Fermi energy due to the moving up of the VBM at the R point [panel ① in Fig. 3.3(b)]. Under a modest strain of 1.45% and 1.75% in the (a,b) plane and along the c -axis, a topological phase transition occurs as the conduction band moves slightly below the valence band at the Γ point [panel ② in Fig. 3.3(b)]. Further increasing strain leads to the formation of distinct surface states around the Γ point [panels ③ and ④ in Fig. 3.3(b)]. A hallmark of nodal-line semimetals is the presence of two-dimensional drumhead-like surface states connecting the projected Dirac nodal points (the projection of the bulk nodal line onto the surface plane) [63, 70], as shown in Fig 3.1(a). These surface states with a divergent density of states can be detected by angle-resolved photoemission measurements [125], and may induce strong correlation phenomena such as high-temperature superconductivity [126].

I next evaluate the role of spin-orbit coupling in β -PbO₂. The crossing bands are comprised of the $6s$ states of the lead atoms and the $2p_{xy}$ states of the light oxygen atoms.

As a consequence, none of these exhibit strong spin-orbit coupling effects, and the band structure and surface states with the inclusion of spin-orbit coupling are similar to those without spin-orbit coupling. Technically, spin-orbit coupling breaks the SU(2) symmetry, generally gapping the nodal line with only one pair of Dirac points along the Γ -Z line remaining [see the red dots in Fig. 3.4(c)], as has been previously observed [115]. The Dirac points are protected by the fourfold screw rotation \tilde{C}_{4z} symmetry, which is a fourfold rotation about the z -axis, followed by a translation by $(a/2, a/2, c/2)$ [124]. Thus the nodal-line semimetal evolves into a Dirac semimetal with the inclusion of spin-orbit coupling. Nonetheless, the weak spin-orbit coupling leads to a small gap of only 1.05 meV and the resulting physics resembles that of a nodal-line semimetal for temperatures over 12.2 K in which the bands merge due to the temperature-induced broadening.

3.2.4 Temperature-promoted gap closing

The behaviour of β -PbO₂ under tensile strain discussed above indicates that, contrary to all known topological materials, thermal expansion should promote topological order in β -PbO₂. I calculate the thermal expansion coefficients using the quasiharmonic approximation [61], in which the equilibrium structure at temperature T is determined by minimising the free energy at that temperature as a function of the (a, b) and the c lattice parameters. All calculations need to be performed at the HSE06 level of theory to correctly reproduce the dynamical stability of β -PbO₂.

Based on the temperature-dependent volume of β -PbO₂, I calculate the change in the band gap arising from thermal expansion, as shown in Fig. 3.5(a). Thermal expansion leads to a decrease in the band gap from 0.29 eV at 0 K to 0.21 eV at 600 K. The 0 K band gap of 0.29 eV is smaller than the static lattice band gap of 0.34 eV due to quantum zero-point motion, which also leads to lattice expansion. Taking the quantum zero-point motion into consideration, the calculated lattice constants at 0 K are $a = 4.988 \text{ \AA}$ and $c = 3.373 \text{ \AA}$. For comparison, the calculated static lattice constants are $a = 4.974 \text{ \AA}$ and $c = 3.365 \text{ \AA}$, and the measured ones are $a = 4.961 \text{ \AA}$ and $c = 3.385 \text{ \AA}$ [117].

I fit a Bose-Einstein oscillator model [127] to the temperature-dependent band gap:

$$E_g(T) = A_0 + \frac{A_1}{e^{\bar{\omega}/k_B T} - 1}, \quad (3.6)$$

where T is temperature, k_B is the Boltzmann constant, and $(A_0, A_1, \bar{\omega})$ are the fitting parameters. This model correctly reproduces the computational data, as shown in Fig. 3.5(a). The 0 K value is given by $A_0 = 0.2923 \text{ eV}$, the coupling strength between band gap and volume is given by $A_1 = -0.1802 \text{ eV}$, and the effective phonon frequency by $\bar{\omega} = 59.80 \text{ meV}$.

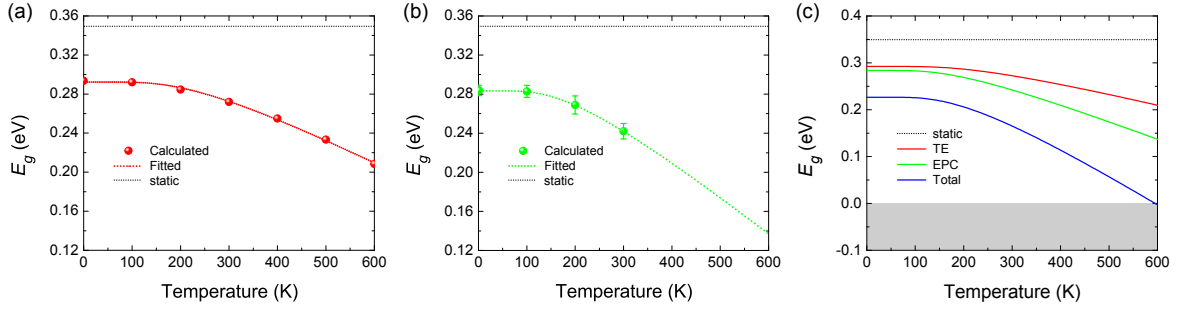


Fig. 3.5 Band gap of β -PbO₂ at the Γ point as a function of temperature with contributions from (a) thermal expansion, (b) electron-phonon coupling, and (c) a combination of both.

In addition to thermal expansion, increasing temperature also enhances electron-phonon coupling. I calculate the change in the band gap of β -PbO₂ arising from electron-phonon coupling by evaluating the expectation value of the band gap with respect to the nuclear vibrational density. The expectation value is calculated using a stochastic sampling technique, accelerated by means of thermal lines [57, 112]. The number of stochastic samples used is different at each temperature, and is chosen so as to reduce the statistical uncertainty to below about 5 meV. All calculations are performed at the HSE06 level of theory using a $4 \times 4 \times 4$ supercell, and the total number of sampled configurations across all considered temperatures (0–300 K) is over 300. I fit a Bose-Einstein oscillator model [127] to the change of the band gap with temperature arising from electron-phonon coupling, as shown in Fig. 3.5(b). The model can extrapolate the calculated results up to 600 K, a necessary step because the computational expense of electron-phonon coupling calculations increases with increasing temperature due to the larger number of configurations that need to be considered at higher temperatures, making explicit calculations at the higher temperature range prohibitive.

As shown in Fig. 3.5(b), including electron-phonon coupling leads to a 0 K band gap of 0.28 eV, which decreases to 0.17 eV at 600 K. For the Bose-Einstein oscillator fit, the 0 K band gap value is $A_0 = 0.2837$ eV, the electron-phonon coupling strength has a fitted value of $A_1 = -0.2234$, and the effective frequency is $\bar{\omega} = 47.82$ meV, corresponding to a phonon frequency of 385.45 cm^{-1} .

The overall temperature dependence of the band gap of β -PbO₂ is a combination of thermal expansion and electron-phonon coupling by summing the static band gap and the band gap changes induced by thermal expansion and electron-phonon coupling. The combined results are shown in Fig. 3.5(c), and show that the band gap at 0 K has a value of 0.23 eV, compared to a static lattice value of 0.34 eV. With increasing temperature, thermal expansion and electron-phonon coupling favour the topological phase. Taking both effects into consideration, a topological phase transition can be induced at 595 K.

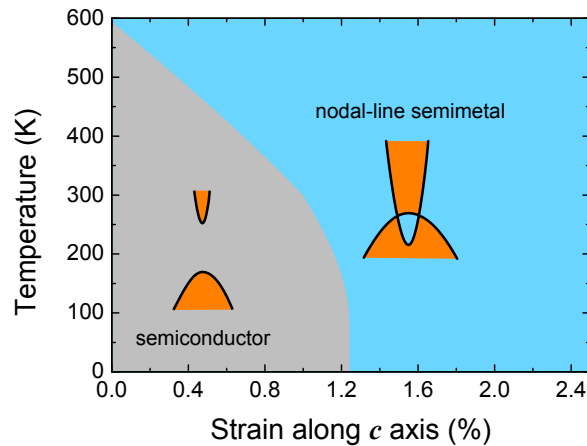


Fig. 3.6 Calculated strain-temperature phase diagram of β -PbO₂.

Figure 3.6 demonstrates the evolution of band topology as a function of temperature including both thermal expansion and electron-phonon coupling contributions, which promote the topological phase at high temperature. For unstrained PbO₂, the band gap closes above a temperature of 595 K, which is close to the temperature at which β -PbO₂ becomes unstable [114]. Above a strain of 1.26%, the system can be driven into a topological phase even at 0 K, and in the intermediate strain regime the temperature-promoted topological phase can be easily tuned to any intermediate temperature. At 0 K the topological phase appears at a c strain of 1.26%, significantly lower than the required strain of around 1.9% at the static lattice level [see Fig. 3.3(a)]. This difference is a purely quantum effect arising from the zero-point motion of the lattice.

The unusual temperature-promoted topological order predicted in β -PbO₂ could be observed experimentally by exploiting the sensitivity of the transition temperature to the c -axis strain, which would enable the tuning of the transition temperature anywhere in the range 0–595 K. Both uniaxial tensile strain along the c -axis, or three-dimensional tensile strain using a stoa-like structure consisting of stylobate (substrate) and column (matrix) with appropriately matched lattice constants, could be used to scan over the phase diagram of β -PbO₂.

The relatively low melting temperature of β -PbO₂ [114] means that it is possible to grow highly crystalline films. The appropriate substrate and matrix materials can be chosen from candidates with lattice constants in the appropriate region of the diagram in Fig. 3.3(a). Using rutile TiO₂ as a substrate, with an in-plane lattice constant of $a = 4.594 \text{ \AA}$, would provide in-plane compression of β -PbO₂ with an associated out-of-plane tension. Epitaxial growth of structurally analogous SnO₂ has been demonstrated on multiple orientations of a columbite

CoNb₂O₆ substrate [128]. These substrates could be good starting points for exploring the topological phase diagram of β -PbO₂.

β -PbO₂ exhibits intrinsic defects that place the Fermi energy within the conduction bands [114, 120]. This implies that the energy of the surface states will not coincide with the Fermi energy, and therefore the topological surface states will coexist with other non-topological surface states. Nonetheless, this is a common feature of many topological materials (see e.g. [129, 130]) that, although detrimental for the observation of isolated topological surface states, it facilitates the use of techniques such as angle-resolved photoemission spectroscopy for the detection of such states.

3.3 Conclusions and outlook

As long as the symmetry requirements are fulfilled, a topological semimetallic phase can be induced by closing the gap of a trivial insulator upon external stimuli such as strain and temperature. With a combination of thermal expansion and electron-phonon coupling, β -PbO₂ transforms from a trivial semiconductor at low temperatures to a topological semimetal at high temperatures. This behaviour contrasts with that of all known topological materials, most of which cannot hold topological order at high temperatures, with notorious examples including Chern insulators and topological superconductors which are currently restricted to few Kelvin at most.

This chapter proposes a microscopic picture of the chemical and physical mechanisms behind the interplay between topological order and temperature, and therefore provides a solid platform to search for novel topological materials whose topological order is robust at high temperatures. Such understanding paves the way for taking topological materials from the laboratory to technological devices.

Chapter 4

Single-gap topology in phonons

The degenerate points and lines within the single gap are closely related to the crystalline symmetry, and the relation between the crystalline symmetry and the degeneracy in the band structures can be extended from electrons to phonons, enabling condensed-matter physicists to explore the topological properties in the spectra of phonons. Topological phonons can be explored as a replica of electronic topology, where the topological properties are formed by two bands that are preferably far away from other bands to mimic single-gap topology in electronic systems. Compared to electrons, phonons are charge-neutral, spinless quasiparticles, and can be treated as spinless systems with time-reversal symmetry. In addition, they are bosonic excitations obeying Bose-Einstein statistics, and the topological properties in their entire frequency spectra can be accessed.

In this chapter, I firstly give a brief review on previous studies on topological phonons from a single-gap topology perspective. I then show that topological properties are ubiquitous in the phonon spectra using oxide perovskites as a representative material family. Most interestingly, I find that light can be used to drive topological phase transitions in the phonons of perovskites even without inducing structural phase transitions, providing the very first example of light-controlled topological phonons in any materials.

This chapter is based on work published in [Bo Peng, Yuchen Hu, Shuichi Murakami, Tiantian Zhang, and Bartomeu Monserrat. *Science Advances* 6 (46), eabd1618 (2020)]. My collaborators Yuchen Hu set up the package to generate tight-binding parameters of the phonon Hamiltonian, Shuichi Murakami analysed the topological features, Tiantian Zhang and Bartomeu Monserrat devised the research idea and supervised the project, while I was responsible for the rest.

4.1 Recent developments of topological phonons

Topological properties in the band structures have been extended from electrons to other quasiparticles including phonons [131–135], photons [136], magnons [137], and excitons [138]. Among all these quasiparticles, phonons are of significant importance because they are intrinsic lattice vibrational modes that are involved in several fundamental states of condensed matter, such as conventional superconductivity [139, 140], electric and thermal transport [95, 141–144], carrier thermalisation [145, 146], structural phase transition [147, 148] and charge density waves [149, 150].

Compared to topological electronic materials where the topological states must be near the Fermi level for experimental detection, phonons are bosons obeying Bose-Einstein statistics, and do not have such a restriction. Thus all the band-crossing points in the whole phonon frequency range can be measured by experimental methods such as inelastic neutron scattering [151–153] and inelastic X-ray scattering [154]. Another difference is that phonons are charge-neutral, spinless quasiparticles, and it is hard to break the time-reversal symmetry of phonons by external magnetic field. Therefore phonons can be treated as spinless systems with time-reversal symmetry, and it is convenient to apply the topological diagnosis method in spinless systems [155, 156] to understand the topological properties of phonons.

The first material realisation of topological phonons was predicted in FeSi in 2018 [133], soon followed by experimental verification using inelastic X-ray scattering [154], which boosts various studies of different types of topological phonons and their related properties in real materials [135, 151, 157–169]. As a replica of electronic topology, the concept of single-gap topology such as nodal lines/rings, Weyl points and Dirac points can be introduced in phonons.

4.2 Topological phonons in oxide perovskites

Oxide perovskites have gained popularity as a material system in the past decades due to hosting multiple competing phases including ferroelectric [170], magnetic [171], or superconducting [140], and also exotic excitations such as skyrmions [172, 173]. Additionally, these competing phases are particularly sensitive to external stimuli, including temperature [174], strain [175], pressure [176], and composition [177]. More recently, theoretical and experimental evidence has demonstrated that light is yet another means by which it is possible to control the crystal symmetry of perovskites [178–182]. As topological order is intimately related to symmetry, the versatility of the perovskite family makes these structures promising platforms to also explore topological properties. However, most oxide perovskites

are large-gap insulators (for example BaTiO_3 , SrTiO_3 , and PbTiO_3), and as a consequence they exhibit no electronic topological states.

In this section, I demonstrate that the phonon spectrum of multiple noncentrosymmetric perovskites can host three types of topological states: nodal rings, nodal lines, and Weyl points; suggesting that topological phonons are pervasive in different structural phases of oxide perovskites. Using the tetragonal BaTiO_3 phase as a prototype, I show that all these types of topological phonon emerge simultaneously when this phase is stabilised by photoexcitation. Additionally, topological order can be controlled with the photoexcited carrier density, driving topological transitions without any associated structural phase change, including the creation and annihilation of Weyl phonons and switching between nodal-ring and nodal-line phonons. In contrast, when the tetragonal phase of BaTiO_3 is stabilised by thermal fluctuations, it only exhibits a more limited number of topological states. This is because the long-range Coulomb interaction leads to a large energy splitting between the longitudinal and transverse optical phonons (LO-TO splitting), reducing the possibility of topological degeneracies between these bands. The photoexcitation route eliminates this problem because photoexcited carriers can screen long-range interactions.

4.2.1 Computational details

Density functional theory (DFT) calculations are performed using the Vienna *ab initio* simulation package (VASP) with the projector-augmented-wave potential method [104, 105]. The generalised gradient approximation (GGA) with the Perdew-Burke-Ernzerhof parameterisation revised for solids (PBEsol) is used as the exchange-correlation functional [183]. A plane-wave basis set is employed with a kinetic energy cutoff of 800 eV and a $7 \times 7 \times 7$ \mathbf{k} -mesh during structural relaxation, which is stopped when forces are below 10^{-3} eV/Å. The band structure of BaTiO_3 is calculated using the HSE06 hybrid functional in the presence of spin-orbit coupling [106]. Photoexcited carriers are simulated by promoting electrons from high-energy valence-band states to low-energy conduction-band states. This Δ self-consistent field (Δ SCF) method introduces non-interacting electron-hole pairs by changing the occupation numbers of the Kohn-Sham orbitals [147, 184–186], and is computationally less demanding compared to other approaches like constrained density functional theory [187] and excited-state force calculations [188]. Nevertheless, it gives consistent phonon spectra compared with those obtained with constrained DFT [178]. The occupancies are fixed with a smearing of 0.01 eV.

The crystal structures in the dark and under photoexcitation are fully relaxed before the phonon calculations. The force constants are calculated based on density functional perturbation theory (DFPT) [59] in a $2 \times 2 \times 2$ supercell with a $5 \times 5 \times 5$ \mathbf{k} -mesh using

VASP. The phonon dispersion is then obtained using PHONOPY [52]. Convergence tests are performed on the supercells with size between $2 \times 2 \times 2$, $3 \times 3 \times 3$, and $4 \times 4 \times 2$, all confirming the existence of Weyl points in illuminated BaTiO₃. The chirality of Weyl points is computed by employing the Wilson-loop method to calculate the Wannier charge center flow, i.e., the monopole charge of a Weyl point [189, 190]. The phonon surface states are obtained using surface Green's functions as implemented in WANNIERTOOLS [50]. The finite-temperature phonon frequencies are calculated using a self-consistent *ab initio* lattice dynamical method [56, 191, 192] in a $2 \times 2 \times 2$ supercell, which includes anharmonic contributions in the free energy of the self-consistent phonon spectrum. The self-consistent cycle is terminated after 240 iterations when the difference in free energy is less than 0.2 meV, and the space-group symmetry is enforced on the resulting force constants. The Born effective charges are calculated using DFPT to obtain the LO-TO splitting in the phonon dispersion in the dark [193]. Under illumination, the photoexcited electrons screen long-range interactions and no LO-TO splitting occurs.

4.2.2 Structural phases of BaTiO₃

As one of the most studied perovskite materials, BaTiO₃ has a cubic ABO₃-type crystal structure at temperatures above 393 K, with the A cation (Ba²⁺) at the corners and the B cation (Ti⁴⁺) at the center of an octahedral cage of oxygen atoms. Upon cooling, BaTiO₃ undergoes an inversion symmetry-breaking phase transition, giving rise to a tetragonal phase with a deformation along the [001] direction [194]. As shown in Fig. 4.1(a), the phase transition breaks inversion symmetry by the polar displacements of Ti and O atoms along the *z* direction, which changes the space group from $Pm\bar{3}m$ (No. 221) to $P4mm$ (No. 99). With further cooling, an orthorhombic $Amm2$ phase appears below 278 K and a rhombohedral $R3m$ phase follows below 183 K. As a result of these temperature-driven phase transitions, the room-temperature tetragonal phase exhibits imaginary harmonic phonon modes, as shown in Fig. 4.1(b). The inclusion of anharmonic vibrations [191] stabilises the tetragonal structure at 300 K, also shown in Fig. 4.1(b).

In addition to temperature, multiple strategies have traditionally been proposed to control structural phase transitions in perovskites, including strain [175], pressure [171, 176], and composition [177]. More recently, it has been shown that photoexcitation provides an alternative route to stabilising multiple perovskite phases [178–182]. Photoexcitation is relatively economical, and can be easier to control compared to other strategies such as heating to change temperature, material synthesis to change composition or strain, or external pressure. Inspired by these recent discoveries, I find that photoexcitation can also stabilise the imaginary phonon modes of the tetragonal phase of BaTiO₃. Figure 4.1(c) shows the

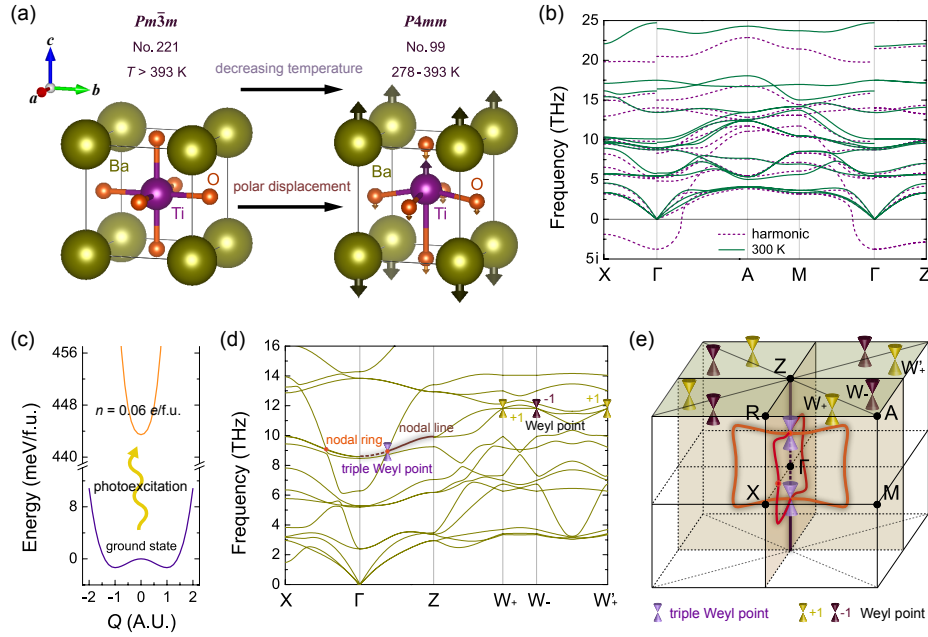


Fig. 4.1 (a) Crystal structures of the high-temperature cubic phase (No. 221, $Pm\bar{3}m$) and of the room-temperature tetragonal phase (No. 99, $P4mm$) of $BaTiO_3$. (b) Phonon dispersion of tetragonal $BaTiO_3$ at the harmonic level and at 300 K including anharmonic vibrations. (c) Ground-state and excited-state potential-energy surfaces along the Γ point phonon mode, which is imaginary within the harmonic approximation in the dark. (d) Phonon dispersion of tetragonal $BaTiO_3$ at $n = 0.06$ *e/f.u.* (e) Bulk Brillouin zone at $n = 0.06$ *e/f.u.* with two nodal rings on the $q_x = 0$ and $q_y = 0$ mirror planes (orange circles, formed by the 10th and 11th bands), one nodal line along the Γ -Z high-symmetry line (brown line, formed by the 10th and 11th bands), one pair of triple Weyl points at the intersection points between the nodal rings and nodal line (violet cones, formed by the 10th, 11th and 12th bands), and four pairs of Weyl points on the $q_z = \pi$ plane (purple and yellow cones, formed by the 10th and 11th bands).

calculated total energy along the imaginary phonon mode of amplitude Q at the Γ point. The double well potential-energy curve becomes a single well upon illumination, indicating the stabilisation of the crystal structure. The underlying physics is that changing the carrier concentration n induced by photoexcitation leads to changes in the potential energy experienced by the ions, which in turn changes the interatomic force constants and the phonon dispersion. For $0.04 < n < 0.10$ *e/f.u.*, the $P4mm$ phase is not only dynamically stable, but it is also thermodynamically more stable than the cubic $Pm\bar{3}m$ phase; whereas for $n > 0.10$ *e/f.u.*, the $P4mm$ phase relaxes to the cubic phase as the latter becomes thermodynamically more stable [178]. Figure 4.1(d) shows the phonon dispersion with a photoexcited carrier density of $n = 0.06$ *e/f.u.*, confirming the dynamical stabilisation of the tetragonal phase.

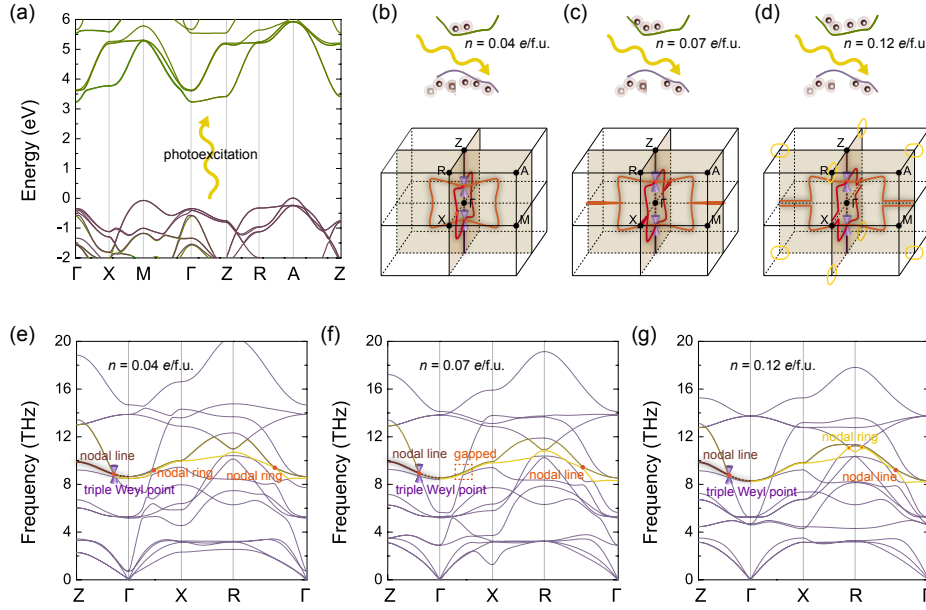


Fig. 4.2 (a) Schematic of the photoexcitation process in tetragonal BaTiO_3 . (b)-(d) Nodal lines and nodal rings formed by the 10^{th} and 11^{th} phonon branches in the bulk Brillouin zone for photoexcited carrier concentrations of 0.04 e/f.u., 0.07 e/f.u., and 0.12 e/f.u. The corresponding phonon dispersions are shown in (e)-(g).

4.2.3 Topological phonons in BaTiO_3

As a large-gap insulator, BaTiO_3 displays trivial topology in its electronic band structure [Fig. 4.2(a)]. However, there are three types of topological states in its phonon dispersion, which are nodal rings, nodal lines, and Weyl points. Since the unit cell of tetragonal BaTiO_3 has 5 atoms, there are 15 branches in the phonon spectrum. I focus on the band crossings formed by the 10^{th} and 11^{th} phonon branches (labelled by increasing energy) because they exhibit rich topological features including nodal rings, nodal lines and Weyl points. Band inversion between the 10^{th} and 11^{th} bands along the X- Γ high-symmetry line is protected by M_x symmetry, which restricts the band crossing to a 1D continuous ring/line on the mirror-invariant plane [77]. Therefore a nodal ring is formed on the $q_x = 0$ plane. Because of the existence of an additional C_{4z} symmetry, there is another nodal ring located on the $q_y = 0$ plane, related to the one on the $q_x = 0$ plane by C_{4z} symmetry [orange circles in Fig. 4.1(e)]. The combination of C_{4z} and mirror symmetries also brings out another type of topological phonon in BaTiO_3 : an endless nodal line along the Γ -Z direction [brown line in Fig. 4.1(e)]. Intersection points between these two nodal rings and the nodal line form two triple Weyl points located along the $Z'(0,0,-\pi)$ - Γ - $Z(0,0,\pi)$ line. Another topological feature of the band crossings between the 10^{th} and 11^{th} bands are eight Weyl points on the $q_z = \pi$ plane [purple and yellow cones in Fig. 4.1(e)].

4.2.4 Controlling topological phonons by light

As discussed above, both photoexcitation with $0.04 < n < 0.10$ *e/f.u.* and temperatures between 278-393 K can stabilise the tetragonal phase of BaTiO₃, as shown in Figs. 4.1(b) and (d). However, the main difference is that without photoexcitation, the long-range Coulomb interaction leads to a large LO-TO splitting [195], which tends to lift band degeneracies, as shown in Fig. 4.1(b). Consequently, the eight conventional Weyl points and the two triple Weyl points that I find in illuminated BaTiO₃ are not observed in temperature-stabilised tetragonal BaTiO₃ at 300 K. In contrast, under illumination, the photoexcited carriers lead to a strong free-carrier screening that suppresses the LO-TO energy splitting and facilitates the appearance of Weyl phonons in tetragonal BaTiO₃. Another advantage of the photoexcitation route is that, as discussed next, it can drive the phononic system between different topological quantum states, including switching between nodal-ring and nodal-line phonons, controlling the position of Weyl points in momentum space, and creating and annihilating these topological states.

As discussed above, changing the photoexcited carrier density brings about not only the transition between nodal rings and nodal lines, but also the creation of new nodal rings. As shown in Fig. 4.2(b)-(c), increasing the photoexcited carrier density from $n = 0.04$ *e/f.u.* to $n = 0.07$ *e/f.u.* drives the two nodal rings to become two nodal lines, and the corresponding phonon spectra are shown in Fig. 4.2(e)-(f). Further increasing n to 0.12 *e/f.u.* (under which conditions the tetragonal structure becomes cubic) leads to the formation of two nodal rings around the R point on the $q_x = 0$ and $q_y = 0$ planes, as shown in Fig. 4.2(d) and (g). Thus, by changing n , nodal rings in the phonon spectra can be created or transformed into nodal lines.

In addition to nodal lines and nodal rings, Weyl phonons are also sensitive to the photoexcited carrier concentration n . Fig. 4.3(a) shows the evolution of eight pairs of Weyl points on the $q_z = \pi$ plane when increasing n from 0.050 to 0.085 *e/f.u.* (four extra pairs of Weyl points emerge when $0.0695 < n < 0.0825$ *e/f.u.*). Below 0.050 *e/f.u.*, BaTiO₃ exhibits no Weyl points between the 10th and 11th branches in its phonon spectrum. At about $n = 0.050$ *e/f.u.*, four pairs of Weyl points are created around the $q_x = q_y$ and $q_x = -q_y$ planes [orange and maroon dots in Fig. 4.3(a)]. As n increases, the Weyl points in each pair with different chirality move away from each other and head to the $q_x = 0$ and $q_y = 0$ planes [yellow and purple arrows in Fig. 4.3(a)]. Once n reaches 0.0815 *e/f.u.*, Weyl points meet on the $q_x = 0$ and $q_y = 0$ planes and annihilate in pairs [light yellow and light magenta dots in Fig. 4.3(a)]. In addition, another four pairs of Weyl points of opposite chirality are created around the $q_x = q_y$ and $q_x = -q_y$ planes at $n = 0.0695$ *e/f.u.*, and annihilate in pairs on the $q_x = \pi$ and $q_y = \pi$ planes when n reaches 0.0825 *e/f.u.* [blue and green dots in Fig. 4.3(a)].

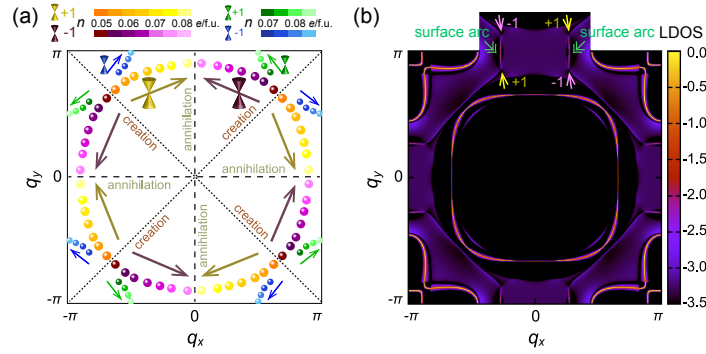


Fig. 4.3 (a) Evolution of the Weyl points on the $q_z = \pi$ plane with increasing n from 0.050 to 0.085 $e/f.u.$ (b) Phonon surface arcs for a phonon frequency of 11.42 THz at $n = 0.07 e/f.u.$

To have a better understanding of the Weyl phonons in tetragonal $BaTiO_3$, I calculate the surface local density of states (LDOS) from the imaginary part of the surface Green's function [50]. The surface LDOS in Fig. 4.3(b) is calculated along the (001) direction at 11.42 THz and $n = 0.07 e/f.u.$ The four pairs of Weyl points connect via surface arcs crossing the Brillouin zone boundaries, so that each surface arc starts from one Weyl point with a positive monopole charge and ends at another with a negative one. Overall, by modulating n I can control the creation and annihilation of Weyl points, and the length of surface arcs in tetragonal $BaTiO_3$.

4.2.5 Topological phonons in $PbTiO_3$ and $SrTiO_3$

Multiple types of topological phonons can also be found in other perovskites with the same $P4mm$ space group, and here I study $PbTiO_3$ and $SrTiO_3$ as additional examples.

$PbTiO_3$

$PbTiO_3$ has a tetragonal $P4mm$ structure for $T < 600$ K, and a cubic structure above that temperature. Although the $P4mm$ phase has the lowest energy in a wide photoexcited density range $n < 0.125 e/f.u.$ [178], it becomes dynamically unstable when $n > 0.05 e/f.u.$ I calculate the excited-state phonon dispersion at $n = 0.025 e/f.u.$, as shown in Fig. 4.4(a).

Similar to $BaTiO_3$, $PbTiO_3$ also has nodal rings, nodal lines, and Weyl points between the 10th and 11th bands. But the triple Weyl points no longer exist as the nodal rings and the nodal line do not touch. The unique band crossings along the Γ -M high-symmetry line bring about four nodal rings on the $q_x = q_y$ and $q_x = -q_y$ planes protected by M_{xy} and $M_{x\bar{y}}$ symmetries. The endless nodal lines along the Γ -Z and M-A directions are robust as well, as they are protected by the C_{4z} symmetry.

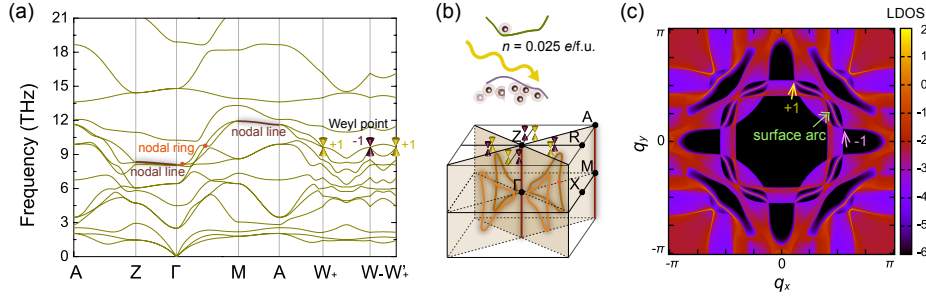


Fig. 4.4 (a) Phonon dispersion of tetragonal $P4mm$ PbTiO_3 at $n = 0.025$ e/f.u. (b) Bulk Brillouin zone at $n = 0.025$ e/f.u. with four nodal rings on the $q_x = q_y$ and $q_x = -q_y$ planes (orange circles), two nodal lines along the Γ -Z and M-A high-symmetry lines (brown line), and eight Weyl points located on $q_z = \pi$ plane (purple and yellow cones). All these three types of topological phonons are composed by the 10th and 11th bands. (c) Phonon surface arcs for a phonon frequency of 9.63 THz at $n = 0.025$ e/f.u.

The surface LDOS in Fig. 4.4(c) is calculated along the (001) direction at 9.63 THz with $n = 0.025$ e/f.u. Four pairs of Weyl points, created at $n = 0.005$ e/f.u., connect with each other via surface arcs crossing the $q_x = q_y$ and $q_x = -q_y$ planes. The location of these four pairs of Weyl points can also be modulated by changing the photoexcitation density until the lattice becomes dynamically unstable for $n > 0.05$ e/f.u.

SrTiO_3

SrTiO_3 has a different phase diagram compared to BaTiO_3 and PbTiO_3 . At low temperatures, it exhibits a centrosymmetric tetragonal phase of space group $I4/mcm$, and undergoes a phase transition to a cubic phase above 106 K. The $P4mm$ phase can only be accessed with small negative strains [196, 197]. The in-plane lattice constants a and b of $P4mm$ SrTiO_3 increase upon photoexcitation. Therefore by fixing a and b to the values in the dark, in-plane negative strain can be induced in illuminated SrTiO_3 . This can be realised experimentally by growing SrTiO_3 on an appropriate substrate. As shown in Fig. 4.5(a), after fixing the in-plane lattice constants a and b and relaxing only the out-of-plane lattice constant c in the $P4mm$ phase, the tetragonal phase can have a lower energy than the cubic $Pm\bar{3}m$ phase.

$P4mm$ SrTiO_3 exhibits imaginary phonon modes in the dark, while adding a photoexcited charge density of $n = 0.09$ e/f.u. stabilises the structure, as shown in Fig. 4.5(b). Similarly to BaTiO_3 , the $P4mm$ phase of SrTiO_3 has two nodal lines on the $q_x = 0$ and $q_y = 0$ mirror planes and one nodal line along the Γ -Z high-symmetry line in the bulk Brillouin zone. The intersection points of the three nodal lines form one pair of triple Weyl points. In contrast to BaTiO_3 , the four pairs of Weyl points are located on the $q_z = 0$ plane rather than the $q_z = \pi$ plane. Weyl phonons in SrTiO_3 can also be manipulated by photoexcitation, and the critical n

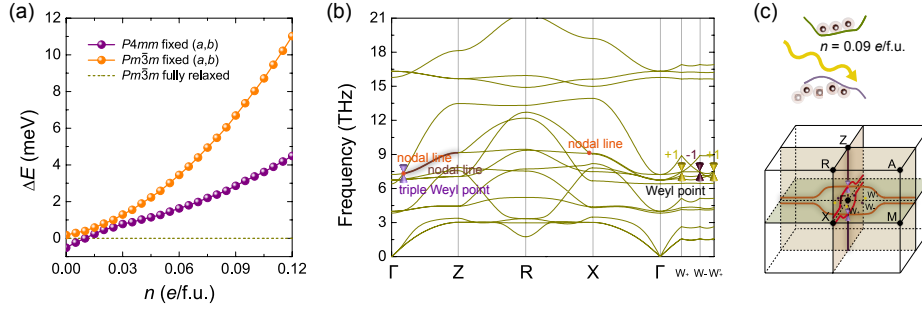


Fig. 4.5 (a) Relative energy difference between the $P4mm$ and $Pm\bar{3}m$ phases with fixed in-plane lattice constants a and b , with the energy of the fully relaxed $Pm\bar{3}m$ phase set to be zero. (b) Phonon dispersion of tetragonal $P4mm$ SrTiO_3 at $n = 0.09$ e/f.u. (c) Bulk Brillouin zone at $n = 0.09$ e/f.u. with two nodal lines on the $q_x = 0$ and $q_y = 0$ planes (orange lines), one nodal line along the Γ -Z high-symmetry line (brown line), one pair of triple Weyl points at the intersection points between the three nodal lines (violet cones), and four pairs of Weyl points on the $q_z = 0$ plane (purple and yellow dots).

for the annihilation of the Weyl points on the $q_x = 0$ and $q_y = 0$ planes is 0.105 e/f.u., which is similar to that in BaTiO_3 .

4.2.6 Discussion

The existence and coexistence of different types of topological phonons, together with their tunability by light, can occur in a variety of other structural phases of perovskites beyond the tetragonal phases investigated above. Furthermore, topological phonons in oxide perovskites can also be manipulated by other tuning parameters beyond photoexcitation, such as strain and temperature. Putting these insights together suggests that topological phonons are ubiquitous in the family of perovskite oxides, which, given their widespread use and versatility, provide a promising platform for exploring topological phonon physics and its interplay with other phases.

Given the proposed ubiquity of topological phonons in perovskites, it should be possible to directly identify them experimentally by looking for “isolated” band crossings, and the prototype materials detailed above are promising starting candidates. Topological bulk phonons can be measured by inelastic neutron scattering [151–153] and inelastic X-ray scattering [154], while the accompanying topological surface states can be detected by high-resolution electron-energy loss spectroscopy [198]. For light-induced topological phonons, although it may be difficult to illuminate the sample to maintain a constant photoexcited carrier density, transient photoexcitation could be used to observe the evolution of nodal

rings, nodal lines and Weyl points as a function of the time-dependent photoexcited carrier density.

In terms of phenomena, topological phonons with non-zero Berry curvature may contribute to the recently observed phonon thermal Hall effect in oxide perovskites [199, 200], as confirmed by a recent study [201]. In addition, novel phonon-phonon and electron-phonon scattering mechanisms could arise from topological phonons, which may provide new insights on the enhanced superconductivity of SrTiO₃ [140, 202]. The emergence of Weyl phonons may be accompanied by other unique physical properties such as a pseudogauge field with a one-way propagating bulk mode [136, 203, 204], topological negative refraction [134], and nonlinear acoustic/optical responses [205, 206], which can offer new routes for designing novel technologies like light-controlled neuromorphic computing in phononic systems [207, 208]. This chapter shows that oxide perovskites provide a promising platform to explore all of these phenomena and applications.

4.3 Conclusion

I find that topological phonons are ubiquitous in oxide perovskites and that photoexcitation provides a promising route for their manipulation. As examples, the noncentrosymmetric tetragonal phases of three oxide perovskites (BaTiO₃, PbTiO₃, and SrTiO₃) exhibit topological nodal rings, nodal lines, and Weyl points in their phonon spectra. Remarkably, I find that photoexcitation is the only way to obtain Weyl phonons in tetragonal BaTiO₃, since the thermally-stabilised tetragonal phase has a large LO-TO energy splitting in the phonon spectrum that prevents band crossings. By contrast, photoexcited carriers screen long-range interactions, suppressing the LO-TO energy splitting and facilitating the band crossings. I also find that the photoexcited carrier density can be used to tune the creation and annihilation of Weyl points and nodal rings/lines without any associated structural phase transitions. Topological phonons in oxide perovskites provide a promising platform to study physical phenomena ranging from the phonon Hall effect to superconductivity, and may also offer new technological opportunities such as the realisation of controllable topological quantum states for neuromorphic computing.

Chapter 5

Surface topology of phonons

Degenerate points/lines in the band structures of crystals have become a staple of the growing number of topological materials. The bulk-boundary correspondence in single-gap topology provides a relation between bulk topology and surface states. While line degeneracies of bulk excitations have been extensively characterised, line degeneracies of surface states are not well understood.

In this chapter, I show that SnIP, a quasi-one-dimensional van der Waals material with a double-helix crystal structure, exhibits topological nodal rings/lines in both the bulk phonon modes and their corresponding surface states. Using a combination of first-principles calculations, symmetry-based indicator theories and Zak phase analysis, I find that two neighbouring bulk nodal rings form doubly degenerate lines in their drumhead-like surface states, which are protected by the combination of time-reversal symmetry \mathcal{T} and glide mirror symmetry \bar{M}_y . My results indicate that surface degeneracies can be generically protected by symmetries such as $\mathcal{T}\bar{M}_y$, and phonons provide an ideal platform to explore such degeneracies.

This chapter is based on work published in [Bo Peng, Shuichi Murakami, Bartomeu Monserrat, and Tiantian Zhang. *npj Computational Materials* 7, 195 (2021)]. My collaborators Shuichi Murakami analysed the topological features, Tiantian Zhang and Bartomeu Monserrat devised the research idea and supervised the project, while I was responsible for the rest.

5.1 Degeneracies in the bulk and surface bands

Degeneracies in the bulk energy bands of crystals were intensively studied in the early days of band theory [15]. Recent breakthroughs have shed new light into this old topic by associating topological invariants with these degenerate points or lines [62, 71, 85]. Among

the degenerate points, twofold-degenerate Weyl points always appear in pairs that can be topologically characterised with opposite Chern numbers [72, 73, 88, 89], and fourfold-degenerate Dirac points have a linear dispersion in both electronic [74, 76, 101, 209–211] and phononic systems [133, 135]. When the band crossings are one-dimensional in momentum space, they can form nodal lines, nodal rings or nodal chains, depending on their shape [68, 70, 125, 212–217], and these line crossings are protected by symmetries such as mirror or $\mathcal{P}\mathcal{T}$ (where \mathcal{P} is the spatial inversion symmetry and \mathcal{T} is the time-reversal symmetry) [77, 78]. Recent advances, using both group theoretical analysis and high-throughput calculations, have enabled a comprehensive understanding of bulk band degeneracies in both electrons [218–220] and phonons [135].

As a result of the bulk-boundary correspondence, the degenerate bulk points and lines are associated with topologically protected surface states, including surface arcs associated with Weyl and Dirac points [86, 87, 221, 222] and drumhead-like flat bands associated with nodal lines [63, 212]. Similar to bulk band degeneracies, surface states can also exhibit band crossings in both semi-infinite slabs and finite slabs (with top and bottom surfaces) [223]. Here I focus on semi-infinite systems with only one surface. For Weyl points with Chern numbers of ± 1 , the associated helicoid surface states, whose isoenergy contours are Fermi arcs, form a continuous 2D surface in the energy-momentum space E - \mathbf{k} and have no degeneracy [224], as schematically shown in Fig. 5.1(a). In topological insulators and topological crystalline insulators, the surface states become degenerate at a single point [129, 225–228], forming a surface Dirac cone, as shown schematically in Fig. 5.1(b). In principle, two surface states can also cross along a line in the surface Brillouin zone, as shown schematically in Fig. 5.1(c). However, like the bulk case, these surface line crossings need to be protected by additional symmetries [224, 229–232]. While nodal line degeneracies in the bulk states have been thoroughly explored in a variety of quasiparticle band structures, the degenerate lines in the surface states have received less attention. The few examples of surface nodal lines all correspond to electronic band structures [224, 229–233] or artificial systems [234, 235]. It is therefore desirable to identify more candidates in other quasiparticle spectra to fully understand the role of surface degeneracies.

5.2 Surface nodal line in quasi-1D double-helix crystal SnIP

In this section, I show that SnIP, an inorganic semiconductor with nodal-ring phonons in the bulk states, exhibits nodal-line surface states in the phonon spectrum using a combination of first-principles calculations, group-theory analysis and Zak phase analysis. These surface states are doubly degenerate in a nodal line on the (100) surface. The surface nodal line is

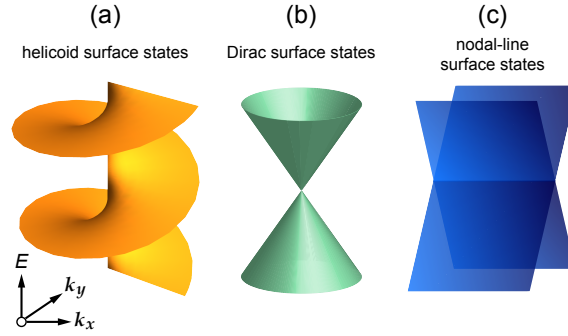


Fig. 5.1 Different types of the surface states in topological materials. (a) Non-degenerate helicoid surface states, (b) zero-dimensional degenerate Dirac surface states, and (c) one-dimensional degenerate nodal-line surface states.

protected by the anti-unitary symmetry $\vartheta = \mathcal{T}\bar{M}_y$, which is a combination of time-reversal symmetry \mathcal{T} and glide mirror symmetry \bar{M}_y . With different surface terminations, two surface nodal lines can be alternatively obtained on different parts of the (100) surface Brillouin zone, which can be understood by different Zak phases in the presence of $\mathcal{T}\bar{M}_y$ symmetry. The results suggest that similar surface degenerate lines/points will be found in other materials when there are extra symmetries to protect these surface degeneracies, and phonons can be a primary platform to study these degeneracies because of the presence of time-reversal symmetry and the flexibility to study the degeneracies in the entire phonon spectrum.

5.2.1 Computational details

All density functional theory (DFT) calculations here are performed using the Vienna *ab-initio* simulation package (VASP) [104, 105]. The generalized gradient approximation (GGA) is used in the Perdew-Burke-Ernzerhof (PBE) parametrisation for the exchange-correlation functional with 14 valence electrons ($4d^{10}5s^25p^2$) for Sn, 7 valence electrons ($5s^25p^5$) for I, and 5 valence electrons ($3s^23p^3$) for P. A plane-wave basis with a kinetic energy cutoff of 600 eV and a $7 \times 5 \times 3$ \mathbf{k} -mesh are used for structural relaxation until the energy difference is lower than 10^{-6} eV and the Hellman-Feynman force difference is lower than 10^{-4} eV \AA^{-1} . The D2 method of Grimme is used to describe the van der Waals interactions between the double helices [236].

The Hessian matrix and phonon frequencies are calculated based on the finite difference method using a $2 \times 2 \times 1$ supercell with a $3 \times 3 \times 3$ \mathbf{k} -mesh. The phonon dispersion is obtained with the PHONOPY code [52, 53]. The convergence of the supercell is checked by comparing the $2 \times 2 \times 1$ and $1 \times 1 \times 2$ supercells. The Born effective charges are also computed using a perturbative approach to account for the splitting between the longitudinal and transverse

optical phonon modes (LO-TO splitting) near the Brillouin-zone center [193], confirming that the LO-TO splitting has a minor influence on the topological properties of phonons because the topological features are far away from the zone center.

To obtain the topological properties of the lattice vibrational modes, WANNIERTOOLS is used to calculate the distribution of the band-crossing points/lines in the whole Brillouin zone [50]. The phonon surface states on the (100) surface are computed using the surface Green's function.

5.2.2 Crystal structure and phonon dispersion

SnIP is an inorganic semiconductor with a double-helix crystal structure, first synthesised in 2016, and it can be formed without any templates [237–239]. The strong covalent bonds along the helices and the weak van der Waals interactions across the helices combine the electronic properties of inorganic semiconductors, such as high electron mobility [240], and the mechanical properties of polymers, such as high flexibility [241]. In addition, by atomic substitution, a large material family with double-helix structures has been predicted using first-principles calculations, providing a wide range of band gaps between 1 and 2.5 eV [242]. With a tunable band gap and high mechanical flexibility, these quasi-one-dimensional semiconductors are extremely promising for next-generation devices ranging from mechanical sensors to optoelectronics [241, 242]. Moreover, they can serve as a material platform to realise one-dimensional physical models such as the Su-Schrieffer-Heeger (SSH) model [243] and Majorana quantum wires [244, 245].

Bulk SnIP crystallises in the monoclinic space group $P2/c$ (No. 13) with two double helices $(\text{SnIP})_7$ in the unit cell with stoichiometry $(\text{SnIP})_{14}$. The two double helices, alternatively left- and right-hand twisted, are stacked along the a direction. Each double helix is formed by an inner helical P chain and an outer helical SnI chain, as shown in Fig. 5.2(a). The $(\text{SnIP})_7$ unit in each SnIP chain winding results in a $7/2$ helix. From one phosphorus (yellow) atom to the next, the turning angle is about $\pm 360^\circ/7$ followed by a translation of $c/7$, and the same holds true for the tin (cyan) and iodine (navy) atoms in the SnI helix [246]. The calculated lattice parameters of $a = 7.889 \text{ \AA}$, $b = 9.768 \text{ \AA}$, $c = 18.422 \text{ \AA}$, and monoclinic distortion $\beta = 110.21^\circ$ match well with the measured ones [237, 239].

The calculated phonon dispersion of SnIP is presented in Fig. 5.2(b). It exhibits wide bandwidths along the helical direction, corresponding to the Γ -Y, C-Z, B-A and E-D high-symmetry lines in Fig. 5.2(c), but, by contrast, phonon bands along other high-symmetry lines, especially those perpendicular to the helices, have a relatively flat dispersion, a result of the quasi-one-dimensional nature of this material. This is consistent with the fact that SnIP has strong covalent bonds along the one-dimensional helices but only weak van der Waals-

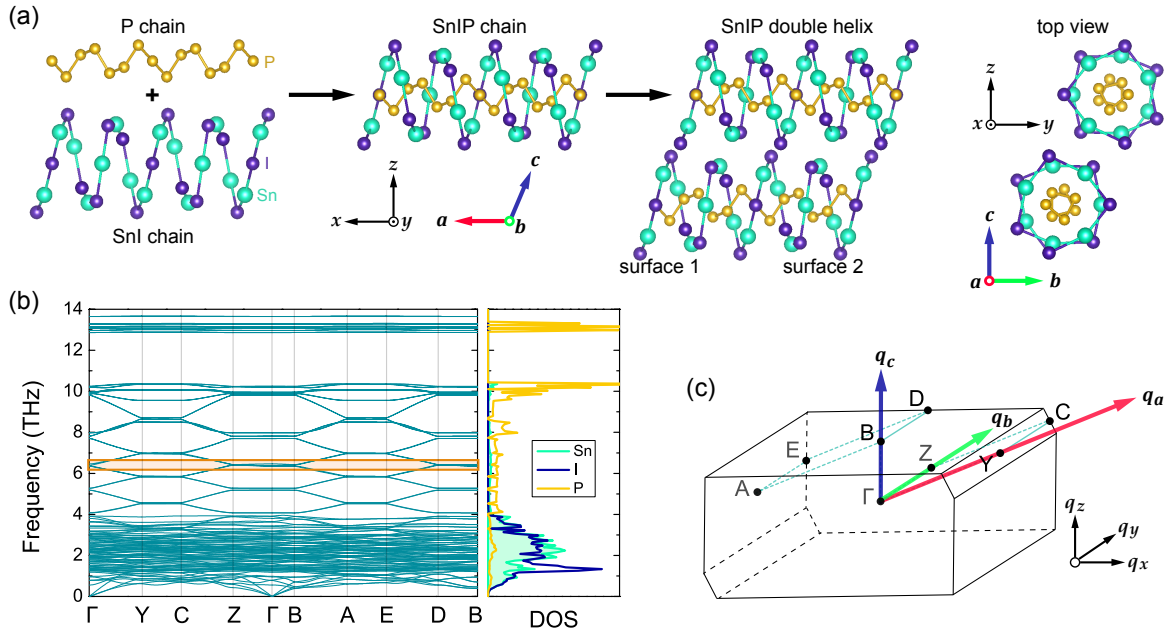


Fig. 5.2 Structural and vibrational properties of SnIP. (a) Crystal structure, (b) phonon dispersion and (c) Brillouin zone of SnIP. The orange region in the phonon dispersion highlighted in (b) corresponds to the topological features. The phonon DOS is also shown in (b).

like interactions between the double helices. As a result, SnIP fibers can be macroscopically bent by up to 90° without any significant Raman mode shifts, indicating that SnIP is an ultrasoft inorganic material and bending the helices has negligible influence on the phononic properties [241].

There are 42 atoms in the unit cell of SnIP, corresponding to 126 phonon branches. The calculated atom-projected phonon density of states (DOS) in Fig. 5.2(b) indicates that the low-frequency modes below 4 THz are mainly vibrations involving the heavier Sn and I atoms, while those between 4-14 THz are dominated by the motion of the lighter P atoms. There are 14 phosphorus atoms in the unit cell, leading to 42 P-dominated bands in the phonon spectra, spanning branches 85 to 126. The phonon modes from 4 to 10 THz (branches 85-108) are more dispersive compared to the almost flat bands between 10 and 14 THz. The two double helices are related to each other by inversion/glide mirror symmetry, so there always exist two bands with similar eigenvalues and similar eigenvectors, corresponding to the P atoms from the two separate P chains, respectively.

Hereafter I focus on the frequency range 4-10 THz because the corresponding phonon bands are relatively “clean” due to the large mass difference between phosphorus and the other two elements that separates them from the lower energy bands, and due to the strong

intrachain vibrations that make them highly dispersive. This makes them an ideal playground for exploring topological features.

5.2.3 Nodal ring phonons in SnIP

For the phonon modes between 4 and 10 THz, dominated by the vibrations of the relatively light P atoms, the phonon bands have a large dispersion along the helical direction but are almost flat along the perpendicular directions, as shown in Fig. 5.2(b). The band folding of the seven P atoms in a single helical P chain [246] leads to several band crossings near the Brillouin zone boundary, especially in the flat band regions. After a comprehensive search for band-crossing points between bands 85-108 (i.e., 4-10 THz), I find that the most promising band crossings are formed by phonon branches 92 and 93 with clean topological features in both bulk and surface states. Marked with # 92 and # 93 in Fig. 5.3(b), these two bands cross along the Γ -Z high-symmetry line.

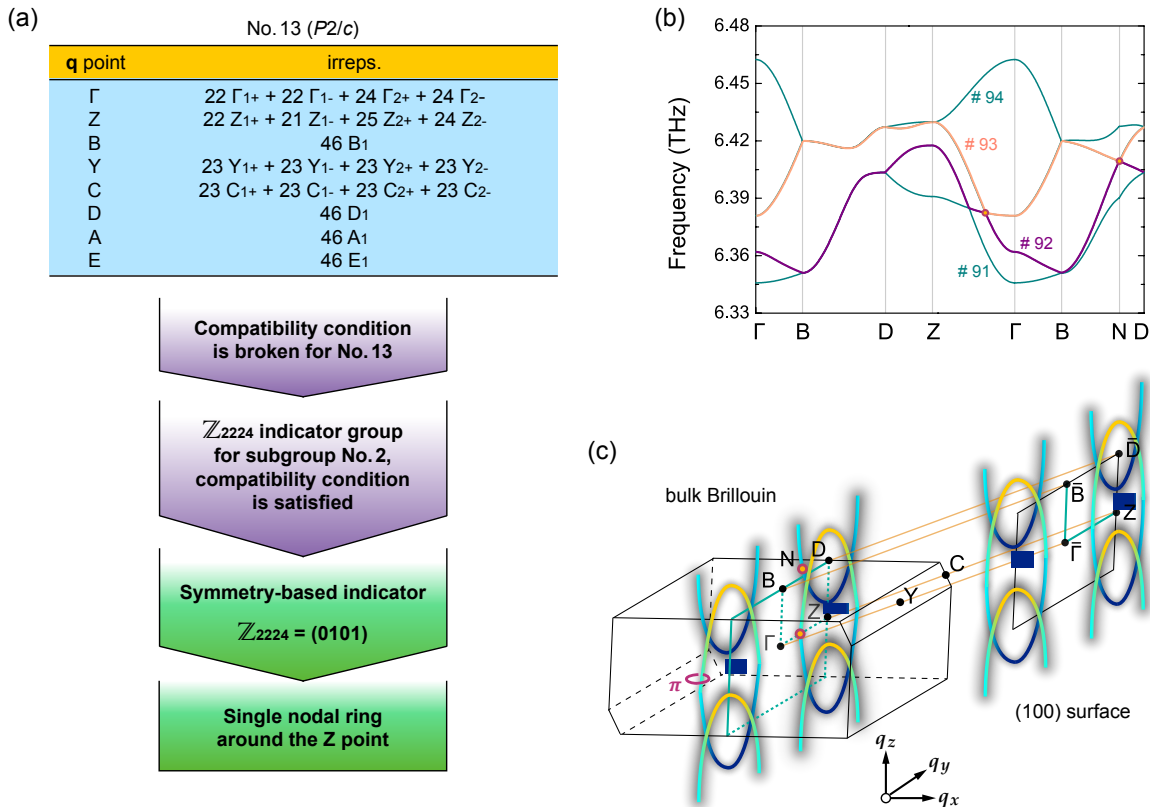


Fig. 5.3 Topological properties of SnIP. (a) Diagnosis process for the single nodal ring around the Z point using symmetry-based indicator theory for the lowest 92 bands. (b) Phonon band crossings between branches 92 and 93, and (c) the nodal rings in the bulk Brillouin zone, as well as their projections on the (100) surface.

To understand the topological information of the band crossings between branches 92 and 93, I use symmetry-based indicator theories to analyse the degeneracies [151, 155, 156, 247–249]. Because of the existence of a band crossing along the Γ -Z high-symmetry line, the compatibility condition is broken for the lowest 92 bands, as the compatibility relations can only be satisfied when the band structures have no (non-accidental) band crossings along any high-symmetry lines or at any high-symmetry points [155]. So I cannot use the symmetry-based indicator for space group No. 13. Instead, I need to find a maximal subgroup of SnIP that simultaneously satisfies the compatibility condition and has a nontrivial symmetry-based indicator. Among all the subgroups of space group No. 13 (space groups No. 2, No. 3 and No. 7), No. 2 is the only subgroup which both satisfies the compatibility condition and has a symmetry-based indicator group: (i) the compatibility condition is satisfied because the twofold rotation symmetry in No. 13 that protects the band crossing along Γ -Z is absent in No. 2; (ii) space group No. 2 has a non-trivial symmetry-based indicator of $\mathbb{Z}_{2224} \equiv \mathbb{Z}_2 \times \mathbb{Z}_2 \times \mathbb{Z}_2 \times \mathbb{Z}_4$, as discussed in detail in Ref. [155]. Therefore I can use \mathbb{Z}_{2224} as indicators to diagnose the topological degeneracy. For space group No. 2, there are eight high-symmetry points, i.e., high-symmetry points (q_a, q_b, q_c) with $q_{a,b,c} = 0, 0.5$ ($q_{a,b,c}$ in units of the reciprocal lattice vector $2\pi/a, 2\pi/b, 2\pi/c$). I obtain the irreducible representations (irreps.) at the eight corresponding high-symmetry points Γ (0,0,0), Z (0,0.5,0), B (0,0,0.5), Y (0.5,0,0), C (0.5,0.5,0), D (0,0.5,0.5), A (0.5,0,0.5), and E (0.5,0.5,0.5), as shown in Fig. 5.3(a). I then compute the indicator accordingly. The resulting indicator (0101) implies that there is a single nodal ring around the Z point in SnIP formed by branches 92 and 93, which is verified by the numerical calculations in Fig. 5.3(c).

I next examine in detail the nodal rings formed by bands 92 and 93. I zoom in on the phonon dispersion on the Γ -B-D-Z plane in Fig. 5.3(b). The band crossing formed by bands 92 and 93 along the Γ -Z high-symmetry line belongs to the single nodal ring around the Z point, carrying a quantised π Berry phase. The nodal ring crosses through the Brillouin-zone boundary around the B-D high-symmetry line, and consequently there are two nodal rings from two neighbouring Brillouin zones formed around the D point. I also plot the phonon dispersion around N $(-0.01, 0.35, 0.51)$, another band-crossing point on the neighbouring nodal ring, as shown in Fig. 5.3(b). Most interestingly, I find that the two neighbouring nodal rings projected on the (100) surface have a large overlap, and the two drumhead-like surface states of the two bulk nodal rings form a doubly degenerate line along \bar{B} - \bar{D} (as discussed below).

5.2.4 Topological surface states of SnIP

The nodal-line surface states are demonstrated by calculating the surface local density of states (LDOS) from the imaginary part of the surface Green's function [50]. I first study the surface along the (100) direction with the termination denoted as surface 1 in Fig. 5.2(a). As shown in Fig. 5.4(a), along the \bar{D} - \bar{Z} and \bar{Z} - $\bar{\Gamma}$ high-symmetry lines, two separate projections of the bulk band crossings (marked by navy and cyan arrows) belong to two single nodal rings from two neighbouring Brillouin zones respectively. The surface states are within the projections of the two bulk nodal rings, forming two non-degenerate drumhead-like surface states marked by navy and cyan triangles in Fig. 5.4(a) respectively. The surface states from the two crossing points along \bar{D} - \bar{Z} and \bar{Z} - $\bar{\Gamma}$ merge with each other at \bar{D} , and result in a doubly degenerate surface nodal line along \bar{B} - \bar{D} (green triangle). The surface nodal line ends at the crossing point of the two projected nodal rings marked by green arrow in Fig. 5.4(a).

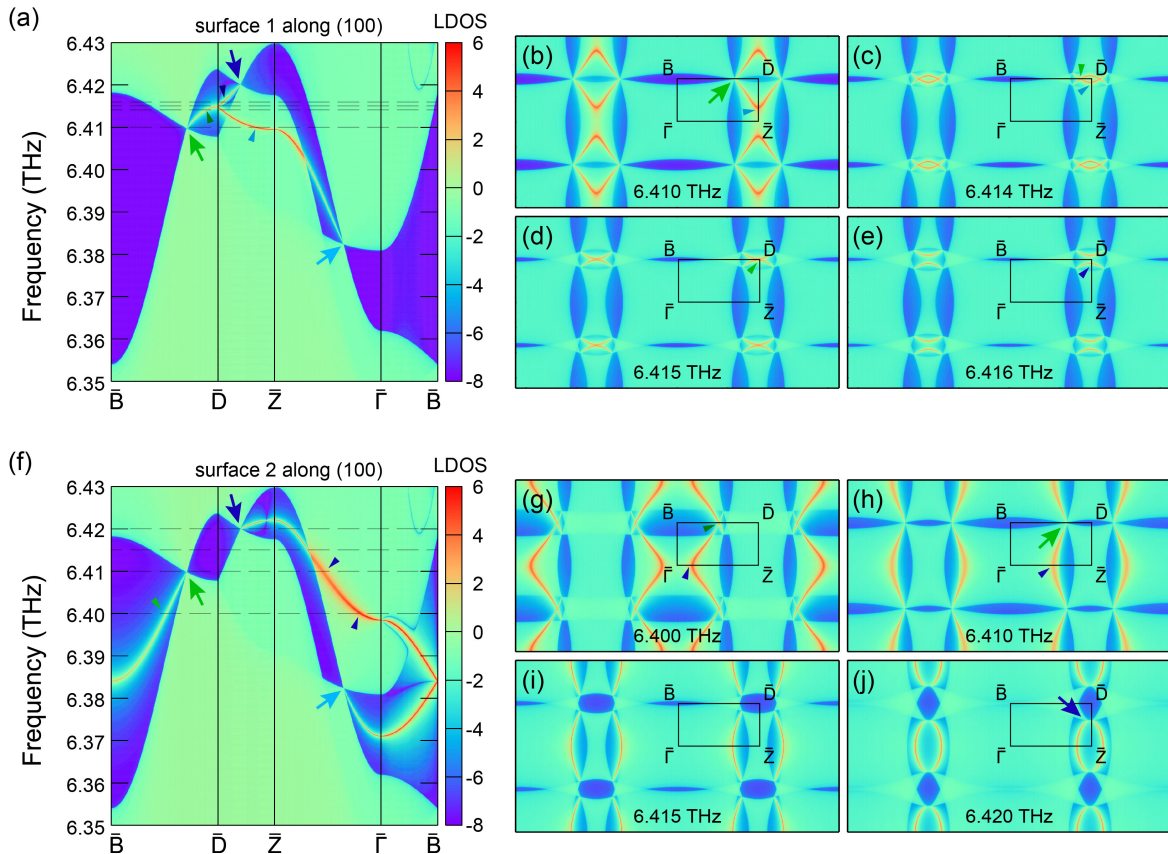


Fig. 5.4 Topological surface states of SnIP. (a) Topological surface states of surface 1 along the (100) direction, as well as the surface arcs for phonon frequencies of (b) 6.410 THz, (c) 6.414 THz, (d) 6.415 THz, and (e) 6.416 THz. (f) Topological surface states of surface 2 along the (100) direction, as well as the surface arcs for phonon frequencies of (g) 6.400 THz, (h) 6.410 THz, (i) 6.415 THz, and (j) 6.420 THz.

To have a better view of the doubly degenerate surface states along the $\bar{B}-\bar{D}$ high-symmetry line, I plot the isofrequency surface arcs for different phonon frequencies in Fig. 5.4(b)-(e). As shown in Fig. 5.4(b), at the exact frequency of the doubly degenerate projected bulk band crossings (green arrow) along $\bar{B}-\bar{D}$ at 6.410 THz, the two surface arcs (cyan triangle) merge at the projected bulk band crossings. For a phonon frequency of 6.414 THz, the two surface arcs (cyan triangle) move towards each other, forming two arc crossing points (green triangle) along $\bar{B}-\bar{D}$ in Fig. 5.4(c). At 6.415 THz, the two arc crossing points move to the \bar{D} point until they merge into a single arc crossing point [green triangle in Fig. 5.4(d)]. Further increasing the phonon frequency eventually leads to two separate surface arcs as the two arcs no longer touch [navy triangle in Fig. 5.4(f)]. The arc crossing points on the isofrequency plane belong to the doubly degenerate surface nodal line in the frequency-momentum space [green triangle in Fig. 5.4(a)].

The surface nodal line in SnIP is protected by the combination of time-reversal symmetry and glide mirror symmetry $\vartheta = \mathcal{T}\bar{M}_y$. For systems with time-reversal symmetry \mathcal{T} and any nonsymmorphic spatial symmetry G , the ‘‘Kramers-like’’ degenerate nodal line appears when $(\mathcal{T}G)^2 = -1$, either along the $\mathcal{T}G$ invariant lines or on the $\mathcal{T}G$ invariant planes, and a degenerate line can thus be protected by the $\mathcal{T}G$ symmetry. This applies to line degeneracies in both the bulk states [250] and the surface states [229–231]. SnIP has glide mirror symmetry $\bar{M}_y = \{M_y | 00\frac{1}{2}\}$, and $(\mathcal{T}\bar{M}_y)^2 = e^{i2\pi q_z}$ (q_z in units of the reciprocal lattice vector $2\pi/c$). On the (100) surface, both $q_z = 0$ and $q_z = 0.5$ are $\mathcal{T}\bar{M}_y$ invariant lines, and $(\mathcal{T}\bar{M}_y)^2 = -1$ only occurs when $q_z = 0.5$, corresponding to the $\bar{B}-\bar{D}$ high-symmetry line. As a result, the doubly degenerate surface nodal line along $\bar{B}-\bar{D}$ is protected by the $\mathcal{T}\bar{M}_y$ symmetry.

If I change the surface termination [denoted as surface 2 in Fig. 5.2(a)] along the (100) direction, the doubly degenerate surface states along the $\bar{B}-\bar{D}$ high-symmetry line in Fig. 5.4(f) no longer exist in the frequency range 6.410-6.415 THz, but move to the lower-frequency range 6.384-6.410 THz. The distribution of the surface nodal line changes to the other side of $\bar{B}-\bar{D}$, from the purple shaded area in Fig. 5.5(a) to that in Fig. 5.5(b).

The alternation between the distributions of the surface nodal line can be understood by how $\mathcal{T}\bar{M}_y$ influences the Zak phase on the (100) surface Brillouin zone. The Zak phase provides information of the distribution of the doubly degenerate surface states on the (100) surface, and can be integrated along the (100) direction,

$$\gamma(q_b, q_c) = i \int_{-\pi}^{\pi} \sum_{\mathbf{v}=\text{occu.}} \langle \psi(\mathbf{q}\mathbf{v}) | \frac{\partial}{\partial q_a} | \psi(\mathbf{q}\mathbf{v}) \rangle dq_a, \quad (5.1)$$

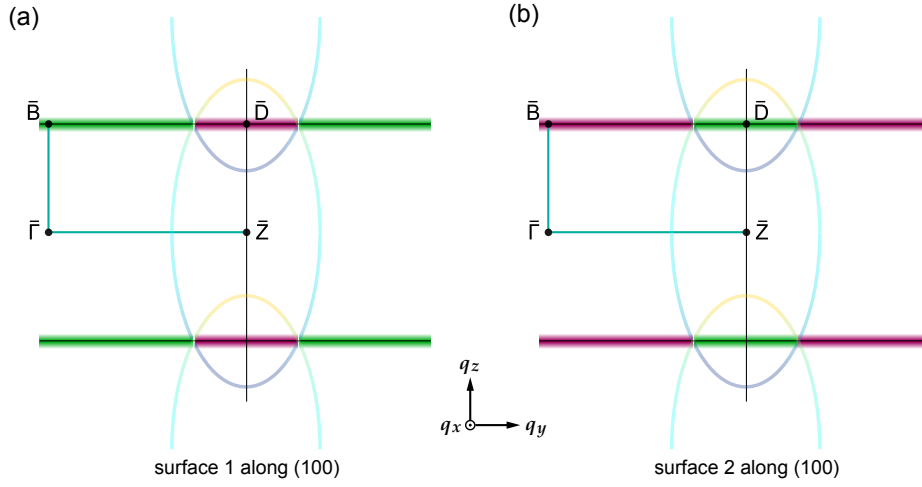


Fig. 5.5 Zak phase analysis. Zak phase of (a) surface 1 and (b) surface 2 along the (100) direction. The purple and green shaded areas correspond to the total Zak phase $\gamma = 2\pi$ and $\gamma = 0$ respectively.

where $\psi(\mathbf{q}\nu)$ is the phonon eigenvector with wave vector \mathbf{q} and band index ν . Note that on the (100) surface Brillouin zone, $q_b \parallel q_y$ and $q_c \parallel q_z$, therefore (q_x, q_y, q_z) is used instead of (q_a, q_b, q_c) to be consistent with $\mathcal{T}\bar{M}_y$. When $q_z = 0.5$, $(\mathcal{T}\bar{M}_y)^2 = -1$, and the phonon eigenvectors can be separated into two mutually related subgroups $\{\psi_1(\mathbf{q})\}$ and $\{\psi_2(\mathbf{q})\}$ with $\psi_1(-q_x, q_y, 0.5) = (\mathcal{T}\bar{M}_y) \cdot \psi_2(q_x, q_y, 0.5)$, i.e., $\{\psi_1(\mathbf{q})\}$ and $\{\psi_2(\mathbf{q})\}$ are $\mathcal{T}\bar{M}_y$ related at constant q_y and $q_z = 0.5$. Therefore, for the $\bar{B}-\bar{D}$ high-symmetry line ($q_z = 0.5$) on the (100) surface Brillouin zone, the Zak phases for the two subgroups $\{\psi_1(\mathbf{q})\}$ and $\{\psi_2(\mathbf{q})\}$ are equal to each other, i.e. $\gamma_1(q_y, 0.5) = \gamma_2(q_y, 0.5)$. Due to $\mathcal{P}\mathcal{T}$, $\gamma_1(q_y, 0.5) = \gamma_2(q_y, 0.5)$ is either 0 or π , which depends on the surface termination (i.e. choice of the inversion center). When $\gamma_1(q_y, 0.5) = \gamma_2(q_y, 0.5) = 0$, there are no surface states as the total Zak phase $\gamma = \gamma_1 + \gamma_2 = 0$. When $\gamma_1(q_y, 0.5) = \gamma_2(q_y, 0.5) = \pi$, the total Zak phase $\gamma = 2\pi$, leading to doubly degenerate surface states. For surface 1, the purple shaded line in Fig. 5.5(a) has a total Zak phase of 2π with two surface states distributed in this area, while the green shaded area corresponds to $\gamma = 0$ and there are no surface states in this area. For surface 2, the Zak phase of the purple shaded area and the colourless area swap, as shown in Fig. 5.5(b), and the distribution of the surface nodal line switches to the new purple shaded area. It should be noticed that the standard definition of Zak phase is in terms of modulo 2π , and a Zak phase of 2π is therefore equal to zero under this definition. However, in SnIP, a total Zak phase of 2π corresponds to $\gamma_1 = \gamma_2 = \pi$, i.e. two π Zak phases within each subgroup, indicating two surface states emerging from each subgroup. On the other hand, a total Zak phase of zero corresponds to two zero Zak phases within each group, leading to vanishing surface states.

It is worth mentioning that bending SnIP rods does not break the time-reversal and glide mirror symmetries on the (100) surface of SnIP. Therefore, the degenerate topological surface states remain unchanged under bending.

5.3 Conclusions and outlook

In summary, I find that double-helical SnIP exhibits nodal-ring phonons in the bulk and nodal-line phonons on the surface based on first-principles calculations and group-theory analysis. Benefiting from a quasi-one-dimensional crystal structure, the lattice vibrational modes of the intrachain phosphorus atoms along the helices are highly dispersive. Due to the winding of the helix P chain, these phonon bands are folded at the Brillouin zone boundary, forming single nodal rings across the whole Brillouin zone. The overlap between the two neighbouring nodal rings on the (100) surface leads to a surface nodal line that is protected by the combination of time-reversal and glide mirror symmetries $\mathcal{T}\bar{M}_y$. Different surface terminations result in different distributions of the surface nodal line, which can be understood by different Zak phases in the presence of $\mathcal{T}\bar{M}_y$. I demonstrate that, similar to the bulk nodal lines, the surface nodal lines can widely exist when protected by extra symmetries. My discoveries may offer opportunities to study the degeneracy of the topological surface states and their transport properties.

In terms of fundamental physics and applications, topological bulk phonons in double-helical SnIP may lead to non-dissipative surface phonons, which offer a promising platform for designing thermal devices. The existence of surface nodal lines also provides opportunities to study surface transport properties for thermoelectric devices. As another example, the bulk and surface nodal lines/rings in the phonon spectra result in large phonon DOS, which may also enhance surface superconductivity. Additionally, because of its quasi-one-dimensional crystal structure, SnIP could also be a promising material platform to investigate one-dimensional physical models such as the SSH model and Majorana quantum wires. With its high mechanical flexibility, it is also interesting to investigate the interplay between flexoelectricity and topology. My work provides a starting point to explore all these phenomena and applications.

Chapter 6

Multi-gap topology in phonons

Single-gap topologies have been extensively explored, and a large number of materials have been theoretically proposed and experimentally observed. These ideas have recently been extended to multi-gap topologies with band nodes that carry non-Abelian charges, characterised by invariants that arise by the momentum-space braiding of such nodes. However, the constraints placed by the Fermi-Dirac distribution to electronic systems have so far prevented the experimental observation of multi-gap topologies in real materials.

In this chapter, I show that multi-gap topologies and the accompanying phase transitions driven by braiding processes can be readily observed in the bosonic phonon spectra. Phonons can carry non-Abelian frame charges at the band-crossing points of their frequency spectrum, and that external stimuli can drive their braiding. I present a general framework to understand the topological configurations of phonons from first-principles calculations using a topological invariant called Euler class, and provide a complete analysis of phonon braiding by combining different topological configurations. Taking a well-known dielectric material, Al_2O_3 , as a representative example, I demonstrate that electrostatic doping gives rise to phonon band inversions that can induce redistribution of the frame charges, leading to non-Abelian braiding of phonons. This work provides a new quasiparticle platform for realisable non-Abelian braiding in reciprocal space, and expands the toolset for studying braiding processes.

This chapter is based on work published in [Bo Peng, Adrien Bouhon, Robert-Jan Slager, and Bartomeu Monserrat. *Physical Review B* 105 (8), 085115 (2022)]. My collaborators Adrien Bouhon and Robert-Jan Slager provided the theoretical description, and Bartomeu Monserrat supervised the computational part, while I was responsible for the rest.

6.1 Multi-gap topology

In single-gap topology, topologically inequivalent band structures can be determined using the band representations at high-symmetry points in the Brillouin zone [248, 251, 252], an approach that matches the full K-theory result in some scenarios [248, 253]. These momentum-space constraints have subsequently been compared to real-space constraints, resulting in versatile classification schemes to characterise topological materials by identifying which of these combinations have an atomic limit [247, 254].

Recent work is uncovering new physics beyond these symmetry-indicated schemes that depends on multi-gap conditions, where the band-crossing points (nodes) carry non-Abelian frame charges [67, 255–259]. The non-Abelian frame charges can only be realised in multi-band systems, and as such is referred to as multi-gap topology, in contrast to the single-gap topology associated with two-band systems. The nodes carrying non-Abelian frame charges in multi-band systems can be described by a real Hamiltonian [67, 256–267]. The real Hamiltonian constraint leads to a real basis of eigenvectors [268, 269] and is fulfilled with the symmetry requirement of either (i) a combination of C_2 rotation symmetry and time-reversal symmetry \mathcal{T} for both spinful and spinless systems, or (ii) a combination of spatial inversion symmetry \mathcal{P} and time-reversal symmetry \mathcal{T} for spinless systems. In any multi-band system with a real Hamiltonian, the band-crossing points carry non-Abelian frame charges. If a pair of nodes within a gap carry the same frame charge (with the same sign), they cannot be annihilated when brought together. Conversely, two nodes within the same gap with opposite frame charges can be annihilated. The stability of the (possibly multiple) pairs of nodes can be characterised with a new invariant, known as the Euler class, which can be computed over patches in the Brillouin zone that contain all the nodes of that two-band subspace. Generically, an Euler class χ indicates the presence of $2|\chi|$ stable nodes (i.e. with the same charge) within the two-band space over that Brillouin zone patch.

The signs of the non-Abelian frame charges of the nodes within one gap can be converted through the braiding of nodes belonging to adjacent energy gaps [258, 260, 261, 270], thus changing the relative stability between pairs of nodes in the same gap. As a consequence, the braiding of nodes is accompanied with the transfer of stable pairs of nodes from one gap to an adjacent gap.

To achieve elementary braiding it is necessary to braid one node of an energy gap with a node of an adjacent gap (the gap immediately above or immediately below in energy). The motion of the nodes can be driven by modifying the band structure of the material with the application of external stimuli. In solid state systems, where the band structure inherits the symmetries of the crystal, braiding involves groups of nodes that are related by symmetry. Moreover, the braid trajectories usually collapse onto the high-symmetry points

of the Brillouin zone. As a consequence, the transfer of a stable pair of nodes from one gap to an adjacent gap is often manifested by a band inversion at one of the high-symmetry points, and such band inversion provides a very direct signature of the braiding process in crystalline systems. This phenomenology is rather general, and reciprocal-space braiding can in principle occur in multi-band systems of any quasiparticle, including electrons and phonons.

I find that phonons are an ideal platform to study the non-Abelian braiding of band nodes in the context of multi-gap topology. As a bosonic excitation associated with ionic vibrations, the entire phonon spectrum is readily accessible to external probes. This contrasts with fermionic excitations such as electrons, in which the Pauli exclusion principle means that only band nodes near the Fermi level can be accessed, placing significant restrictions to the full exploitation of multi-gap topologies. Additionally, phonons are charge neutral, spinless quasiparticles, and time-reversal symmetry \mathcal{T} is hard to break in phonons because they do not directly couple to magnetic fields. For these reasons, the symmetry requirements of real Hamiltonians can be easily fulfilled by phonons in a wide range of materials, suggesting that many will exhibit non-Abelian frame charges in their phonon dispersion. Therefore, I can extend the study of phonon bands from single-gap topologies to multi-gap topologies.

6.2 Theoretical background

The main purpose of this section is to provide a general framework to review the theoretical background behind non-Abelian frame charges. The key mathematical objects to study multi-gap topologies are (i) non-Abelian frame charges, and (ii) a topological invariant called Euler class, which captures the relative stability of a pair of nodes within the same gap, that is, whether annihilation of the nodes is possible or not, and that in turn depends on their trajectory with respect to the nodes of the adjacent gaps.

6.2.1 Non-Abelian frame charges

I start by introducing non-Abelian frame charges in the context of a three-band Bloch Hamiltonian of a two-dimensional system with $C_2\mathcal{T}$ symmetry. The spectral decomposition of the 3×3 Hamiltonian gives

$$H = \sum_{n=1,2,3} |e_n\rangle E_n \langle e_n|, \quad (6.1)$$

with the ordered eigenvalues $E_1 < E_2 < E_3$ (which are assumed to be gapped) and the eigenvectors $\{|e_n\rangle\}_{n=1,2,3}$ that can be chosen to be real in an appropriate basis [67]. As a result, the three real and normalised eigenvectors form a three-dimensional orthonormal frame $(|e_1\rangle, |e_2\rangle, |e_3\rangle) \in \mathbb{R}^3 \times \mathbb{R}^3$, that is, an orthogonal matrix $O(3)$, or, fixing the handedness (i.e. the orientation of the frame), a 3D rotation matrix $SO(3)$. For real eigenvectors, the gauge phase degree of freedom of complex eigenvectors turns into a $+/-$ sign degree of freedom [67, 261]; specifically, $(|e_1\rangle, |e_2\rangle, |e_3\rangle)$, $(|e_1\rangle, -|e_2\rangle, -|e_3\rangle)$, $(-|e_1\rangle, |e_2\rangle, -|e_3\rangle)$, and $(-|e_1\rangle, -|e_2\rangle, |e_3\rangle)$ all represent the same state (the orientation of the frame is not preserved if only one sign flips). Therefore, the order-parameter space of the Hamiltonian can be expressed as $SO(3)$ modulo the group of π rotations that flip the sign of two eigenvectors, namely $SO(3)/D_2$ (the dihedral point group $D_2 = \{E, C_2, C_2', C_2''\}$ is composed of three independent and perpendicular π -rotations) [270].

For a band-crossing point (node) in a three-band system, I can define a topological frame charge by the geometry of the $SO(3)$ rotations encircling the node in momentum space, as the acquired angle can be calculated by decomposing the 3D rotation matrix around the encircled node [67, 258, 261, 271]. A closed path in $SO(3)/D_2$ can be characterised by the fundamental homotopy group $\pi_1[SO(3)/D_2] = \mathbb{Q}$, where $\mathbb{Q} = (\pm i, \pm j, \pm k, -1, +1)$ is the quaternion group with $i^2 = j^2 = k^2 = -1$, $ij = k$, $jk = i$, $ki = j$, and where the charges $\{i, j, k\}$ anti-commute [261]. Lifting the $SO(3)$ -frame in the covering spin group $\text{Spin}(3) = \text{SU}(2)$ and using the correspondence $(-i\sigma_x, -i\sigma_y, -i\sigma_z) \mapsto (i, k, j)$ from the parallel-transported spin-frames over a base loop l and the quaternion charges, I can assign a quaternion frame charge to any node formed by the bands within the region bounded by the loop l [261]. The nodes formed by the lower two bands can thus be characterised by the frame charge $\pm i$, and the nodes formed by the upper two bands can be characterised by $\pm j$. A pair of nodes, one formed by the lower two bands and the other formed by the upper two bands, can be denoted by $\pm k$ as $k = ij$. The sign of the charges is fixed by (i) the gauge chosen for the frame at a base point of the loop, and (ii) the orientation of the parallel-transport over the base loop. The stability of a pair of nodes formed by the same two bands can then be characterised by -1 , because two nodes with the same frame charge cannot annihilate when brought together, as can be deduced from the algebra of the quaternion charges, i.e. $i^2 = j^2 = k^2 = -1$ (note $k^2 = i \cdot j \cdot i \cdot j = i \cdot j \cdot (-j) \cdot i = i^2 = -1$). The -1 frame charge is gauge invariant since $(+i)^2 = (-i)^2$, and similarly for j and k . On the other hand, two nodes with opposite frame charges can be annihilated or created pairwise, with a total frame charge of $(-i)(+i) = (-j)(+j) = +1$.

The quaternion group is non-Abelian, as captured by the non-commutativity of the charges $\{i, j, k\}$ and the non-trivial action of their conjugation, e.g. $j^{-1}ij = -jij = j^2i = -i$.

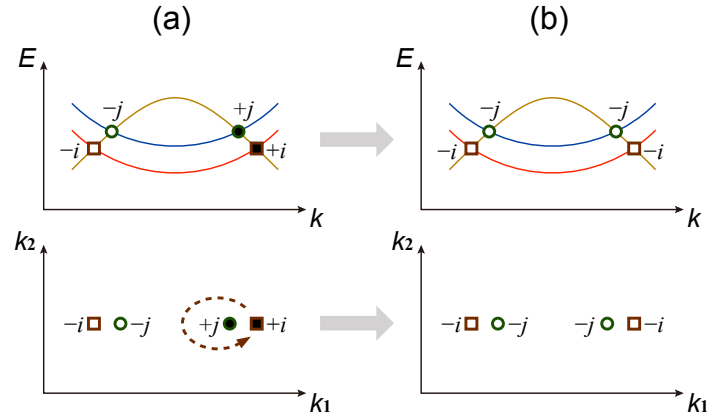


Fig. 6.1 Topological configurations (a) before and (b) after the braiding. Squares (circles) represent the nodes formed by the lower (upper) two bands, and open (closed) symbols represent the nodes with negative (positive) frame charges. Importantly, the frame charges of the nodes are unambiguously defined only once a base point, an oriented base loop and choice of gauge have been fixed.

This indicates the possibility of flipping the non-Abelian frame charge of a node. The frame charges are defined for a fixed base point with a fixed oriented base loop, and through the composition of oriented loops, a conjugation operation, say $j^{-1}ij = -i$, corresponds to the braiding of a node, i , around a node in an adjacent gap, j [261]. Therefore, the band nodes in three-band systems can carry a non-Abelian charge, and the sign of the topological frame charge can be flipped by a braiding process, as schematically shown in Fig. 6.1. Hereafter I use open (closed) symbols to represent the nodes with negative (positive) frame charges. Different from the topological invariants formed only by two bands in single-gap topologies, in three-band systems the frame charge depends on the braiding of the nodes formed by both the lower two and the upper two bands, which involve all three bands [255]. For clarity, I use squares (circles) to represent the nodes formed by the lower (upper) two bands. As shown in Fig. 6.1(a), a node formed by the lower two bands with a frame charge $+i$ (labelled as a closed square) can circle another node formed by the upper two bands with a frame charge $+j$ (labelled as a closed circle), and as a result, the signs of the frame charges are changed to be $-i$ and $-j$ respectively [labelled as an open square and an open circle in Fig. 6.1(b)]. This process can create an obstruction to annihilate two opposite nodes, e.g. $+i$ and $-i$ in Fig. 6.1(a), by braiding one node around another node formed by the neighbouring bands, so the frame charges of the pair of nodes become the same, e.g. the two nodes with the same frame charge of $-i$ in Fig. 6.1(b).

While the quaternion charges intrinsically unveil the non-Abelian nature of the multi-gap topology of systems described by a real Hamiltonian, they are cumbersome to use in real

material band structures because crystal point-group symmetries lead to node multiplicities. Fortunately, there exists a complementary quasi-two-dimensional topological invariant which not only simplifies the computation of the topological charges, but also greatly refines the characterisation of the topological stability of nodes belonging to the same gap. This is the patch Euler class that I introduce next.

6.2.2 Patch Euler class

In the following, I number the bands from lower to higher energy with $E_n \leq E_{n+1}$, and I label the partial gap between two successive bands n and $(n+1)$ as $\{\Delta_n\}$ with $E_n \leq \Delta_n \leq E_{n+1}$. Similar to the Berry curvature in single-gap topologies, the Euler curvature (Euler form) can be computed for bands n and $(n+1)$ in gap Δ_n [67, 256, 265]:

$$\text{Eu}_n(\mathbf{k}) = \langle \partial_{k_1} e_n | \partial_{k_2} e_{n+1} \rangle - \langle \partial_{k_2} e_n | \partial_{k_1} e_{n+1} \rangle, \quad (6.2)$$

where $|e_n\rangle$ and $|e_{n+1}\rangle$ are eigenvectors of bands n and $(n+1)$ respectively, and $\mathbf{k} = (k_1, k_2)$ are the coordinates of the Brillouin zone. Assuming that there is no node connecting the bands n and $(n+1)$ to other bands on \mathcal{D} , the Euler class χ_n for the bands n and $(n+1)$ over a patch \mathcal{D} of the Brillouin zone is then defined by [67, 256]

$$\chi_n[\mathcal{D}] = \frac{1}{2\pi} \left[\int_{\mathcal{D}} \text{Eu}_n(\mathbf{k}) dk_1 dk_2 - \oint_{\partial\mathcal{D}} \mathbf{a}_n \cdot d\mathbf{k} \right], \quad (6.3)$$

where $\partial\mathcal{D}$ is the boundary of the patch, and with the Euler connection $\mathbf{a}_{n,i} = \langle e_n | \partial_{k_i} | e_{n+1} \rangle$ for $i = 1, 2$.

When integrated over the whole Brillouin zone, the Euler class χ_n is an integer \mathbb{Z} [255, 256, 260, 272, 273], and indicates the presence of $|\chi_n|$ pairs of stable nodes formed by a two-band subspace. When integrated over a patch \mathcal{D} , the Euler class in Eq. (6.3) can either have integer or half-integer values, indicating the presence of $2|\chi_n|$ stable nodes within the patch. For instance, assuming the presence of two nodes within the patch, an Euler class of 0 indicates that the nodes can annihilate [Fig. 6.2(a)], whereas an Euler class of ± 1 means that they cannot annihilate when brought together [Fig. 6.2(b)]. Importantly, the Euler class is related to the frame charges discussed above: for a patch containing only one node, a patch Euler class of $\chi_1 = \pm 1/2$ ($\chi_2 = \pm 1/2$) can be associated to the frame charge $\pm i$ ($\pm j$) and such a node is referred to as a linear node [Fig. 6.2(c)], while the value $|\chi_n| = 1$ indicates the frame charge is -1 and such a node is referred to as a quadratic node [Fig. 6.2(d)]. Hereafter, I label a quadratic node of $|\chi_n| = 1$ as two concentric symbols since it can be interpreted as the superposition of two linear nodes.

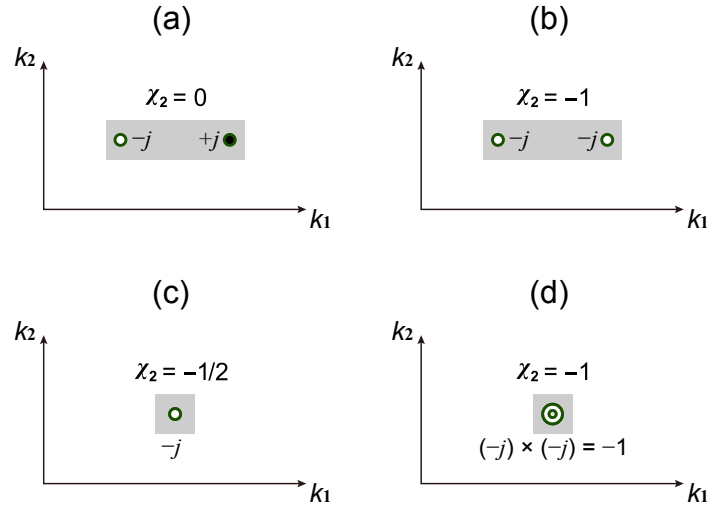


Fig. 6.2 Patch Euler class for two nodes in the same gap Δ_2 (a) with opposite frame charges and (b) with the same frame charges, as well as the patch Euler class for (c) a linear node and (d) a quadratic node. I use open (closed) symbols to represent the nodes with negative (positive) frame charges, and one symbol (two concentric symbols) to represent the linear (quadratic) node.

The Euler class refines the topological analysis since, contrary to the frame charges, it keeps track of the stability of an arbitrary number of nodes formed by two bands, taking a half-integer (integer) value for an odd (even) number of stable nodes. However, this requires that the two bands under consideration must be disconnected from all the other bands over the patch. The direct computation of the frame charges remains useful when more than two bands are degenerate at a single point, which can happen at critical points during a band inversion.

One interesting feature of the Euler class is that it gives the lower bound of the power-like dispersion of the bands at a band crossing [262, 265]. More precisely, the number $2|\chi_n|$ gives the lower bound of the exponent of the leading term in a Taylor expansion of the energy eigenvalues at the band crossing. At this stage, a clarification is necessary to distinguish between electrons and phonons, as the frequencies of the phonon bands correspond to the square root of the eigenvalues of the dynamical matrix that defines the topology. Interestingly, the order of band crossings in phonon band structures is almost always doubled, with the exception of the dispersion of the acoustic bands at Γ corresponding to the Goldstone modes of the system [264].

Because the gauge sign (± 1) of the real eigenvectors is not fixed, the absolute sign of the topological charges is not uniquely defined. For example, if the gauge signs of the orthonormal frame of eigenvectors flip from $(|e_1\rangle, |e_2\rangle, |e_3\rangle)$ to $(|e_1\rangle, -|e_2\rangle, -|e_3\rangle)$, the sign of the patch Euler class χ_2 also flips, and similarly for the frame charges. Therefore, the

sign of the Euler class and of the non-Abelian frame charge is gauge dependent, and for an individual node taken in isolation this sign has no physical meaning. However, the relative sign between two distinct nodes is not gauge dependent as it provides information on the stability of the nodes. Therefore, the Euler class can be computed for different patches, and the sign of the topological frame charges can be assigned to get a consistent global topological configuration where the relative signs of all nodes agree with their gauge invariant relative stability. Such a global picture can be obtained by fixing the gauge globally [265]. For this, I introduce in Sec. 6.2.3 the last conceptual object that is needed, namely the Dirac string [256].

6.2.3 Dirac strings

Considering two linear nodes in gap Δ_n , each band eigenvector forming the nodes $\{|e_n\rangle, |e_{n+1}\rangle\}$ carries a π Berry phase on any loop encircling one node at the time, thus indicating a π disinclination line connecting the two nodes. The gauge sign of the eigenvectors must then flip when crossing this line [273]. A Dirac string can be visualised as the line connecting the two nodes, in analogy with the Dirac string connecting two Weyl nodes in 3D indicating the winding of the $U(1)$ gauge phase of complex eigenvectors.

The trajectory of the Dirac string is not unique because the gauge signs of the eigenvectors can be changed (although such a local change does not affect the topological stability of whether any pair of nodes can be annihilated when merged). Despite the fact that different Dirac strings can be assigned for the same pair of nodes, the trajectory of a Dirac string between two nodes is constrained by the gauge freedoms of all other nodes, collectively leading to what are known as the “Dirac string rules” [256, 262]:

1. All linear nodes formed by the same two bands must be connected by Dirac strings in pairs, whereas the quadratic nodes can be interpreted as two linear nodes merged together with an internal Dirac string.
2. The sign of the frame charge of a node in Δ_n changes when crossing a Dirac string connecting two nodes in the neighbouring gaps (Δ_{n-1} or Δ_{n+1}). This can be realised either by moving the node in Δ_n across a fixed Dirac string in Δ_{n-1} or Δ_{n+1} [Fig. 6.3(a)] or by moving a Dirac string in the neighbouring gap across the fixed node [Fig. 6.3(b)].
3. All the Dirac strings connecting the nodes in the same gap can be re-assigned by changing their start and end nodes. For example, in Fig. 6.4 I can connect node 1 with node 3 and node 2 with node 4, or connect node 1 with node 2 and node 3 with node 4, or connect node 1 with node 4 and node 2 with node 3.

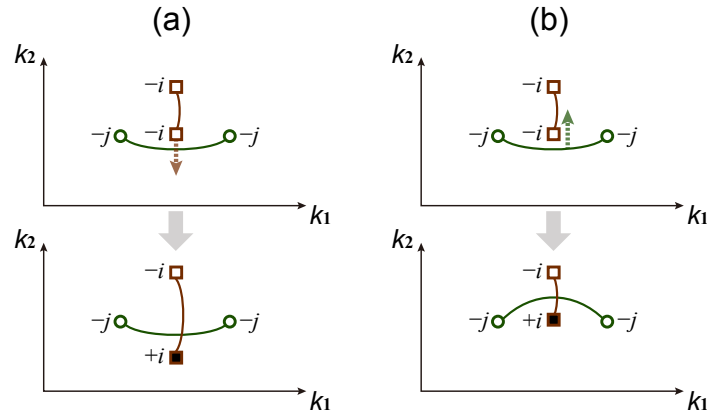


Fig. 6.3 Flipping of the sign of the frame charge by (a) moving the node across a fixed Dirac string or (b) moving a Dirac string across the fixed node. These processes amount to the same thing.

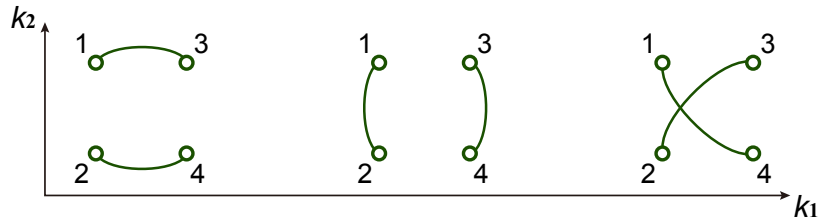


Fig. 6.4 Dirac strings re-assigned by changing the start and end nodes.

By systematically computing the Euler class of every single band crossing, and then of every pair of band crossings in the same gap, a signed frame charge can be assigned to every node, as well as the Dirac strings that connect every pair of linear nodes, such that a consistent global topological configuration can be obtained [262, 265], as discussed in the next subsection. This procedure works like a puzzle: the sign, i.e. the gauge, of an initial node is arbitrarily fixed and then the Dirac strings of the neighbouring nodes can be iteratively assigned in a consistent manner, i.e. under the constraint of the gauge-invariant values of all the patch Euler classes previously computed.

6.2.4 Global topological configuration

To obtain the global topological configuration, the Brillouin zone needs to be divided into different patches, each containing a pair of nodes in the same gap, and the patches cover all the nodes. Then the Euler class is calculated for each patch, which provides information on the relative stability within each and every pair of nodes.

The relative signs of the frame charges are then specified for all the nodes based on the patch Euler class calculations, and afterwards all the linear nodes are connected in pairs by

Dirac strings to make the Euler class for all the patches consistent with each other. Even within each patch there are two possible configurations: a patch Euler class of ± 1 (0) can either correspond to two nodes with the same (opposite) frame charge(s), or contain two opposite (same) charge nodes and an extra Dirac string in the neighbouring gap.

I next check whether the assignment of frame charges and Dirac strings is physically consistent for the global topological configuration. As long as the frame charges and the Dirac string of one patch are fixed, the rest of the global topological configuration can be deduced like a puzzle based on the computed Euler class for all the patches and the Dirac string rules.

Because the local gauge sign is not fixed, the start and end nodes of the Dirac strings, as well as the corresponding trajectory, are not unique. Therefore, for a given set of patch Euler classes, there may be many different (but consistent) global topological configurations. The difference comes from the local and global gauge choices. However, the different global topological configurations capture the same physics, for example, whether a pair of nodes will annihilate or not, which is gauge invariant.

I can apply the same strategy, based on the calculated Euler class and the Dirac string rules, to obtain the topological configurations during the braiding processes that take place when the system undergoes a transformation of its band structure, i.e. during a topological phase transition upon band inversion. However, once the global topological configuration of the system is known, the topological configuration of any other phases reached upon the displacement of the nodes and band inversions can be readily predicted by applying the conversion rules presented above.

In real materials, where the crystal symmetries constrain the movement of the nodes and often collapse the braid trajectories to the high-symmetry points, these rules need to be complemented with the crystal symmetry rules contained in the irreducible representations which dictate when a band crossing can be avoided or not. These concepts are exemplified in Sec. 6.3, which describes the braiding of phonons in aluminium oxide.

Overall, this establishes a theoretical framework to study non-Abelian braiding of any quasiparticle with three bands in their spectra, as long as the system has $C_2\mathcal{T}$ symmetry so that the corresponding Hamiltonian is real [67]. The theoretical formalism can also be extended to spinless systems of any dimensions with \mathcal{PT} symmetry.

In this section, I describe the calculation of the Euler class for phonon bands using the phonon eigenvectors that can be obtained from a first-principles lattice-dynamics calculation. I also explain how to then use the Euler class to derive the global topological configurations of all the nodes in the multi-band system.

The key quantity in the theoretical formalism described in the previous section is the Euler form in Eq. (6.2). Its evaluation requires the eigenvectors of the quasiparticles as input, and these eigenvectors can be directly calculated from first principles for a range of quasiparticles. I use phonons as an example quasiparticle to describe how to calculate the patch Euler class. As discussed earlier, I focus on phonons because (i) their bosonic nature means the entire spectrum is accessible (in contrast to the restriction to the Fermi energy in fermionic systems), and (ii) the time-reversal symmetry \mathcal{T} is hard to break in phononic systems.

6.3 Case study: phonon braiding in monolayer Al_2O_3

In this section, I exemplify the calculation of the Euler class and associated non-Abelian braiding using first-principles methods. To do so, I explore non-Abelian braiding in the phonon spectrum of monolayer Al_2O_3 as controlled by electrostatic doping.

6.3.1 Computational details

first-principles calculations

Density functional theory (DFT) calculations are performed with the Vienna *ab initio* Simulation Package (VASP) [104, 105]. The generalised gradient approximation (GGA) with the Perdew-Burke-Ernzerhof (PBE) parameterisation is used as the exchange-correlation functional [183]. A plane-wave basis with a kinetic energy cutoff of 800 eV and a 9×9 \mathbf{k} -mesh are used for monolayer Al_2O_3 . The self-consistent field calculations are stopped when the energy difference between successive steps is below 10^{-6} eV, and the structural relaxation is stopped when forces are below 10^{-3} eV/Å. A vacuum spacing larger than 20 Å is used to eliminate interactions between adjacent layers. Electrostatic doping is simulated by introducing extra charges with a compensating background. I keep the lattice constants fixed upon doping to mimic the material growth on a substrate, and the ionic positions remain the same upon doping under structural relaxation.

The force constants to determine the phonons are computed using the finite-differences method in a 3×3 supercell (equivalent to a 3×3 phonon \mathbf{q} -mesh) with a 3×3 electronic \mathbf{k} -mesh using VASP. The phonon dispersion and phonon eigenvectors are obtained using PHONOPY [52, 53]. This is consistent with the fact that no out-of-plane dipole is observed upon doping, and it is therefore sufficient to use the compensating background charge when introducing the extra charges, without the need to include a Coulomb cutoff in the vacuum spacing [274]. I focus on hole doping because imaginary phonon modes are observed upon

electron doping, indicating that the lattice becomes dynamically unstable in the latter case. The splitting between the longitudinal and transverse optical phonons (LO-TO splitting) is neglected because in 2D materials no LO-TO splitting occurs at Γ and only the slope of phonon bands changes [275], which implies that the nodal structure will remain unchanged.

The phonon band-crossing points for all the bands are calculated using WANNIERTOOLS [50]. After obtaining all the nodes in gap Δ_n , I divide the 2D Brillouin zone into different patches, and each patch contains either one node or a pair of nodes in Δ_n . Each patch in the 2D Brillouin zone is sampled with a 30×30 \mathbf{q} -mesh, and the phonon eigenvectors $\mathbf{e}_{\mathbf{q}n}$ and $\mathbf{e}_{\mathbf{q}(n+1)}$ are computed at each of the points sampled, and subsequently rotated to the real basis. The real eigenvectors are then used to calculate the patch Euler class using a modified version of a publicly available MATHEMATICA code [276], with the calculated real eigenvectors as input.

Euler class calculations

After obtaining the phonon dispersion and eigenvectors, I need to find all the phonon band-crossing points in gap Δ_n . Then I divide the 2D Brillouin zone into different patches, and each patch contains either one node or a pair of nodes in Δ_n . The phonon eigenvectors $\mathbf{e}_{\mathbf{q}n}$ and $\mathbf{e}_{\mathbf{q}(n+1)}$ are computed on a discretised grid over the patch. The patch for nodes in Δ_n should not overlap with the positions of nodes in the neighbouring gaps Δ_{n-1} and Δ_{n+1} .

The Euler form in Eq. (6.2) is calculated for all the patches in gap Δ_n with the phonon eigenvectors $\mathbf{e}_{\mathbf{q}n}$ and $\mathbf{e}_{\mathbf{q}(n+1)}$ as input. For each band and \mathbf{q} -point, the eigenvector is generally composed of a set of three complex values associated with each atom along the Cartesian axes. In the presence of $C_2\mathcal{T}$ symmetry (or $\mathcal{P}\mathcal{T}$ symmetry) that squares to the identity, there always exists a unitary transformation under which the dynamical matrix becomes real, and the associated eigenvectors are then also real. This unitary transformation is obtained through the Takagi factorisation of the matrix representation of the $C_2\mathcal{T}$ symmetry, which turns out to be symmetric [67]. Then, isolating the unitary part of the matrix representation of $C_2\mathcal{T}$, the Takagi factorisation can be readily obtained through singular-value decomposition [266, 277].

Using the real basis I can directly evaluate the expression in Eq (6.3), which is implemented in a publicly available MATHEMATICA code [276]. Alternatively, the patch Euler class of nodes can be calculated by employing Wilson-loop methods [67, 260]. Because of the random sign gauge $+/-$ and the presence of the Dirac string with a gauge transformation, I can smooth the eigenvectors by computing the Berry phase and fixing the position of the Dirac strings. As a result, the eigenvectors $\mathbf{e}_{\mathbf{q}n}$ and $\mathbf{e}_{\mathbf{q}(n+1)}$ vary smoothly away from the Dirac strings, with both states flipping their signs simultaneously when crossing a Dirac string. The Berry phase calculations also provide information on the positions and the Berry

curvature of the nodes, which helps to verify whether the patch contains the node(s) I am interested in. The gauged eigenvectors can then be used to compute Eq. (6.3) over the patch \mathcal{D} .

After evaluating the relative stability of each pair of nodes, I can assign the frame charges to all the nodes based on the Euler class of all the patches, as well as the Dirac strings that connect all the linear nodes. I repeat this procedure until a global topological configuration is obtained.

6.3.2 Crystal structure and phonon dispersion

Monolayer Al₂O₃ is predicted to crystallise in a honeycomb lattice [278]. The aluminum and oxygen atoms are in the same plane, with the oxygen atoms forming a Kagome lattice in 2D, as shown in Fig. 6.5(a). The calculated lattice constant of 5.842 Å agrees well with previous calculations [278]. Monolayer Al₂O₃ belongs to the $P6/mmm$ space group (No. 191), which has C_2 rotation symmetry. In addition, in phonons the time-reversal symmetry \mathcal{T} is automatically satisfied. With $C_2\mathcal{T}$ symmetry, phonons in monolayer Al₂O₃ can be described by a real Hamiltonian (dynamical matrix), and consequently I can assign non-Abelian frame charges to different nodes in any three-band subsystem in the entire phonon spectrum.

Figure 6.5(b) shows the calculated phonon dispersion. No imaginary phonon modes are observed, indicating the dynamical stability of monolayer Al₂O₃. There are 5 atoms in the unit cell, leading to 15 phonon branches. I focus on the top three bands, i.e. bands 13–15 marked in the blue area between 30 and 35 THz in Figure 6.5(b), because they are isolated from other phonon bands and are more sensitive to electrostatic doping, thus providing an ideal platform to explore multi-gap topology and non-Abelian braiding.

6.3.3 Band inversion upon electrostatic doping

Bulk Al₂O₃ is a well-known dielectric material used in electronic devices. Therefore, electrostatic doping of monolayer Al₂O₃ by gate voltage can be easily incorporated into the existing microelectronics industry. I simulate the phonon spectra of Al₂O₃ upon electrostatic doping. As shown in Fig. 6.6, the phonon frequencies of bands 13–15 at the Γ point have only slight changes upon doping. On the other hand, the highest phonon bands at the K point with double degeneracy move to much lower frequency with increasing doping concentration, whereas the frequency of the non-degenerate single band at K remains nearly the same. Therefore, the band order at K is inverted at -0.14 e/f.u., with the doubly degenerate band becoming lower than the single band.

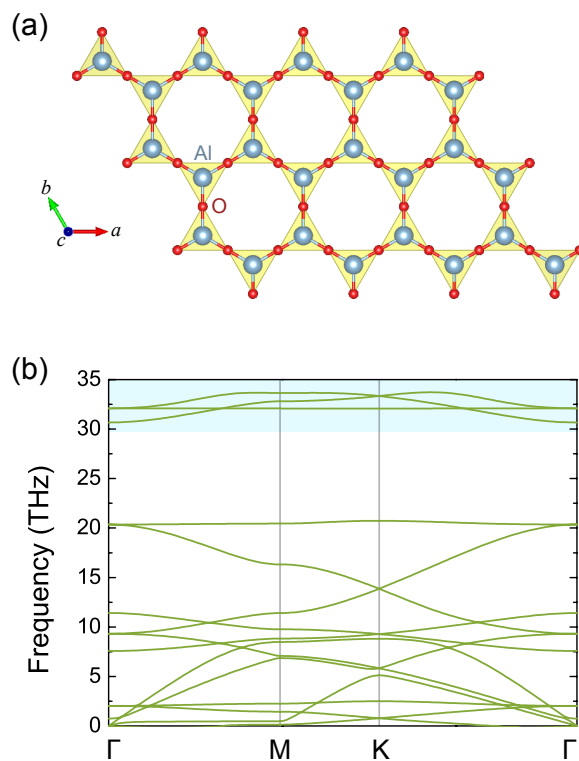


Fig. 6.5 (a) Crystal structure and (b) phonon dispersion of monolayer Kagome Al_2O_3 .

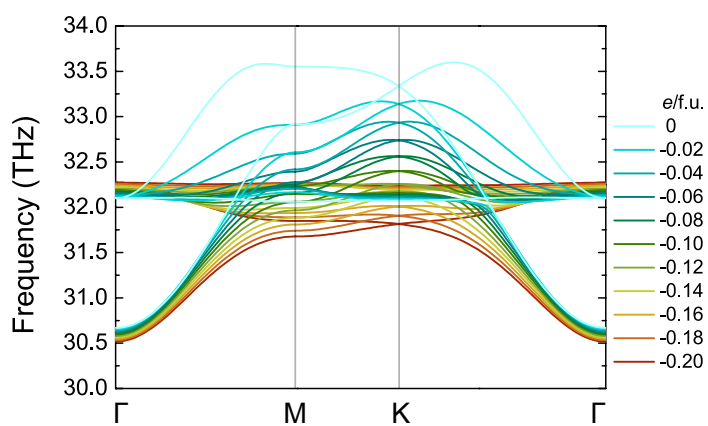


Fig. 6.6 Evolution of phonon bands 13 – 15 upon electrostatic doping.

Such phonon band inversion redistributes the band nodes in two neighbouring gaps Δ_{13} and Δ_{14} , and consequently induces conversions of the frame charges. The transfer of frame charges between different gaps is accompanied by the non-Abelian braiding of the nodes. It is however important to note that the crystalline symmetries of the system constrain the movements of the nodes over the Brillouin zone with, as a consequence, the collapse of the braid trajectories onto the high-symmetry points Γ and K . In the next subsections I first investigate the topological configurations at different doping concentrations individually, and then obtain the complete picture of the braiding processes upon electrostatic doping.

6.3.4 Frame charges of undoped Al₂O₃

I first investigate the phonon band-crossing points formed by band 13, 14 and 15 of undoped Al₂O₃. To be consistent with the notation introduced in the theoretical background section (Section 6.2), I use squares to represent single nodes in gap Δ_{13} formed by bands 13 and 14, and circles for single nodes in gap Δ_{14} formed by bands 14 and 15. As shown in Fig. 6.7(a), a band-crossing point is formed when the two crossing bands belong to different irreducible representations (irreps), whereas two bands with the same irrep remain gapped. To be specific, the violet square node along Γ -M formed by bands 13 and 14 [red and blue lines in Fig. 6.7(a)] is not gapped as the two bands belong to irreps Σ_1 and Σ_2 , but these two bands have an avoided crossing along K - Γ because in that case they belong to the same irrep Λ_4 . In addition, there are two circle nodes at Γ and K formed by bands 14 and 15 [blue and yellow lines in Fig. 6.7(a)] with 2D irreps Γ_6^- and K_5 respectively.

Figure 6.7(b) shows the positions of all the nodes. I first compute the Euler class for single nodes, as indicated by patches 1–3 in Fig. 6.7(b). In patch 1, the dark yellow circle at the Γ point has an Euler class of -1 , indicating a quadratic node. This agrees well with the quadratic dispersion near Γ . Consistent with Section 6.2, I label the quadratic node by a small circle inside a large circle because it can be viewed as two linear nodes merged together. On the other hand, the Euler class for the dark green circle in Δ_{14} at the K point (patch 2) and the violet square in Δ_{13} along the Γ -M high-symmetry line (patch 3) is $\pm 1/2$, indicating two linear nodes. Note that for a single node the sign of the Euler class has no physical meaning due to the $+/-$ sign freedom, but the relative signs of two nodes in the same gap provide information on their stability. To be consistent with Section 6.2, I use open (closed) symbols to represent the nodes with negative (positive) frame charges, as shown in Fig. 6.7(b).

I next compute the Euler class for all the patches containing pairs of *linear nodes*. For the neighbouring dark green circles in patch 4, $\chi_{14} = 0$, indicating that these two nodes can either carry opposite frame charges or have the same frame charge with a nearby Dirac string in Δ_{13} . For convenience, I connect the neighbouring pair of violet nodes in Δ_{13} in patch 5

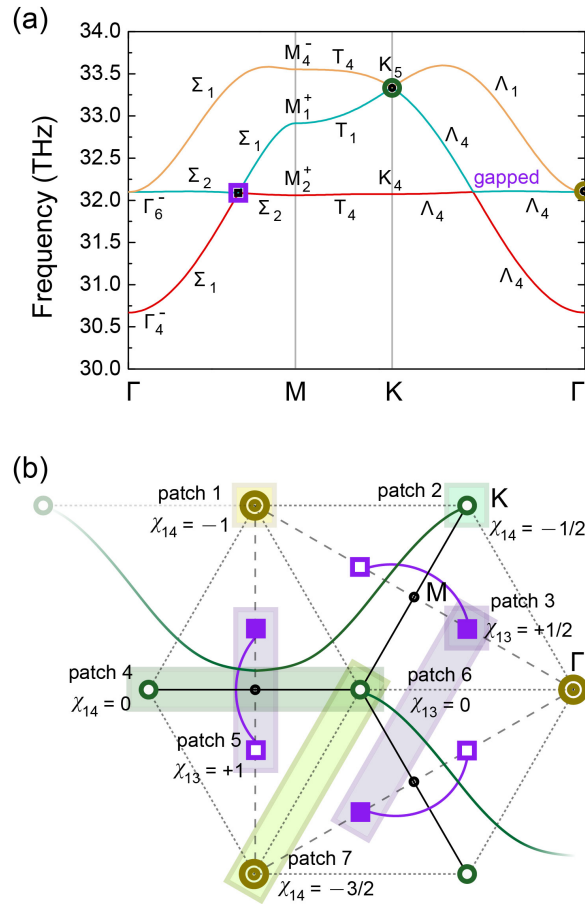


Fig. 6.7 (a) Phonon band-crossing points and (b) patch Euler class of undoped Al_2O_3 . I use squares (circles) to represent the nodes formed by the lower (upper) two bands, open (closed) symbols to represent the nodes with negative (positive) frame charges, and one circle (two concentric circles) to represent the linear (quadratic) node.

with a violet Dirac string, and assign the same frame charge to the dark green nodes in patch 4. I also connect the pair of dark green nodes with a dark green Dirac string.

I then calculate the Euler class for all the patches containing all neighbouring pairs of the violet square nodes in Δ_{13} . For patch 5, $\chi_{13} = 1$, indicating that the two nearest nodes along Γ -M can either carry the same frame charge or have opposite frame charges with a nearby Dirac string in Δ_{14} . Because of the presence of a dark green Dirac string in their neighbouring gap Δ_{14} that crosses patch 5, I can assign the opposite frame charges to the violet nodes in Δ_{13} in patch 5. In patch 6, $\chi_{13} = 0$, and I can assign the same frame charges to the corresponding violet nodes as there is a Dirac string in Δ_{14} crossing patch 6. I then assign the Dirac strings for the neighbouring violet squares, and obtain the complete global topological configuration shown in Fig. 6.7(b).

Finally, I check the consistency of the global topological configuration by computing the Euler class for patch 7. The calculated $\chi_{14} = -3/2$ is consistent with the presence of a quadratic node with $\chi_{14} = -1$ at Γ and a linear node with $\chi_{14} = -1/2$.

6.3.5 Frame charges of -0.08 *e/f.u.*-doped Al_2O_3

At -0.08 *e/f.u.*, several band inversions take place around the Γ and M high-symmetry points, as shown in Fig. 6.8(a). Along Γ -M the top two bands with irreps Σ_1 and Σ_2 start to be inverted, and the top two bands along K- Γ with irreps Λ_1 and Λ_4 are inverted as well. Because these two bands along both Γ -M and K- Γ have different irreps, there are two new circle nodes in Δ_{14} formed along these two high-symmetry lines, and I label the nodes along Γ -M in blue and those along K- Γ in green. In addition, at the M point, bands 13 and 14 are also inverted, as the band with irrep M_1^+ now becomes lower than that with irrep M_2^+ . As a result, the nodes in Δ_{13} transfer from Γ -M to M-K. These band inversions significantly change the number and positions of the band nodes in gaps Δ_{13} and Δ_{14} , and the distribution of the topological frame charges is completely different from that in undoped Al_2O_3 .

I start the Euler class calculations from the patches containing single nodes. The Euler class of the quadratic node at Γ and the linear node at K remains the same. All other nodes, created by the band inversions, are linear nodes as their patch Euler class is $\pm 1/2$.

For the magenta square nodes in Δ_{13} along M-K, the Euler class for the two magenta patches, containing the first and second nearest neighbours in Fig. 6.8(b), is 1 and 0 respectively. Because there is no Dirac string in Δ_{14} crossing these two patches, I can assign the same frame charge for all the nearest pairs of magenta square nodes, while keeping the second nearest pairs either with the opposite frame charges or with the same frame charge and a nearby Dirac string in Δ_{14} .

I then calculate the Euler class for pairs of the neighbouring green circles in Δ_{14} , and obtain $\chi_{14} = 1$ for all the patches. Because the green circle nodes are far away from the square nodes in Δ_{13} (and their Dirac strings), I can safely assign the same frame charge for all the green circle nodes.

For the blue circle nodes along Γ -M, the patch Euler class for the nearest pair around M is 0, while the second nearest neighbour of nodes has a patch Euler class of $\chi_{14} = -1$. Thus I can assign all the blue circles with the same negative frame charge, with a Dirac string in Δ_{13} connecting the two magenta square nodes around M. I can also connect the second nearest neighbours of the blue circle nodes in pairs with the Dirac strings, without influencing the topological configurations in Δ_{13} .

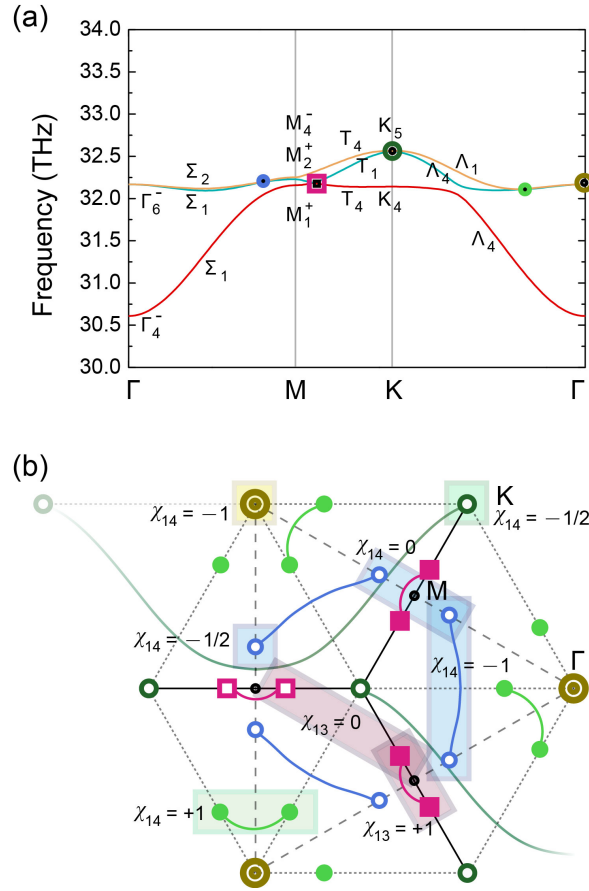


Fig. 6.8 (a) Phonon band-crossing points and (b) patch Euler class of -0.08 $e/f.u.$ -doped Al_2O_3 .

The consistent global topological configuration is summarised in Fig. 6.8(b), which is also consistent with the conversion of frame charges from undoped Al_2O_3 to -0.08 $e/f.u.$ -doped Al_2O_3 (as discussed later).

6.3.6 Frame charges of -0.10 $e/f.u.$ -doped Al_2O_3

At -0.10 $e/f.u.$, the top two bands are inverted at M, and the M_2^+ band becomes higher than the M_4^- band [Fig. 6.9(a)]. Consequently the top two bands along Γ -M are fully inverted as well, as the Σ_2 band is the highest all along the Γ -M high-symmetry line. As a result, the blue circle nodes in Δ_{14} along Γ -M disappear.

As the inversion of bands 14 and 15 occurs at M, the two nearest blue nodes in Δ_{14} meet each other at M. Before they meet at M, one of them must cross the magenta Dirac string in Δ_{13} , which flips the sign of its frame charge. Therefore, the two blue nodes, now with the opposite frame charge, can annihilate when brought together at M. The Dirac strings of three

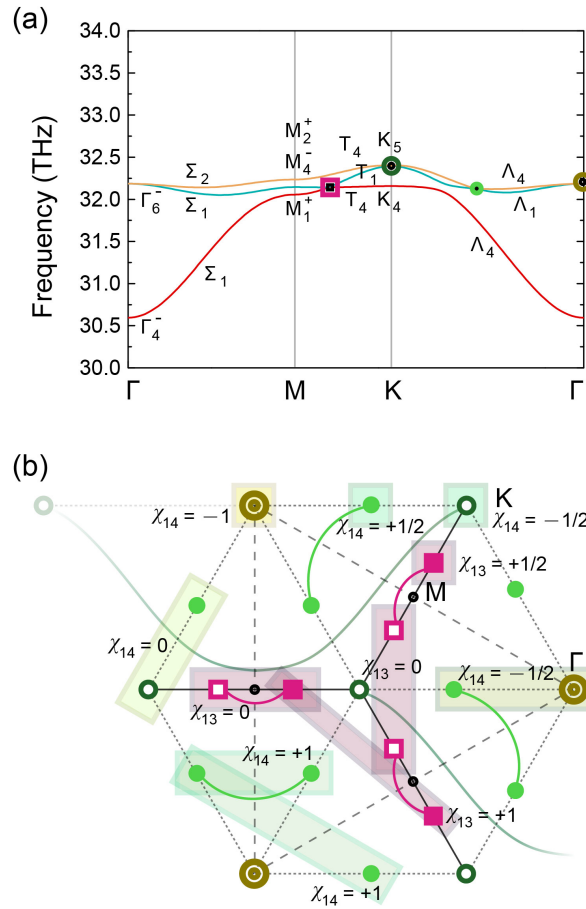


Fig. 6.9 (a) Phonon band-crossing points and (b) patch Euler class of -0.10 *e/f.u.*-doped Al_2O_3 .

pairs of the blue nodes now merge into a closed loop connecting the three neighbouring M points, encircling the K point in the middle. By shrinking the closed Dirac string towards K, the Dirac string disappears, and this also flips the sign of the frame charges of the three magenta nodes inside the loop. Consequently, the two nearest magenta square nodes along M-K now carry opposite frame charges.

To verify this I compute the patch Euler class in Fig. 6.9(b). The calculated Euler class for the magenta nodes is consistent with the deduction that the two nearest magenta nodes have opposite frame charges. In addition, as the braiding only takes place around M, the topological frame charges remain unchanged for other nodes away from M. This is also confirmed by the Euler class calculations.

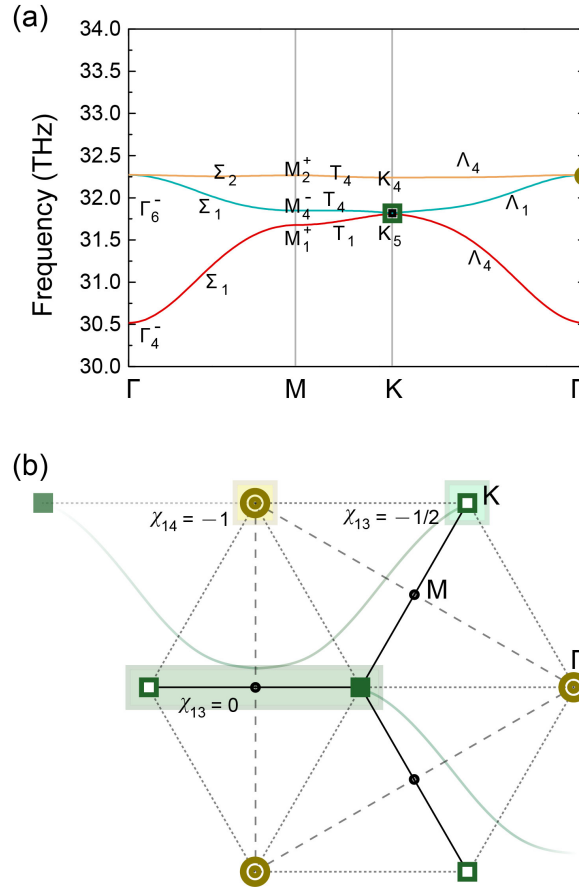


Fig. 6.10 (a) Phonon band-crossing points and (b) patch Euler class of -0.20 $e/f.u.$ -doped Al_2O_3 .

6.3.7 Frame charges of -0.20 $e/f.u.$ -doped Al_2O_3

At -0.14 $e/f.u.$, the doubly degenerate band with K_5 irrep becomes lower than the K_4 band, and upon further doping the topological configurations remain the same as no additional band inversion occurs. The phonon dispersion and the corresponding global topological configuration at -0.20 $e/f.u.$ are shown in Fig. 6.10. The bands are well separated from each other at this doping density so I can label the irreps more clearly.

I compute the Euler class for all the single nodes first, and the calculated $\chi_{14} = -1$ at Γ and $\chi_{13} = -1/2$ at K indicate a robust quadratic node in Δ_{14} at Γ and a linear node in Δ_{13} at K . I also compute the Euler class for the patch containing two nearest K points, and obtain $\chi_{13} = 0$. Therefore I can assign opposite frame charges to the K points, and connect each pair of them with a Dirac string.

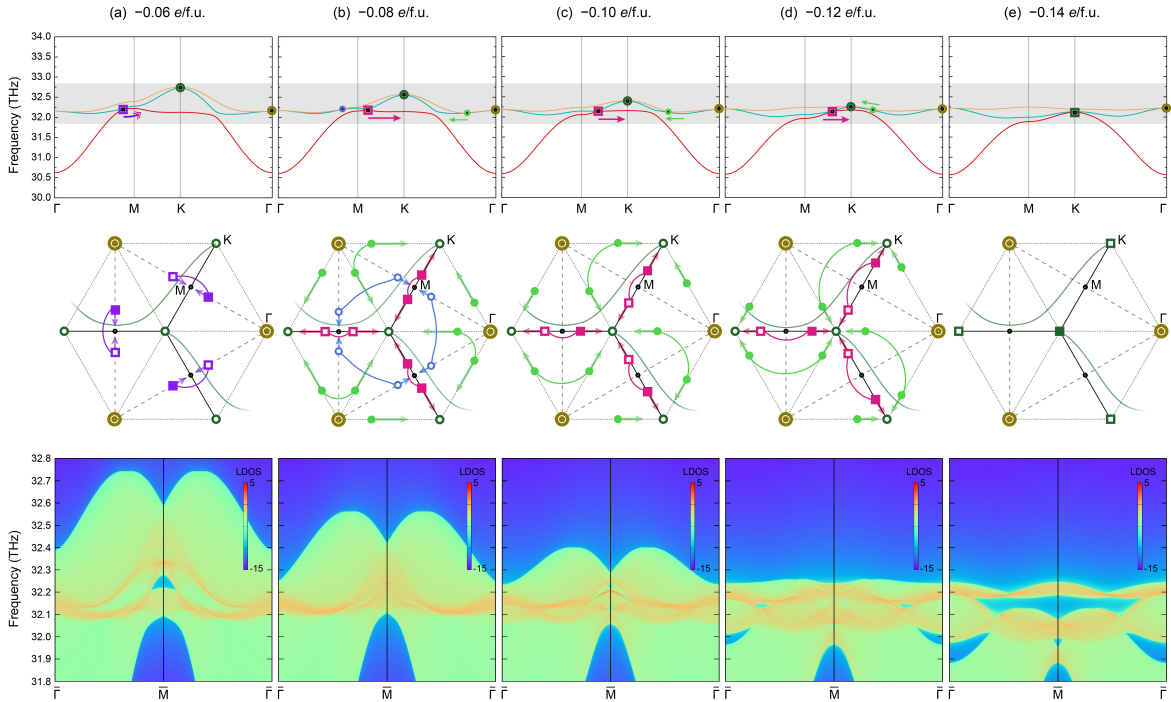


Fig. 6.11 Phonon spectra (top panel) and topological configurations (middle panel) of monolayer Al_2O_3 upon electrostatic doping at (a) -0.06 *e/f.u.*, (b) -0.08 *e/f.u.*, (c) -0.10 *e/f.u.*, (d) -0.12 *e/f.u.*, and (e) -0.14 *e/f.u.* For the topological configurations in the middle panel, I use squares (circles) to represent the nodes formed by the lower (upper) two bands, open (closed) symbols to represent the nodes with negative (positive) frame charges, and one symbol (two concentric symbols) to represent the linear (quadratic) node. The edge states along the (100) direction are also shown in the bottom panel, corresponding to the grey area of the phonon spectra in the top panel.

6.3.8 Complete picture of braiding upon doping

The complete picture, summarised in Fig. 6.11, provides a detailed description of the conversion of non-Abelian frame charge upon electrostatic doping from -0.06 to -0.14 *e/f.u.*

From the undoped case to a doping concentration of -0.06 *e/f.u.*, the band inversion between bands 13 and 14 [red and blue lines in Fig. 6.11(a)] becomes stronger along Γ -M, pushing the violet square nodes along Γ -M closer to the M high-symmetry point.

Further increasing the doping concentration to -0.08 *e/f.u.* brings the two neighbouring violet nodes together at M. At M, each neighbouring pair of violet nodes carries the same frame charge, because the nodes with opposite frame charges must cross the dark green Dirac string and the charge of one of the pair is flipped. Therefore, the pairs of violet nodes do not annihilate. Instead, they “bounce” to the M-K high-symmetry lines with each pair carrying the same frame charge, and I now label them as magenta squares in Fig. 6.11(b) because

their trajectories change. The inversion between bands 14 and 15 also creates three pairs of same charged blue nodes and three pairs of same charged green nodes along Γ -M and K- Γ respectively, indicating that the blue nodes must carry opposite frame charge with the green nodes so they can be created at the same time at Γ , or be annihilated simultaneously when brought back to Γ by decreasing the doping concentrations from -0.08 to -0.06 $e/f.u.$

At -0.10 $e/f.u.$ the nearest pairs of the blue nodes along Γ -M are brought together to M when the bands are fully inverted at M. During this process, one of the blue nodes in each pair must cross a Dirac string of the magenta nodes and thus flips its sign. Now that each nearest pair of the blue nodes near M has the opposite frame charge, they will be annihilated when meeting at M. As shown in Fig. 6.11(c), at -0.10 $e/f.u.$ the blue nodes and their corresponding Dirac strings disappear. The disappearance of the blue Dirac string also flips the sign of the three magenta nodes around the K point inside the Dirac string.

At -0.12 $e/f.u.$, the inversion between bands 13 and 14 further increases, and as a result the magenta nodes move further from M to K. Similarly, the green nodes move further from Γ to K. During this process there is no conversion between the frame charges as no nodes meet together and no adjacent Dirac strings are crossed. As shown in Fig. 6.11(d), the global topological configuration is nearly the same, except that the magenta and green nodes move closer to K.

The braiding process ends at -0.14 $e/f.u.$, when all the bands are fully inverted and no further inversion occurs with increasing doping concentration. When the three magenta nodes and three green nodes meet at K, there are two open magenta squares, one closed magenta square, and three closed green circles, as well as the open dark green circle at K. The two closed green nodes can be braided with one open magenta node and one closed magenta node so their charges are flipped. Eventually there will be one open magenta square, two closed magenta squares, one open green circle, two closed green circles, and one open dark green circle. There are two open and two closed circles in total, so the circles can be annihilated when brought together at K. The remaining open square and two closed squares can also recombine to form a closed square. Therefore there is a closed dark green square at K in the middle of the 2D Brillouin zone in Fig. 6.11(e). The braiding processes around other K points are similar.

6.3.9 Topological edge states

Despite the fact that the bulk-boundary correspondence for multi-gap topologies has not yet been fully characterised (and is beyond the scope of this work), I can still investigate the evolution of the topological edge states of monolayer Al_2O_3 upon electrostatic doping. The surface local densities of states (LDOS) are calculated from the imaginary part of the surface

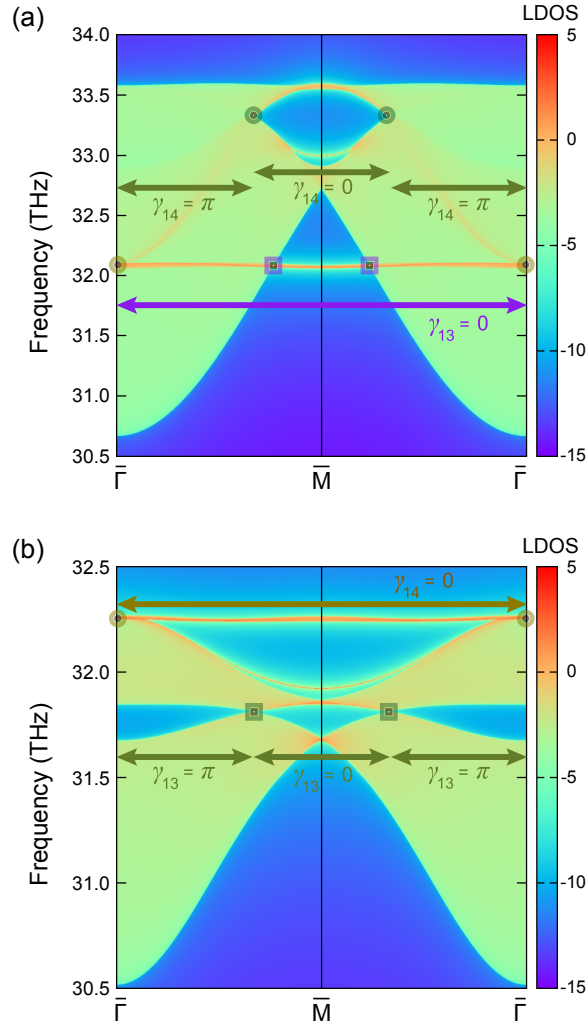


Fig. 6.12 Topological edge states along the (100) direction for (a) undoped and (b) -0.20 *e/f.u.*-doped Al_2O_3 .

Green's function as implemented in WANNIERTOOLS [50]. I first compare the edge states for undoped and -0.20 *e/f.u.*-doped Al_2O_3 in Fig. 6.12.

For undoped Al_2O_3 , the edge states connecting the projections of a pair of bulk nodes in Δ_{14} at K (dark green circles) are clearly visible, as shown in Fig. 6.12(a). In addition, the projections of the flat bulk band cross the entire edge Brillouin zone, ending at the projections of a pair of bulk nodes in Δ_{14} at Γ (dark yellow circles). The emergence of the edge states can be understood by computing the Zak phase γ [279]. In Δ_{13} , I obtain $\gamma_{13} = 0$ along the entire edge Brillouin zone except at $\bar{\Gamma}$. In Δ_{14} , $\gamma_{13} = 0$ corresponds to emerging edge states between the projections of dark green nodes at K, while $\gamma_{13} = \pi$ corresponds to vanishing edge states.

For -0.20 *e/f.u.*-doped Al_2O_3 , the flat band has the highest energy, and the projections of the pair of bulk nodes at Γ (dark yellow circles) are also higher than the projections of other bulk nodes, as shown in Fig. 6.12(b). The edge states merge from the projections of dark yellow circles in Δ_{14} at Γ . The projections of the other pair of bulk nodes at K (dark green squares) are inverted to lower frequencies, redistributing their non-Abelian frame charges from Δ_{14} to Δ_{13} . Similar to the Zak phase in the undoped case, for -0.20 *e/f.u.*-doped Al_2O_3 , $\gamma_{13} = 0$ and $\gamma_{14} = 0$ correspond to emerging edge states, while $\gamma_{13} = \pi$ corresponds to vanishing edge states.

This is consistent with the fact that the oxygen atoms, as the atomic centers, are on the boundary of the unit cell. The Zak phase measures the displacement between the Wannier functions and the atomic centers. In Al_2O_3 , a Zak phase of zero indicates that the phonon Wannier functions occupy the center of the unit cell and are localised away from the atomic centers on the unit cell boundary, leading to an ‘‘anomaly’’ with localised edge states [262, 264]. On the other hand, a Zak phase of π indicates that the phonon Wannier states and the atoms are at the same places on the unit cell boundary, corresponding to vanishing edge states. While this \mathbb{Z}_2 -quantised Berry phase is a good quantum number for 1D edge states [279] and traces in some gaps the edge states faithfully, it is worth repeating that a full bulk boundary relation describing topological phases obtained by non-Abelian processes is still subject to intense research activity.

I also show the evolution of the edge states under phonon braiding upon electrostatic doping from -0.06 to -0.14 *e/f.u.* in the bottom panel of Fig. 6.11, which can provide information on the conversion of non-Abelian frame charges in the bulk states. Because the bulk nodes are distributed in a narrow frequency range between $31.8 - 32.8$ THz, the topological edge states are not well-separated from each other.

6.4 Conclusions and outlook

The findings of Section 6.3 suggest a broad relevance to the fields of topology, phonons, dielectrics, first-principles modelling and information storage.

From a topological perspective, I find that phonons can be a primary platform to study multi-gap topologies. When studying multi-gap topologies in electronic systems, all three neighbouring bands must be near the Fermi level, which severely limits the potential material candidates. On the other hand, phonons do not have the restriction of the Fermi level because they are bosonic excitations. In addition, the time-reversal symmetry \mathcal{T} in phononic systems is hard to break, making it more convenient to find material candidates with $C_2\mathcal{T}$ symmetry or $\mathcal{P}\mathcal{T}$ symmetry. As phonons can be treated as spinless systems, several existing models can

be applied, such as the three-band spinless model with a Kagome lattice [262], to phononic systems. I can also extend the ideas of non-Abelian braiding to other quasiparticles such as magnons [137] and excitons [138]. An open question is the bulk-boundary correspondence of multi-gap topologies, and phonon dispersions with fewer, cleaner band crossings, e.g. phonon systems with only one or two atoms in the unit cell, could provide an ideal platform for its study.

For the phonon community, this work opens a new research direction for these emergent excitations. Traditional studies of phonons mainly involve conventional superconductivity [139, 140], electrical and thermal transport [95, 141–144], carrier thermalisation [145, 146], structural phase transition [147, 148] and charge density waves [149, 150]. Here I show that the reciprocal-space braiding of phonon band-crossing points can also form the basis for next-generation phononic computation. Several strategies could be used to experimentally verify the non-Abelian braiding of phonons, including inelastic neutron scattering [151–153], inelastic X-ray scattering [154], and high-resolution electron energy-loss spectroscopy [198]. Additionally, the first-principles evaluation of the band-inversion processes can provide references for the experimental observation of the evolution of the phonon band nodes upon electrostatic doping.

For dielectrics, I provide an experimentally realisable way to control the braiding in a well-known dielectric material upon electrostatic doping. Monolayer Al_2O_3 has been widely used as a gate dielectric in electronic devices [280–283]. Therefore, electrostatic doping of monolayer Al_2O_3 can be experimentally feasible and has the potential to be incorporated into existing devices based on Al_2O_3 , opening the door for studying topology-related phenomena in this otherwise well-studied material. In addition, electrostatic doping-induced phonon frequency shifts have been intensively studied in low-dimensional materials, which can be probed directly using Raman spectroscopy [274, 284]. It is therefore interesting to investigate how doping or gating redistributes the charge density and how the redistributed charge couples to the lattice vibrational modes.

For first-principles modelling, the computational techniques described in this article offer a route to understand non-Abelian braiding of any quasiparticle. The Euler class can be computed using the eigenvectors/eigenstates of these quasiparticles as input. I offer a detailed description of all the theoretical background and computational methodology to analyse the non-Abelian frame charges formed by any three-band subsystems in the spectra of any quasiparticle, as long as the symmetry requirements are fulfilled. The potential braiding processes rely on control of band inversion and the corresponding redistribution of non-Abelian frame charge. Future simulation work could focus on various strategies to control

the phonon braiding, including nonlinear effects [182, 285–287], anharmonicity [288–291], and ultrafast pumps [292–295].

Finally, as a further distant and more speculative perspective, the braiding processes might find use in storing information. The idea is that information may be robust against perturbations from the environment because the non-trivial frame charges can only become trivial by unbraiding the non-Abelian frame charges via introducing a third phonon band. In addition, these non-Abelian frame charges and their braiding can be controlled by electrostatic doping, offering new opportunities for a conceptually new computation hardware based on phonons. Moreover, the braiding of multiple nodes takes place simultaneously when these nodes are related to each other by the space group symmetry, suggesting the possibility of storing information in the frame charges combining the topological and the symmetry information together. While such information could be encoded in phonons, this nevertheless leaves open the exciting question of whether phonons could be suitable to implement quantum algorithms.

Chapter 7

Non-Abelian braiding of phonons: From three bands to four bands

Non-Abelian states of matter, in which the final state depends on the order of the interchanges of two quasiparticles, can encode information immune from environmental noise with the potential to provide a robust platform for topological quantum computation. As described in the previous chapter, the band-crossing points for any three-band systems with a real Hamiltonian carry non-Abelian frame charges, and by inverting the band order, the crossing points in the same gap or in the adjacent gaps can meet each other in reciprocal space. As a result, a pair of points with opposite frame charges in the same gap can be annihilated when brought together while those with the same frame charge in the same gap cannot be annihilated, and interchanges of points in adjacent gaps flip the frame charges, mimicking the non-Abelian braiding in real space.

In this chapter, I provide another example of non-Abelian braiding of phonons in monolayer silicates. The associated braiding process can be controlled by means of an electric field and epitaxial strain, and involves, for the first time, more than three bands. Most interestingly, I propose that the band-inversion processes at the Γ point can be tracked by following the evolution of the Raman spectrum, providing a clear signature for the experimental verification of the band inversion accompanied by the braiding process.

This chapter is based on work published in [Bo Peng, Adrien Bouhon, Bartomeu Monserrat, and Robert-Jan Slager. *Nature Communications* 13, 423 (2022)]. My collaborators Adrien Bouhon and Robert-Jan Slager provided the theoretical description, and Bartomeu Monserrat supervised the computational part, while I was responsible for the rest.

7.1 Introduction

Non-Abelian states of matter arise from non-commutative interchanges of quasiparticles [296]. In this process, called braiding, the winding of one quasiparticle around another can encode information, creating non-Abelian states that are immune from external noise: as long as the braiding occurs, the information is topologically protected. This process can form the basis for topological quantum bits (qubits), and a variety of strategies for non-Abelian braiding have been proposed, including braiding of quasiparticles in intrinsic topological states such as fractional quantum Hall systems [297], and also in symmetry-protected topological states such as half-quantum vortices in superconductors with p -wave symmetry [298] and Majorana modes in hybrid systems [299]. Multiple variants of these proposed architectures exist [300, 301], and experimental evidence has started to emerge in the past few years [302, 303], providing a proof-of-principle for the existence of non-Abelian quasiparticles. However, multiple difficulties remain in exploiting these quasiparticles for braiding, for example Majorana fermions are boundary states that have proven challenging to observe [304]. It would therefore be desirable to find alternative platforms in which non-Abelian braiding exists.

I propose that phonons, which are a bosonic excitation not subject to Fermi-Dirac statistics, provide a viable platform to observe non-Abelian braiding. I identify a monolayer silicate as a candidate material, and show that an electric field and epitaxial strain can be used to induce band inversions which are accompanied by the transfer of nodes between adjacent gaps, thereby transferring non-Abelian frame charges and non-trivial patch Euler class. This is achieved through the symmetry-constrained braiding of band nodes, resulting in a multi-gap topological phase. Different from the braiding in the metamaterial [262], both three-band and four-band braiding processes can be realised in phonons of monolayer silicate. I further show that the evolution of Raman peaks can be used to track the band inversions and the accompanying braiding process, providing a clear experimental signature to identify multi-gap topology in real materials. Interest in the topological features of phonon bands has recently grown, but for single-gap topology, phonons have traditionally received less attention than electrons. The bosonic nature of phonons should make them the prime platform for the study of multi-gap topology and non-Abelian braiding.

7.2 Non-Abelian braiding of phonons in monolayer silicates

7.2.1 Computational details

First-principles calculations using density functional theory are performed with the Vienna *ab initio* Simulation Package (VASP) [104, 105]. The generalised gradient approximation

(GGA) with the Perdew-Burke-Ernzerhof (PBE) parameterisation is used as the exchange-correlation functional [183]. A plane-wave basis with a kinetic energy cutoff of 800 eV is employed, together with a $9 \times 9 \times 1$ \mathbf{k} -mesh to sample the electronic Brillouin zone. The self-consistent field calculations are stopped when the energy difference between successive steps is below 10^{-8} eV, and the structural relaxation is stopped when forces are below 10^{-3} eV/Å. A vacuum spacing larger than 20 Å is used to eliminate interactions between adjacent layers.

The ionic positions with and without electric fields are fully relaxed while the lattice constants are fixed, corresponding to material synthesis on substrates at fixed strain. When applying an external electrostatic field, dipole corrections are included to avoid interactions between the periodically repeated images.

For the phonon calculations, the force constants are evaluated using the finite differences method in a $3 \times 3 \times 1$ supercell with a $3 \times 3 \times 1$ electronic \mathbf{k} -mesh using VASP. The phonon dispersion is then obtained using PHONOPY [52]. Convergence tests have been performed comparing supercells of sizes between $3 \times 3 \times 1$ and $6 \times 6 \times 1$. In 2D monolayers, no splitting between the longitudinal and transverse optical phonons (LO-TO splitting) occurs at Γ , and only the slope of phonon bands changes [275]. Therefore, LO-TO splitting is ignored as it does not influence the phonon band crossings. The phonon edge states are obtained using surface Green's functions as implemented in WANNIERTOOLS [50].

The patch Euler class is obtained by integrating phonon eigenvectors within a patch around two nodes, and a unitary rotation is applied to make the eigenvectors real. The Euler class is computed from a pair of bands on a rectangular region that contains the nodes [276]. The frame charges are then assigned to all the nodes, as well as Dirac strings that connect the frame charges. This process is repeated for all the patches and get the complete topological configuration.

7.2.2 Silicates

Layered silicates are ubiquitous in soils and minerals throughout the world [305, 306]. The surface layer of silicates consists of a silicon-centered tetrahedron, with the oxygen atoms forming a coplanar hexagonal Kagome lattice, as shown in Fig. 7.1(a). Physical models based on the two-dimensional (2D) Kagome lattice exhibit rich phenomenology, from Dirac fermions to flat bands, and as a result there is much interest in this structural pattern. The experimental realisation of monolayer Kagome silicates can be dated back to the 1990s [307], but more recently various synthesis strategies have been developed to obtain 2D Kagome silicate or silica on multiple substrates [308–312]. These developments enable researchers to study the structural [313–319], vibrational [320–322], electronic [323–325],

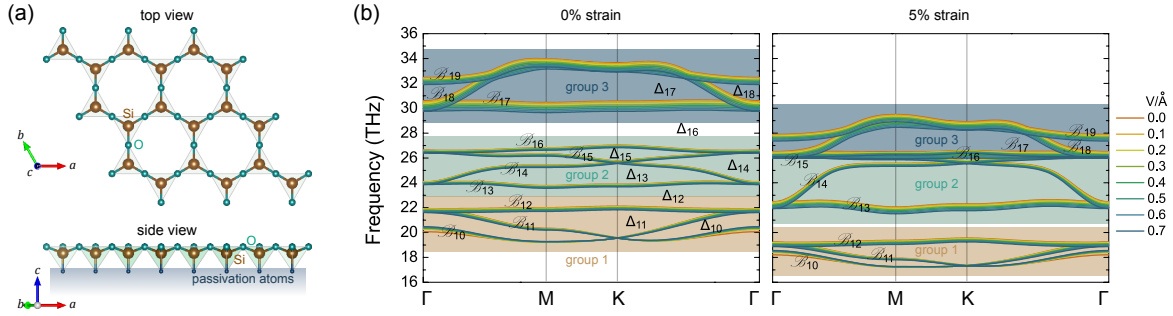


Fig. 7.1 Phonons in monolayer Kagome silicate Si_2O_3 . (a) Crystal structure of monolayer Kagome silicate Si_2O_3 . (b) Kagome bands of the phonon spectra of 0% and 5% strained silicate under different electric fields.

mechanical [326, 327], and chemical properties [328] of this material family and to explore the various physical phenomena associated with 2D Kagome lattices.

7.2.3 Phonon band structure

The monolayer Kagome silicate Si_2O_3 crystallises in the $P6mm$ space group (No. 183). Unlike free-standing bilayer silica, monolayer silicate Si_2O_3 is grown on a substrate, as shown in Fig. 7.1(a). Using passivating hydrogen atoms to mimic the substrate, I compute the phonon dispersion of monolayer Si_2O_3 from first principles. The resulting phonon dispersion has three groups of Kagome flat bands between 18-36 THz [Fig. 7.1(b)]. Group 1 (orange region) contains typical Kagome bands with two Dirac bands capped by another flat band, which belong to bands 10-12 in the full phonon dispersion. Group 2 (green region) consists of four bands (bands 13-16), with two flat bands capping the Dirac bands in the middle. Group 3 (navy region) contains bands 17-19, and the flat band is below the Dirac bands. In the following, I number the bands $\{\mathcal{B}_n\}_{n=1,\dots,21}$ from lower to higher frequencies, and I label the partial gaps between each two successive bands $(\mathcal{B}_n, \mathcal{B}_{n+1})$ as $\{\Delta_n\}_{n=1,\dots,20}$ with frequencies $E_n \leq \Delta_n \leq E_{n+1}$ (see Fig. 7.1).

7.2.4 Electric field induced band inversions and braiding

The key discovery of this work is that it is possible to controllably braid Kagome band nodes in monolayer Si_2O_3 using strain and/or an external electric field. Interestingly, I find two types of braiding. The first type involves the three bands in group 1 (orange region) in Fig. 7.1(b), and represents a realistic proposal for the first material realisation of a multi-gap phase. The second type of braiding involves four bands in groups 2 and 3, shown in the green

and navy regions in Fig. 7.1(b), and represents the first proposal of a system that can host these many-band (more than three) braiding processes.

In the generic braiding process for three bands [180, 258, 260, 262], the frame charges q associated with the band nodes take values in the conjugacy classes $\pm q$ of the quaternion group \mathbb{Q} , where $q \in \{1, i, j, k\}$ satisfying $i^2 = j^2 = k^2 = -1$, $ij = k$, $jk = i$ and $ki = j$. Specifically, $\pm i$ and $\pm j$ characterise single nodes in each of the respective gaps (first and second), whereas $\pm k$ represents a pair of nodes in each gap. Finally, -1 captures the stability of two nodes of the same gap. These charges can be manipulated through the braiding process of band nodes of different gaps in momentum space to arrive at configurations where a specific gap features the same charges. This results in an obstruction to annihilation that can be quantified via a non-trivial Euler invariant over a patch in the Brillouin zone that contains all the nodes of this band subspace.

As an extension to the three-band setup characterised by the quaternion group, when more bands are present the above ideas must be generalised to the so-called Salingaros' vee groups. The main property of interest for the braiding processes is that nodes of adjacent gaps reproduce the three-band case and have anti-commuting charges, whereas charges of non-neighbouring gaps commute. In particular, any stable simple node in a gap is characterised by the charge q that takes, as before, $\pm q$ values, while the charge $q^2 = -1$ indicates a stable pair of nodes. In other words, these configurations pose an intricate extension of the three-band case, featuring opposite types of each charge and a charge of -1 in each gap. The regions where several adjacent gaps $(\Delta_n, \dots, \Delta_{n+M})$ are each hosting a simple node can be characterised through products of non-Abelian charges $(q_n \cdots q_{n+M})$.

Importantly, the configurations of the nodes are constrained by the crystalline symmetries of the system, leading to a projection of the braid trajectories on the different high-symmetry points and lines of the Brillouin zone. The band inversions at these momenta thus readily indicate the braiding processes. I corroborate the non-Abelian nature of the band inversions through the direct computation from the first-principle data of the patch Euler classes and the non-Abelian charges of the nodes transferred across adjacent gaps.

The band order of the Kagome bands can be inverted at different strains and under different electric fields. I calculate the strain-dependent (from -2% to 8%) phonon dispersion under electric fields from -0.9 to 2.0 V/Å. No imaginary modes are observed even for 7% strained Si_2O_3 under an electric field of 2.0 V/Å, indicating the dynamical stability. In addition, I distort the crystal structures by creating a rotated Kagome lattice similar to Ref. [320], and structural relaxation at different electric fields always removes the rotation distortion. Experimentally it has been found that both monolayer silicate and bilayer silica can be grown on various substrates with biaxial strains varying from -5.6% to 5.7% [308,

312, 316, 317, 328, 329]. In addition, theoretical calculations have shown that defect-free 2D silica can be deformed up to a maximum strain of 10.4%, while for defective samples no abrupt material failure is observed at strains around 7.8-8.1% [327]. Regarding the electric field, by applying bias voltage between the tip of the scanning tunneling microscopy (STM) and the sample, a maximum electric field of 1.7 V/Å can be obtained [330]. Therefore, both the strain and the electric field used in the calculations are experimentally feasible.

The most interesting regime is provided by tensile strain [exemplified with the 5% case in Fig. 7.1(b)]. Under these conditions, the bandwidth of the three Kagome bands in group 1 decreases, reducing the frequency difference between the three bands at the Γ point. As a result, experimentally feasible electric fields can be used to drive phonon band inversion under strain. Similarly, the Kagome bands in groups 2 and 3 become closer at larger strains, again facilitating electric field manipulation.

Hereafter I focus on phonon dispersions at fixed strains under tunable electric field, because the strain is fixed by the material synthesis and determined by the substrate, while the electric field can be tuned using a gate voltage. I only focus on the three groups of Kagome bands because they are more sensitive to the electric field.

7.2.5 Three-band braiding in group 1

I first study the braiding process of the Kagome bands in group 1 formed by the phonon branches $\mathcal{B}_{10,11,12}$ at 7% strained silicate. As shown in Fig. 7.2(a), without an electric field, the Kagome bands at the Γ point are comprised of a single band \mathcal{B}_{10} associated with a 1D irreducible representation (irrep) Γ_1 and a doubly degenerate band $\mathcal{B}_{11,12}$ associated with a 2D irrep Γ_5 . Away from Γ , the doubly degenerate bands split, each carrying a different 1D irrep along the Γ -M and K- Γ high-symmetry lines.

Applying an electric field increases the frequency of the non-degenerate band \mathcal{B}_{10} at Γ while reducing the frequency of the degenerate bands $\mathcal{B}_{11,12}$. The \mathcal{B}_{10} vibrational mode at Γ corresponds to an out-of-plane displacement of silicon atoms and an opposite-direction displacement of oxygen atoms, and the $\mathcal{B}_{11,12}$ mode consists of both the in-plane displacements of silicon atoms and the out-of-plane displacements of oxygen atoms. For the \mathcal{B}_{10} mode, the two types of atoms carry out-of-plane Born effective charges of +1.0 and -0.5, respectively, and an out-of-plane electric field can enhance the opposite out-of-plane motions of two types of atoms with opposite signs of Born effective charge, which hardens the vibrational mode and increases the frequency of \mathcal{B}_{10} at Γ . For the $\mathcal{B}_{11,12}$ mode at Γ , the out-of-plane electric field increases the out-of-plane distance between Si and O atoms, leading to weakened interatomic interactions and reduced phonon frequencies. Upon the electric field, the frequency of the lower \mathcal{B}_{10} increases while the frequency of the higher

$\mathcal{B}_{11,12}$ decreases, and a phonon band inversion takes place at an electric field of 0.7 V/\AA . As a result, new nodes are formed by the inverted bands with different irreps. For bands \mathcal{B}_{10} and \mathcal{B}_{11} , a node forms near Γ along the K- Γ high-symmetry line as the two bands belong to different Λ_1 and Λ_2 irreps. On the other hand, there is no crossing point along Γ -M because the two bands belong to the same Σ_1 irrep. Due to the C_6 rotational symmetry of the system, there are six nodes in total within the gap Δ_{10} along the different K- Γ lines in the full Brillouin zone, as indicated by the yellow circles in Fig. 7.2(b). For bands \mathcal{B}_{11} and \mathcal{B}_{12} , six nodes form along Γ -M as they belong to the distinct irreps Σ_1 and Σ_2 , while there is no crossing point along K- Γ since there the two bands belong to the same irrep Λ_1 . As a result, six nodes are created near the Γ point within the gap Δ_{11} at 0.7 V/\AA , as indicated by the cyan triangles in Fig. 7.2(b).

Further increasing the electric field enhances the phonon band inversion, such that the six nodes of gap Δ_{10} (yellow circles) move away from Γ towards the K points, and the six nodes of gap Δ_{11} (cyan triangles) move away from Γ towards the M points. At a threshold field of about 1.8 V/\AA , the Λ_2 band becomes lower than the other two Λ_1 bands over the whole K- Γ line, and the yellow nodes disappear upon reaching the K point. On the other hand, the cyan nodes remain in the middle of the Γ -M high-symmetry line even upon applying higher electric fields.

Throughout this entire process, there is also a nodal point in gap Δ_{10} at K with a 2D irrep K_3 . This band-crossing point remains nearly unchanged with varying electric field.

I now come to the topological characterisation of the above processes. In particular, I characterise the transfer of nodes from one gap to adjacent gaps with an associated transfer of patch Euler class and non-Abelian frame charges. Because of the $P6mm$ space group, the system has C_2 rotation symmetry. In addition, in phonons the time-reversal symmetry is automatically satisfied. Therefore, monolayer Si_2O_3 has $C_2\mathcal{T}$ symmetry and its band nodes at neighbouring gaps can host non-Abelian charges. Although there might be some defects in monolayer silicate due to the imperfection of the growth processes [319, 320, 324], the impurities cannot destroy the non-Abelian charges as long as the $C_2\mathcal{T}$ symmetry is preserved.

In the following, I label the frame charges and the patch Euler classes according to the gap to which the nodes they describe belong, i.e. for the n^{th} gap with $n \in \{1, \dots, 20\}$, I write the frame charges and the patch Euler classes as $\{\pm q_n\}$ and χ_n respectively.

The topological configurations can be determined by the numerical calculation of the patch Euler class for every single band crossing and for every pair of band crossings of the same gap. I then show how the original data of the computed patch Euler classes can be combined with the assignment of Dirac strings to build the non-Abelian topological

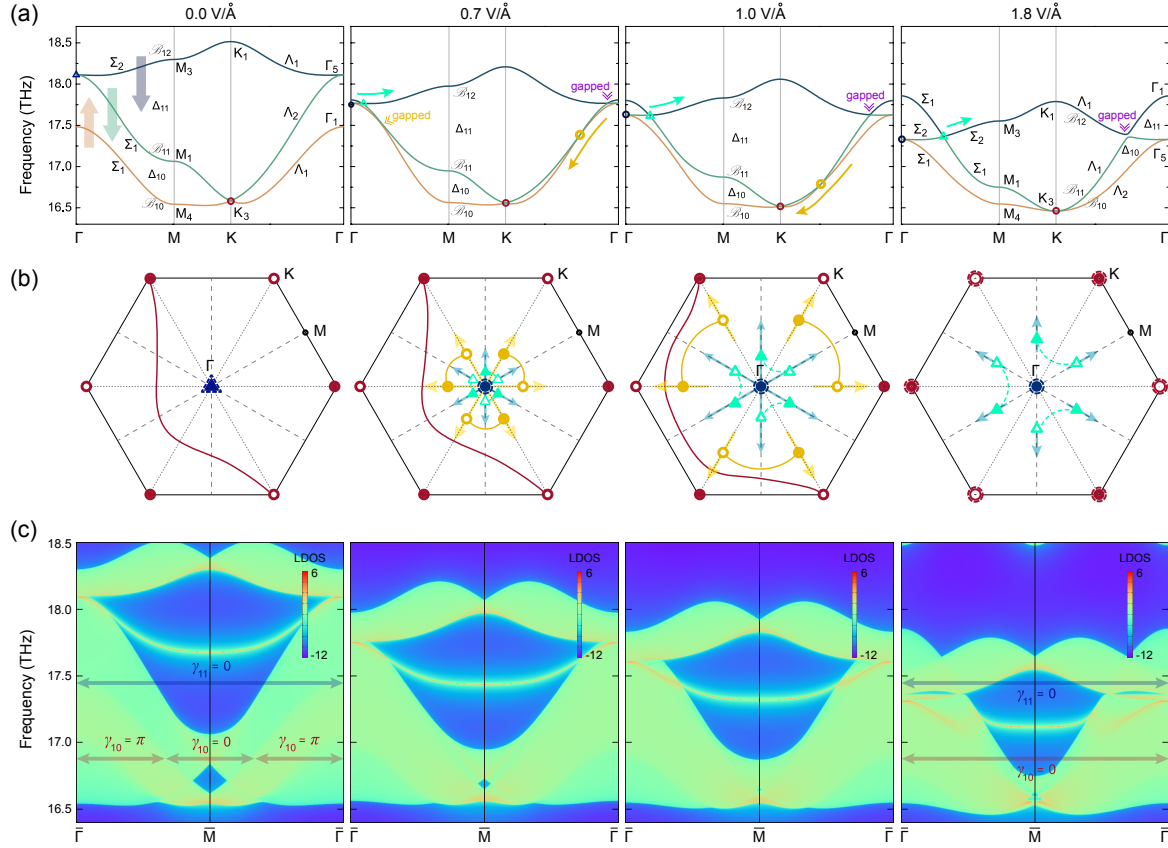


Fig. 7.2 Braiding of phonons in group 1. (a) Kagome bands and (b) their corresponding nodes in the 2D Brillouin zone formed by phonon branches \mathcal{B}_{10-12} of 7% strained silicate under electric fields of 0.0 V/Å, 0.7 V/Å, 1.0 V/Å, and 1.8 V/Å. The topological configurations with nodes in different gaps (different symbols) and Dirac string configurations are shown in (b). The large blue triangle (at 0.0 V/Å) and the large blue circles (at 0.7 – 1.8 V/Å) with dashed boundary at Γ , as well as the large dark red circles with dashed boundary at K (at 1.8 V/Å), are quadratic nodes. Note that crossing a Dirac string in the same gap (same symbols) does not convert the charge and that moving nodes to the K point ensures that three charges meet in the extended zone. Hence moving the yellow nodes to K gives stable nodes with stable Euler class at K upon moving from the third to the last panel in (b). The corresponding phonon edge states on the (100) edge are shown in (c), with the $\{0, \pi\}$ -quantised Zak phases $\{\gamma_n\}_{n=10,11}$ for gaps $\{\Delta_n\}_{n=10,11}$ indicated by the arrows.

configuration of the nodes over the whole Brillouin zone. The results are then corroborated through the direct computation of the non-Abelian charge of nodes located in connected multi-band subspaces.

Let me illustrate this strategy with the example of group 1 composed of three connected bands. Focusing on gap Δ_{10} in 7% strained silicate under an electric field of 1.0 V/\AA , I compute the patch Euler class from the numerically calculated phonon eigenvectors $|u_{10}\rangle$ and $|u_{11}\rangle$, of \mathcal{B}_{10} and \mathcal{B}_{11} respectively, for every single band crossing and for every pair of band crossings within the gap. In Fig. 7.3(a), where I use the convention that the symbols of circle and triangle correspond to nodes in gap Δ_{10} and Δ_{11} respectively, I draw the patches that contain a pair of band crossings located at distinct regions of the Brillouin zone, with the calculated Euler classes indicated for all the patches. The Euler classes of the patches containing a single band crossing are indicated by the size of the symbols, i.e. the small circles indicate $|\chi_{10}| = 0.5$ (e.g. the nodes at K) and the large circles with dashed boundary indicate $|\chi_{10}| = 1$ (e.g. the node at Γ), and I use the convention that the fullness and openness of the symbols indicate the signs $+$ and $-$ respectively. This can be verified by direct computation showing that each Euler class of ± 0.5 corresponds to a three-band partial-frame charge $q_{10} = \pm i \in \mathbb{Q}$, while the Euler class of ± 1 corresponds to a three-band partial frame charge of $-1 \in \mathbb{Q}$.

The quadratic nodes can be viewed as two linear nodes merged together. This is explicitly verified under the breaking of C_6 where the double node at Γ splits into two simple nodes. Thus, for every band crossing and for every pair of band crossings within the gap, the patch Euler class takes integer values when it indicates an even number of stable nodes, or half-integer values when it indicates an odd number of stable nodes within the patch, as shown in Fig. 7.3(a). Since the rotation of a patch by a symmetry of the point group C_{6v} leads to an equal Euler class, I only need to consider the patches over the irreducible Brillouin zone. Importantly, the sign of the Euler class on each patch taken separately is gauge dependent, and similarly for the sign of the frame charges q_{10} . This motivates the puzzle approach, which focuses on the relative stability of the nodes, because their relative stability is gauge invariant.

As a next step, I choose one initial patch containing a pair of band crossings, starting from patch 1 in Fig. 7.3(a) for which I obtain an Euler class of 0, and a *signed* non-Abelian charge can be assigned to each crossing. With an Euler class of 0, I can assign opposite charges to the pair of yellow nodes in patch 1 with no adjacent Dirac string crossing the patch. The remaining yellow nodes, and the Dirac strings connecting them, are then fixed by the C_6 symmetry. For patch 2, an Euler class of $\chi_{10} = 0.5$ is compatible with the quadratic (blue) node of Euler class $\chi_{10}[\Gamma] = +1$ at Γ and the linear (yellow) node of Euler class

$\chi_{10}[\Gamma\text{-K}] = -0.5$ along $\Gamma\text{-K}$. For patch 3, $\chi_{10} = 0$, and I can assign opposite frame charges to the yellow node and the dark red node. Similarly, I then assign signed frame charges to all the other nodes, as well as Dirac strings that connect them. While there are relative gauge freedoms in doing so, once the charges of the initial patch are fixed, the charges for all neighbouring patches become fixed by consistency, like completing a puzzle. By repeating this process for all the patches, the complete topological configuration can be obtained, as summarised in Fig. 7.3(a). When a node in gap Δ_n crosses a Dirac string connecting nodes residing in neighbouring gap Δ_{n-1} or Δ_{n+1} , the sign of the charge in Δ_n changes. It should also be noticed that the configurations of the Dirac string are not unique, since moving the Dirac string flips the gauge sign of the eigenvectors locally. Nevertheless, the requirement of consistency in the assignment of the signed frame charges, together with the location of the Dirac strings, eventually guarantees the full indication of the relative stability of the nodes that is gauge independent.

A similar procedure can be applied to study the topological configurations for 7% strained silicate under an electric field of 1.8 V/\AA . As shown in Fig. 7.3(c), patch 1 in Δ_{10} contains a dark red node at K, a quadratic blue node at Γ , and a Dirac string connecting the cyan nodes in Δ_{11} . With an Euler class $\chi_{10} = 0$, the dark red node at K must carry the same frame charge with the blue node at Γ . In addition, patch 2 has an Euler class of 0, indicating that the neighbouring dark red nodes carry opposite frame charges. For the cyan nodes in Δ_{11} , there is no nearby Dirac string in Δ_{10} during the whole braiding process, and their frame charges remain the same.

Once an initial topological configuration is known, I can determine any future topological configurations resulting from a band inversion by simply applying the rules of braiding together with the constraints of the crystal symmetries. Figure 7.2(b) represents the conversion of the topological configuration through the band inversion within the bands of group 1. I start with the topological configuration at 0.0 V/\AA showing two linear nodes in Δ_{10} at K ($-q_{10}$, open dark red circle) and K' (q_{10} , closed dark red circle) connected by a Dirac string (dark red line), and one quadratic node in Δ_{11} at Γ (large blue triangle with dashed boundary) with a patch Euler class $\chi_{11}[\Gamma] = +1$, corresponding to a three-band frame charge $q[\Gamma] = -1$ (computed for a base loop encircling the Γ point while avoiding the nodes at the K points).

From the irreps of the bands given in Fig. 7.2(a) I have predicted the formation of symmetry protected nodes on the $\Gamma\text{-M}$ lines in Δ_{11} and on the $\Gamma\text{-K}$ lines in Δ_{10} under the inversion of the bands at Γ . Figure 7.2(b) shows the complementary topological configurations of the nodes. It is important to note the relative signs of the charges, which are not accidental. Imagining the reverse band-inversion process, i.e. from 1.0 V/\AA to 0.0 V/\AA in Fig. 7.2(b) while relaxing the C_6 symmetry but conserving $C_2\mathcal{T}$ symmetry, i.e. allowing the nodes to

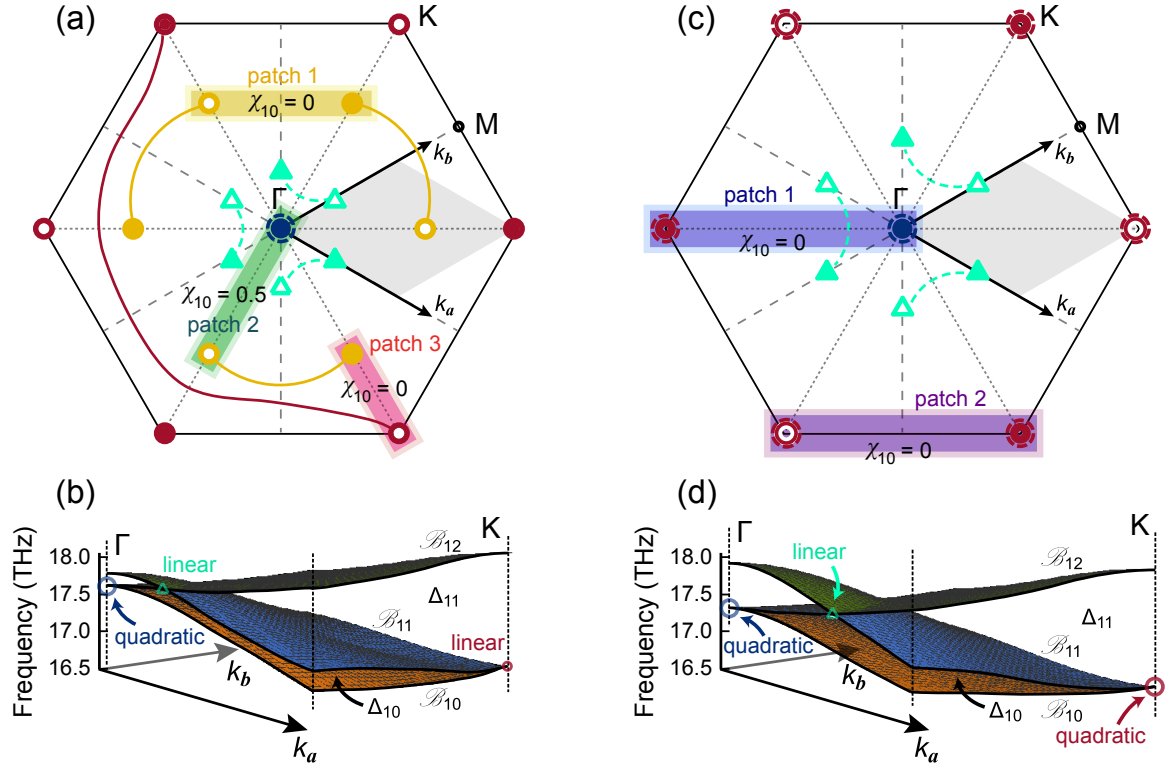


Fig. 7.3 Euler class calculations. (a) Patches in the Brillouin zone and their corresponding Euler class for 7% strained silicate under an electric field of 1.0 V/Å. The Euler class χ_{10} is calculated from the phonon eigenvectors of \mathcal{B}_{10} and \mathcal{B}_{11} within the patches. The resultant patch Euler class in the yellow (patch 1), green (patch 2) and magenta (patch 3) areas are 0, 0.5 and 0, respectively (the patch Euler class χ_{11} is also calculated, but not shown in the figure). The large blue circle with dashed boundary at Γ is a quadratic node with the patch Euler class of 1. (b) 3D band structures in the grey areas of (a), with two linear nodes – one (cyan triangle) in Δ_{11} along Γ -M and one (dark red circle) in Δ_{10} at K, as well as a quadratic node (blue circle) in Δ_{10} at Γ . These dispersions are rooted in the stability of Euler class, meaning that a stable double node produces a quadratic dispersion. (c) Patches in the Brillouin zone to calculate the Euler class for 7% strained silicate under an electric field of 1.8 V/Å. The patch Euler class in the blue (patch 1) and purple (patch 2) patches are both 0 (the patch Euler class χ_{11} is also calculated, but not shown in the figure). The large blue circle with dashed boundary at Γ and the large dark red circles with dashed boundary at K are quadratic nodes with the patch Euler class of 1. (d) 3D band structures in the grey areas of (c), with one linear node (cyan triangle) in Δ_{11} along Γ -M and two quadratic nodes in Δ_{10} at Γ (blue circle) and K (dark red circle).

move freely on the $C_2\mathcal{T}$ symmetric plane where they are pinned. The circles in Δ_{10} can be recombined by bringing the yellow nodes of the Γ -K lines to the Γ point. By doing so, the three filled yellow circles must cross the dashed-line (cyan) Dirac strings and the three open triangles are crossed by the full-line (yellow) Dirac strings, which implies a flip of their frame charges. Thus six closed cyan triangles are obtained inside the Brillouin zone, together with six open yellow circles and two filled blue circles (obtained after splitting the quadratic node at Γ). The circle nodes recombine, leaving four open circles and six closed triangles. Braiding two of the open circles with two of the closed triangles, two pairs of circles and triangles are obtained and can be annihilated, leaving a single pair of closed triangles, i.e. at the topological configuration at 0.0 V/\AA in Fig. 7.2(b).

By moving the nodes in Δ_{10} (yellow circles) on the Γ -K lines to the K points, the topological configuration of the fourth panel is obtained in Fig. 7.2(b) with quadratic nodes at K ($\chi_{10}[\text{K}] = +1$) and K' ($\chi_{10}[\text{K}'] = -1$).

Summarising the general philosophy behind the determination of topological phase transitions in the non-Abelian topological phases protected by $C_2\mathcal{T}$ symmetry, I first have a puzzle “game” followed by a braiding “game”.

7.2.6 Four-band braiding in groups 2 and 3

I next focus on the band inversion and the resulting braiding of the phonon bands in groups 2 and 3 under 5% strain, which become connected as the electric field increases. As shown in Fig. 7.4(a), at a negative electric field of -0.3 V/\AA , the two groups of phonon bands are well-separated. At -0.2 V/\AA , the highest band in group 2 (\mathcal{B}_{16}) and the lowest band in group 3 (\mathcal{B}_{17}) touch at K, and six nodes [cyan circles in Fig. 7.4(b)] are created along K- Γ as the two bands belong to the different irreps Λ_1 and Λ_2 (there are also six nodes created on the M-K line at 0.0 V/\AA , which annihilate in pairs at the M point upon increasing the electric field, a process that I do not show here). The cyan nodes move towards Γ upon increased electric field, and touch the Γ point around 0.5 V/\AA causing a band inversion at Γ . Instead of being annihilated, these six nodes bounce back along their original path.

In addition to the cyan nodes formed by \mathcal{B}_{16} and \mathcal{B}_{17} , there are also six nodes (purple squares) formed by \mathcal{B}_{17} and \mathcal{B}_{18} , as well as six nodes (yellow triangles) formed by \mathcal{B}_{15} and \mathcal{B}_{16} , along the Γ -M high-symmetry line, see Fig. 7.4(b). They are all created at about 0.5 V/\AA near the Γ point, and move towards M with increasing electric field. The yellow nodes move much faster than the purple ones, which is due to stronger band inversion.

I now discuss the topological features of the band inversion between the bands in groups 2 and 3. Again, the determination of the initial topological configuration (i.e. fixing the frame charges and the Dirac strings) is achieved through the puzzle construction detailed in the

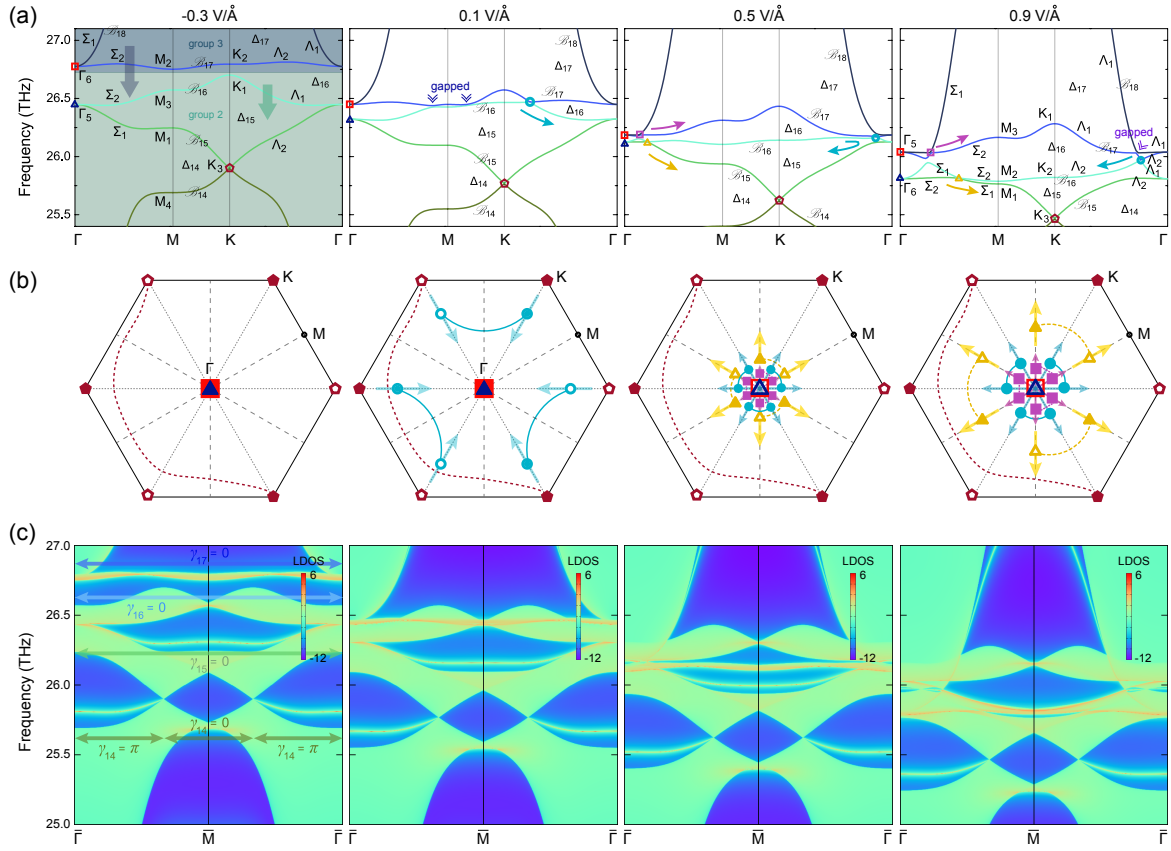


Fig. 7.4 Braiding of phonons in groups 2 and 3. (a) Phonon branches \mathcal{B}_{14-18} and their corresponding nodes of 5% strained silicate under electric fields of -0.3 V/\AA , 0.1 V/\AA , 0.5 V/\AA , and 0.9 V/\AA . The panels in (b) show the nodes and their topological charges. As before, different symbols characterise topological charges in different gaps, whereas open versus closed symbols indicate the sign of the charge. Dirac strings are drawn as lines. The large blue triangles and the large red squares at Γ are quadratic nodes. The corresponding phonon edge states on the (100) edge are shown in (c), with the $\{0, \pi\}$ -quantised Zak phases $\{\gamma_n\}_{n=14, \dots, 17}$ for the gaps $\{\Delta_n\}_{n=14, \dots, 17}$ indicated by the arrows.

previous subsection. The transitions to the other topological configurations upon the band inversions then follow the rules of (symmetry-constrained) braiding. First, \mathcal{B}_{16} and \mathcal{B}_{17} are inverted at the K point. The irreps of Fig. 7.4(a) predict the formation of six nodes along the K- Γ lines and six nodes along the M-K lines (at 0.0 V/\AA , not shown here), all in Δ_{16} and protected by symmetry. Figure 7.4(b) shows the charges for the nodes in Δ_{16} (cyan circles), and for the adjacent quadratic nodes at Γ in Δ_{15} ($\chi_{15}[\Gamma] = +1$, large blue filled triangle) and in Δ_{17} ($\chi_{17}[\Gamma] = +1$, large red filled square). Imagining the reverse band-inversion process from 0.1 V/\AA to -0.3 V/\AA , while the C_6 crystalline symmetry is relaxed but the $C_2 \mathcal{T}$ symmetry is conserved (i.e. allowing the nodes to move freely on the $C_2 \mathcal{T}$ symmetric plane). After bringing all the circles to K and K' they must annihilate, leaving a pair of

closed Dirac strings (loops) behind. Since one Dirac string marks a flip of gauge sign of the eigenvectors, the merging of two Dirac strings corresponds to the identity, such that the two closed Dirac strings can merge and annihilate.

The conversion from the first to second panel in Fig. 7.4(b) follows the creation and the moving of the nodes on the K- Γ line from K towards Γ . When the nodes in Δ_{16} (cyan circles) reach Γ , the band inversion happens between the two doubly-degenerate irreps Γ_5 and Γ_6 . From the irreps of the bands [Fig. 7.4(a)] I can predict the formation of six nodes (yellow triangles) on the Γ -M lines in Δ_{15} , six nodes (cyan circles) on the K- Γ lines in Δ_{16} , and six nodes (purple squares) on the Γ -M lines in Δ_{17} . The corresponding topological configurations are shown in the third panel of Fig. 7.4(b), from which I can verify that the reversing of the band inversion by recombining the nodes must lead to the second panel. The linear nodes at the K point (full and open dark red pentagons) together with their Dirac string (dashed dark red line) in Δ_{14} affect the behaviour of the triangle nodes when they reach the M point upon applying higher electric fields, i.e. these cannot annihilate and instead scatter apart from one another (not shown here).

Similar to the group 1, the non-Abelian frame charges within the groups 2 and 3, corresponding to the patch Euler class of the single band crossings, can be verified through a direct computation. While the band inversion in group 1 at Γ is mediated by a triply degenerate point with a frame charge of $q = -1$ [262], the band inversion at Γ between group 2 and 3 is mediated by a quadruple-degenerate point with a total frame charge $q = (-1) * (-1) = +1$. Even though the frame charge of the quadruple-degenerate node is trivial, because of the crystalline symmetries it must be formed by the superposition of two quadratic nodes, each with a non-zero patch Euler class $|\chi_{15}| = |\chi_{17}| = 1$, and six linear nodes with the frame charges $\pm q_{16}$.

7.2.7 Edge states

I also study the evolution of topological edge states with varying electric field by calculating the surface local density of states (LDOS) from the imaginary part of the surface Green's function [50]. Figure 7.2(c) shows the edge states of 7% strained silicate. On the (100) edge (i.e. the zigzag direction for the Si atoms), there is an edge arc connecting two adjacent nodes at the neighbouring Γ points. Upon increasing electric field, new band-crossing points appear around Γ . At 1.8 V/Å, there are two clear projections of the new Dirac cones on the (100) edge around 17.36 THz. I calculate the Zak phase γ (i.e. the Berry phase along a non-contractible path of the Brillouin zone which is here quantised to $\{0, \pi\}$ by the $C_2\mathcal{T}$ symmetry) in gap Δ_{10} and Δ_{11} at 0.0 and 1.8 V/Å. As shown in Fig. 7.2(c), a Zak phase of zero corresponds to the emergence of the edge states, while $\gamma = \pi$ leads to vanishing

edge states. This indicates that the band Wannier states (the Wannier states are the Fourier transform of the Bloch eigenstates) have their centers (the “band centers”) shifted from the center of the atomic Wannier states (the “atomic centers”), leading to a charge anomaly and, following, the localisation of an edge state. Furthermore, the fact that the edge states appear when the Zak phase is zero simply means that the band centers occupy the center of the unit cell, while the atomic centers lie on the boundary of the unit cell [262, 264]. Indeed, the \mathbb{Z}_2 quantised Berry phase is a good quantum number in 1D, which indicates the band center (i.e. its Wyckoff position) [279].

The Zak phase for the given edge termination can be predicted from the bulk topology. The Zak phase at a fixed gap is given (modulo 2π) by the parity of the number of Dirac strings that are crossed by the straight path of integration perpendicular to the edge axis, i.e. for the (100) edge these are the paths $l_{k_{\parallel}} \in \{k_{\perp}(\mathbf{b}_1 - \mathbf{b}_2) + k_{\parallel}(\mathbf{b}_1/2 + \mathbf{b}_2/2) | k_{\perp} \in [0, 1]\}$ at a fixed $k_{\parallel} \in [0, 1]$, with k_{\parallel} the coordinate of the horizontal axis in Fig. 7.2(c) and Fig. 7.4(c) [262].

Figure 7.4(c) shows the topological edge states of 5% strained silicate on the (100) edge. Besides the edge arc that connects two adjacent nodes at the neighbouring Γ points around 26.45 THz, there is also a new edge arc connecting two adjacent nodes around 25.90 THz located at neighbouring K points with 2D irrep K_3 . Under an electric field of 0.9 V/Å, extra edge arcs emerge near $\bar{\Gamma}$ at 25.97 THz. The arc connecting K_3 moves downwards upon increasing electric field and is robust. For the four-band braiding processes, the Zak phase argument fails, as the Zak phases γ_{14-17} in Fig. 7.4(c) do not show a consistent behaviour. I stress that, apart from effective Zak phase diagnoses [262], the full multi-gap bulk-boundary correspondence remains an open question. Hence, I take here a “spectator” view by directly visualising the edge states but without addressing the fundamental mechanisms behind them.

7.2.8 Experimental signature: Raman spectra

I finally propose that the band-inversion processes described above can be directly observed experimentally by following the evolution of the Raman spectrum of the material. All the relevant modes are Raman-active. I calculate the evolution of the Raman spectrum associated with the modes involved in the two braiding processes described in Figs. 7.2 and 7.4. Figure 7.5(a) shows the two Raman modes of the three Kagome bands in group 1. Without an electric field, \mathcal{B}_{10} at Γ , with 1D irrep Γ_1 , belongs to the Raman-active A_1 mode at 583.1 cm^{-1} . \mathcal{B}_{11} and \mathcal{B}_{12} at Γ , with 2D irrep Γ_5 , correspond to the E_2 mode, and are also Raman-active at 604.1 cm^{-1} . The Raman peak of the E_2 mode is stronger than that of the A_1 mode. With increasing electric field, the frequency of the stronger E_2 mode decreases, until reaching the critical field of 0.7 V/Å, where its phonon frequency of 592.7 cm^{-1} becomes

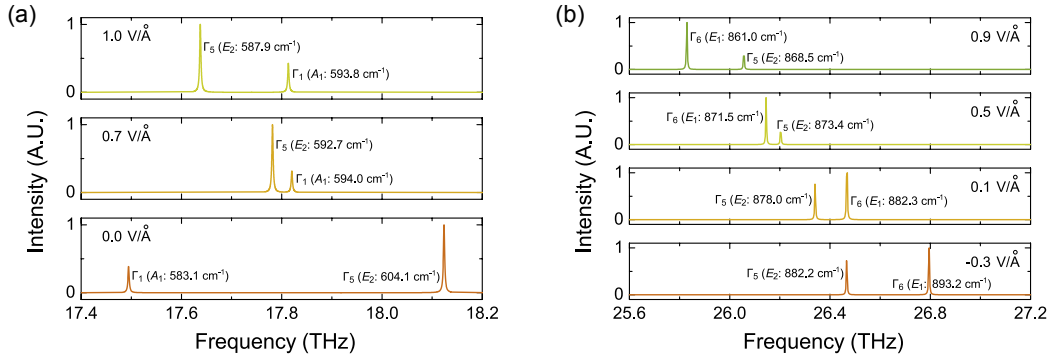


Fig. 7.5 Raman signature. Simulated Raman spectra (A.U. = arbitrary units) for (a) 7% and (b) 5% strained monolayer silicate Si_2O_3 under various electric fields.

lower than that of the weaker A_1 mode (594.0 cm^{-1}). Further increasing the electric field enlarges the frequency difference between the two Raman-active modes.

For the two Raman modes involved in the braiding processes between groups 2 and 3, the band inversion between the Raman modes with different intensities is also clearly visible. As shown in Fig. 7.5(b), both the E_2 and E_1 modes, corresponding to the 2D irreps of Γ_5 and Γ_6 respectively, are Raman-active, and the E_1 peak with a higher frequency of 893.2 cm^{-1} has a stronger intensity. Although the frequencies of both the stronger E_1 mode and the weaker E_2 mode become lower as the electric field increases, the frequency of the E_1 mode decreases much faster than that of the E_2 mode. As a result, the two bands invert at 0.5 V/\AA .

These calculations show that Raman spectroscopy can be a promising tool for characterising the band-inversion processes and the accompanying non-Abelian braiding of phonons in 2D materials such as monolayer silicate. Alternatively, inelastic neutron scattering [151–153] and inelastic X-ray scattering [154] can be used to observe the bulk band crossings directly, while high-resolution electron energy-loss spectroscopy [198] can be used to observe the topological surface states.

7.3 Conclusion

I show that the phonon bands in layered silicates provide a versatile platform to observe new multi-gap topologies. I find that under experimentally feasible strain and/or external electric-field conditions, the phonon bands can exhibit the required braiding processes to induce multi-gap topological phases characterised by non-Abelian frame charges and Euler class. Given the feasibility of the proposed material and experimental setup, this study provides an impetus to investigate phonon bands, and this material realisation in particular, to experimentally observe multi-gap topology.

Chapter 8

Side projects

In addition to the main project of topological phonons, I have also done a series of side projects, including:

(a) Tunable emission of Nd-doped CsPbBr₃. This section is based on work published in [Yujun Xie*, Bo Peng* (contributed equally), Ivona Bravić, Yan Yu, Yurong Dong, Rongqing Liang, Qiongrong Ou, Bartomeu Monserrat, and Shuyu Zhang. *Advanced Science* 7, 2001698 (2020)]. My collaborators Yujun Xie synthesised the nanocrystals and measured the optical properties, Ivona Bravić provided the microscopic mechanisms for strain-induced changes in exciton oscillator strength, Bartomeu Monserrat supervised the theoretical part, and Shuyu Zhang supervised the experimental part, while I was responsible for the *ab initio* calculations.

(b) Tunable photostriction of halide perovskites through energy dependent photoexcitation. This section is based on work published in [Bo Peng, Daniel Bennett, Ivona Bravić, and Bartomeu Monserrat. *Physical Review Materials* 6 (8), L082401 (2022)]. My collaborators Daniel Bennett verified the results with ABINIT, Ivona Bravić provided the group-theory analysis, and Bartomeu Monserrat supervised the project, while I was responsible for the rest.

(c) Photo-induced phase transition in monolayer MoTe₂. This section is based on work published in [Bo Peng, Hao Zhang, Weiwen Chen, Bowen Hou, Zhi-Jun Qiu, Hezhu Shao, Heyuan Zhu, Bartomeu Monserrat, Desheng Fu, Hongming Weng, and Costas M Soukoulis. *npj 2D Materials and Applications* 4, 14 (2020)]. My collaborators Bartomeu Monserrat provided the microscopic mechanisms for Peierls-like phase transition, Desheng Fu applied the Landau theory, and Hao Zhang devised the research idea and supervised the project, while I was responsible for the rest.

(d) Phonon-assisted electronic states modulation of few-layer PdSe₂ at terahertz frequencies. This section is based on work published in [Ziqi Li*, Bo Peng* (contributed equally), Miao-Ling Lin, Yu-Chen Leng, Bin Zhang, Chi Pang, Ping-Heng Tan, Bartomeu Monserrat,

and Feng Chen. *npj 2D Materials and Applications* 5, 87 (2021)]. My collaborators Ziqi Li synthesised the samples and measured the optical properties, Bartomeu Monserrat supervised the theoretical part, and Feng Chen supervised the experimental part, while I was responsible for the *ab initio* calculations.

(e) Photocatalysis and stability of monolayer fullerene networks. This section is based on work published in [Bo Peng. *Journal of the American Chemical Society* 144 (43), 19921 (2022)] and [Bo Peng. *Nano Letters* 23(2), 652 (2023)].

8.1 Tunable emission of Nd-doped CsPbBr₃

In collaboration with experimentalists, I perform first-principles calculations to understand the optical properties of Nd-doped CsPbBr₃. My experimental colleagues prepare neodymium (III) (Nd³⁺) doped CsPbBr₃ nanocrystals (NCs) through the ligand-assisted reprecipitation method at room temperature with tunable photoemission from green to deep blue. A blue-emitting nanocrystal with a central wavelength at 459 nm, an exceptionally high photoluminescence quantum yield of 90%, and a spectral width of 19 nm is achieved. My first-principles calculations reveal that the increase in photoluminescence quantum yield (PLQY) upon doping is driven by an enhancement of the exciton binding energy due to increased electron and hole effective masses, and an increase in oscillator strength due to shortening of the Pb-Br bond. Putting these results together, I demonstrate that B-site composition engineering is a reliable strategy to further exploit the perovskite family for wider optoelectronic applications.

8.1.1 Accurate description of the band gap of CsPbBr₃

I first compare the band gaps in the presence of spin-orbit coupling calculated by the PBEsol functional [183], the hybrid HSE functional [106–108], and many-body perturbation theory in the G_0W_0 and $QPGW$ frameworks [331–335]. As shown in Table 8.1, the PBEsol band gap of 0.33 eV is much smaller than the experimental band gap, because DFT severely underestimates the single-particle band gap. The HSE band gap increases to 0.87 eV but is still much smaller than the experimental value. The calculations suggest that the $QPGW$ can describe the system much better. To compare the calculated band gap using a static lattice with experimental data measured at finite temperatures, I use a finite-temperature correction ΔT of 0.45 ± 0.06 eV, taken from previous work [336]. The band-gap renormalisation at finite temperatures mainly comes from structure distortions that result in changes to metal-halide-metal bond angles and metal-halide bond lengths. The band gap is thus estimated to

Table 8.1 Calculated band gaps (eV) of CsPbBr₃ using PBEsol, HSE, G_0W_0 and $QPGW$. The measured value is also included for comparison.

PBE	HSE	G_0W_0	$QPGW$	$E_g^{QPGW} + \Delta T$	Experiment
0.33	0.87	1.16	1.89	2.34	2.41

be $E_g = E_g^{QPGW} + \Delta T = 2.34$ eV, where E_g^{QPGW} is the $QPGW$ band gap calculated for the static lattice. The estimate agrees with measured band gaps. Due to quantum confinement in nanocrystals, which is being neglected in our first-principles bulk calculations, the measured photoluminescence peak increases to 2.41 eV.

In subsequent calculations with Nd dopands I use the PBEsol band structure with a scissor shift to raise the unoccupied DFT eigenstates, as PBEsol correctly captures the band-gap trend with doping and the orbital character of the band-edge states.

8.1.2 Dopant-induced band-gap blueshift

Fig. 8.1(a) shows the normalised photoluminescence (PL) and absorbance spectra of doped CsPbBr₃ NC solutions. As the doping ratio increases, both the absorption onset and the PL peak exhibit a continuous blueshift. Using first-principles methods, I calculate the band gap of CsPbBr₃ as a function of doping concentration, and Fig. 8.1(b) shows that the resulting band-gap blueshift is in good agreement with the experimental trend. In the calculations I include all of structural effects, many-body effects, spin-orbit coupling and thermal effects using state-of-the-art many-body GW calculations and also including a correction to account for thermal effects. Despite including all these terms, there is still a disagreement in the value of the band gap compared to experiment, which is due to quantum-confinement effects in NCs.

To rationalise the effect of B-site doping of Nd³⁺ ions on the optical properties of CsPbBr₃, I calculate the electronic structure of bulk pristine and Nd³⁺-doped CsPbBr₃. The calculated band structure of pristine CsPbBr₃ is shown in Fig. 8.2(a). A direct band gap of 2.34 ± 0.06 eV is obtained at the R-point of the Brillouin zone, which agrees well with the experimental photoluminescence peak at 2.41 eV when considering the weak quantum-confinement effect present in the NCs. The valence-band maximum (VBM) results from the antibonding interaction between Pb 6s and Br 5p orbitals, leading to a destabilised state with respect to the isolated Pb 6s and Br 5p states. This interaction results in an isotropic delocalised state along the Pb-Br vertices of the lattice with nodes on the Pb-Br bond [Fig. 8.2(b)]. The conduction-band minimum (CBM) consists of empty Pb 6p states

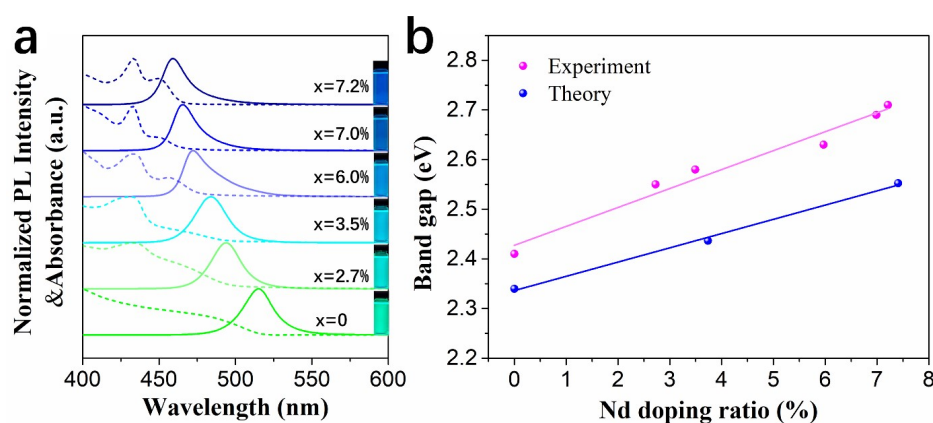


Fig. 8.1 (a) Normalised PL and absorbance spectra of $\text{CsPbBr}_3:x\text{Nd}^{3+}$ NC colloidal solutions with different Nd/(Nd+Pb) doping ratios: PL emission (solid line, excitation at 365 nm) and UV-visible absorbance spectra (dashed line). The inset shows the corresponding images of luminescent $\text{CsPbBr}_3:x\text{Nd}^{3+}$ NC colloidal solutions under UV excitation. (b) Broadening of the band gap with the increasing Nd doping ratio.

that hybridise to build a bonding and stabilised conduction-band minimum with respect to the atomic orbitals [Fig. 8.2(b)].

The band-structure calculations with Nd dopants at Pb sites show that the band gap increases with increasing doping concentration. Fig. 8.2(c) depicts the electronic structure of $\text{CsPbBr}_3:x\text{Nd}^{3+}$ ($x = 12.5\%$), in which the band gap increases from 2.34 eV to 2.59 eV. When Pb is replaced with Nd, the formation of the valence band described above is perturbed, giving a band that mostly resembles the energetically lower lying isolated Br 5p orbitals. This is shown in Fig. 8.2(d) by the VBM with dominant Br contributions, by the change in dispersiveness towards a more localised state compared to the pristine case, and by the change in the spatial charge distribution of the VBM. Similarly, the periodic overlap of the CBM Pb 6p orbitals is perturbed, which leads to a destabilisation of the conduction band towards the atomic 6p levels. The simultaneous stabilisation of the VBM and destabilisation of the CBM results in the observed band gap increase.

After a systematic theoretical study on the individual contributions as well as the interplay between electronic effects, spin-orbit coupling, and structural effects including lattice contraction and octahedral distortion, I demonstrate that the blueshift is dominated by electronic effects. As an example, at 12.5% doping, the electronically-induced blueshift is 0.24 eV, structural relaxation leads to a redshift of 0.08 eV, and spin-orbit coupling results in a blueshift of 0.09 eV, leading to an overall blueshift of 0.25 eV. This microscopic understanding provides new insights to guide further experimental studies of composition engineering in colloidal CsPbX_3 NCs, and provides a framework for further study of doping effects in other material systems.

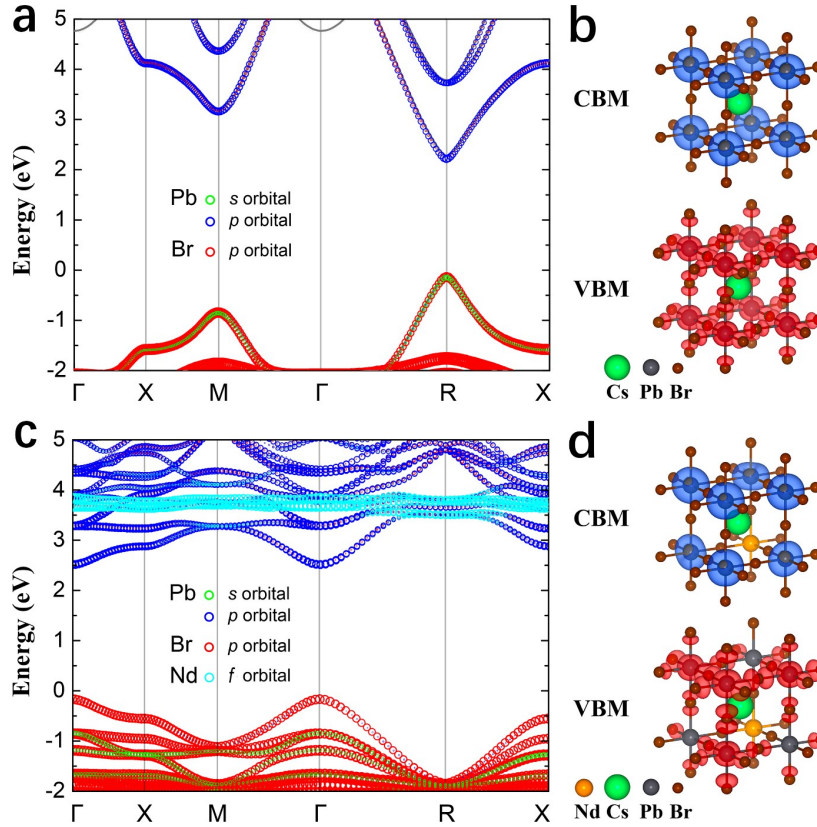


Fig. 8.2 (a) Calculated band structure of pristine CsPbBr₃. The orbital characters are plotted as a fat-band structure showing Pb 6s, 6p and Br 4p orbitals. (b) Partial charge densities of the VBM and the CBM of pristine CsPbBr₃. (c) Calculated band structure of CsPbBr₃:xNd³⁺ (x = 12.5%). The orbital characters are plotted as a fat-band structure showing Pb 6s, 6p and Br 4p orbitals, as well as Nd 5d orbitals. (d) Partial charge densities of the VBM and the CBM of Nd³⁺-doped CsPbBr₃.

8.1.3 Enhanced photoluminescence quantum yield

My experimental colleagues also find that the PLQY is significantly enhanced upon doping. In addition, the dominant mechanism is the increased radiative recombination k_r , and I perform first-principles calculations on the defect-free system to understand how k_r increases with doping.

I identify two microscopic mechanisms to explain the increase of k_r with increasing doping observed experimentally. The first mechanism is associated with the flattening of the valence and conduction bands upon doping [Fig. 8.2(c)], increasing the electron and hole effective masses. According to the Wannier-Mott model, larger effective masses lead to stronger spatial confinement of the exciton and to an increase in its binding energy.

The second mechanism is associated with the doping-driven decrease in the Pb-Br bond length. The lowest-energy bright exciton is dominated by the electron-hole pair at the band edges, implying that photoexcitation leads to a transfer of an electron along the Pb-Br bond towards the Pb ion, while the hole remains delocalised over both elements. This suggests that decreasing the Pb-Br bond length pushes the system towards a brighter state, leading to an increase in the k_r . To demonstrate the lattice-contraction mechanism, I conduct exciton oscillator-strength calculations for the pristine system, but using the smaller primitive cell parameters that correspond to those of the 12.5% Nd-doped system. As expected, I find that the oscillator strength of the first bright exciton increases by 67.2% with respect to the fully relaxed pristine perovskite, proving that lattice contraction is one of the key factors driving the increase in k_r . This is due to the increase in the overlap between the wave function of electron and hole states that form the exciton. Based on first-principles calculations, I show that the PLQY of defect-free CsPbBr₃ can be further enhanced by lattice contraction.

8.1.4 Summary

In summary, I demonstrate that the band gap tunability is mostly driven by dopant-induced electronic changes, while the increase in PLQY is associated with increased exciton binding energy driven by dopant-induced electronic changes and enhanced exciton oscillator strength driven by dopant-induced structural changes. This microscopic understanding opens new possibilities for B-site composition engineering in colloidal CsPbX₃ NCs.

8.2 Tunable photostriction of halide perovskites

Halide perovskites exhibit giant photostriction, that is, volume or shape changes upon illumination. However, the microscopic origin of this phenomenon remains unclear and there are experimental reports of both light-induced lattice expansion and contraction. I establish a general method, based on first-principles calculations and molecular orbital theory, which provides a microscopic picture of photostriction in insulators based on the orbital characters of their electronic bands near the Fermi level. For lead-halide perovskites, I find that different valence states have different bonding characters, leading to opposing strengthening or weakening of bonds depending on the photoexcitation energy. The overall trend is that light induces lattice contraction at low excitation energies, while giant lattice expansion occurs at high excitation energies, rationalising experimental reports.

8.2.1 Photostriction in halide perovskites

Photostriction is the process of non-thermal deformation of materials under illumination. It has been well studied in ferroelectric materials such as SbSI [337] and oxide perovskites [338–340] due to promising applications in microactuators, sensors, and photonic devices [341]. These studies reveal that the driving mechanism behind photostriction can have different microscopic origins. For example, in polar materials the photoexcited carriers screen the polarisation, which can change the internal electric field, inducing the converse piezoelectric effect [342–344]. By contrast, in non-polar materials, the introduction of electron-hole pairs under illumination can cause changes in atomic bonds that lead to lattice deformations [341].

The recent discovery of giant photostriction in halide perovskites [345–347] has been shown to boost the power-conversion efficiency of perovskite-based solar cells [347], to influence phase segregation [348, 349] and moisture degradation [350], and also provides insights into the observed light-induced intensity changes of photoluminescence [351, 352]. Additionally, photostriction could offer new pathways to use halide perovskites in optomechanical devices [345, 346].

The microscopic origin of photostriction in halide perovskites remains unclear. It is still debated whether the giant lattice expansion of up to 1.4% under illumination can be induced by electronic excitation alone [346, 347, 353–356]. In addition, both light-induced lattice expansion and contraction have been observed in experiments: the giant lattice expansion is observed when the sample is illuminated by light sources such as a halogen lamp and a standard 1-sun source with excitation energies much greater than the band gap [346, 347, 355], whereas lattice contraction occurs at an excitation energy of just 0.04 eV above the band gap [356]. The observations of both lattice contraction and expansion, and the large magnitude of the volume changes, call for a better understanding of the microscopic mechanism behind photostriction in halide perovskites.

8.2.2 Microscopic mechanism

In this work, I introduce a physically intuitive method to understand photostriction in semiconductors and insulators using a combination of electronic structure theory and molecular orbital theory, based on the nature of the orbital characters near the band edges. Motivated by contradictory experimental results in lead-halide perovskites, I study the effect of photoexcited carriers on the volume of cubic CsPbX_3 ($X = \text{Cl}, \text{Br}, \text{I}$), and demonstrate that exciting electrons from valence bands with different orbital characters leads to tunable photostriction. When electrons are promoted from the strong antibonding states in the top valence band to the weaker antibonding conduction states, the lattice is contracted as a result of an overall

weakened antibonding interaction. On the other hand, when electrons are promoted from the deeper, non-bonding valence bands to the antibonding conduction states, the antibonding interaction increases and leads to lattice expansion. I reproduce the maximum experimentally reported lattice expansion of 1.4% at a photoexcited carrier density of 0.8 – 0.9 electrons per formula unit ($e/f.u.$) that requires photoexcitation energies of 3 – 4 eV above the band gap. These findings pave the way to photocontrollable optoelectronic properties in lead-halide perovskites – a desirable feature for technological applications.

To understand how bonding character affects photostrictive behaviour, I first consider excitation processes between the VB and CB states. Based on the irreducible band representations (irreps), these excitations are allowed by symmetry. The fundamental band gap of the system is located at the R point, which belongs to the point group O_h . The valence-band maximum (VBM) arises from the antibonding hybridisation of Pb 6s orbitals and Br 4p orbitals (irrep. R_1^+), and the CBM corresponds to an antibonding state of Pb 6p orbitals (irrep. R_4^-). Selection rules demand that optical excitations in systems with inversion symmetry are allowed only when the two irreps of the electronic states have opposite parities, denoted with the descriptors even (+) and odd (–) in our notation. In this case, the VBM and the CBM have opposite parities, making the optical excitation dipole-allowed. Despite both being antibonding states, the antibonding interaction in the VBM is stronger than that in the CBM because the former has a larger overlap between the Pb 6s states and the Br 4p states compared to the relatively isolated 6p states around the Pb atoms in the CBM. As a result, the symmetry-allowed bright excitation from the VBM to the CBM redistributes an electron from a strong antibonding state to a weaker antibonding one, which consequently leads to a reduced antibonding interaction and to lattice contraction.

To verify this picture computationally, I selectively excite electrons from the VB to the CB within the Δ self-consistent-field (Δ SCF) approach and calculate the resulting relaxed volume, as shown by the orange curve in Fig. 8.3(b). I start by only exciting electrons near the minimum band gap at the R point, leading to small photoexcited carrier densities ($n \lesssim 0.3$ $e/f.u.$). In this regime I observe lattice contraction. Exciting additional electrons from the VB to the CB at \mathbf{k} -points that are increasingly away from the minimum band gap at R (with a corresponding increase in the photoexcited carrier density $n \gtrsim 0.3$ $e/f.u.$), involves the excitation from weakened antibonding states and leads to diminished lattice contraction. Continuing in this fashion, the antibonding interaction becomes so weak that exciting these states to the relatively stronger antibonding CB states results in lattice expansion [not shown in Fig. 8.3(b)]. The results of this computational experiment confirm the bonding picture for excitations between the VB and the CB.

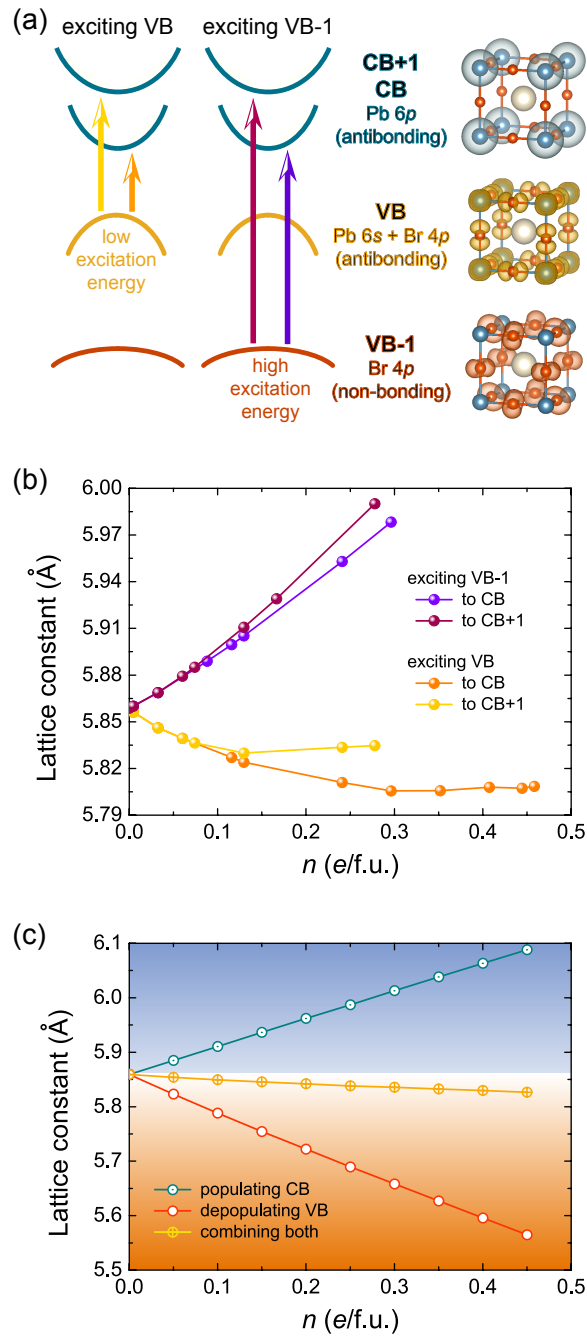


Fig. 8.3 (a) Selective excitation of the antibonding VB state and the non-bonding VB-1 state at the band gap of CsPbBr₃. Evolution of the lattice constant of CsPbBr₃ (b) with increasing photoexcited carrier density n upon selective excitation, and (c) with increasing electron/hole doping concentration n that populates/depopulates the CB/VB states.

To further explore the relative strength of the antibonding interactions in the VB and CB states, I calculate the evolution of the lattice constant upon doping, considering both the population of the CB states (electron doping) or the depopulation of the VB states (hole doping). As shown in Fig. 8.3(c), when populating the CB states, the lattice expands, indicating an enhanced antibonding interaction. Similarly, the decreased lattice constant when depopulating the VB states demonstrates a weakened antibonding strength. The relative strength of the VB and CB states can be estimated from the slope of the corresponding red and blue curves in Fig. 8.3(c). The decrease of lattice constant by depopulating the VB states is faster than the increase of lattice constant by populating the CB states, indicating that the antibonding strength of the VB is stronger than that of the CB. Therefore the average lattice constant decreases, as demonstrated by the yellow curve in Fig. 8.3(c).

I next consider excitations from the VB-1 states. These non-bonding states do not contribute to the bonding-antibonding interaction, and therefore the depopulation of these states has a negligible effect on the lattice constant. On the other hand, the optical transition populates the conduction bands of antibonding orbitals, increasing the interaction between the delocalised Pb $6p$ orbitals and enhancing the repulsion between Pb atoms. Consequently, selective excitation from VB-1 to CB results in lattice expansion.

To verify this picture computationally, I selectively promote electrons from the VB-1 to the CB using the Δ SCF method. I highlight that this computational experiment does not correspond to a physically realisable photoexcitation process because band overlaps and energy conservation may dictate that electrons from the VB should also be excited for a given photoexcitation energy, but it is a convenient model to isolate the role of the VB-1 band. The results are shown by the violet curve in Fig. 8.3(b), confirming the lattice expansion from the bonding picture.

For completeness, I also consider excitations from the VB and VB-1 bands to the CB+1 band in Fig. 8.3(b). However, the character of the CB+1 band is similar to that of the CB band, so the results are largely independent of the conduction bands into which electrons are excited.

Overall, the combined analysis based on molecular orbital theory and first-principles calculations shows that the nature of photostriction is dominated by the changes in the valence states from which electrons are excited rather than the conduction states into which they are excited.

8.2.3 Overall effects

Having established the role of different bands in the photostriction response of CsPbBr₃ by (unphysically) exciting electrons from and to selected bands only, I next combine our

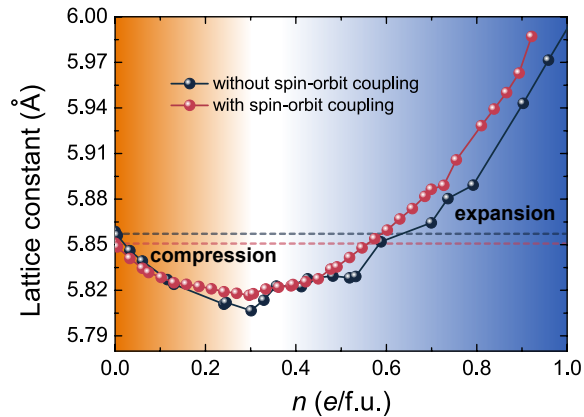


Fig. 8.4 Photostriction of CsPbBr_3 with and without spin-orbit coupling as a function of photoexcited carrier density.

results to rationalise experimental photostriction reports. I use the ΔSCF method to create photoexcited configurations with fixed carrier densities. To achieve a given photoexcited carrier density, I promote the necessary number of electrons from the valence bands, starting from the VBM state and then promoting electrons with decreasing energy, and simultaneously populate the conduction bands starting from the CBM state and then occupying states with increasing energy. The final configuration corresponds to a steady out-of-equilibrium state with electrons populating the lowest energy conduction bands and holes populating the highest energy valence bands.

To achieve this configuration experimentally, it is necessary to use photon energies at least up to the largest energy difference between the highest occupied conduction band and the lowest unoccupied valence band, and in the following this maximum energy difference is called as the excitation energy. To promote the required number of electrons to achieve a given photoexcited carrier density, it is also necessary to use appropriate fluences. The maximum reported carrier densities can be realised by an experimentally feasible fluence of about 10 mJ/cm^2 [357, 358].

The volume of CsPbBr_3 as a function of photoexcited carrier density is depicted in Fig. 8.4. For carrier densities below $n \lesssim 0.245 \text{ e/f.u.}$ (corresponding to excitation energies below 4.40 eV), only strong antibonding VB states are excited, leading to an overall lattice contraction. For higher carrier densities (excitation energies exceeding 4.40 eV), electrons from the VB-1 band start to be promoted, emptying the non-bonding VB-1 states and populating the antibonding conduction states. Therefore, the antibonding interaction is significantly enhanced, resulting in stronger repulsion between the Pb atoms which causes the lattice to expand.

I obtain the maximum experimentally observed uniform strain of 1.4% at a photoexcited carrier density $n \sim 0.8 - 0.9$ e/f.u. (corresponding to an excitation energy of 5.5 – 6.0 eV).

I then discuss the role of spin-orbit coupling (SOC) in photostriction. The inclusion of SOC has a dramatic effect on the electronic structures of halide perovskites [359]. SOC splits the triply degenerate (sixfold degenerate when considering spin up and down) CBM state at the R point into a doubly degenerate CB state and a fourfold degenerate CB+1 state [360]. This spin-orbit splitting decreases the CB energy and increases the CB+1 energy, reducing the G_0W_0 band gap to 1.46 eV. Despite these SOC-driven changes to the band structure, the general microscopic mechanisms and resulting photostriction as a function of photoexcited carrier density remain largely unchanged, as shown in Fig. 8.4. The robustness of the results with respect to the inclusion or exclusion of SOC arises because the band characters are similar between the two situations. However, this may not be true in other materials, especially when SOC induces band inversion between orbitals, and should be carefully checked.

The complete picture, summarised in Fig. 8.4, shows that, at lower carrier densities (corresponding to low excitation energies) there is light-induced lattice contraction, while at larger carrier densities there is lattice expansion. These results allow me to rationalise the various experimental findings. It has been reported that by using halogen lamps or a standard 1-sun source with photoexcitation energies far above the band gap, lattice expansion of up to 1.4% can take place [346, 347, 355], but that a much smaller excitation energy of just 0.04 eV above the band gap induces compressive strain [356]. This study of the microscopic mechanism for photoexcitation in these materials explains the origin and conditions for both types of photostriction, providing a unified picture for the various experimental reports.

8.2.4 Summary

I provide a comprehensive microscopic description of photostriction in lead-halide perovskites starting from a simple consideration of the orbital characters of their band structure. When exciting from strong antibonding states in the top valence band to the weaker antibonding conduction states, lattice contraction results from a weakened antibonding interaction. In contrast, for larger excitation energies that promote electrons from the deeper, non-bonding valence bands to the antibonding conduction states, the resulting enhanced antibonding interaction leads to lattice expansion. The overall effect is that light induces lattice contraction at low excitation energies, while lattice expansion occurs at higher excitation energies. These findings help to rationalise the experimental observation that lattice expansion of up to 1.4% can be induced by light of energy far above the band gap [346, 347, 355], while excitation energies close to the gap induce compressive strain that contracts the lattice [356]. The ability

to control photostriction via the excitation energy may offer new opportunities for solar cells, light-emitting diodes, and memory devices with ultrafast control of their optical properties. More generally, this approach illustrates the important role that the orbital characters of the electron bands can play in photoexcited phenomena. The combination of molecular orbital theory and first-principles calculations should be generally applicable to understand photoinduced phenomena in other systems.

8.3 Photo-induced phase transition in monolayer MoTe₂

In the photo-induced topological phase transition in two-dimensional MoTe₂ [361], the system undergoes changes in temperature, strain, electronic excitation, chemical state, and lattice-vibrational modes triggered by laser irradiation. The transition may depend on one of these factors or on a combination of them. Consequently, experimental optimisation of these factors is time consuming and costly. Instead, I exploit computational techniques to model the quantum behaviour of MoTe₂ and investigate the microscopic mechanism virtually. This approach allows me to quickly explore the vast degrees of freedom to identify the most possible mechanism, and to accomplish this at a small cost compared to experiments.

I reveal the underlying physics by simulating atomic displacements in the excited state to see whether (and how) a phase transition may be triggered [147]. By promoting valence electrons from high-lying valence band states to low-lying conduction band states, I calculate the potential-energy surfaces along the phonon eigenvectors at different excitation energies. And by comparing the potential-energy surfaces at different excitation energies, I identify the correct microscopic mechanism.

The photo-induced phase transition can be triggered by photoexcited carriers alone that soften multiple lattice-vibrational modes. These softenings lead to structural symmetry breaking within sub-picosecond timescales (Fig. 8.5), which is shorter than the timescale of a thermally driven phase transition. The transition is predicted to be triggered by photons with energies over 1.96 eV. The microscopic picture of the phase transition is analogous to a Peierls distortion, with a red shift of the conduction bands that are occupied upon photoexcitation that lowers the overall energy of the system. Therefore, the transition mechanism under laser irradiation can be explained without introducing other factors such as local heat, thermal strain and Te vacancies.

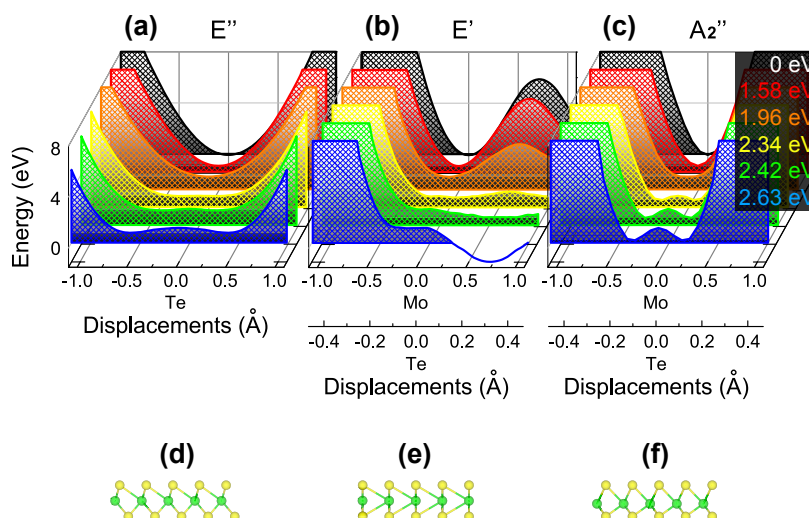


Fig. 8.5 potential-energy surface at different excitation energies along the eigenvectors of (a) E'' , (b) E' , and (c) A_2'' modes, and their corresponding structures (d)-(f) at the minima of the potential-energy surface at 2.63 eV.

8.4 Phonon-assisted electronic states modulation of PdSe₂

Information technology demands high-speed optoelectronic devices, but going beyond the one terahertz (THz) barrier is challenging due to the difficulties associated with generating, detecting, and processing high-frequency signals. In collaboration with my experimental colleagues, I show that femtosecond-laser-driven phonons can be utilised to coherently manipulate the excitonic properties of semiconductors at THz frequencies. Combining ultralow-frequency Raman spectroscopy with first-principles calculations, I identify the unique probe-energy-dependent features of electron-phonon interactions in layered PdSe₂. Two distinctive types of coherent phonon excitations could couple preferentially to different types of electronic excitations: the intralayer (4.3 THz) mode to carriers and the interlayer (0.35 THz) mode to excitons. This work provides new insights to understand the excited-state phonon interactions of 2D materials, and to achieve future applications of optoelectronic devices operating at THz frequencies.

Figure 8.6(a) demonstrates the calculated phonon dispersion of eight-layer PdSe₂, showing this configuration to be dynamically stable. The phonon occupation number N_{ph} is obtained from the Bose-Einstein distribution function at 300 K. The calculated displacement patterns in Fig. 8.6(b) confirm that the higher frequencies around 4.3 THz (144.6 cm^{-1}) are dominated by intralayer vibrations of Se atoms, whilst the low-frequency modes below 1 THz (33.3 cm^{-1}) are dominated by interlayer vibrations of both Pd and Se atoms.

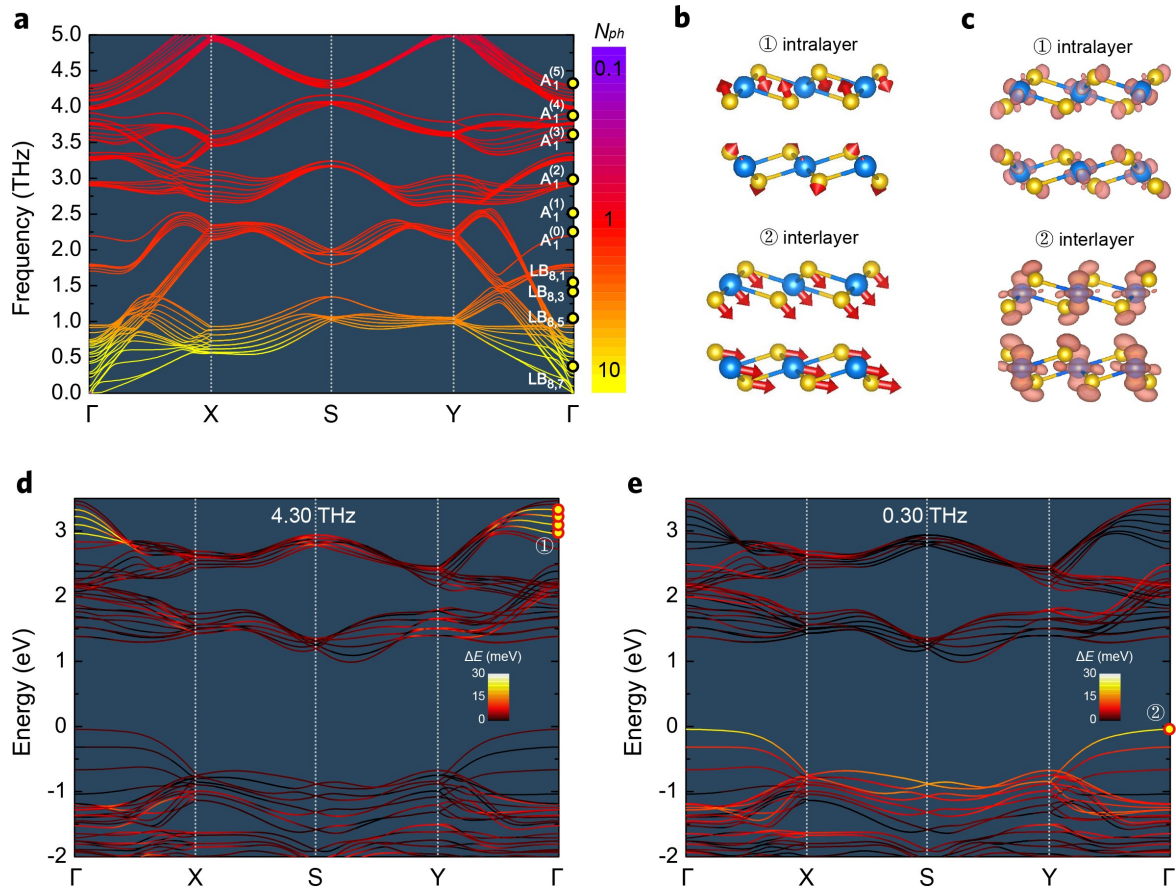


Fig. 8.6 Lattice dynamics and electron-phonon coupling in PdSe₂. (a) Calculated phonon dispersion spectrum of eight-layer PdSe₂. (b) Displacement patterns of the intralayer and interlayer modes. (c) Partial charge density of the electronic states that couple most strongly to the corresponding atomic displacements. Electronic structure modulated by (d) intralayer mode at 4.30 THz and (e) interlayer mode at 0.30 THz.

The strength of electron-phonon coupling is estimated using a frozen-phonon approach along the normal modes with frequencies around 4.3 and 0.35 THz at the Γ point. It is found that there are two modes with much stronger coupling strength than their neighbouring modes. As shown in Fig. 8.6(d), the high-frequency intralayer mode at 4.30 THz significantly modulates the high-lying conduction bands around 3 eV. This is because the high-lying conduction bands come from the intralayer orbitals along the Pd-Se bonds [Fig. 8.6(c)], and only strong intralayer displacements can influence their wave function. By contrast, the interlayer mode of 0.30 THz strongly couples with the highest valence bands. These bands, consisting mainly of d_{z^2} orbitals of Pd and p_z orbitals of Se, are the dominant hole states in the formation of the A exciton. The d_{z^2} orbitals of Pd and p_z orbitals of Se, oriented along the out-of-plane direction, are extremely sensitive to the interlayer breathing mode, which strongly

couples to their charge distribution [Fig. 8.6(c)]. The calculated electron-phonon dynamics are consistent with the observed ultrafast periodic modulation in the broadband pump-probe experiments, in which the high-energy carriers are more sensitive to the intralayer mode, while the A exciton is more sensitive to the interlayer mode.

In conclusion, these findings provide a guidance for the future development of THz frequency optoelectronic devices that based on layered PdSe₂. Furthermore, the observed vibrational phenomena combined with theoretical calculations provide an intuitive picture for exciton-phonon and electron-phonon interactions in 2D layered materials, which is supported by the ultralow-frequency Raman spectroscopy with frequencies down to 5 cm⁻¹.

8.5 Monolayer fullerene networks

Recent attempts to synthesise layers of connected buckyballs, i.e. C₆₀ molecules linked by carbon-carbon bonds, have obtained different arrangements of cluster cages through the formation of bonds between neighbouring C₆₀ molecules [362, 363]. The obtained allotropes include a few-layer rectangular structure in which each C₆₀ molecule has four neighbouring buckyballs and a monolayer hexagonal structure in which each C₆₀ cage binds to six neighbours, namely, a few-layer quasi-tetragonal phase (qTP) and a monolayer quasi-hexagonal phase (qHP) respectively. Great efforts have been devoted to stabilising the linking bonds between neighbouring cluster cages by introducing magnesium atoms to form a quasi-2D fullerene network with strong intralayer covalent bonds [362] because Mg atoms tend to promote covalent bonds [364, 365]. To aid exfoliation, the Mg ions that hold the C₆₀ cages together can be then replaced by large organic ions, which can be removed afterwards by hydrogen peroxide, leading to pure, charge neutral fullerene networks in 2D [362, 366].

8.5.1 Monolayer fullerene networks as photocatalysts for water splitting

Photocatalytic water splitting can produce hydrogen in an environmentally friendly way and provide alternative energy sources to reduce global carbon emissions. Recently, 2D fullerene networks have been successfully synthesised in monolayer and few-layer forms [362, 363], offering new material candidates for photocatalysis because of their large surface area with abundant active sites, feasibility to be combined with other 2D materials to form heterojunctions, and the C₆₀ cages for potential hydrogen storage. However, efficient photocatalysts need a combination of a suitable band gap and appropriate positions of the band edges with sufficient driving force for water splitting.

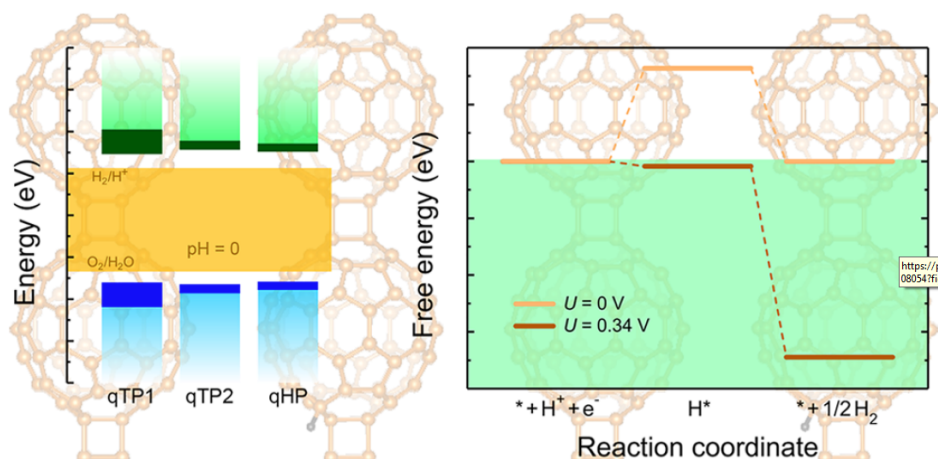


Fig. 8.7 Band alignment of different phases of C_{60} monolayers, as well as their free-energy diagram for a hydrogen reduction reaction at pH = 0 and room temperature.

In this side project, I employ semilocal density functional theory and hybrid functional calculations to investigate the electronic structures of monolayer fullerene networks. I find that only the weakly screened hybrid functional, in combination with time-dependent Hartree-Fock calculations to include the exciton binding energy, can reproduce the experimentally obtained optical band gap of monolayer C_{60} . All the phases of monolayer fullerene networks have suitable band gaps with high carrier mobility and appropriate band edges to thermodynamically drive overall water splitting, as shown in Fig. 8.7. In addition, the optical properties of monolayer C_{60} are studied, and different phases of fullerene networks exhibit distinct absorption and recombination behaviour, providing unique advantages either as an electron acceptor or as an electron donor in photocatalysis.

8.5.2 Stability and strength of monolayer polymeric C_{60}

Ever since the discovery of C_{60} [367], the formation mechanism and stability of the fullerene molecules are far from completely understood [368–371]. When forming structural units of C_{60} clusters in a 2D plane, it is unclear whether ordered structures of monolayer polymeric C_{60} are stable under ambient conditions such as strain and temperature. Unfortunately, only qHP C_{60} has been obtained as monolayers, while all the qTP C_{60} flakes are few-layer [362]. These results raise doubts regarding the stability of monolayer fullerene networks.

Recent first-principles calculations have investigated various structural phases of monolayer C_{60} with different bonding characters [372–377]. The mechanical stability of several phases has been confirmed [372, 373, 376]. More recently, the thermal stability of monolayer C_{60} has been addressed using molecular dynamics simulations, showing that both qTP and

qHP C_{60} monolayers can remain stable at temperatures near 800 K [378], which is partially consistent with the experimental result that monolayer qHP C_{60} does not decompose at 600 K [362]. However, previous analysis based on mechanical and thermal stability cannot explain why the qTP monolayers have not yet been exfoliated experimentally. Furthermore, the dynamic stability of monolayer fullerene networks with respect to lattice vibrations, which indicates whether the crystal structure is in a local minimum of the potential-energy surface [379–382], is still unexplored. Additionally, the thermodynamic stability of different phases, which energetically classifies the stability (especially at finite temperatures) [383–395], remains unknown. Because of such knowledge gaps, several questions need to be answered to understand the phase stability of monolayer fullerene networks: (i) Are qTP and qHP C_{60} , as pure carbon monolayers without extra Mg or organic ions to bind the C_{60} cages together, dynamically stable? (ii) What is their relative stability in a thermodynamic aspect? (iii) Can the calculated mechanical strength support their phase stability?

In this side project, I investigate the mechanical, dynamic and thermodynamic stability of monolayer qTP and qHP C_{60} by using first-principles calculations. Structural relaxation obtains two crystal structures of the quasi-tetragonal phase: a quasi-1D monolayer and a tightly bound monolayer (denoted as qTP1 and qTP2 respectively). I show that the qTP1 monolayer, albeit being thermodynamically stable at all temperatures above 380 K, possesses low dynamic and mechanical stability due to its weak bonding perpendicular to the straight chains of C_{60} buckyballs. On the other hand, although qTP2 fullerene might be the ground-state structure with the lowest Gibbs free energy at 0 K and exhibits good dynamic and mechanical stability, it is only thermodynamically stable with respect to qTP1 C_{60} at low temperatures. Instead, monolayer qHP C_{60} should be experimentally accessible owing to their dynamic and mechanical stability, in spite of its lowest thermodynamic stability among all three phases. The relative thermodynamic stability of monolayer fullerene networks is summarised in Fig. 8.8. In addition, qHP C_{60} has the highest strength under various strains (hydrostatic, uniaxial and shear) because of the closely packed crystal structures.

These results are in line with the experimental findings. It has been reported that fullerene monolayers can only be isolated experimentally for the honeycomb structure qHP, whereas the obtained rectangular structure qTP is few-layered [362]. Although qTP2 C_{60} is thermodynamically favoured over qTP1 C_{60} at low temperatures, clearly qTP1 C_{60} is thermodynamically more stable than the other two phases at all temperatures above 150 K. However, thermodynamic stability of qTP1 C_{60} does not guarantee high dynamic stability in the presence of interchain (out-of-plane) vibrations perpendicular to the quasi-1D chains. In addition, the low moduli and strength of qTP1 C_{60} originated from the chain crystal structures, in addition to its low shear resistance, indicate that qTP1 C_{60} cannot be intrinsically resilient under

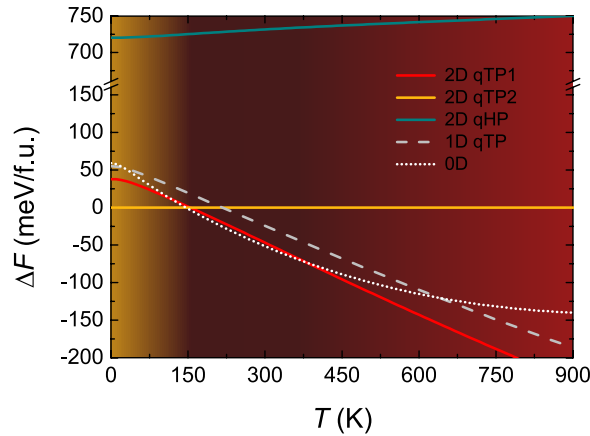


Fig. 8.8 Relative thermodynamic stability of monolayer fullerene networks, one-dimensional fullerene chain and zero-dimensional fullerene molecule, with the Gibbs free energy F of monolayer qTP2 C_{60} set to zero to compare the relative stability.

deformation. Moreover, monolayer qTP1 C_{60} is thermodynamically less stable than 0D C_{60} molecule for temperatures between 120 and 380 K. These results indicate the plausibility that monolayer qTP1 fullerene network can be further split into individual 1D chains or 0D molecules by thermal fluctuations, interchain acoustic vibrations, or external strains. In contrast, qHP C_{60} is both dynamically and mechanically more stable with respect to qTP1 C_{60} . Therefore, monolayer polymeric C_{60} has so far only been exfoliated from the quasi-hexagonal bulk single crystals. These results indicate that a systematic analysis of mechanical, dynamic and thermodynamic stabilities is necessary to rationalise the experimental data.

Chapter 9

Conclusions and outlook

This thesis discusses a range of topological properties in both the band structures of electrons and in particular vibrational spectra of nuclei. First, I discuss the concept of single-gap topology in electronic systems, i.e. topological semimetals, and present the very first example of temperature-promoted topological semimetallic phase in an otherwise trivial insulator at low temperatures in Chapter 3. Then I demonstrate the phonon counterparts of electronic topology where Weyl and nodal-line/ring phonons can be viewed as a replica to topological semimetals and predict the very first material family with light-controlled topological phonons in Chapter 4. In Chapter 5, I show that phonons have their own advantages as charge neutral, spinless bosonic excitations in terms of the preservation of time-reversal symmetry and the accessibility to the entire spectra, enabling the feasibility of finding line degeneracy on the surface of semi-infinite slabs. I then introduce the concept of multi-gap topology, and explain why phonons are an ideal platform to study such topology and the associated non-Abelian braiding compared with the electrons in Chapter 6. In Chapter 7, I propose the very first material candidate with non-Abelian braiding involving both three and four phonon bands, and study the possible experimental signatures. I also summarise a few side projects that I have done during my PhD in Chapter 8, including optical properties and photostriction in halide perovskites, photo-induced phase transition in monolayer MoTe_2 , electron-phonon coupling in few-layer PdSe_2 , and various chemical/physical properties of monolayer fullerene networks such as photocatalysis and thermodynamic stability.

In this final chapter I outline my research plans in the future that are derived from this thesis.

9.1 Non-Abelian braiding of nodal lines

Non-Abelian braiding of nodal lines, based on previous studies on braiding of nodal points, holds potential for advancing our understanding of multi-gap topology. Building upon the foundation laid by the braiding of points on a 2D plane, the braiding of nodal lines in a 3D space aims to explore the rich phenomenology arising from different dimensions. The extra dimension in 3D can be viewed as another tuning parameter rather than external stimuli such as electric fields or strain. In that sense, the braiding can take place as a function of the wave vector in the 3D momentum space, enabling the characterisation of entire braiding processes in one material sample by one single measurement.

One possible research direction involves extending the implications from high-energy physics to condensed matter systems. Investigating the creation and annihilation of points of intersection between the nodal line and the 2D plane can provide insights into fundamental principles of non-Abelian frame charges.

Another intriguing avenue for research lies in the study of higher-dimensional generalisations of non-Abelian braiding. By considering higher-dimensional nodal objects, such as nodal surfaces or higher-dimensional analogues of nodal lines, it is possible to explore the emergence of higher-order topological phases and the corresponding braiding operations. This research could unveil new avenues for controlling and manipulating quantum information, paving the way for the development of topological quantum computing and other advanced technologies.

9.2 Light-switchable topological phases

Future research directions in investigating light-switchable topological phases can further advance the understanding of topological properties out of equilibrium. A starting point can be the two-Fermi level approach by fixing the number of electrons and holes in the excited state Kohn-Sham equation. The manipulation of topological properties can be realised through the controlled tuning of photoexcitation.

One important avenue is to study both-single gap and multi-gap topology upon photoexcitation. The two-Fermi level approach allows for the exploration of how carrier density and electronic temperature can give rise to distinct structural and topological phases, enabling the design of materials with tailored topological properties that can be switched on and off by light.

Moreover, future research in this field can focus on developing theoretical frameworks and computational methods that accurately capture the non-equilibrium dynamics to study

the complex interplay between light and topology in both electrons and phonons. This involves refining existing models and algorithms to incorporate the dynamics of light-matter interactions and the time-dependent nature of excitations. By combining first principles simulations with sophisticated light-matter coupling theories, deeper insights can be gained into the mechanisms governing light-induced topological phase transitions and devise strategies to engineer and control these phases.

References

- [1] Leonhard Euler. *Solutio problematis ad geometriam situs pertinentis*. *Comment. Acad. Sci. U. Petrop*, 8:128–140, 1741.
- [2] Horst Sachs, Michael Stiebitz, and Robin J. Wilson. An historical note: Euler’s Königsberg letters. *J. Graph Theory*, 12(1):133–139, March 1988.
- [3] F. D. M. Haldane. Model for a Quantum Hall Effect without Landau Levels: Condensed-Matter Realization of the “Parity Anomaly”. *Phys. Rev. Lett.*, 61:2015–2018, Oct 1988.
- [4] W. Heisenberg. Über quantentheoretische Umdeutung kinematischer und mechanischer Beziehungen. *Zeitschrift für Physik*, 33(1):879–893, 1925.
- [5] M. Born and P. Jordan. Zur quantenmechanik. *Zeitschrift für Physik*, 34(1):858–888, 1925.
- [6] William A. Fedak and Jeffrey J. Prentis. The 1925 Born and Jordan paper “On quantum mechanics”. *American Journal of Physics*, 77(2):128–139, January 2009.
- [7] E. Schrödinger. Quantisierung als eigenwertproblem. *Ann. Phys.*, 384(4):361–376, January 1926.
- [8] E. Schrödinger. An undulatory theory of the mechanics of atoms and molecules. *Phys. Rev.*, 28:1049–1070, Dec 1926.
- [9] Paul Adrien Maurice Dirac. The quantum theory of the electron. *Proc. R. Soc. Lond. A*, 117(778):610–624, January 1928.
- [10] Paul Adrien Maurice Dirac. The quantum theory of the electron. part ii. *Proc. R. Soc. Lond. A*, 118(779):351–361, January 1928.
- [11] Paul Adrien Maurice Dirac. Quantum mechanics of many-electron systems. *Proc. R. Soc. Lond. A*, 123(792):714–733, January 1929.
- [12] Hermann Weyl. Elektron und gravitation. i. *Zeitschrift für Physik*, 56(5):330–352, 1929.
- [13] Hermann Weyl. Gravitation and the electron1. *Proc Natl Acad Sci*, 15(4):323–334, April 1929.
- [14] Ettore Majorana. Teoria simmetrica dell’elettrone e del positrone. *Il Nuovo Cimento (1924-1942)*, 14(4):171–184, 1937.

- [15] Conyers Herring. Accidental degeneracy in the energy bands of crystals. *Phys. Rev.*, 52:365–373, Aug 1937.
- [16] J. von Neumann and E. P. Wigner. Über merkwürdige diskrete Eigenwerte. In *The Collected Works of Eugene Paul Wigner: Part A: The Scientific Papers*, pages 291–293. Springer Berlin Heidelberg, Berlin, Heidelberg, 1993.
- [17] Michael Victor Berry. Quantal phase factors accompanying adiabatic changes. *Proc. R. Soc. Lond. A*, 392(1802):45–57, January 1997.
- [18] Shiing-shen Chern. Characteristic classes of hermitian manifolds. *Annals of Mathematics*, 47(1):85–121, 1946.
- [19] C. L. Kane and E. J. Mele. Quantum Spin Hall Effect in Graphene. *Phys. Rev. Lett.*, 95:226801, Nov 2005.
- [20] C. L. Kane and E. J. Mele. Z_2 Topological Order and the Quantum Spin Hall Effect. *Phys. Rev. Lett.*, 95:146802, Sep 2005.
- [21] B. Andrei Bernevig, Taylor L. Hughes, and Zhang Shou-Cheng. Quantum Spin Hall Effect and Topological Phase Transition in HgTe Quantum Wells. *Science*, 314(5806):1757–1761, December 2006.
- [22] Markus König, Steffen Wiedmann, Christoph Brüne, Andreas Roth, Hartmut Buhmann, Laurens W. Molenkamp, Xiao-Liang Qi, and Shou-Cheng Zhang. Quantum Spin Hall Insulator State in HgTe Quantum Wells. *Science*, 318(5851):766–, November 2007.
- [23] Lord Kelvin. I. nineteenth century clouds over the dynamical theory of heat and light. *The London, Edinburgh, and Dublin Philosophical Magazine and Journal of Science*, 2(7):1–40, July 1901.
- [24] Oliver Passon. Kelvin’s clouds. *American Journal of Physics*, 89(11):1037–1041, October 2021.
- [25] Max Planck. Ueber das thermodynamische Gleichgewicht von Gasgemengen. *Ann. Phys.*, 255(6):358–378, January 1883.
- [26] Max Planck. Ueber die Elementarquanta der Materie und der Elektrizität. *Ann. Phys.*, 309(3):564–566, January 1901.
- [27] A. Einstein. Die Plancksche Theorie der Strahlung und die Theorie der spezifischen Wärme. *Ann. Phys.*, 327(1):180–190, January 1907.
- [28] P. Debye. Zur Theorie der spezifischen Wärmen. *Ann. Phys.*, 344(14):789–839, January 1912.
- [29] Paul Adrien Maurice Dirac. The quantum theory of the emission and absorption of radiation. *Proc. R. Soc. Lond. A*, 114(767):243–265, January 1927.
- [30] Ig. Tamm. Über die Quantentheorie der molekularen Lichtstreuung in festen Körpern. *Zeitschrift für Physik*, 60(5):345–363, 1930.

- [31] J. Frenkel. On the transformation of light into heat in solids. i. *Phys. Rev.*, 37:17–44, Jan 1931.
- [32] J. Frenkel. On the transformation of light into heat in solids. ii. *Phys. Rev.*, 37:1276–1294, May 1931.
- [33] J.I. Frenkel. *Wave Mechanics: Elementary Theory*. International series of monographs on physics. Clarendon Press, 1932.
- [34] Hans Hellmann. *Einführung in die Quantenchemie*. Deuticke, Leipzig und Wien, 1937.
- [35] Max Born and Kun Huang. *Dynamical theory of crystal lattices*. Clarendon Press, Oxford, 1954.
- [36] J. M. Ziman. *Electrons and Phonons: The Theory of Transport Phenomena in Solids*. Oxford University Press, 1960.
- [37] Paul Adrien Maurice Dirac. A theory of electrons and protons. *Proc. R. Soc. Lond. A*, 126(801):360–365, January 1930.
- [38] P. Hohenberg and W. Kohn. Inhomogeneous electron gas. *Phys. Rev.*, 136:B864–B871, Nov 1964.
- [39] W. Kohn and L. J. Sham. Self-consistent equations including exchange and correlation effects. *Phys. Rev.*, 140:A1133–A1138, Nov 1965.
- [40] W. Kohn. Nobel lecture: Electronic structure of matter—wave functions and density functionals. *Rev. Mod. Phys.*, 71:1253–1266, Oct 1999.
- [41] M. C. Payne, M. P. Teter, D. C. Allan, T. A. Arias, and J. D. Joannopoulos. Iterative minimization techniques for *ab initio* total-energy calculations: molecular dynamics and conjugate gradients. *Rev. Mod. Phys.*, 64:1045–1097, Oct 1992.
- [42] H. Hellmann. A new approximation method in the problem of many electrons. *J. Chem. Phys.*, 3(1):61–61, November 1935.
- [43] G. Kresse and D. Joubert. From ultrasoft pseudopotentials to the projector augmented-wave method. *Phys. Rev. B*, 59:1758–1775, Jan 1999.
- [44] Nicola Marzari and David Vanderbilt. Maximally localized generalized Wannier functions for composite energy bands. *Phys. Rev. B*, 56:12847–12865, Nov 1997.
- [45] Ivo Souza, Nicola Marzari, and David Vanderbilt. Maximally localized Wannier functions for entangled energy bands. *Phys. Rev. B*, 65:035109, Dec 2001.
- [46] Arash A. Mostofi, Jonathan R. Yates, Young-Su Lee, Ivo Souza, David Vanderbilt, and Nicola Marzari. Wannier90: A tool for obtaining maximally-localised Wannier functions. *Computer Physics Communications*, 178(9):685–699, 2008.
- [47] Nicola Marzari, Arash A. Mostofi, Jonathan R. Yates, Ivo Souza, and David Vanderbilt. Maximally localized Wannier functions: Theory and applications. *Rev. Mod. Phys.*, 84:1419–1475, Oct 2012.

- [48] Arash A. Mostofi, Jonathan R. Yates, Giovanni Pizzi, Young-Su Lee, Ivo Souza, David Vanderbilt, and Nicola Marzari. An updated version of Wannier90: A tool for obtaining maximally-localised Wannier functions. *Computer Physics Communications*, 185(8):2309–2310, 2014.
- [49] Giovanni Pizzi, Valerio Vitale, Ryotaro Arita, Stefan Blügel, Frank Freimuth, Guillaume Géranton, Marco Gibertini, Dominik Gresch, Charles Johnson, Takashi Koretsune, Julen Ibañez-Azpiroz, Hyungjun Lee, Jae-Mo Lihm, Daniel Marchand, Antimo Marrazzo, Yuriy Mokrousov, Jamal I Mustafa, Yoshiro Nohara, Yusuke Nomura, Lorenzo Paulatto, Samuel Poncé, Thomas Ponweiser, Junfeng Qiao, Florian Thöle, Stepan S Tsirkin, Malgorzata Wierzbowska, Nicola Marzari, David Vanderbilt, Ivo Souza, Arash A Mostofi, and Jonathan R Yates. Wannier90 as a community code: new features and applications. *J. Phys.: Condens. Matter*, 32(16):165902, 2020.
- [50] QuanSheng Wu, ShengNan Zhang, Hai-Feng Song, Matthias Troyer, and Alexey A. Soluyanov. WannierTools: An open-source software package for novel topological materials. *Computer Physics Communications*, 224:405–416, 2018.
- [51] M. Born and R. Oppenheimer. Zur Quantentheorie der Molekeln. *Ann. Phys.*, 389(20):457–484, January 1927.
- [52] Atsushi Togo and Isao Tanaka. First principles phonon calculations in materials science. *Scripta Materialia*, 108:1–5, 2015.
- [53] Atsushi Togo, Fumiyasu Oba, and Isao Tanaka. First-principles calculations of the ferroelastic transition between rutile-type and CaCl₂-type SiO₂ at high pressures. *Phys. Rev. B*, 78:134106, Oct 2008.
- [54] R. P. Feynman. Forces in molecules. *Phys. Rev.*, 56:340–343, Aug 1939.
- [55] K. Kunc and Richard M. Martin. Ab Initio Force Constants of GaAs: A New Approach to Calculation of Phonons and Dielectric Properties. *Phys. Rev. Lett.*, 48:406–409, Feb 1982.
- [56] Dario Alfè. PHON: A program to calculate phonons using the small displacement method. *Computer Physics Communications*, 180(12):2622–2633, 2009.
- [57] Bartomeu Monserrat. Electron-phonon coupling from finite differences. *Journal of Physics: Condensed Matter*, 30(8):083001–, 2018.
- [58] Xavier Gonze. Adiabatic density-functional perturbation theory. *Phys. Rev. A*, 52:1096–1114, Aug 1995.
- [59] Stefano Baroni, Stefano de Gironcoli, Andrea Dal Corso, and Paolo Giannozzi. Phonons and related crystal properties from density-functional perturbation theory. *Rev. Mod. Phys.*, 73:515–562, Jul 2001.
- [60] G. P. Srivastava. *The Physics of Phonons*. Hilger, Bristol, 1990.
- [61] Martin T. Dove. *Introduction to Lattice Dynamics*. Cambridge University Press, 1993.

- [62] T. T. Heikkilä, N. B. Kopnin, and G. E. Volovik. Flat bands in topological media. *JETP Letters*, 94(3):233, 2011.
- [63] A. A. Burkov, M. D. Hook, and Leon Balents. Topological nodal semimetals. *Phys. Rev. B*, 84:235126, Dec 2011.
- [64] D. T. Son and B. Z. Spivak. Chiral anomaly and classical negative magnetoresistance of weyl metals. *Phys. Rev. B*, 88:104412, Sep 2013.
- [65] Jun Xiong, Satya K. Kushwaha, Tian Liang, Jason W. Krizan, Max Hirschberger, Wudi Wang, R. J. Cava, and N. P. Ong. Evidence for the chiral anomaly in the Dirac semimetal Na_3Bi . *Science*, 350(6259):413, October 2015.
- [66] Ilya Belopolski, Kaustuv Manna, Daniel S. Sanchez, Guoqing Chang, Benedikt Ernst, Jiaxin Yin, Songtian S. Zhang, Tyler Cochran, Nana Shumiya, Hao Zheng, Bahadur Singh, Guang Bian, Daniel Multer, Maksim Litskevich, Xiaoting Zhou, Shin-Ming Huang, Baokai Wang, Tay-Rong Chang, Su-Yang Xu, Arun Bansil, Claudia Felser, Hsin Lin, and M. Zahid Hasan. Discovery of topological Weyl fermion lines and drumhead surface states in a room temperature magnet. *Science*, 365(6459):1278, September 2019.
- [67] Adrien Bouhon, QuanSheng Wu, Robert-Jan Slager, Hongming Weng, Oleg V. Yazyev, and Tomáš Bzdušek. Non-Abelian reciprocal braiding of Weyl points and its manifestation in ZrTe . *Nature Physics*, 16(11):1137–1143, 2020.
- [68] Shuo-Ying Yang, Hao Yang, Elena Derunova, Stuart S. P. Parkin, Binghai Yan, and Mazhar N. Ali. Symmetry demanded topological nodal-line materials. *Advances in Physics: X*, 3(1):1414631, January 2018.
- [69] Junjie He, Xiao Li, Pengbo Lyu, and Petr Nachtigall. Near-room-temperature Chern insulator and Dirac spin-gapless semiconductor: nickel chloride monolayer. *Nanoscale*, 9(6):2246–2252, 2017.
- [70] Hongming Weng, Yunye Liang, Qiunan Xu, Rui Yu, Zhong Fang, Xi Dai, and Yoshiyuki Kawazoe. Topological node-line semimetal in three-dimensional graphene networks. *Phys. Rev. B*, 92:045108, Jul 2015.
- [71] Andrei Bernevig, Hongming Weng, Zhong Fang, and Xi Dai. Recent Progress in the Study of Topological Semimetals. *J. Phys. Soc. Jpn.*, 87(4):041001, March 2018.
- [72] Su-Yang Xu, Ilya Belopolski, Nasser Alidoust, Madhab Neupane, Guang Bian, Chenglong Zhang, Raman Sankar, Guoqing Chang, Zhujun Yuan, Chi-Cheng Lee, Shin-Ming Huang, Hao Zheng, Jie Ma, Daniel S. Sanchez, BaoKai Wang, Arun Bansil, Fangcheng Chou, Pavel P. Shibayev, Hsin Lin, Shuang Jia, and M. Zahid Hasan. Discovery of a Weyl fermion semimetal and topological Fermi arcs. *Science*, 349(6248):613–617, 2015.
- [73] Hongming Weng, Chen Fang, Zhong Fang, B. Andrei Bernevig, and Xi Dai. Weyl semimetal phase in noncentrosymmetric transition-metal monophosphides. *Phys. Rev. X*, 5:011029, Mar 2015.

- [74] Zhijun Wang, Yan Sun, Xing-Qiu Chen, Cesare Franchini, Gang Xu, Hongming Weng, Xi Dai, and Zhong Fang. Dirac semimetal and topological phase transitions in $A_3\text{Bi}$ ($A = \text{Na, K, Rb}$). *Phys. Rev. B*, 85:195320, May 2012.
- [75] Zhijun Wang, Hongming Weng, Quansheng Wu, Xi Dai, and Zhong Fang. Three-dimensional Dirac semimetal and quantum transport in Cd_3As_2 . *Phys. Rev. B*, 88:125427, Sep 2013.
- [76] Z. K. Liu, B. Zhou, Y. Zhang, Z. J. Wang, H. M. Weng, D. Prabhakaran, S.-K. Mo, Z. X. Shen, Z. Fang, X. Dai, Z. Hussain, and Y. L. Chen. Discovery of a Three-Dimensional Topological Dirac Semimetal, Na_3Bi . *Science*, 343(6173):864, February 2014.
- [77] Chen Fang, Hongming Weng, Xi Dai, and Zhong Fang. Topological nodal line semimetals. *Chinese Physics B*, 25(11):117106, 2016.
- [78] Bo Peng, Ivona Bravić, Judith L. MacManus-Driscoll, and Bartomeu Monserrat. Topological semimetallic phase in PbO_2 promoted by temperature. *Phys. Rev. B*, 100:161101, Oct 2019.
- [79] B. Andrei Bernevig. It's been a Weyl coming. *Nat Phys*, 11(9):698–699, September 2015.
- [80] H.B. Nielsen and M. Ninomiya. Absence of neutrinos on a lattice. *Nuclear Physics B*, 185(1):20–40, 1981.
- [81] H.B. Nielsen and M. Ninomiya. Absence of neutrinos on a lattice. *Nuclear Physics B*, 193(1):173–194, 1981.
- [82] Xiangang Wan, Ari M. Turner, Ashvin Vishwanath, and Sergey Y. Savrasov. Topological semimetal and Fermi-arc surface states in the electronic structure of pyrochlore iridates. *Phys. Rev. B*, 83:205101, May 2011.
- [83] Gang Xu, Hongming Weng, Zhijun Wang, Xi Dai, and Zhong Fang. Chern Semimetal and the Quantized Anomalous Hall Effect in HgCr_2Se_4 . *Phys. Rev. Lett.*, 107:186806, Oct 2011.
- [84] Hongming Weng, Rui Yu, Xiao Hu, Xi Dai, and Zhong Fang. Quantum anomalous Hall effect and related topological electronic states. *Advances in Physics*, 64(3):227–282, May 2015.
- [85] Hongming Weng, Xi Dai, and Zhong Fang. Topological semimetals predicted from first-principles calculations. *Journal of Physics: Condensed Matter*, 28(30):303001, 2016.
- [86] Shin-Ming Huang, Su-Yang Xu, Ilya Belopolski, Chi-Cheng Lee, Guoqing Chang, BaoKai Wang, Nasser Alidoust, Guang Bian, Madhab Neupane, Chenglong Zhang, Shuang Jia, Arun Bansil, Hsin Lin, and M. Zahid Hasan. A Weyl Fermion semimetal with surface Fermi arcs in the transition metal monpnictide TaAs class. *Nat Commun*, 6:7373, June 2015.

- [87] Yan Sun, Shu-Chun Wu, and Binghai Yan. Topological surface states and Fermi arcs of the noncentrosymmetric Weyl semimetals TaAs, TaP, NbAs, and NbP. *Phys. Rev. B*, 92:115428, Sep 2015.
- [88] B. Q. Lv, H. M. Weng, B. B. Fu, X. P. Wang, H. Miao, J. Ma, P. Richard, X. C. Huang, L. X. Zhao, G. F. Chen, Z. Fang, X. Dai, T. Qian, and H. Ding. Experimental Discovery of Weyl Semimetal TaAs. *Phys. Rev. X*, 5:031013, Jul 2015.
- [89] L. X. Yang, Z. K. Liu, Y. Sun, H. Peng, H. F. Yang, T. Zhang, B. Zhou, Y. Zhang, Y. F. Guo, M. Rahn, D. Prabhakaran, Z. Hussain, S.-K. Mo, C. Felser, B. Yan, and Y. L. Chen. Weyl semimetal phase in the non-centrosymmetric compound TaAs. *Nat Phys*, 11(9):728–732, September 2015.
- [90] B. Q. Lv, N. Xu, H. M. Weng, J. Z. Ma, P. Richard, X. C. Huang, L. X. Zhao, G. F. Chen, C. E. Matt, F. Bisti, V. N. Strocov, J. Mesot, Z. Fang, X. Dai, T. Qian, M. Shi, and H. Ding. Observation of Weyl nodes in TaAs. *Nat Phys*, 11(9):724–727, September 2015.
- [91] Zhilin Li, Hongxiang Chen, Shifeng Jin, Di Gan, Wenjun Wang, Liwei Guo, and Xiaolong Chen. Weyl Semimetal TaAs: Crystal Growth, Morphology, and Thermodynamics. *Crystal Growth & Design*, 16(3):1172–1175, March 2016.
- [92] Xiaochun Huang, Lingxiao Zhao, Yujia Long, Peipei Wang, Dong Chen, Zhanhai Yang, Hui Liang, Mianqi Xue, Hongming Weng, Zhong Fang, Xi Dai, and Genfu Chen. Observation of the Chiral-Anomaly-Induced Negative Magnetoresistance in 3D Weyl Semimetal TaAs. *Phys. Rev. X*, 5:031023, Aug 2015.
- [93] Cheng-Long Zhang, Su-Yang Xu, Ilya Belopolski, Zhujun Yuan, Ziquan Lin, Bingbing Tong, Guang Bian, Nasser Alidoust, Chi-Cheng Lee, Shin-Ming Huang, Tay-Rong Chang, Guoqing Chang, Chuang-Han Hsu, Horng-Tay Jeng, Madhab Neupane, Daniel S. Sanchez, Hao Zheng, Junfeng Wang, Hsin Lin, Chi Zhang, Hai-Zhou Lu, Shun-Qing Shen, Titus Neupert, M. Zahid Hasan, and Shuang Jia. Signatures of the Adler-Bell-Jackiw chiral anomaly in a Weyl fermion semimetal. *Nat Commun*, 7:10735, February 2016.
- [94] Chenglong Zhang, Zhujun Yuan, Suyang Xu, Ziquan Lin, Bingbing Tong, M Zahid Hasan, Junfeng Wang, Chi Zhang, and Shuang Jia. Tantalum monoarsenide: an exotic compensated semimetal. *arXiv*:, 1502:00251, 2015.
- [95] Bo Peng, Hao Zhang, Hezhu Shao, Hongliang Lu, David Wei Zhang, and Heyuan Zhu. High thermoelectric performance of Weyl semimetal TaAs. *Nano Energy*, 30:225–234, 2016.
- [96] Bohm-Jung Yang and Naoto Nagaosa. Classification of stable three-dimensional Dirac semimetals with nontrivial topology. *Nat Commun*, 5:4898, September 2014.
- [97] Z. K. Liu, J. Jiang, B. Zhou, Z. J. Wang, Y. Zhang, H. M. Weng, D. Prabhakaran, S.-K. Mo, H. Peng, P. Dudin, T. Kim, M. Hoesch, Z. Fang, X. Dai, Z. X. Shen, D. L. Feng, Z. Hussain, and Y. L. Chen. A stable three-dimensional topological Dirac semimetal Cd₃As₂. *Nat Mater*, 13(7):677–681, July 2014.

- [98] Sergey Borisenko, Quinn Gibson, Danil Evtushinsky, Volodymyr Zabolotnyy, Bernd Büchner, and Robert J. Cava. Experimental Realization of a Three-Dimensional Dirac Semimetal. *Phys. Rev. Lett.*, 113:027603, Jul 2014.
- [99] Sangjun Jeon, Brian B. Zhou, Andras Gyenis, Benjamin E. Feldman, Itamar Kimchi, Andrew C. Potter, Quinn D. Gibson, Robert J. Cava, Ashvin Vishwanath, and Ali Yazdani. Landau quantization and quasiparticle interference in the three-dimensional Dirac-semimetal Cd_3As_2 . *Nat Mater*, 13(9):851–856, September 2014.
- [100] Madhab Neupane, Su-Yang Xu, Raman Sankar, Nasser Alidoust, Guang Bian, Chang Liu, Ilya Belopolski, Tay-Rong Chang, Horng-Tay Jeng, Hsin Lin, Arun Bansil, Fangcheng Chou, and M. Zahid Hasan. Observation of a three-dimensional topological Dirac semimetal phase in high-mobility Cd_3As_2 . *Nat Commun*, 5:3786, May 2014.
- [101] Bo Peng, Changming Yue, Hao Zhang, Zhong Fang, and Hongming Weng. Predicting Dirac semimetals based on sodium ternary compounds. *npj Computational Materials*, 4(1):68, 2018.
- [102] Takahiro Yamada, Takuji Ikeda, Ralf P. Stoffel, Volker L. Deringer, Richard Dronskowski, and Hisanori Yamane. Synthesis, Crystal Structure, and High-Temperature Phase Transition of the Novel Plumbide Na_2MgPb . *Inorg. Chem.*, 53(10):5253–5259, May 2014.
- [103] H. Matthes, R. & Schuster. Ternary Sodium Phases with Cadmium or Mercury and Tin or Lead. *Zeitschrift für Naturforschung B*, 35(6):778–780, 1980.
- [104] G. Kresse and J. Furthmüller. Efficient iterative schemes for *ab initio* total-energy calculations using a plane-wave basis set. *Phys. Rev. B*, 54:11169–11186, Oct 1996.
- [105] G. Kresse and J. Furthmüller. Efficiency of ab-initio total energy calculations for metals and semiconductors using a plane-wave basis set. *Computational Materials Science*, 6(1):15 – 50, 1996.
- [106] Jochen Heyd, Gustavo E. Scuseria, and Matthias Ernzerhof. Hybrid functionals based on a screened Coulomb potential. *J. Chem. Phys.*, 118:8207, 2003.
- [107] Jochen Heyd, Gustavo E. Scuseria, and Matthias Ernzerhof. Erratum: “Hybrid functionals based on a screened Coulomb potential” [J. Chem. Phys.118, 8207 (2003)]. *J. Chem. Phys.*, 124:219906, 2006.
- [108] Juan E. Peralta, Jochen Heyd, Gustavo E. Scuseria, and Richard L. Martin. Spin-orbit splittings and energy band gaps calculated with the Heyd-Scuseria-Ernzerhof screened hybrid functional. *Phys. Rev. B*, 74:073101, Aug 2006.
- [109] John P. Perdew, Kieron Burke, and Matthias Ernzerhof. Generalized gradient approximation made simple. *Phys. Rev. Lett.*, 77:3865–3868, Oct 1996.
- [110] Wei Zhang, Rui Yu, Hai-Jun Zhang, Xi Dai, and Zhong Fang. First-principles studies of the three-dimensional strong topological insulators Bi_2Te_3 , Bi_2Se_3 and Sb_2Te_3 . *New Journal of Physics*, 12(6):065013, 2010.

- [111] Jonathan H. Lloyd-Williams and Bartomeu Monserrat. Lattice dynamics and electron-phonon coupling calculations using nondiagonal supercells. *Phys. Rev. B*, 92:184301, Nov 2015.
- [112] Bartomeu Monserrat. Vibrational averages along thermal lines. *Phys. Rev. B*, 93:014302, Jan 2016.
- [113] Bartomeu Monserrat. Correlation effects on electron-phonon coupling in semiconductors: Many-body theory along thermal lines. *Phys. Rev. B*, 93:100301, Mar 2016.
- [114] J. P. Carr and N. A. Hampson. Lead dioxide electrode. *Chem. Rev.*, 72(6):679–703, December 1972.
- [115] Wei Wang, Linjie Deng, Na Jiao, Pan Zhou, and Lizhong Sun. Three-Dimensional Dirac Semimetal β -PbO₂. *Phys. Status Solidi RRL*, 11(10):1700271, October 2017.
- [116] Tong Chen, Dexi Shao, Pengchao Lu, Xiaomeng Wang, Juefei Wu, Jian Sun, and Dingyu Xing. Anharmonic effect driven topological phase transition in PbO₂ predicted by first-principles calculations. *Phys. Rev. B*, 98:144105, Oct 2018.
- [117] Lucia Burgio, Robin J. H. Clark, and Steven Firth. Raman spectroscopy as a means for the identification of plattnerite (PbO₂), of lead pigments and of their degradation products. *Analyst*, 126(2):222–227, 2001.
- [118] David O. Scanlon, Aoife B. Kehoe, Graeme W. Watson, Martin O. Jones, William I. F. David, David J. Payne, Russell G. Egdell, Peter P. Edwards, and Aron Walsh. Nature of the Band Gap and Origin of the Conductivity of PbO₂ Revealed by Theory and Experiment. *Phys. Rev. Lett.*, 107:246402, Dec 2011.
- [119] H. Harada, Y. Sasa, and M. Uda. Crystal data for β -PbO₂. *Journal of Applied Crystallography*, 14(2):141–142, Apr 1981.
- [120] D.J. Payne, G. Paolicelli, F. Offi, G. Panaccione, P. Lacovig, G. Beamson, A. Fondacaro, G. Monaco, G. Vanko, and R.G. Egdell. A study of core and valence levels in β -PbO₂ by hard X-ray photoemission. *Journal of Electron Spectroscopy and Related Phenomena*, 169(1):26–34, 2009.
- [121] Zhenwei Wang and Guangtao Wang. A new strongly topological node-line semimetal β -PbO₂. *Physics Letters A*, 381(34):2856–2859, 2017.
- [122] David J. Payne, Russell G. Egdell, Danny S. L. Law, Per-Anders Glans, Timothy Learmonth, Kevin E. Smith, Jinghua Guo, Aron Walsh, and Graeme W. Watson. Experimental and theoretical study of the electronic structures of α -PbO and α -PbO₂. *J. Mater. Chem.*, 17(3):267–277, 2007.
- [123] Fengxian Ma, Yalong Jiao, Guoping Gao, Yuantong Gu, Ante Bilic, Stefano Sanvito, and Aijun Du. Substantial Band-Gap Tuning and a Strain-Controlled Semiconductor to Gapless/Band-Inverted Semimetal Transition in Rutile Lead/Stannic Dioxide. *ACS Appl. Mater. Interfaces*, 8(39):25667–25673, October 2016.
- [124] Rokyoon Kim, Bohm-Jung Yang, and Choong H. Kim. Crystalline topological Dirac semimetal phase in rutile structure β' -PtO₂. *Phys. Rev. B*, 99:045130, Jan 2019.

- [125] Guang Bian, Tay-Rong Chang, Raman Sankar, Su-Yang Xu, Hao Zheng, Titus Neupert, Ching-Kai Chiu, Shin-Ming Huang, Guoqing Chang, Ilya Belopolski, Daniel S. Sanchez, Madhab Neupane, Nasser Alidoust, Chang Liu, BaoKai Wang, Chi-Cheng Lee, Horng-Tay Jeng, Chenglong Zhang, Zhujun Yuan, Shuang Jia, Arun Bansil, Fangcheng Chou, Hsin Lin, and M. Zahid Hasan. Topological nodal-line fermions in spin-orbit metal PbTaSe_2 . *Nature Communications*, 7:10556, February 2016.
- [126] N. B. Kopnin, T. T. Heikkilä, and G. E. Volovik. High-temperature surface superconductivity in topological flat-band systems. *Phys. Rev. B*, 83:220503, Jun 2011.
- [127] Bartomeu Monserrat, G. J. Conduit, and R. J. Needs. Extracting semiconductor band gap zero-point corrections from experimental data. *Phys. Rev. B*, 90:184302, Nov 2014.
- [128] Julia Wittkamper, Zhongnan Xu, Boopathy Kombaiyah, Farangis Ram, Marc De Graef, John R. Kitchin, Gregory S. Rohrer, and Paul A. Salvador. Competitive Growth of Scrutinyite ($\alpha\text{-PbO}_2$) and Rutile Polymorphs of SnO_2 on All Orientations of Columbite CoNb_2O_6 Substrates. *Crystal Growth & Design*, 17(7):3929–3939, July 2017.
- [129] Y. L. Chen, J. G. Analytis, J.-H. Chu, Z. K. Liu, S.-K. Mo, X. L. Qi, H. J. Zhang, D. H. Lu, X. Dai, Z. Fang, S. C. Zhang, I. R. Fisher, Z. Hussain, and Z.-X. Shen. Experimental Realization of a Three-Dimensional Topological Insulator, Bi_2Te_3 . *Science*, 325(5937):178, July 2009.
- [130] Rui Lou, Pengjie Guo, Man Li, Qi Wang, Zhonghao Liu, Shanshan Sun, Chenghe Li, Xuchuan Wu, Zilu Wang, Zhe Sun, Dawei Shen, Yaobo Huang, Kai Liu, Zhong-Yi Lu, Hechang Lei, Hong Ding, and Shancai Wang. Experimental observation of bulk nodal lines and electronic surface states in ZrB_2 . *npj Quantum Materials*, 3(1):43, 2018.
- [131] Olaf Stenull, C. L. Kane, and T. C. Lubensky. Topological Phonons and Weyl Lines in Three Dimensions. *Phys. Rev. Lett.*, 117:068001, Aug 2016.
- [132] Yizhou Liu, Yong Xu, Shou-Cheng Zhang, and Wenhui Duan. Model for topological phononics and phonon diode. *Phys. Rev. B*, 96:064106, Aug 2017.
- [133] Tiantian Zhang, Zhida Song, A. Alexandradinata, Hongming Weng, Chen Fang, Ling Lu, and Zhong Fang. Phonons in Transition-Metal Monosilicides. *Phys. Rev. Lett.*, 120:016401, Jan 2018.
- [134] Hailong He, Chunyin Qiu, Liping Ye, Xiangxi Cai, Xiyang Fan, Manzhu Ke, Fan Zhang, and Zhengyou Liu. Topological negative refraction of surface acoustic waves in a Weyl phononic crystal. *Nature*, 560(7716):61–64, 2018.
- [135] Jiangxu Li, Jiayi Liu, Stanley A. Baronett, Mingfeng Liu, Lei Wang, Ronghan Li, Yun Chen, Dianzhong Li, Qiang Zhu, and Xing-Qiu Chen. Computation and data driven discovery of topological phononic materials. *Nature Communications*, 12(1):1204, 2021.
- [136] Hongwei Jia, Ruixing Zhang, Wenlong Gao, Qinghua Guo, Biao Yang, Jing Hu, Yangang Bi, Yuanjiang Xiang, Chaoping Liu, and Shuang Zhang. Observation of chiral zero mode in inhomogeneous three-dimensional Weyl metamaterials. *Science*, 363(6423):148, January 2019.

- [137] Fei-Ye Li, Yao-Dong Li, Yong Baek Kim, Leon Balents, Yue Yu, and Gang Chen. Weyl magnons in breathing pyrochlore antiferromagnets. *Nature Communications*, 7(1):12691, 2016.
- [138] Fengcheng Wu, Timothy Lovorn, and A. H. MacDonald. Topological Exciton Bands in Moiré Heterojunctions. *Phys. Rev. Lett.*, 118:147401, Apr 2017.
- [139] A. P. Drozdov, M. I. Eremets, I. A. Troyan, V. Ksenofontov, and S. I. Shylin. Conventional superconductivity at 203 kelvin at high pressures in the sulfur hydride system. *Nature*, 525(7567):73–76, 2015.
- [140] Kaveh Ahadi, Luca Galletti, Yuntian Li, Salva Salmani-Rezaie, Wangzhou Wu, and Susanne Stemmer. Enhancing superconductivity in SrTiO₃ films with strain. *Sci Adv*, 5(4):eaaw0120, April 2019.
- [141] Bo Peng, Zeyu Ning, Hao Zhang, Hezhu Shao, Yuanfeng Xu, Gang Ni, and Heyuan Zhu. Beyond Perturbation: Role of Vacancy-Induced Localized Phonon States in Thermal Transport of Monolayer MoS₂. *J. Phys. Chem. C*, 120(51):29324–29331, December 2016.
- [142] Bo Peng, Hao Zhang, Hezhu Shao, Ke Xu, Gang Ni, Jing Li, Heyuan Zhu, and Costas M. Soukoulis. Chemical intuition for high thermoelectric performance in monolayer black phosphorus, α -arsenene and aW-antimonene. *J. Mater. Chem. A*, 6(5):2018–2033, 2018.
- [143] Bo Peng, Bohayra Mortazavi, Hao Zhang, Hezhu Shao, Ke Xu, Jing Li, Gang Ni, Timon Rabczuk, and Heyuan Zhu. Tuning Thermal Transport in C₃N Monolayers by Adding and Removing Carbon Atoms. *Phys. Rev. Applied*, 10:034046, Sep 2018.
- [144] Bo Peng, Haodong Mei, Hao Zhang, Hezhu Shao, Ke Xu, Gang Ni, Qingyuan Jin, Costas M. Soukoulis, and Heyuan Zhu. High thermoelectric efficiency in monolayer PbI₂ from 300 K to 900 K. *Inorg. Chem. Front.*, 6(4):920–928, 2019.
- [145] Marco Bernardi, Derek Vigil-Fowler, Johannes Lischner, Jeffrey B. Neaton, and Steven G. Louie. Ab initio study of hot carriers in the first picosecond after sunlight absorption in silicon. *Phys. Rev. Lett.*, 112:257402, Jun 2014.
- [146] Ziqi Li, Bo Peng, Miao-Ling Lin, Yu-Chen Leng, Bin Zhang, Chi Pang, Ping-Heng Tan, Bartomeu Monserrat, and Feng Chen. Phonon-assisted electronic states modulation of few-layer PdSe₂ at terahertz frequencies. *npj 2D Materials and Applications*, 5:87, 2021.
- [147] Bo Peng, Hao Zhang, Weiwen Chen, Bowen Hou, Zhi-Jun Qiu, Hezhu Shao, Heyuan Zhu, Bartomeu Monserrat, Desheng Fu, Hongming Weng, and Costas M. Soukoulis. Sub-picosecond photo-induced displacive phase transition in two-dimensional MoTe₂. *npj 2D Materials and Applications*, 4(1):14, 2020.
- [148] Fangyuan Gu, Éamonn Murray, and Paul Tangney. Carrier-mediated control over the soft mode and ferroelectricity in BaTiO₃. *Phys. Rev. Materials*, 5:034414, Mar 2021.

- [149] Heather M. Hill, Sugata Chowdhury, Jeffrey R. Simpson, Albert F. Rigosi, David B. Newell, Helmuth Berger, Francesca Tavazza, and Angela R. Hight Walker. Phonon origin and lattice evolution in charge density wave states. *Phys. Rev. B*, 99:174110, May 2019.
- [150] Li Yue, Shangjie Xue, Jiarui Li, Wen Hu, Andi Barbour, Feipeng Zheng, Lichen Wang, Ji Feng, Stuart B. Wilkins, Claudio Mazzoli, Riccardo Comin, and Yuan Li. Distinction between pristine and disorder-perturbed charge density waves in ZrTe_3 . *Nature Communications*, 11(1):98, 2020.
- [151] T. T. Zhang, H. Miao, Q. Wang, J. Q. Lin, Y. Cao, G. Fabbris, A. H. Said, X. Liu, H. C. Lei, Z. Fang, H. M. Weng, and M. P. M. Dean. Phononic Helical Nodal Lines with \mathcal{PT} Protection in MoB_2 . *Phys. Rev. Lett.*, 123:245302, Dec 2019.
- [152] Xing He, Dipanshu Bansal, Barry Winn, Songxue Chi, Lynn Boatner, and Olivier Delaire. Anharmonic Eigenvectors and Acoustic Phonon Disappearance in Quantum Paraelectric SrTiO_3 . *Phys. Rev. Lett.*, 124:145901, Apr 2020.
- [153] Narayani Choudhury, Eric J. Walter, Alexander I. Kolesnikov, and Chun-Keung Loong. Large phonon band gap in SrTiO_3 and the vibrational signatures of ferroelectricity in ATiO_3 perovskites: First-principles lattice dynamics and inelastic neutron scattering. *Phys. Rev. B*, 77:134111, Apr 2008.
- [154] H. Miao, T. T. Zhang, L. Wang, D. Meyers, A. H. Said, Y. L. Wang, Y. G. Shi, H. M. Weng, Z. Fang, and M. P. M. Dean. Observation of Double Weyl Phonons in Parity-Breaking FeSi . *Phys. Rev. Lett.*, 121:035302, Jul 2018.
- [155] Zhida Song, Tiantian Zhang, and Chen Fang. Diagnosis for nonmagnetic topological semimetals in the absence of spin-orbital coupling. *Phys. Rev. X*, 8:031069, Sep 2018.
- [156] Tiantian Zhang, Ling Lu, Shuichi Murakami, Zhong Fang, Hongming Weng, and Chen Fang. Diagnosis scheme for topological degeneracies crossing high-symmetry lines. *Phys. Rev. Research*, 2:022066, Jun 2020.
- [157] Jiangxu Li, Qing Xie, Sami Ullah, Ronghan Li, Hui Ma, Dianzhong Li, Yiyi Li, and Xing-Qiu Chen. Coexistent three-component and two-component Weyl phonons in TiS , ZrSe , and HfTe . *Phys. Rev. B*, 97:054305, Feb 2018.
- [158] B. W. Xia, R. Wang, Z. J. Chen, Y. J. Zhao, and H. Xu. Symmetry-Protected Ideal Type-II Weyl Phonons in CdTe . *Phys. Rev. Lett.*, 123:065501, Aug 2019.
- [159] Bo Peng, Yuchen Hu, Shuichi Murakami, Tiantian Zhang, and Bartomeu Monserrat. Topological phonons in oxide perovskites controlled by light. *Sci Adv*, 6(46):eabd1618, November 2020.
- [160] Qing-Bo Liu, Yuting Qian, Hua-Hua Fu, and Zhijun Wang. Symmetry-enforced Weyl phonons. *npj Computational Materials*, 6(1):95, 2020.
- [161] Zhenwei Wang, Weiqing Zhou, A. N. Rudenko, and Shengjun Yuan. Lattice dynamics and topological surface phonon states in cuprous oxide Cu_2O . *Phys. Rev. B*, 103:195137, May 2021.

- [162] Dao-Sheng Tang and Bing-Yang Cao. Topological effects of phonons in GaN and AlGaN: A potential perspective for tuning phonon transport. *Journal of Applied Physics*, 129(8):085102, February 2021.
- [163] Qing-Bo Liu, Hua-Hua Fu, and Ruqian Wu. Topological phononic nodal hexahedron net and nodal links in the high-pressure phase of the semiconductor CuCl. *Phys. Rev. B*, 104:045409, Jul 2021.
- [164] Peng-Fei Liu, Jingyu Li, Xin-Hai Tu, Hang Li, Junrong Zhang, Ping Zhang, Qiang Gao, and Bao-Tian Wang. First-principles prediction of ideal type-II Weyl phonons in wurtzite ZnSe. *Phys. Rev. B*, 103:094306, Mar 2021.
- [165] Qing-Bo Liu, Zhe-Qi Wang, and Hua-Hua Fu. Ideal topological nodal-surface phonons in RbTeAu-family materials. *Phys. Rev. B*, 104:L041405, Jul 2021.
- [166] Jing-Yang You, Xian-Lei Sheng, and Gang Su. Topological gimbal phonons in *t*-carbon. *Phys. Rev. B*, 103:165143, Apr 2021.
- [167] Chengwu Xie, Ying Liu, Zeying Zhang, Feng Zhou, Tie Yang, Minquan Kuang, Xiaotian Wang, and Gang Zhang. Sixfold degenerate nodal-point phonons: Symmetry analysis and materials realization. *Phys. Rev. B*, 104:045148, Jul 2021.
- [168] Baobing Zheng, Fangyang Zhan, Xiaozhi Wu, Rui Wang, and Jing Fan. Hourglass phonons jointly protected by symmorphic and nonsymmorphic symmetries. *Phys. Rev. B*, 104:L060301, Aug 2021.
- [169] Jianhua Wang, Hongkuan Yuan, Minquan Kuang, Tie Yang, Zhi-Ming Yu, Zeying Zhang, and Xiaotian Wang. Coexistence of zero-, one-, and two-dimensional degeneracy in tetragonal SnO₂ phonons. *Phys. Rev. B*, 104:L041107, Jul 2021.
- [170] Ronald E. Cohen. Origin of ferroelectricity in perovskite oxides. *Nature*, 358(6382):136–138, 1992.
- [171] Y. Moritomo, H. Kuwahara, Y. Tomioka, and Y. Tokura. Pressure effects on charge-ordering transitions in perovskite manganites. *Phys. Rev. B*, 55:7549–7556, Mar 1997.
- [172] Y. Nahas, S. Prokhorenko, L. Louis, Z. Gui, I. Kornev, and L. Bellaiche. Discovery of stable skyrmionic state in ferroelectric nanocomposites. *Nature Communications*, 6(1):8542, 2015.
- [173] S. Das, Y. L. Tang, Z. Hong, M. A. P. Goncalves, M. R. McCarter, C. Klewe, K. X. Nguyen, F. Gómez-Ortiz, P. Shafer, E. Arenholz, V. A. Stoica, S.-L. Hsu, B. Wang, C. Ophus, J. F. Liu, C. T. Nelson, S. Saremi, B. Prasad, A. B. Mei, D. G. Schlom, J. Íñiguez, P. García-Fernández, D. A. Muller, L. Q. Chen, J. Junquera, L. W. Martin, and R. Ramesh. Observation of room-temperature polar skyrmions. *Nature*, 568(7752):368–372, 2019.
- [174] A. Mahmoud, A. Erba, Kh. E. El-Kelany, M. Rérat, and R. Orlando. Low-temperature phase of BaTiO₃: Piezoelectric, dielectric, elastic, and photoelastic properties from ab initio simulations. *Phys. Rev. B*, 89:045103, Jan 2014.

- [175] K. H. Ahn, T. Lookman, and A. R. Bishop. Strain-induced metal-insulator phase coexistence in perovskite manganites. *Nature*, 428(6981):401–404, 2004.
- [176] Yuichi Shirako, Hiroshi Kojitani, Masaki Akaogi, Kazunari Yamaura, and Eiji Takayama-Muromachi. High-pressure phase transitions of CaRhO_3 perovskite. *Physics and Chemistry of Minerals*, 36(8):455, 2009.
- [177] Leonid L. Rusevich, Guntars Zvejnieks, Eugene A. Kotomin, Marjeta Macek Krzmann, Anton Meden, Spela Kunej, and Ioana D. Vlaicu. Theoretical and Experimental Study of $(\text{Ba,Sr})\text{TiO}_3$ Perovskite Solid Solutions and $\text{BaTiO}_3/\text{SrTiO}_3$ Heterostructures. *J. Phys. Chem. C*, 123(4):2031–2036, January 2019.
- [178] Charles Paillard, Engin Torun, Ludger Wirtz, Jorge Íñiguez, and Laurent Bellaiche. Photoinduced phase transitions in ferroelectrics. *Phys. Rev. Lett.*, 123:087601, Aug 2019.
- [179] T. F. Nova, A. S. Disa, M. Fechner, and A. Cavalleri. Metastable ferroelectricity in optically strained SrTiO_3 . *Science*, 364(6445):1075, June 2019.
- [180] Youngjun Ahn, Anastasios Pateras, Samuel D. Marks, Han Xu, Tao Zhou, Zhenlin Luo, Zuhuang Chen, Lang Chen, Xiaoyi Zhang, Anthony D. DiChiara, Haidan Wen, and Paul G. Evans. Nanosecond Optically Induced Phase Transformation in Compressively Strained BiFeO_3 on LaAlO_3 . *Phys. Rev. Lett.*, 123:045703, Jul 2019.
- [181] M. Porer, M. Fechner, M. Kubli, M. J. Neugebauer, S. Parchenko, V. Esposito, A. Narayan, N. A. Spaldin, R. Huber, M. Radovic, E. M. Bothschafter, J. M. Glowia, T. Sato, S. Song, S. L. Johnson, and U. Staub. Ultrafast transient increase of oxygen octahedral rotations in a perovskite. *Phys. Rev. Research*, 1:012005, Aug 2019.
- [182] D. M. Juraschek, M. Fechner, and N. A. Spaldin. Ultrafast structure switching through nonlinear phononics. *Phys. Rev. Lett.*, 118:054101, Jan 2017.
- [183] John P. Perdew, Adrienn Ruzsinszky, Gábor I. Csonka, Oleg A. Vydrov, Gustavo E. Scuseria, Lucian A. Constantin, Xiaolan Zhou, and Kieron Burke. Restoring the Density-Gradient Expansion for Exchange in Solids and Surfaces. *Phys. Rev. Lett.*, 100:136406, Apr 2008.
- [184] R. O. Jones and O. Gunnarsson. The density functional formalism, its applications and prospects. *Rev. Mod. Phys.*, 61:689–746, Jul 1989.
- [185] Andreas Görling. Density-functional theory for excited states. *Phys. Rev. A*, 54:3912–3915, Nov 1996.
- [186] A. Hellman, B. Razaznejad, and B. I. Lundqvist. Potential-energy surfaces for excited states in extended systems. *J. Chem. Phys.*, 120(10):4593–4602, March 2004.
- [187] Francesco Mauri and Roberto Car. First-principles study of excitonic self-trapping in diamond. *Phys. Rev. Lett.*, 75:3166–3169, Oct 1995.
- [188] Sohrab Ismail-Beigi and Steven G. Louie. Excited-State Forces within a First-Principles Green’s Function Formalism. *Phys. Rev. Lett.*, 90:076401, Feb 2003.

- [189] Alexey A. Soluyanov and David Vanderbilt. Computing topological invariants without inversion symmetry. *Phys. Rev. B*, 83:235401, Jun 2011.
- [190] Rui Yu, Xiao Liang Qi, Andrei Bernevig, Zhong Fang, and Xi Dai. Equivalent expression of \mathbb{Z}_2 topological invariant for band insulators using the non-Abelian Berry connection. *Phys. Rev. B*, 84:075119, Aug 2011.
- [191] P. Souvatzis, O. Eriksson, M. I. Katsnelson, and S. P. Rudin. Entropy driven stabilization of energetically unstable crystal structures explained from first principles theory. *Phys. Rev. Lett.*, 100:095901, Mar 2008.
- [192] Bo Cai, Xi Chen, Meiqiu Xie, Shengli Zhang, Xuhai Liu, Jinlong Yang, Wenhan Zhou, Shiyang Guo, and Haibo Zeng. A class of Pb-free double perovskite halide semiconductors with intrinsic ferromagnetism, large spin splitting and high Curie temperature. *Mater. Horiz.*, 5(5):961–968, 2018.
- [193] M. Gajdoš, K. Hummer, G. Kresse, J. Furthmüller, and F. Bechstedt. Linear optical properties in the projector-augmented wave methodology. *Phys. Rev. B*, 73:045112, Jan 2006.
- [194] H. F. KAY and R. G. RHODES. Barium titanate crystals. *Nature*, 160(4056):126–127, 1947.
- [195] W. Zhong, R. D. King-Smith, and David Vanderbilt. Giant LO-TO splittings in perovskite ferroelectrics. *Phys. Rev. Lett.*, 72:3618–3621, May 1994.
- [196] Oswaldo Diéguez, Karin M. Rabe, and David Vanderbilt. First-principles study of epitaxial strain in perovskites. *Phys. Rev. B*, 72:144101, Oct 2005.
- [197] Lihong Ni, Yong Liu, Chenlu Song, Wei Wang, Gaorong Han, and Yankai Ge. First-principle study of strain-driven phase transition in incipient ferroelectric SrTiO₃. *Physica B: Condensed Matter*, 406(21):4145–4149, 2011.
- [198] Xun Jia, Shuyuan Zhang, Raman Sankar, Fang-Cheng Chou, Weihua Wang, K. Kempa, E. W. Plummer, Jiandi Zhang, Xuetao Zhu, and Jiandong Guo. Anomalous acoustic plasmon mode from topologically protected states. *Phys. Rev. Lett.*, 119:136805, Sep 2017.
- [199] Yi-feng Yang, Guang-Ming Zhang, and Fu-Chun Zhang. Universal Behavior of the Thermal Hall Conductivity. *Phys. Rev. Lett.*, 124:186602, May 2020.
- [200] Xiaokang Li, Benoît Fauqué, Zengwei Zhu, and Kamran Behnia. Phonon Thermal Hall Effect in Strontium Titanate. *Phys. Rev. Lett.*, 124:105901, Mar 2020.
- [201] Wei Luo, Junyi Ji, Peng Chen, Yang Xu, Lifa Zhang, Hongjun Xiang, and Laurent Bellaïche. Nonlinear phonon hall effects in ferroelectrics: Existence and nonvolatile electrical control. *Phys. Rev. B*, 107:L241107, Jun 2023.
- [202] J. J. Lee, F. T. Schmitt, R. G. Moore, S. Johnston, Y.-T. Cui, W. Li, M. Yi, Z. K. Liu, M. Hashimoto, Y. Zhang, D. H. Lu, T. P. Devereaux, D.-H. Lee, and Z.-X. Shen. Interfacial mode coupling as the origin of the enhancement of T_c in FeSe films on SrTiO₃. *Nature*, 515(7526):245–248, 2014.

- [203] Sthitadhi Roy, Michael Kolodrubetz, Nathan Goldman, and Adolfo G Grushin. Tunable axial gauge fields in engineered Weyl semimetals: semiclassical analysis and optical lattice implementations. *2D Materials*, 5(2):024001, 2018.
- [204] Valerio Peri, Marc Serra-Garcia, Roni Ilan, and Sebastian D. Huber. Axial-field-induced chiral channels in an acoustic Weyl system. *Nature Physics*, 15(4):357–361, 2019.
- [205] Jeongwoo Kim, Kyoung-Whan Kim, Dongbin Shin, Sang-Hoon Lee, Jairo Sinova, Noejung Park, and Hosub Jin. Prediction of ferroelectricity-driven berry curvature enabling charge- and spin-controllable photocurrent in tin telluride monolayers. *Nature Communications*, 10(1):3965, 2019.
- [206] P. O. Sukhachov and H. Rostami. Acoustogalvanic Effect in Dirac and Weyl Semimetals. *Phys. Rev. Lett.*, 124:126602, Mar 2020.
- [207] Nikolaos Farmakidis, Nathan Youngblood, Xuan Li, James Tan, Jacob L. Swett, Zengguang Cheng, C. David Wright, Wolfram H. P. Pernice, and Harish Bhaskaran. Plasmonic nanogap enhanced phase-change devices with dual electrical-optical functionality. *Sci Adv*, 5(11):eaaw2687, November 2019.
- [208] J. Feldmann, N. Youngblood, C. D. Wright, H. Bhaskaran, and W. H. P. Pernice. All-optical spiking neurosynaptic networks with self-learning capabilities. *Nature*, 569(7755):208–214, 2019.
- [209] K. S. Novoselov, A. K. Geim, S. V. Morozov, D. Jiang, Y. Zhang, S. V. Dubonos, I. V. Grigorieva, and A. A. Firsov. Electric Field Effect in Atomically Thin Carbon Films. *Science*, 306(5696):666, October 2004.
- [210] Yuanbo Zhang, Yan-Wen Tan, Horst L. Stormer, and Philip Kim. Experimental observation of the quantum Hall effect and Berry’s phase in graphene. *Nature*, 438(7065):201–204, November 2005.
- [211] N. P. Armitage, E. J. Mele, and Ashvin Vishwanath. Weyl and Dirac semimetals in three-dimensional solids. *Rev. Mod. Phys.*, 90:015001, Jan 2018.
- [212] Chen Fang, Yige Chen, Hae-Young Kee, and Liang Fu. Topological nodal line semimetals with and without spin-orbital coupling. *Phys. Rev. B*, 92:081201, Aug 2015.
- [213] Rui Yu, Hongming Weng, Zhong Fang, Xi Dai, and Xiao Hu. Topological Node-Line Semimetal and Dirac Semimetal State in Antiperovskite Cu_3PdN . *Phys. Rev. Lett.*, 115:036807, Jul 2015.
- [214] Tomas Bzdusek, QuanSheng Wu, Andreas Ruegg, Manfred Sigrist, and Alexey A. Soluyanov. Nodal-chain metals. *Nature*, 538(7623):75–78, 2016.
- [215] Huaqing Huang, Jianpeng Liu, David Vanderbilt, and Wenhui Duan. Topological nodal-line semimetals in alkaline-earth stannides, germanides, and silicides. *Phys. Rev. B*, 93:201114, May 2016.

- [216] Jin Hu, Zhijie Tang, Jinyu Liu, Xue Liu, Yanglin Zhu, David Graf, Kevin Myhro, Son Tran, Chun Ning Lau, Jiang Wei, and Zhiqiang Mao. Evidence of Topological Nodal-Line Fermions in ZrSiSe and ZrSiTe. *Phys. Rev. Lett.*, 117:016602, Jun 2016.
- [217] Jinling Lian, Lixian Yu, Qi-Feng Liang, Jian Zhou, Rui Yu, and Hongming Weng. Multi-loop node line states in ternary MgSrSi-type crystals. *npj Computational Materials*, 5(1):10, 2019.
- [218] Tiantian Zhang, Yi Jiang, Zhida Song, He Huang, Yuqing He, Zhong Fang, Hongming Weng, and Chen Fang. Catalogue of topological electronic materials. *Nature*, 566(7745):475–479, 2019.
- [219] Feng Tang, Hoi Chun Po, Ashvin Vishwanath, and Xiangang Wan. Comprehensive search for topological materials using symmetry indicators. *Nature*, 566(7745):486–489, 2019.
- [220] M. G. Vergniory, L. Elcoro, Claudia Felser, Nicolas Regnault, B. Andrei Bernevig, and Zhijun Wang. A complete catalogue of high-quality topological materials. *Nature*, 566(7745):480–485, 2019.
- [221] Ke Deng, Guoliang Wan, Peng Deng, Kenan Zhang, Shijie Ding, Eryin Wang, Mingzhe Yan, Huaqing Huang, Hongyun Zhang, Zhilin Xu, Jonathan Denlinger, Alexei Fedorov, Haitao Yang, Wenhui Duan, Hong Yao, Yang Wu, Shoushan Fan, Haijun Zhang, Xi Chen, and Shuyun Zhou. Experimental observation of topological Fermi arcs in type-II Weyl semimetal MoTe₂. *Nature Physics*, 12:1105, September 2016.
- [222] A. Tamai, Q. S. Wu, I. Cucchi, F. Y. Bruno, S. Riccò, T. K. Kim, M. Hoesch, C. Barreteau, E. Giannini, C. Besnard, A. A. Soluyanov, and F. Baumberger. Fermi Arcs and Their Topological Character in the Candidate Type-II Weyl Semimetal MoTe₂. *Phys. Rev. X*, 6:031021, Aug 2016.
- [223] Ryo Okugawa and Shuichi Murakami. Dispersion of Fermi arcs in Weyl semimetals and their evolutions to Dirac cones. *Phys. Rev. B*, 89:235315, Jun 2014.
- [224] Chen Fang, Ling Lu, Junwei Liu, and Liang Fu. Topological semimetals with helicoid surface states. *Nature Physics*, 12(10):936–941, 2016.
- [225] Liang Fu, C. L. Kane, and E. J. Mele. Topological insulators in three dimensions. *Phys. Rev. Lett.*, 98:106803, Mar 2007.
- [226] Haijun Zhang, Chao-Xing Liu, Xiao-Liang Qi, Xi Dai, Zhong Fang, and Shou-Cheng Zhang. Topological insulators in Bi₂Se₃, Bi₂Te₃ and Sb₂Te₃ with a single Dirac cone on the surface. *Nat Phys*, 5(6):438–442, June 2009.
- [227] P. Dziawa, B. J. Kowalski, K. Dybko, R. Buczko, A. Szczerbakow, M. Szot, E. Lusakowska, T. Balasubramanian, B. M. Wojek, M. H. Berntsen, O. Tjernberg, and T. Story. Topological crystalline insulator states in Pb_{1-x}Sn_xSe. *Nature Materials*, 11:1023, September 2012.

- [228] B. M. Wojek, M. H. Berntsen, V. Jonsson, A. Szczerbakow, P. Dziawa, B. J. Kowalski, T. Story, and O. Tjernberg. Direct observation and temperature control of the surface Dirac gap in a topological crystalline insulator. *Nature Communications*, 6:8463, October 2015.
- [229] Zhijun Wang, A. Alexandradinata, R. J. Cava, and B. Andrei Bernevig. Hourglass fermions. *Nature*, 532:189, April 2016.
- [230] A. Alexandradinata, Zhijun Wang, and B. Andrei Bernevig. Topological insulators from group cohomology. *Phys. Rev. X*, 6:021008, Apr 2016.
- [231] Motohiko Ezawa. Hourglass fermion surface states in stacked topological insulators with nonsymmorphic symmetry. *Phys. Rev. B*, 94:155148, Oct 2016.
- [232] Chin-Shen Kuo, Tay-Rong Chang, Su-Yang Xu, and Horng-Tay Jeng. Unconventional topological phase transition in non-symmorphic material KHgX (X = As, Sb, Bi). *npj Computational Materials*, 5(1):65, 2019.
- [233] M. Mofazzel Hosen, Klauss Dimitri, Ashis K. Nandy, Alex Aperis, Raman Sankar, Gyanendra Dhakal, Pablo Maldonado, Firoza Kabir, Christopher Sims, Fangcheng Chou, Dariusz Kaczorowski, Tomasz Durakiewicz, Peter M. Oppeneer, and Madhab Neupane. Distinct multiple fermionic states in a single topological metal. *Nature Communications*, 9(1):3002, 2018.
- [234] Hengbin Cheng, Yixin Sha, Rongjuan Liu, Chen Fang, and Ling Lu. Discovering Topological Surface States of Dirac Points. *Phys. Rev. Lett.*, 124:104301, Mar 2020.
- [235] Xiangxi Cai, Liping Ye, Chunyin Qiu, Meng Xiao, Rui Yu, Manzhu Ke, and Zhengyou Liu. Symmetry-enforced three-dimensional Dirac phononic crystals. *Light: Science & Applications*, 9(1):38, 2020.
- [236] Stefan Grimme. Semiempirical GGA-type density functional constructed with a long-range dispersion correction. *Journal of Computational Chemistry*, 27(15):1787–1799, 2006.
- [237] Daniela Pfister, Konrad Schäfer, Claudia Ott, Birgit Gerke, Rainer Pöttgen, Oliver Janka, Maximilian Baumgartner, Anastasia Efimova, Andrea Hohmann, Peer Schmidt, Sabarinathan Venkatachalam, Leo van Wüllen, Ulrich Schürmann, Lorenz Kienle, Viola Duppel, Eric Parzinger, Bastian Miller, Jonathan Becker, Alexander Holleitner, Richard Wehrich, and Tom Nilges. Inorganic Double Helices in Semiconducting SnIP. *Adv. Mater.*, 28(44):9783–9791, November 2016.
- [238] Liban M. A. Saleh, Rafal Dziedzic, and Alexander M. Spokoyny. An inorganic twist in nanomaterials: Making an atomically precise double helix. *ACS Cent. Sci.*, 2(10):685–686, October 2016.
- [239] André Utrap, Ng Yan Xiang, and Tom Nilges. A yield-optimized access to double-helical SnIP via a Sn/SnI₂ approach. *Journal of Crystal Growth*, 475:341–345, 2017.

- [240] Xinru Li, Ying Dai, Yandong Ma, Mengmeng Li, Lin Yu, and Baibiao Huang. Landscape of DNA-like inorganic metal free double helical semiconductors and potential applications in photocatalytic water splitting. *J. Mater. Chem. A*, 5(18):8484–8492, 2017.
- [241] Claudia Ott, Felix Reiter, Maximilian Baumgartner, Markus Pielmeier, Anna Vogel, Patrick Walke, Stefan Burger, Michael Ehrenreich, Gregor Kieslich, Dominik Daisenberger, Jeff Armstrong, Ujwal Kumar Thakur, Pawan Kumar, Shunda Chen, Davide Donadio, Lisa S. Walter, R. Thomas Weitz, Karthik Shankar, and Tom Nilges. Flexible and Ultrasoft Inorganic 1D Semiconductor and Heterostructure Systems Based on SnIP. *Adv. Funct. Mater.*, 29(18):1900233, May 2019.
- [242] Maximilian Baumgartner, Richard Weihrich, and Tom Nilges. Inorganic SnIP-Type Double Helices in Main-Group Chemistry. *Chem. Eur. J.*, 23(26):6452–6457, May 2017.
- [243] W. P. Su, J. R. Schrieffer, and A. J. Heeger. Soliton excitations in polyacetylene. *Phys. Rev. B*, 22:2099–2111, Aug 1980.
- [244] A Yu Kitaev. Unpaired Majorana fermions in quantum wires. *Physics-Uspekhi*, 44(10S):131–136, 2001.
- [245] Marcel Franz. Majorana’s wires. *Nature Nanotechnology*, 8(3):149–152, 2013.
- [246] Ulrich Müller. Die Symmetrie von Spiralketten. *Acta Crystallographica Section B*, 73(3):443–452, Jun 2017.
- [247] Hoi Chun Po, Ashvin Vishwanath, and Haruki Watanabe. Symmetry-based indicators of band topology in the 230 space groups. *Nature Communications*, 8(1):50, 2017.
- [248] Jorrit Kruthoff, Jan de Boer, Jasper van Wezel, Charles L. Kane, and Robert-Jan Slager. Topological classification of crystalline insulators through band structure combinatorics. *Phys. Rev. X*, 7:041069, Dec 2017.
- [249] Tiantian Zhang and Shuichi Murakami. Predicting topological materials: symmetry-based indicator theories and beyond. *Journal of Physics D: Applied Physics*, 54(41):414002, 2021.
- [250] Ryo Takahashi, Motoaki Hirayama, and Shuichi Murakami. Spinless hourglass nodal-line semimetals. *Phys. Rev. B*, 96:155206, Oct 2017.
- [251] Robert-Jan Slager, Andrej Mesaros, Vladimir Juričić, and Jan Zaanen. The space group classification of topological band-insulators. *Nature Physics*, 9(2):98–102, 2013.
- [252] Adrien Bouhon and Annica M. Black-Schaffer. Global band topology of simple and double Dirac-point semimetals. *Phys. Rev. B*, 95:241101, Jun 2017.
- [253] Ken Shiozaki, Masatoshi Sato, and Kiyonori Gomi. Topological crystalline materials: General formulation, module structure, and wallpaper groups. *Phys. Rev. B*, 95:235425, Jun 2017.

- [254] Barry Bradlyn, L. Elcoro, Jennifer Cano, M. G. Vergniory, Zhijun Wang, C. Felser, M. I. Aroyo, and B. Andrei Bernevig. Topological quantum chemistry. *Nature*, 547(7663):298–305, 2017.
- [255] Adrien Bouhon, Tomáš Bzdušek, and Robert-Jan Slager. Geometric approach to fragile topology beyond symmetry indicators. *Phys. Rev. B*, 102:115135, Sep 2020.
- [256] Junyeong Ahn, Sungjoon Park, and Bohm-Jung Yang. Failure of Nielsen-Ninomiya Theorem and Fragile Topology in Two-Dimensional Systems with Space-Time Inversion Symmetry: Application to Twisted Bilayer Graphene at Magic Angle. *Phys. Rev. X*, 9:021013, Apr 2019.
- [257] Junyeong Ahn and Bohm-Jung Yang. Symmetry representation approach to topological invariants in $C_{2z}T$ -symmetric systems. *Phys. Rev. B*, 99:235125, Jun 2019.
- [258] Apoorv Tiwari and Tomáš Bzdušek. Non-Abelian topology of nodal-line rings in \mathcal{PT} -symmetric systems. *Phys. Rev. B*, 101:195130, May 2020.
- [259] F. Nur Ünal, Adrien Bouhon, and Robert-Jan Slager. Topological Euler Class as a Dynamical Observable in Optical Lattices. *Phys. Rev. Lett.*, 125:053601, Jul 2020.
- [260] Adrien Bouhon, Annica M. Black-Schaffer, and Robert-Jan Slager. Wilson loop approach to fragile topology of split elementary band representations and topological crystalline insulators with time-reversal symmetry. *Phys. Rev. B*, 100:195135, Nov 2019.
- [261] QuanSheng Wu, Alexey A. Soluyanov, and Tomáš Bzdušek. Non-Abelian band topology in noninteracting metals. *Science*, 365(6459):1273, September 2019.
- [262] Bin Jiang, Adrien Bouhon, Zhi-Kang Lin, Xiaoxi Zhou, Bo Hou, Feng Li, Robert-Jan Slager, and Jian-Hua Jiang. Experimental observation of non-Abelian topological acoustic semimetals and their phase transitions. *Nature Physics*, 17(11):1239–1246, 2021.
- [263] Adrien Bouhon, Gunnar F. Lange, and Robert-Jan Slager. Topological correspondence between magnetic space group representations and subdimensions. *Phys. Rev. B*, 103:245127, Jun 2021.
- [264] Gunnar F. Lange, Adrien Bouhon, and Robert-Jan Slager. Subdimensional topologies, indicators, and higher order boundary effects. *Phys. Rev. B*, 103:195145, May 2021.
- [265] Bo Peng, Adrien Bouhon, Bartomeu Monserrat, and Robert-Jan Slager. Phonons as a platform for non-Abelian braiding and its manifestation in layered silicates. *Nature Communications*, 13(1):423, 2022.
- [266] Siyu Chen, Adrien Bouhon, Robert-Jan Slager, and Bartomeu Monserrat. Manipulation and braiding of Weyl nodes using symmetry-constrained phase transitions. *arXiv:2108.10330*, 2021.
- [267] Viktor Könye, Adrien Bouhon, Ion Cosma Fulga, Robert-Jan Slager, Jeroen van den Brink, and Jorge I. Facio. Chirality flip of Weyl nodes and its manifestation in strained MoTe_2 . *Phys. Rev. Research*, 3:L042017, Nov 2021.

- [268] Y. X. Zhao and Y. Lu. *PT*-Symmetric Real Dirac Fermions and Semimetals. *Phys. Rev. Lett.*, 118:056401, Feb 2017.
- [269] Benjamin J Wieder and B Andrei Bernevig. The axion insulator as a pump of fragile topology. *arXiv:1810.02373*, 2018.
- [270] Aron J. Beekman, Jaakko Nissinen, Kai Wu, Ke Liu, Robert-Jan Slager, Zohar Nussinov, Vladimir Cvetkovic, and Jan Zaanen. Dual gauge field theory of quantum liquid crystals in two dimensions. *Physics Reports*, 683:1–110, 2017.
- [271] Niklas Johansson and Erik Sjöqvist. Optimal Topological Test for Degeneracies of Real Hamiltonians. *Phys. Rev. Lett.*, 92:060406, Feb 2004.
- [272] Fang Xie, Zhida Song, Biao Lian, and B. Andrei Bernevig. Topology-bounded superfluid weight in twisted bilayer graphene. *Phys. Rev. Lett.*, 124:167002, Apr 2020.
- [273] Junyeong Ahn, Dongwook Kim, Youngkuk Kim, and Bohm-Jung Yang. Band Topology and Linking Structure of Nodal Line Semimetals with Z_2 Monopole Charges. *Phys. Rev. Lett.*, 121:106403, Sep 2018.
- [274] Thibault Sohier, Evgeniy Ponomarev, Marco Gibertini, Helmuth Berger, Nicola Marzari, Nicolas Ubrig, and Alberto F. Morpurgo. Enhanced electron-phonon interaction in multivalley materials. *Phys. Rev. X*, 9:031019, Aug 2019.
- [275] Thibault Sohier, Marco Gibertini, Matteo Calandra, Francesco Mauri, and Nicola Marzari. Breakdown of optical phonons’ splitting in two-dimensional materials. *Nano Lett.*, 17(6):3758–3763, June 2017.
- [276] Tomáš Bzdušek. Euler class of a pair of energy bands on a manifold with a boundary. *ResearchGate*, 2019.
- [277] Alexander M. Chebotarev and Alexander E. Teretenkov. Singular value decomposition for the Takagi factorization of symmetric matrices. *Applied Mathematics and Computation*, 234:380–384, 2014.
- [278] Ting Ting Song, Ming Yang, Jian Wei Chai, Martin Callsen, Jun Zhou, Tong Yang, Zheng Zhang, Ji Sheng Pan, Dong Zhi Chi, Yuan Ping Feng, and Shi Jie Wang. The stability of aluminium oxide monolayer and its interface with two-dimensional materials. *Scientific Reports*, 6(1):29221, 2016.
- [279] J. Zak. Berry’s phase for energy bands in solids. *Phys. Rev. Lett.*, 62:2747–2750, Jun 1989.
- [280] D. C. Gilmer, R. Hegde, R. Cotton, R. Garcia, V. Dhandapani, D. Triyoso, D. Roan, A. Franke, R. Rai, L. Prabhu, C. Hobbs, J. M. Grant, L. La, S. Samavedam, B. Taylor, H. Tseng, and P. Tobin. Compatibility of polycrystalline silicon gate deposition with HfO_2 and $\text{Al}_2\text{O}_3/\text{HfO}_2$ gate dielectrics. *Appl. Phys. Lett.*, 81(7):1288–1290, August 2002.
- [281] Kazuyuki Hirama, Hisashi Sato, Yuichi Harada, Hideki Yamamoto, and Makoto Kasu. Diamond Field-Effect Transistors with 1.3 A/mm Drain Current Density by Al_2O_3 Passivation Layer. *Jpn. J. Appl. Phys.*, 51:090112–, 2012.

- [282] Z. Ren, J. Zhang, J. Zhang, C. Zhang, S. Xu, Y. Li, and Y. Hao. Diamond Field Effect Transistors With MoO₃ Gate Dielectric. *IEEE Electron Device Letters*, 38(6):786–789, June 2017.
- [283] Hyuk-Min Kwon, Dae-Hyun Kim, and Tae-Woo Kim. Instability in In_{0.7}Ga_{0.3}As Quantum-Well MOSFETs with Single-Layer Al₂O₃ and Bi-Layer Al₂O₃/HfO₂ Gate Stacks Caused by Charge Trapping under Positive Bias Temperature (PBT) Stress. *Electronics*, 9(12):2039, 2020.
- [284] Li Zhang, Limin Huang, Stephen P. O’Brien, and Zhonghua Yu. Electrostatic doping-induced phonon shift of metallic single-wall carbon nanotubes. *J. Phys. Chem. C*, 112(51):20118–20122, December 2008.
- [285] Guru Khalsa and Nicole A. Benedek. Ultrafast optically induced ferromagnetic/antiferromagnetic phase transition in GdTio₃ from first principles. *npj Quantum Materials*, 3(1):15–, 2018.
- [286] Dominik M. Juraschek, Tomáš Neuman, Johannes Flick, and Prineha Narang. Cavity control of nonlinear phononics. *Phys. Rev. Research*, 3:L032046, Aug 2021.
- [287] Guru Khalsa, Nicole A. Benedek, and Jeffrey Moses. Ultrafast Control of Material Optical Properties via the Infrared Resonant Raman Effect. *Phys. Rev. X*, 11:021067, Jun 2021.
- [288] Miguel Borinaga, Ion Errea, Matteo Calandra, Francesco Mauri, and Aitor Bergara. Anharmonic effects in atomic hydrogen: Superconductivity and lattice dynamical stability. *Phys. Rev. B*, 93:174308, May 2016.
- [289] Mohamed Boukhicha, Matteo Calandra, Marie-Aude Measson, Ophelie Lancry, and Abhay Shukla. Anharmonic phonons in few-layer MoS₂: Raman spectroscopy of ultralow energy compression and shear modes. *Phys. Rev. B*, 87:195316, May 2013.
- [290] K. H. Michel, S. Costamagna, and F. M. Peeters. Theory of anharmonic phonons in two-dimensional crystals. *Phys. Rev. B*, 91:134302, Apr 2015.
- [291] Lucy D. Whalley, Jonathan M. Skelton, Jarvist M. Frost, and Aron Walsh. Phonon anharmonicity, lifetimes, and thermal transport in CH₃NH₃PbI₃ from many-body perturbation theory. *Phys. Rev. B*, 94:220301, Dec 2016.
- [292] Kunie Ishioka, Muneaki Hase, Masahiro Kitajima, Ludger Wirtz, Angel Rubio, and Hrvoje Petek. Ultrafast electron-phonon decoupling in graphite. *Phys. Rev. B*, 77:121402, Mar 2008.
- [293] Sven Reichardt and Ludger Wirtz. Nonadiabatic exciton-phonon coupling in Raman spectroscopy of layered materials. *Sci Adv*, 6(32):eabb5915, August 2020.
- [294] Chiara Trovatello, Henrique P. C. Miranda, Alejandro Molina-Sánchez, Rocío Borrego-Varillas, Cristian Manzoni, Luca Moretti, Lucia Ganzer, Margherita Maiuri, Junjia Wang, Dumitru Dumcenco, Andras Kis, Ludger Wirtz, Andrea Marini, Giancarlo Soavi, Andrea C. Ferrari, Giulio Cerullo, Davide Sangalli, and Stefano Dal Conte. Strongly Coupled Coherent Phonons in Single-Layer MoS₂. *ACS Nano*, 14(5):5700–5710, May 2020.

- [295] Daniel Karlsson, Robert van Leeuwen, Yaroslav Pavlyukh, Enrico Perfetto, and Gianluca Stefanucci. Fast Green's Function Method for Ultrafast Electron-Boson Dynamics. *Phys. Rev. Lett.*, 127:036402, Jul 2021.
- [296] Ady Stern. Non-Abelian states of matter. *Nature*, 464(7286):187–193, 2010.
- [297] Sankar Das Sarma, Michael Freedman, and Chetan Nayak. Topologically Protected Qubits from a Possible Non-Abelian Fractional Quantum Hall State. *Phys. Rev. Lett.*, 94:166802, Apr 2005.
- [298] Sankar Das Sarma, Chetan Nayak, and Sumanta Tewari. Proposal to stabilize and detect half-quantum vortices in strontium ruthenate thin films: Non-Abelian braiding statistics of vortices in a $p_x + ip_y$ superconductor. *Phys. Rev. B*, 73:220502, Jun 2006.
- [299] Liang Fu and C. L. Kane. Superconducting Proximity Effect and Majorana Fermions at the Surface of a Topological Insulator. *Phys. Rev. Lett.*, 100:096407, Mar 2008.
- [300] Thomas Iadecola, Thomas Schuster, and Claudio Chamon. Non-Abelian Braiding of Light. *Phys. Rev. Lett.*, 117:073901, Aug 2016.
- [301] Motohiko Ezawa. Non-Abelian braiding of Majorana-like edge states and topological quantum computations in electric circuits. *Phys. Rev. B*, 102:075424, Aug 2020.
- [302] Stevan Nadj-Perge, Ilya K. Drozdov, Jian Li, Hua Chen, Sangjun Jeon, Jungpil Seo, Allan H. MacDonald, B. Andrei Bernevig, and Ali Yazdani. Observation of Majorana fermions in ferromagnetic atomic chains on a superconductor. *Science*, 346(6209):602, October 2014.
- [303] Dongfei Wang, Lingyuan Kong, Peng Fan, Hui Chen, Shiyu Zhu, Wen Yao Liu, Lu Cao, Yujie Sun, Shixuan Du, John Schneeloch, Ruidan Zhong, Genda Gu, Liang Fu, Hong Ding, and Hong-Jun Gao. Evidence for Majorana bound states in an iron-based superconductor. *Science*, 362(6412):333–, October 2018.
- [304] Hao Zhang, Chun-Xiao Liu, Sasa Gazibegovic, Di Xu, John A. Logan, Guanzhong Wang, Nick van Loo, Jouri D. S. Bommer, Michiel W. A. de Moor, Diana Car, Roy L. M. Op het Veld, Petrus J. van Veldhoven, Sebastian Koelling, Marcel A. Verheijen, Mihir Pendharkar, Daniel J. Pennachio, Borzoyeh Shojaei, Joon Sue Lee, Chris J. Palmstrøm, Erik P. A. M. Bakkers, S. Das Sarma, and Leo P. Kouwenhoven. Retracted article: Quantized majorana conductance. *Nature*, 556(7699):74–79, 2018.
- [305] M. H. Milford and M. L. Jackson. Specific surface determination of expansible layer silicates. *Science*, 135(3507):929, March 1962.
- [306] J. M. Gales and S. D. Mahanti. Lattice-dynamical study of layered silicates. *Phys. Rev. B*, 40:12319–12327, Dec 1989.
- [307] U. Starke, J. Schardt, J. Bernhardt, and K. Heinz. Reconstructed oxide structures stable in air: Silicate monolayers on hexagonal SiC surfaces. *Journal of Vacuum Science & Technology A*, 17(4):1688–1692, July 1999.

- [308] Hui Guo, Xueyan Wang, Li Huang, Xin Jin, Zhenzhong Yang, Zhang Zhou, Hai Hu, Yu-Yang Zhang, Hongliang Lu, Qinghua Zhang, Chengmin Shen, Xiao Lin, Lin Gu, Qing Dai, Lihong Bao, Shixuan Du, Werner Hofer, Sokrates T. Pantelides, and Hong-Jun Gao. Insulating SiO₂ under Centimeter-Scale, Single-Crystal Graphene Enables Electronic-Device Fabrication. *Nano Lett.*, 20(12):8584–8591, December 2020.
- [309] J. Weissenrieder, S. Kaya, J.-L. Lu, H.-J. Gao, S. Shaikhutdinov, H.-J. Freund, M. Sierka, T. K. Todorova, and J. Sauer. Atomic Structure of a Thin Silica Film on a Mo(112) Substrate: A Two-Dimensional Network of SiO₄ Tetrahedra. *Phys. Rev. Lett.*, 95:076103, Aug 2005.
- [310] Hiroshi Tochihara, Tetsuroh Shirasawa, Takayuki Suzuki, Toshio Miyamachi, Takashi Kajiwara, Kazuma Yagyū, Shunsuke Yoshizawa, Toshio Takahashi, Satoru Tanaka, and Fumio Komori. Scanning tunneling microscopic and spectroscopic studies on a crystalline silica monolayer epitaxially formed on hexagonal SiC(0001) surfaces. *Appl. Phys. Lett.*, 104(5):051601, February 2014.
- [311] Pinshane Y. Huang, Simon Kurasch, Anchal Srivastava, Viera Skakalova, Jani Kottakoski, Arkady V. Krasheninnikov, Robert Hovden, Qingyun Mao, Jannik C. Meyer, Jurgen Smet, David A. Muller, and Ute Kaiser. Direct imaging of a two-dimensional silica glass on graphene. *Nano Lett.*, 12(2):1081–1086, February 2012.
- [312] Shamil Shaikhutdinov and Hans-Joachim Freund. Ultrathin silica films on metals: The long and winding road to understanding the atomic structure. *Adv. Mater.*, 25(1):49–67, January 2013.
- [313] Leonid Lichtenstein, Markus Heyde, and Hans-Joachim Freund. Crystalline-vitreous interface in two dimensional silica. *Phys. Rev. Lett.*, 109:106101, Sep 2012.
- [314] Pinshane Y. Huang, Simon Kurasch, Jonathan S. Alden, Ashivni Shekhawat, Alexander A. Alemi, Paul L. McEuen, James P. Sethna, Ute Kaiser, and David A. Muller. Imaging atomic rearrangements in two-dimensional silica glass: Watching silica’s dance. *Science*, 342(6155):224, October 2013.
- [315] Andrei Malashevich, Sohrab Ismail-Beigi, and Eric I. Altman. Directing the structure of two-dimensional silica and silicates. *J. Phys. Chem. C*, 120(47):26770–26781, December 2016.
- [316] M. Heyde, S. Shaikhutdinov, and H.-J. Freund. Two-dimensional silica: Crystalline and vitreous. *Chemical Physics Letters*, 550:1–7, 2012.
- [317] Chao Zhou, Xin Liang, Gregory S. Hutchings, Jin-Hao Jhang, Zachary S. Fishman, Rongting Wu, Adrian Gozar, Udo D. Schwarz, Sohrab Ismail-Beigi, and Eric I. Altman. Tuning two-dimensional phase formation through epitaxial strain and growth conditions: silica and silicate on Ni_xPd_{1-x}(111) alloy substrates. *Nanoscale*, 11(44):21340–21353, 2019.
- [318] Leonid Lichtenstein, Markus Heyde, and Hans-Joachim Freund. Atomic arrangement in two-dimensional silica: From crystalline to vitreous structures. *J. Phys. Chem. C*, 116(38):20426–20432, September 2012.

- [319] Shashank Mathur, Sergio Vlaic, Eduardo Machado-Charry, Anh-Duc Vu, Valérie Guisset, Philippe David, Emmanuel Hadji, Pascal Pochet, and Johann Coraux. Degenerate epitaxy-driven defects in monolayer silicon oxide on ruthenium. *Phys. Rev. B*, 92:161410, Oct 2015.
- [320] Torbjörn Björkman, Viera Skakalova, Simon Kurasch, Ute Kaiser, Jannik C. Meyer, Jürgen H. Smet, and Arkady V. Krasheninnikov. Vibrational Properties of a Two-Dimensional Silica Kagome Lattice. *ACS Nano*, 10(12):10929–10935, December 2016.
- [321] Nina F. Richter, Felix E. Feiten, Jagriti Pal, Agata Plucienik, Emre Emmez, Shamil Shaikhutdinov, Helmut Kuhlenbeck, Thomas Risse, Hans-Joachim Freund, Itziar Goikoetxea, Radosław Włodarczyk, and Joachim Sauer. Characterization of phonon vibrations of silica bilayer films. *J. Phys. Chem. C*, 123(12):7110–7117, March 2019.
- [322] Jorge Anibal Boscoboinik, Xin Yu, Bing Yang, Frank Daniel Fischer, Radosław Włodarczyk, Marek Sierka, Shamil Shaikhutdinov, Joachim Sauer, and Hans-Joachim Freund. Modeling zeolites with metal-supported two-dimensional aluminosilicate films. *Angew. Chem. Int. Ed.*, 51(24):6005–6008, June 2012.
- [323] R. Włodarczyk, M. Sierka, J. Sauer, D. Löffler, J. J. Uhlrich, X. Yu, B. Yang, I. M. N. Groot, S. Shaikhutdinov, and H.-J. Freund. Tuning the electronic structure of ultrathin crystalline silica films on Ru(0001). *Phys. Rev. B*, 85:085403, Feb 2012.
- [324] Geoffroy Kremer, Juan Camilo Alvarez Quiceno, Simone Lisi, Thomas Pierron, César González, Muriel Sicot, Bertrand Kierren, Daniel Malterre, Julien E. Rault, Patrick Le Fèvre, François Bertran, Yannick J. Dappe, Johann Coraux, Pascal Pochet, and Yannick Fagot-Revurat. Electronic Band Structure of Ultimately Thin Silicon Oxide on Ru(0001). *ACS Nano*, 13(4):4720–4730, April 2019.
- [325] Geoffroy Kremer, Juan Camilo Alvarez-Quiceno, Thomas Pierron, César González, Muriel Sicot, Bertrand Kierren, Luc Moreau, Julien E Rault, Patrick Le Fèvre, François Bertran, Yannick J Dappe, Johann Coraux, Pascal Pochet, and Yannick Fagot-Revurat. Dispersing and semi-flat bands in the wide band gap two-dimensional semiconductor bilayer silicon oxide. *2D Materials*, 8(3):035021, 2021.
- [326] Enlai Gao, Bo Xie, and Zhiping Xu. Two-dimensional silica: Structural, mechanical properties, and strain-induced band gap tuning. *Journal of Applied Physics*, 119(1):014301, January 2016.
- [327] Franz Bamer, Firaz Ebrahim, and Bernd Markert. Athermal mechanical analysis of Stone-Wales defects in two-dimensional silica. *Computational Materials Science*, 163:301–307, 2019.
- [328] Christin Büchner and Markus Heyde. Two-dimensional silica opens new perspectives. *Progress in Surface Science*, 92(4):341–374, 2017.
- [329] Ferdaous Ben Romdhane, Torbjörn Björkman, Julio A. Rodríguez-Manzo, Ovidiu Cretu, Arkady V. Krasheninnikov, and Florian Banhart. In situ growth of cellular two-dimensional silicon oxide on metal substrates. *ACS Nano*, 7(6):5175–5180, June 2013.

- [330] Dogan Kaya. The effect of electric field on a fullerene molecule on a metal surface by a nano STM tip. *Physica B: Condensed Matter*, 557:126–131, 2019.
- [331] M. Shishkin and G. Kresse. Implementation and performance of the frequency-dependent *GW* method within the PAW framework. *Phys. Rev. B*, 74:035101, Jul 2006.
- [332] M. van Schilfgaarde, Takao Kotani, and S. Faleev. Quasiparticle Self-Consistent *GW* Theory. *Phys. Rev. Lett.*, 96:226402, Jun 2006.
- [333] M. Shishkin and G. Kresse. Self-consistent *GW* calculations for semiconductors and insulators. *Phys. Rev. B*, 75:235102, Jun 2007.
- [334] M. Shishkin, M. Marsman, and G. Kresse. Accurate Quasiparticle Spectra from Self-Consistent *GW* Calculations with Vertex Corrections. *Phys. Rev. Lett.*, 99:246403, Dec 2007.
- [335] F. Fuchs, J. Furthmüller, F. Bechstedt, M. Shishkin, and G. Kresse. Quasiparticle band structure based on a generalized Kohn-Sham scheme. *Phys. Rev. B*, 76:115109, Sep 2007.
- [336] Julia Wiktor, Ursula Rothlisberger, and Alfredo Pasquarello. Predictive determination of band gaps of inorganic halide perovskites. *J. Phys. Chem. Lett.*, 8(22):5507–5512, November 2017.
- [337] V. M. Fridkin, I. I. Groshik, V. A. Lakhovizkaya, M. P. Mikhailov, and V. N. Nosov. Current saturation and photoferroelectric effect in SbSI. *Applied Physics Letters*, 10(12):354–356, 1967.
- [338] B. Kundys, M. Viret, D. Colson, and D. O. Kundys. Light-induced size changes in BiFeO₃ crystals. *Nature Materials*, 9(10):803–805, 2010.
- [339] Tzu-Chiao Wei, Hsin-Ping Wang, Heng-Jui Liu, Dung-Sheng Tsai, Jr-Jian Ke, Chung-Lun Wu, Yu-Peng Yin, Qian Zhan, Gong-Ru Lin, Ying-Hao Chu, and Jr-Hau He. Photostriction of strontium ruthenate. *Nature Communications*, 8(1):15018, 2017.
- [340] Hongrui Fu, Yingang Wang, Hao Guo, Yulun Lu, Neng Wang, Huan Zheng, and Fugang Chen. Boosting the photostriction properties of (K_{0.5}Na_{0.5})NbO₃-based ceramics modulated by introducing Ba(Ni_{0.5}Nb_{0.5})O₃- δ . *J. Mater. Chem. C*, 8(17):5904–5912, 2020.
- [341] B. Kundys. Photostrictive materials. *Applied Physics Reviews*, 2(1):011301–, January 2015.
- [342] Charles Paillard, Bin Xu, Brahim Dkhil, Grégory Geneste, and L. Bellaïche. Photostriction in ferroelectrics from density functional theory. *Phys. Rev. Lett.*, 116:247401, Jun 2016.
- [343] Charles Paillard, Sergey Prosandeev, and L. Bellaïche. Ab initio approach to photostriction in classical ferroelectric materials. *Phys. Rev. B*, 96:045205, Jul 2017.

- [344] Raad Haleoot, Charles Paillard, Thaneshwor P. Kaloni, Mehrshad Mehboudi, Bin Xu, L. Bellaiche, and Salvador Barraza-Lopez. Photostrictive two-dimensional materials in the monochalcogenide family. *Phys. Rev. Lett.*, 118:227401, May 2017.
- [345] Xiang-Feng Zhou, Artem R. Oganov, Zhenhai Wang, Ivan A. Popov, Alexander I. Boldyrev, and Hui-Tian Wang. Two-dimensional magnetic boron. *Phys. Rev. B*, 93:085406, Feb 2016.
- [346] Tzu-Chiao Wei, Hsin-Ping Wang, Ting-You Li, Chun-Ho Lin, Ying-Hui Hsieh, Ying-Hao Chu, and Jr-Hau He. Photostriction of $\text{CH}_3\text{NH}_3\text{PbBr}_3$ Perovskite Crystals. *Adv. Mater.*, 29(35):1701789, September 2017.
- [347] Hsinhan Tsai, Reza Asadpour, Jean-Christophe Blancon, Constantinos C. Stoumpos, Olivier Durand, Joseph W. Strzalka, Bo Chen, Rafael Verduzco, Pulickel M. Ajayan, Sergei Tretiak, Jacky Even, Muhammad Ashraf Alam, Mercouri G. Kanatzidis, Wanyi Nie, and Aditya D. Mohite. Light-induced lattice expansion leads to high-efficiency perovskite solar cells. *Science*, 360(6384):67, April 2018.
- [348] Wenxin Mao, Christopher R. Hall, Stefano Bernardi, Yi-Bing Cheng, Asaph Widmer-Cooper, Trevor A. Smith, and Udo Bach. Light-induced reversal of ion segregation in mixed-halide perovskites. *Nature Materials*, 20(1):55–61, 2021.
- [349] Loreta A. Muscarella, Eline M. Hutter, Francesca Wittmann, Young Won Woo, Young-Kwang Jung, Lucie McGovern, Jan Versluis, Aron Walsh, Huib J. Bakker, and Bruno Ehrler. Lattice compression increases the activation barrier for phase segregation in mixed-halide perovskites. *ACS Energy Lett.*, 5(10):3152–3158, October 2020.
- [350] Ying-Bo Lu, Wei-Yan Cong, ChengBo Guan, Hui Sun, Yanqing Xin, Kunlun Wang, and Shumei Song. Light enhanced moisture degradation of perovskite solar cell material $\text{CH}_3\text{NH}_3\text{PbI}_3$. *J. Mater. Chem. A*, 7(48):27469–27474, 2019.
- [351] Ronen Gottesman, Laxman Gouda, Basanth S. Kalanoor, Eynav Haltzi, Shay Tirosh, Eli Rosh-Hodesh, Yaakov Tischler, Arie Zaban, Claudio Quarti, Edoardo Mosconi, and Filippo De Angelis. Photoinduced Reversible Structural Transformations in Free-Standing $\text{CH}_3\text{NH}_3\text{PbI}_3$ Perovskite Films. *J. Phys. Chem. Lett.*, 6(12):2332–2338, June 2015.
- [352] Dane W. DeQuilettes, Wei Zhang, Victor M. Burlakov, Daniel J. Graham, Tomas Leijtens, Anna Osherov, Vladimir Bulović, Henry J. Snaith, David S. Ginger, and Samuel D. Stranks. Photo-induced halide redistribution in organic-inorganic perovskite films. *Nature Communications*, 7(1):11683, 2016.
- [353] Hsinhan Tsai, Wanyi Nie, and Aditya D. Mohite. Response to Comment on “Light-induced lattice expansion leads to high-efficiency solar cells”. *Science*, 368(6488):eaba6295, April 2020.
- [354] Nicholas Rolston, Ross Bennett-Kennett, Laura T. Schelhas, Joseph M. Luther, Jeffrey A. Christians, Joseph J. Berry, and Reinhold H. Dauskardt. Comment on “Light-induced lattice expansion leads to high-efficiency perovskite solar cells”. *Science*, 368(6488):eaay8691, April 2020.

- [355] Yang Zhou, Lu You, Shiwei Wang, Zhiliang Ku, Hongjin Fan, Daniel Schmidt, Andriwo Rusydi, Lei Chang, Le Wang, Peng Ren, Liufang Chen, Guoliang Yuan, Lang Chen, and Junling Wang. Giant photostriction in organic-inorganic lead halide perovskites. *Nature Communications*, 7(1):11193, 2016.
- [356] Yongtao Liu, Anton V. Ievlev, Liam Collins, Nikolay Borodinov, Alex Belianinov, Jong K. Keum, Miaosheng Wang, Mahshid Ahmadi, Stephen Jesse, Kai Xiao, Bobby G. Sumpter, Bin Hu, Sergei V. Kalinin, and Olga S. Ovchinnikova. Light-ferroic interaction in hybrid organic-inorganic perovskites. *Adv. Optical Mater.*, 7(23):1901451, December 2019.
- [357] J. Faure, J. Mauchain, E. Papalazarou, M. Marsi, D. Boschetto, I. Timrov, N. Vast, Y. Ohtsubo, B. Arnaud, and L. Perfetti. Direct observation of electron thermalization and electron-phonon coupling in photoexcited bismuth. *Phys. Rev. B*, 88:075120, Aug 2013.
- [358] Shaohua Zhou, Changhua Bao, Benshu Fan, Hui Zhou, Qixuan Gao, Haoyuan Zhong, Tianyun Lin, Hang Liu, Pu Yu, Peizhe Tang, Sheng Meng, Wenhui Duan, and Shuyun Zhou. Pseudospin-selective floquet band engineering in black phosphorus. *Nature*, 614(7946):75–80, 2023.
- [359] Claudine Katan, Nicolas Mercier, and Jacky Even. Quantum and dielectric confinement effects in lower-dimensional hybrid perovskite semiconductors. *Chem. Rev.*, 119(5):3140–3192, March 2019.
- [360] Michael A. Becker, Roman Vaxenburg, Georgian Nedelcu, Peter C. Sercel, Andrew Shabaev, Michael J. Mehl, John G. Michopoulos, Samuel G. Lambrakos, Noam Bernstein, John L. Lyons, Thilo Stöferle, Rainer F. Mahrt, Maksym V. Kovalenko, David J. Norris, Gabriele Rainò, and Alexander L. Efros. Bright triplet excitons in caesium lead halide perovskites. *Nature*, 553(7687):189–193, 2018.
- [361] Suyeon Cho, Sera Kim, Jung Ho Kim, Jiong Zhao, Jinbong Seok, Dong Hoon Keum, Jaeyoon Baik, Duk-Hyun Choe, K. J. Chang, Kazu Suenaga, Sung Wng Kim, Young Hee Lee, and Heejun Yang. Phase patterning for ohmic homojunction contact in MoTe₂. *Science*, 349(6248):625, August 2015.
- [362] Lingxiang Hou, Xueping Cui, Bo Guan, Shaozhi Wang, Ruian Li, Yunqi Liu, Daoben Zhu, and Jian Zheng. Synthesis of a monolayer fullerene network. *Nature*, 606(7914):507–510, 2022.
- [363] Elena Meirzadeh, Austin M. Evans, Mehdi Rezaee, Milena Milich, Connor J. Dionne, Thomas P. Darlington, Si Tong Bao, Amymarie K. Bartholomew, Taketo Handa, Daniel J. Rizzo, Ren A. Wiscons, Mahniz Reza, Amirali Zangiabadi, Natalie Fardian-Melamed, Andrew C. Crowther, P. James Schuck, D. N. Basov, Xiaoyang Zhu, Ashutosh Giri, Patrick E. Hopkins, Philip Kim, Michael L. Steigerwald, Jingjing Yang, Colin Nuckolls, and Xavier Roy. A few-layer covalent network of fullerenes. *Nature*, 613(7942):71–76, 2023.
- [364] Daniele Pontiroli, Matteo Aramini, Mattia Gaboardi, Marcello Mazzani, Alessandra Gorreri, Mauro Riccò, Irene Margiolaki, and Denis Sheptyakov. Ionic conductivity in the Mg intercalated fullerene polymer Mg₂C₆₀. *Carbon*, 51:143–147, 2013.

- [365] Masashi Tanaka and Shoji Yamanaka. Vapor-Phase Growth and Structural Characterization of Single Crystals of Magnesium Doped Two-Dimensional Fullerene Polymer Mg_2C_{60} . *Crystal Growth & Design*, 18(7):3877–3882, July 2018.
- [366] J. Michael Gottfried. Molecular soccer balls connected to make a 2D material. *Nature*, 606:470–471, 2022.
- [367] H. W. Kroto, J. R. Heath, S. C. O’Brien, R. F. Curl, and R. E. Smalley. C_{60} : Buckminsterfullerene. *Nature*, 318(6042):162–163, 1985.
- [368] H. W. Kroto. The stability of the fullerenes C_n , with $n = 24, 28, 32, 36, 50, 60$ and 70 . *Nature*, 329(6139):529–531, 1987.
- [369] Harold Kroto. C_{60} , fullerenes, giant fullerenes and soot. *Pure and Applied Chemistry*, 62(3):407–415, 1990.
- [370] Nancy S. Goroff. Mechanism of fullerene formation. *Acc. Chem. Res.*, 29(2):77–83, February 1996.
- [371] J. J. Bernal, P. Haenecour, J. Howe, T. J. Zega, S. Amari, and L. M. Ziurys. Formation of Interstellar C_{60} from Silicon Carbide Circumstellar Grains. *The Astrophysical Journal Letters*, 883(2):L43, 2019.
- [372] Raphael M. Tromer, Luiz A. Ribeiro, and Douglas S. Galvão. A DFT study of the electronic, optical, and mechanical properties of a recently synthesized monolayer fullerene network. *Chemical Physics Letters*, 804:139925, 2022.
- [373] Linfeng Yu, Jinyuan Xu, Bo Peng, Guangzhao Qin, and Gang Su. Anisotropic optical, mechanical, and thermoelectric properties of two-dimensional fullerene networks. *J. Phys. Chem. Lett.*, 13(50):11622–11629, December 2022.
- [374] Danwen Yuan, Hanqi Pi, Yi Jiang, Yuefang Huand Liqin Zhou, Yujin Jia, Gang Su, Zhong Fang, Hongming Weng, Xinguo Ren, and Wei Zhang. Highly in-plane anisotropic optical properties of fullerene monolayers. *arXiv:2207.11366*, 2022.
- [375] Bo Peng. Monolayer fullerene networks as photocatalysts for overall water splitting. *J. Am. Chem. Soc.*, 144(43):19921–19931, November 2022.
- [376] Penghua Ying, Haikuan Dong, Ting Liang, Zheyong Fan, Zheng Zhong, and Jin Zhang. Atomistic insights into the mechanical anisotropy and fragility of monolayer fullerene networks using quantum mechanical calculations and machine-learning molecular dynamics simulations. *Extreme Mechanics Letters*, 58:101929, 2023.
- [377] Haikuan Dong, Chenyang Cao, Penghua Ying, Zheyong Fan, Ping Qian, and Yanjing Su. Anisotropic and high thermal conductivity in monolayer quasi-hexagonal fullerene: A comparative study against bulk phase fullerene. *arXiv:2208.03982*, 2022.
- [378] L.A. Ribeiro, M.L. Pereira, W.F. Giozza, R.M. Tromer, and Douglas S. Galvão. Thermal stability and fracture patterns of a recently synthesized monolayer fullerene network: A reactive molecular dynamics study. *Chemical Physics Letters*, 807:140075, 2022.

- [379] Bo Peng, Hao Zhang, Hezhu Shao, Zeyu Ning, Yuanfeng Xu, Gang Ni, Hongliang Lu, David Wei Zhang, and Heyuan Zhu. Stability and strength of atomically thin borophene from first principles calculations. *Materials Research Letters*, 5(6):399–407, November 2017.
- [380] Oleksandr I. Malyi, Kostiantyn V. Sopiha, and Clas Persson. Energy, phonon, and dynamic stability criteria of two-dimensional materials. *ACS Appl. Mater. Interfaces*, 11(28):24876–24884, July 2019.
- [381] Dongbao Luo, Ketao Yin, and Richard Dronskowski. Existence of BeCN₂ and Its First-Principles Phase Diagram: Be and C Introducing Structural Diversity. *J. Am. Chem. Soc.*, 144(11):5155–5162, March 2022.
- [382] Ioanna Pallikara, Prakriti Kayastha, Jonathan M Skelton, and Lucy D Whalley. The physical significance of imaginary phonon modes in crystals. *Electron. Struct.*, 4(3):033002, 2022.
- [383] Pasquale Pavone, Stefano Baroni, and Stefano de Gironcoli. $\alpha \leftrightarrow \beta$ phase transition in tin: A theoretical study based on density-functional perturbation theory. *Phys. Rev. B*, 57:10421–10423, May 1998.
- [384] Pasquale Pavone. Old and new aspects in lattice-dynamical theory. *Journal of Physics: Condensed Matter*, 13(34):7593–7610, 2001.
- [385] Akira Masago, Koun Shirai, and Hiroshi Katayama-Yoshida. Crystal stability of α - and β -boron. *Phys. Rev. B*, 73:104102, Mar 2006.
- [386] Michiel J. van Setten, Matthé A. Uijtewaal, Gilles A. de Wijs, and Robert A. de Groot. Thermodynamic stability of boron: The role of defects and zero point motion. *J. Am. Chem. Soc.*, 129(9):2458–2465, March 2007.
- [387] Ralf Peter Stoffel, Claudia Wessel, Marck-Willem Lumey, and Richard Dronskowski. Ab initio thermochemistry of solid-state materials. *Angew. Chem. Int. Ed.*, 49(31):5242–5266, July 2010.
- [388] R. F. Zhang, Z. J. Lin, Ho-Kwang Mao, and Yusheng Zhao. Thermodynamic stability and unusual strength of ultra-incompressible rhenium nitrides. *Phys. Rev. B*, 83:060101, Feb 2011.
- [389] Volker L. Deringer, Ralf P. Stoffel, and Richard Dronskowski. Thermochemical Ranking and Dynamic Stability of TeO₂ Polymorphs from Ab Initio Theory. *Crystal Growth & Design*, 14(2):871–878, February 2014.
- [390] Volker L. Deringer, Ralf P. Stoffel, and Richard Dronskowski. Vibrational and thermodynamic properties of GeSe in the quasiharmonic approximation. *Phys. Rev. B*, 89:094303, Mar 2014.
- [391] Mary Anne White, Anthony B. Cerqueira, Catherine A. Whitman, Michel B. Johnson, and Tadashi Ogitsu. Determination of phase stability of elemental boron. *Angew. Chem. Int. Ed.*, 54(12):3626–3629, March 2015.

-
- [392] Jonas Nyman, Orla Sheehan Pundyke, and Graeme M. Day. Accurate force fields and methods for modelling organic molecular crystals at finite temperatures. *Phys. Chem. Chem. Phys.*, 18(23):15828–15837, 2016.
- [393] Jonathan M. Skelton, Lee A. Burton, Fumiyasu Oba, and Aron Walsh. Chemical and lattice stability of the tin sulfides. *J. Phys. Chem. C*, 121(12):6446–6454, March 2017.
- [394] Ioanna Pallikara and Jonathan M. Skelton. Phase stability of the tin monochalcogenides SnS and SnSe: a quasi-harmonic lattice-dynamics study. *Phys. Chem. Chem. Phys.*, 23(35):19219–19236, 2021.
- [395] Christopher J. Bartel. Review of computational approaches to predict the thermodynamic stability of inorganic solids. *Journal of Materials Science*, 57(23):10475–10498, 2022.

